

Experimental and theoretical studies on the particle formation process of particles for the improvement of pulmonary drug delivery

by

Alberto Baldelli

A thesis submitted in partial fulfillment of the requirements for the degree of

Doctor of Philosophy

Department of Mechanical Engineering
University of Alberta

© Alberto Baldelli, 2016

Abstract

The formation of dry microparticles from evaporating solution droplets was investigated and analyzed. The particle formation involved the creation and production of spray dried microparticles used for the delivery of drugs to treat pulmonary diseases. Studies of particle formation were conducted using a monodisperse droplet chain, which was created using a piezoceramic dispenser with an inner diameter of 30 μm for all the cases analyzed. The initial droplets ranged from 70 to 100 μm , and the final dried microparticles ranged from 0.3 μm to 25 μm , a range relevant to pulmonary drug delivery. The distance between two consecutive droplets was recorded; from these parameters, the main properties of the particle formation process, such as density, mass, aerodynamic diameter, volume equivalent diameter and velocity, were obtained. Studies varied from crystallizing to non-crystallizing systems. For the first group, cellulose acetate butyrate (CAB) in acetone was chosen for its high molecular weight. Such a substance generates high Peclet numbers, a phenomenon previously not analyzed in a monodisperse droplet chain. Initial concentrations of 0.37 and 10 mg/ml were chosen. External temperatures of 30, 40, and 55 $^{\circ}\text{C}$ were selected.

For crystallizing systems, the material chosen for particle formation studies was sodium nitrate (NaNO_3). The reasons for this choice were the properties of NaNO_3 : its crystallinity, its chemical structure and its high solubility in water. The use of NaNO_3 as a solute allowed investigations of the time for crystallization, data unobtainable in prior experimental approaches. Systematic investigations of particle formation in the NaNO_3 system were conducted using an appropriate selection of independent variables and analytical techniques suitable to the evaluation of evaporation and particle properties,. The independent variables and levels were the concentrations

of the initial solution, which ranged from 5×10^{-5} mg/ml to 5 mg/ml, and the temperature of the drying gas, which ranged from 25 to 150 °C. The properties of the final dried particles most closely analyzed were density, void fraction, shell thickness, morphology and surface roughness. The analysis of morphology and roughness were correlated with cohesion forces between two microparticles.

Cohesion forces varied from 1 to 100 nN depending on size, roughness and asperities, and peak-to-peak distances of the microparticles. The microparticles selected ranged between 15 and 1 μm , in diameter, between 1710 and 1 nm in roughness, and between 7000 nm and 50 nm in asperities. The experimental results were compared with theoretical results in the literature and the Rabinovich model chosen as the best theoretical method of determining cohesion forces between two rough microparticles. A multicomponent particle formation process involved the formation of microparticles from more than one solute. The multicomponent particle formation has previously been poorly studied, despite its impact on the quality of respiratory drug delivery. Potassium nitrate (KNO_3), chosen for its similarities in molecular weight and solubility, was added to the evaporation of NaNO_3 droplets. Initial conditions of environmental temperatures of 50 and 100°C, concentrations of 1 to 10 mg/ml, and molar percentages of NaNO_3 and KNO_3 of 30:70, 50:50, and 70:30 influenced the time to reach saturation and, therefore, the distribution of chemical components on the shell of the final dried microparticles. The influence of the time to reach saturation on the distribution of final dried microparticles was verified. The solute with a shorter time to reach saturation composed the surface of the shell of final dried microparticles.

Preface

A portion of the work herein is the result of an international collaboration with the University of Bristol. Professor Jonathan Reid and his staff provided the viscosity values of NaNO_3 as a function of its mass fraction in water (data shown in Chapter 3). The remainder of Chapter 3 and all data shown in Chapters 2, 4, and 5 were personally obtained. From Chapter 2 to 5, the bases for the theoretical model were obtained from previous investigations [1, 2]. Results personally achieved include the theoretical implementation outlined in Chapter 3, and the experimental approaches described in Chapters 2, 3, 4 and 5. The technical apparatus referred to in Chapters 2 and 3 was built by my supervisor, Professor Reinhard Vehring, for earlier experiments presented elsewhere [2], while all other implementations shown in Chapters 2 and 3 were performed by myself.

The results presented in Chapter 2 have been published as “Analysis of the Particle Formation Process of Structured Microparticles,” Alberto Baldelli, Mohammed Boray, David Nobes, Reinhard Vehring, *Journal of Molecular Pharmaceutics*, 2015, 12 (8), pp 2562-2573. The results shown in Chapter 3 have been published as “Effect of Crystallization Kinetics on the Properties of Spray Dried Microparticles,” Alberto Baldelli, Rachael Miles, Rory M. Power, Jonathan Reid, Reinhard Vehring, *Aerosol Science and Technology*, 2016, 50 (7), pp 693-704. Chapter 4 shows results submitted to the journal *Colloids and Surfaces A: Physicochemical and Engineering Aspects* as “Analysis of Cohesion Forces of Monodisperse and Monomorph Microparticles”, Alberto Baldelli, Reinhard Vehring,. The results shown in Chapter 5 have been submitted to *Aerosol Science and Technology* as “Impact of Crystallization Kinetics on the Distribution of Chemical Components in Spray Dried Microparticles,” Alberto Baldelli, Reinhard Vehring.

To my beloved family

Acknowledgements

I would like to thank first of all Professor Reinhard Vehring for offering me the opportunity of a PhD program at a moment of great doubt and uncertainty in my career. He introduced me to the interesting field of particle engineering, in which I hope to continue to work in the future. His extensive guidance has dramatically improved my writing and research skills and my data-analysis and problem-solving abilities—all of them invaluable to my future career. I would also like to thank Professor Alidad Amirfazli for allowing me to start my doctorate at the University of Alberta, and Professors Majid Karimi of Indiana University of Pennsylvania and Alberto Salvadori of the University of Brescia, for supporting my earlier studies and enthusiastically helping me to find a PhD placement at a respected university.

I likewise wish to thank my colleagues Hui Wang, David Barona-Arias, Dr. Mohammed Boraey, James Ivey, and Nick Carrigy for always supporting me in times of need and providing me with greatly appreciated assistance in tackling the many scientific problems I encountered along the way. Further acknowledgements are due to those who in many ways enabled the success of my project: David Dibbs, who helped me build part of the experimental setup used, Shiau-Yin Wu, who taught me how to properly use an Atomic Microscope Force, Arlene Oatway, who helped me section some microparticles, and Peng Li and Anqiang He, who taught me the use of several analytical tools.

Finally, my heartfelt thanks to all those without whose love and moral support my scientific work would have been difficult, if not wholly impossible: my fiancée, Hale Oguzlu, who stood by me at every moment and helped me keep my psychological balance; my parents, Luisa and Sergio, who always believed in and pushed me to test my abilities; my aunt Luigina and uncle Paolo, my beloved sisters, Silva and Delia, and my grandmother Alda—all of them loving sources of my persistence and strength—and my adopted family, soon-to-be parents-in-law Şenğul and Nasip, and new sister, Gizem, all of whom have helped me increase my self-confidence through their full acceptance. Close friends as well as family have also been the source of my positive attitude towards life and this project; thus, I would like also to thank my dear friends Andrea, Marco, Diego, Fabio, Shichao, Vianey and Shadi.

Table of content

1	Introduction	1
1.1	Background.....	1
1.2	Generation of drug microparticles: Spray drying	3
1.3	Principles of particle formation	5
1.4	Techniques used to experimentally produce droplets and analyze the droplet evaporation	11
1.5	Analysis of a droplet evaporation: The monodisperse droplet chain method	13
1.6	Analysis of the properties of the final microparticles	14
1.7	Objectives and Experimental Approach.....	18
1.8	Thesis structure.....	18
2	Analysis of the Particle Formation Process of Structured Microparticles.....	21
2.1	Abstract	21
2.2	Nomenclature.....	21
2.3	Introduction	23
2.4	Experimental section.....	27
2.4.1	Chemicals	27
2.4.2	Experimental setup.....	27
2.4.3	Measurement and derivation of the droplet or particle diameter.....	31
2.4.4	Experimental determination of droplet or particle density and mass	33
2.4.5	Particle formation model.....	34
2.4.6	Uncertainty analysis	35
2.5	Result and discussion	36

2.5.1	Method suitability	36
2.5.2	Tracking of the particle formation process.....	37
2.6	Conclusion.....	44
2.7	Acknowledgements.....	45
3	Effect of Crystallization Kinetics on the Properties of Spray Dried Microparticles.....	46
3.1	Abstract	46
3.2	Introduction	46
3.3	Experimental section.....	49
3.3.1	Chemicals	49
3.3.2	Experimental setup.....	49
3.3.3	Measurement and derivation of the main parameters of the particle formation process.....	52
3.4	Results	57
3.5	Discussion.....	62
3.6	Conclusion.....	64
3.7	Acknowledgements.....	65
3.8	Supplemental Information	65
3.8.1	Experimental details.....	65
3.8.2	Experimental setup.....	65
4	Analysis of Cohesion Forces between Monodisperse Microparticles with Rough Surfaces.....	69
4.1	Abstract	69
4.2	Nomenclature.....	69
4.3	Introduction	70

4.4	Materials and methods	74
4.4.1	Chemicals	74
4.4.2	Methods.....	75
4.4.2.1	Generation of monodisperse microparticles.....	75
4.4.2.2	Microparticle characterization: SEM and FIB	75
4.4.2.3	AFM analyses.....	76
4.4.2.4	Surface energy analysis.....	78
4.4.3	Theory and Calculations.....	80
4.5	Results	83
4.6	Discussion.....	89
4.7	Conclusions	91
4.8	Acknowledgements.....	92

5 Control of the Radial Distribution of Chemical Components in Spray Dried Crystalline Microparticles.....93

5.1	Abstract	93
5.2	Introduction	93
5.3	Experimental section.....	96
5.3.1	Chemicals	96
5.4	Experimental approach.....	96
5.4.1.1	Monodisperse droplet chain	96
5.4.1.2	Microparticles characterization: final properties.....	96
5.4.1.3	Samples used for the TEM analysis.....	98
5.5	Theoretical approach.....	98
5.6	Results and Discussion.....	101
5.7	Conclusion.....	113

5.8	Acknowledgements.....	114
6	Conclusions.....	115
6.1	Main results	115
6.1.1	Theoretical developments.....	115
6.1.2	Experimental implementations	115
6.1.3	Particle formation analysis	115
6.2	Future recommendations	117
6.2.1	Experimental future developments	117
6.2.2	Theoretical future implementations	119
6.2.3	Particle formation future studies.....	120
	References.....	121
	Appendix A. Generation and monitoring size change of monodisperse droplets in a conditioned flow tube	143
	Appendix B. Particle formation process with a constant higher Peclet number	148
	Appendix C. Impact of the Crystallization Window on Properties of Spray Dried Microparticles	157
	Appendix D. Analysis of Cohesion Forces between Monodisperse Microparticles with Rough Surfaces.....	167
	Appendix E. Control on the Distribution of Chemical Components in Spray Dried Microparticles	171

List of Figures

Figure 1.1	Example of a monodisperse droplet chain achieved in experiments shown in Chapter 2. A few theoretical parameters are shown: initial concentration C_0 , initial volume V_0 , initial density ρ_0 , initial diameter d_0 , spacing between two consecutive droplets or particles Δy , diameter of droplets or particles at a time step t $d(t)$, settling velocity v_s , gas velocity v_G , final concentration C_f , final volume V_f , final density ρ_f and final diameter d_f	6
Figure 1.2	Diagram demonstrating the principle of operation of a piezoceramic dispenser. The voltage V causes compression of the piezoceramic. Consequently, the glass capillary is squeezed. Acoustic waves are created in the liquid contained. A portion of the liquid is pushed forward and a second portion is pushed backward. The forward portion generates a droplet.	14
Figure 1.3	Example of force curve of a common AFM force measurements. Five steps define the approach and the retract part of an AFM force measurement.	17
Figure 2.1	Schematic of the feeding and collection systems. The feeding system supplied the test solutions to the piezoceramic dispenser and consisted of valves, tubing, and a reservoir. The feeding system has the purpose to supply Clean Dry Air (CDA) and liquid to the piezoceramic dispenser. At the end of a flow tube dried microparticles were collected using hollowed SEM stubs onto which a filter was placed using a double-sided adhesive ring.	28
Figure 2.2	Schematic illustration of the imaging system.	30
Figure 2.3	Annotated example of a typical droplet chain image. Δy is the spacing between two consecutive droplets, d_0 the initial droplet diameter, $d(t)$ the diameter of a droplet at time t , v_s the settling velocity and v_g the velocity of the gas flow.	31
Figure 2.4	Comparison between the aerodynamic diameters obtained with the “Spacing” method and the “Imaging” method.	36
Figure 2.5	Comparison between the volume equivalent and the aerodynamic diameter for the cases considered: a) 0.37 mg/ml - 30°C, b) 10 mg/ml - 30°C, c) 10 mg/ml - 40°C and d) 10 mg/ml - 55°C. The first diameter ejected from the dispenser is omitted. The line indicates the linear fit to the first part of the volume equivalent diameter curve, indicating the initial evaporation rate	37

Figure 2.6 Droplet or particle density normalized by the true density of cellulose acetate butyrate as a function of time for different gas temperatures (a) and different initial concentrations (b).....	39
Figure 2.7 Change of the normalized droplet or particle mass for different drying temperatures.	40
Figure 3.1 Main components of the experimental setup. Liquid is fed to a piezoceramic dispenser, which produces a monodisperse droplet chain. This chain follows the streamline of a temperature regulated gas flow. Dried microparticles are collected at the bottom of the flow tube onto a Scanning Electron Microscope sample stub. The flow tube is double walled for insulation. The flow tube has a square cross section facilitating the recording of images of the droplet chain. The images are recorded using a pulsed diode laser that highlights the chain of droplets and a camera that can be moved vertically to image all the droplets in the chain.....	51
Figure 3.2 Viscosity as a function of mass fraction of sodium nitrate in an aqueous solution.	52
Figure 3.3 Determination of aerodynamic and volume equivalent diameter as a function of time in a droplet chain for a gas temperature of 25°C and an initial concentration of 5 mg/ml. The dashed line represents the final diameter of the dried particles. The dash-dot line is an approximation for a hypothetical constant evaporation rate case.	54
Figure 3.4 Particle density as a function of time during the particle formation process for three sample cases, 5 mg/ml at 25°C, 5×10^{-2} mg/ml at 75°C and 5×10^{-4} mg/ml at 125°C. The full black squares show the predicted time to reach saturation and the empty black squares the predicted time for onset of crystallization. The right part of each curve, described with full symbols, is obtained using Equation 3.5. The part of the curves, described with empty symbols, is obtained using Equation 3.4.	60
Figure 3.5 Predicted droplet surface concentration of NaNO ₃ as a function of time during the evaporation process. The horizontal dashed lines indicate the solubility limit; the vertical dashed lines the time to reach saturation.....	60
Figure 3.6 Relationship between the predicted time available for crystallization, ϵ and the final particle density normalized by the true density of the solute. For each line, the six data points are obtained increasing the concentration in the initial solution.	61

Figure 3.7 Crystallinity of the final particles as a function of crystallization window. Raman spectra of six typical cases are shown in the left panel. The right panel shows the normalized peak area of the crystal lattice mode at 96 and 185 cm^{-1} , a measure of order in the solid phase.62

Figure 4.1 Procedure to attach a microparticle on an AFM tipless cantilever: 1) dipping the cantilever into the glue , 2) removing excess glue, 3) verifying under a Confocal Scanning Microscope the glue amount, 4) pushing the cantilever downwards until the microparticle is contacted, 5) picking up the microparticle and 6) verifying that the microparticle is attached to the cantilever.78

Figure 4.2 Production steps of a flat and smooth substrate of sodium nitrate: 1) melting of sodium nitrate powder, 2) squeezing the molten sodium nitrate in between two glass microscope slides, 3) verifying the smoothness with a Confocal Scanning Microscope. The image shown has a magnification of 20x.79

Figure 4.3 Comparison between experimental results and theoretical predictions of the cohesion forces between two microparticles. The solid black columns indicate the experimental data.89

Figure 5.1 The particle density as a function of time during evaporation and particle formation for droplets with equal molar amounts of NaNO_3 and KNO_3 . The full symbol curves were calculated assuming no voids in the particle, i.e. a non-crystallizing system. The open symbol curves were calculated using the final diameter of the actual dry particles. The larger data point approximates the onset of shell formation..... 103

Figure 5.2 Particle density of the final dried microparticles as a function of the precipitation window for the component that first saturates on the surface. The continue lines indicate the true densities of KNO_3 and NaNO_3 108

Figure 5.3 Surface concentrations of NaNO_3 and KNO_3 in evaporating droplets as a function of time for the cases with initial concentration of 1 mg/ml at 50°C drying gas temperature and molar percentage of NaNO_3 of 30% or 70% or weight percentages of NaNO_3 of 26.5% or 66.2%. t_s indicates the time to reach saturation. On the right hand side, the plot of normalized surface saturation with the solubility of each solute is shown. The time to reach saturation is simply obtained when the ratio between surface concentration and solubility is equal to 1. The time for crystallization is reached in a

supersaturation level, around 1.6 for NaNO ₃ and 1.9 for KNO ₃ . The time for crystallization is all reached for a further ratio between the surface concentration and solubility.	109
Figure A. 1 Components of the system used to generate a monodisperse droplet chain.	143
Figure B. 1 Trend of the evaporation rate of acetone respect the wet bulb temperature. The polynomial equation is used to easily calculate the evaporation rate for different wet bulb temperatures.	148
Figure B. 2 Images of the monodisperse droplet chain for different frequencies of the piezoceramic dispenser. The droplets are composed of deionized water.	149
Figure B. 3 Images of the monodisperse droplet chain for the cases studies. In addition, a monodisperse droplet chain composed by pure acetone is shown for comparison purposes.	150
Figure B. 4 Microscope images of droplets or particles at different time steps of the particle formation process.	151
Figure B. 5 Aerodynamic diameter calculated with both Spacing and Imaging methods for the cases: 10 mg/ml at 30°C, 10 mg/ml at 40°C and 10 mg/ml at 55°C.	152
Figure B. 6 Trend of density and mass for the cases of 0.37 mg/ml at 30°C and 10 mg/ml at 30°C. The picture refers to the density curves. The comparison between the two cases shows the impact of the initial concentration on the particle formation process.	153
Figure B. 7 Trend of velocity in time for all the cases analyzed.	153
Figure B. 8 Differences between the theoretical method and experimental derivations. On the left hand side, the drying time is shown; on the right hand side, the time to reach saturation is shown. The results are shown for the cases of 10 mg/ml at the temperatures of 30, 40 and 55°C.	154
Figure C. 1 Graphical abstract of the main concept of this project. The solute distributes in the droplet during the particle formation process. According to the time allowed for crystallization the final dried microparticle changes in morphology.	157
Figure C. 2 Flow chart of the methods used and main parameters of the particle formation process found.	158

Figure C. 3 Drawing of the flow tube in the experiments to identify the impact of crystallization kinetics on the particle formation process. Few dimensions of the flow tube are shown. 158

Figure C. 4 Images of the highlighted monodisperse droplet chain for five reference cases. 160

Figure C. 5 Comparison between time-constant and time-variable models. The dashed line identifies the evaporation rate achieved with a time-constant model. The aerodynamic and volume equivalent diameter are obtained with a time-variable model. 161

Figure C. 6 Trend of final diameter and crystallization window. In addition, few main SEM images are connected with their respective cases. 162

Figure C. 7 On the left hand side, the trend of the density for each case is shown. Only the method concerning the voids in the forming particle is used. On the right hand side, the trend of mass for the same cases is shown. 165

Figure C. 8 Trend of time to reach saturation and density of the final dried microparticles. The cases shown are the main six sample cases shown in Chapter 3. 165

Figure C. 9 Raman spectroscopy of all the cases studied. The plots are separated according to the temperature of the external environment. 166

Figure C. 10 Trend of peak width, on the left, and the trend of peak height related to the crystallization window of each case studied. 166

List of tables

Table 2.1 Experimentally derived evaporation rate, initial droplet diameter, and droplet life time for the four cases considered	38
Table 2.2 Theoretical derivations of Peclet number (Pe), Enrichment (E) and the ratio between the time to reach saturation (τ_{sat}) and the drying time (τ_D).....	41
Table 2.3 Morphology analysis by SEM and FIB for the cases considered.....	42
Table 2.4 Sketch of the profiles for two main axes of the dried particles collected for the four cases analyzed.	43
Table 2.5 Densities of dry particles in kg/m^3 and ratio between the final density and the CAB true density (1250 kg/ m^3) for all the cases studied.....	44
Table 3.1 Experimental matrix with the predicted precipitation window (Δt_p) and crystallization window (Δt_c). The cases are distinguished by initial solution concentration (C_0) and drying gas temperature (T). The indicated errors were obtained by uncertainty propagation of the imaging resolution error.	57
Table 3.2 Focused Ion Beam (FIB) and Scanning Electron Microscope (SEM) images of the final dried microparticles. The cases are, from right to left, 5 mg/ml at 50°C , $5 \cdot 10^{-1} \text{ mg/ml}$ at 75°C , $5 \cdot 10^{-2} \text{ mg/ml}$ at 100°C and $5 \cdot 10^{-4} \text{ mg/ml}$ at 150°C . Final particle density and crystallization window are shown for each case.	58
Table 3.3 Comparison between predicted and experimentally observed void fractions of the final particles.....	59
Table 4.1 List of the five morphology types considered. Initial solution concentration, drying gas temperature, profile, particle diameter and crystallization window are shown for every case.	83
Table 4.2 Illustration of the morphology of the five types of microparticles. The morphology is analyzed with SEM, for the outside of the shell, and with FIB, for the inner side of the shell. Images of more than one microparticle are shown to demonstrate their similarity.	84
Table 4.3 Tapping mode AFM analysis of the surface morphology of the microparticles. The AFM images are shown in two and three dimensions using a scanning area of $0.0625 \mu\text{m}^2$	85

Table 4.4 Root mean squared roughness, R_q , in nm for the cases studied as a function of scanning area. The bolded cases are selected as $R_{q,1}$ in Equation 4.9.....	86
Table 4.5 Cohesion forces between pairs of microparticles of similar (bold) and dissimilar morphology. For selected cases, the comparison of adhesion forces between a microparticle and a glue drop is shown.	87
Table 5.1 SEM images showing surface morphology, including crystal size, of the dried microparticles.....	102
Table 5.2 Helium Ion Microscope images of sectioned microparticles dried from droplets with an initial concentration of 10 mg/ml.	105
Table 5.3 Low frequency shift Raman spectra of dried microparticles compared with the reference spectra of crystalline NaNO_3 and crystalline KNO_3 . Cases with initial concentration of 10 mg/ml are shown. Molar percentages are shown as a reference.	106
Table 5.4 SEM/EDX maps of the chemical components near the surface of the dried particles. Below each map the measured molar ratio of NaNO_3 to KNO_3 is listed together with the time differences between saturation and crystallization events for the components. Positive values indicate earlier saturation and crystallization for KNO_3	111
Table 5.5 Elemental composition across the shell of sectioned microparticles determined by S-TEM. Peaks shifted to the left represent the chemical components present on the surface. Cases with solution concentration of 10 mg/ml dried at 50°C for molar percentages of 70% of NaNO_3 and 30% of KNO_3 and 50% of NaNO_3 and 50% of KNO_3 .are shown.	113
Table B. 1 SEM images of a high magnification for the cases analyzed.	155
Table B. 2 SEM images for the cases 0.37 mg/ml at 30°C. Different magnifications are reported.	156
Table C. 1 Additional SEM images for each case studied. A scale bar is shown for each case.	163
Table D. 1 Examples of the morphology of the microparticles for each case studied. The morphology is shown in a 2D image.....	167
Table D. 2 SEM and AFM images of three cases studied. These cases are considered because they showed close values of precipitation window.	168
Table D. 3 List of asperities and Lamba values for the cases studied.	169

Table D. 4 Images of an example of contact angle between a flat surface of sodium nitrate and a drop of the three solvents used.....	170
Table E. 1 Examples of images of sectioned microparticles recorded with a TEM.	173

1 Introduction

1.1 Background

Studies in drug delivery are increasingly focusing on particle engineering [3-8], a fairly new discipline that brings together knowledge from such diverse areas as chemistry, biology, heat and mass transfer, thermo- and fluid dynamics, and aerosol science [9-11]. In the context of medicinal applications, the main goal of particle engineering is improving the efficiency and efficacy of the delivery of drug microparticles [7]. The field focuses on the generation of microparticles made of active drugs; these microparticles are commonly delivered to the patient's respiratory system in order to treat respiratory diseases [12].

The drugs are typically delivered to the patient through two pathways: nasal and oral airways [13, 14]. The most common delivery methods are inhalation and instillation [15-17]. Liquid instillation is used in critical care situations, typically for acute, life-threatening diseases such as pulmonary embolism or lung cancer [18]. By definition, this technique is invasive and rarely required. The most common technique for the delivery of drugs for pulmonary diseases is inhalation [19, 20]. The wide use of drug inhalation is attributable to its multiple advantages. For instance, compared to those of liquid instillation, the risks involved are minimal [21]. Furthermore, inhalation is a non-invasive treatment that patients can self-administer [22]. Like every technique, inhalation carries disadvantages, the main one being drug loss; typically a large portion of the drugs, whether through the nasal or the oral tract, does not reach the desired site of the lung [22].

The deposition of a drug occurs by five main physical mechanisms: impaction, settling, diffusion, interception and electrostatic deposition [23]. All five of these mechanisms are influenced by properties of drug microparticles, such as the particle's size, density and shape, as well as by the individual's airway geometry and breathing pattern [24]. For instance, it has been demonstrated that smaller particles can reach different locations in the respiratory tract [25], with particles in the range of 1 μm being able to reach deeper locations in the respiratory tract [25]. Other studies have demonstrated that particles with a greater size range but a lower density are able to reach the same positions in the respiratory tract: a structure that is porous or contains voids helps the microparticles to deposit further in the respiratory tract [26, 27]. Respiratory drugs can show different solid phases: crystalline, amorphous or a mixture of the two [28]. Each state can affect

efficacy and stability of respiratory drugs [28]. For example, proteins in a crystalline phase remain stable for a longer time during the delivery than they do in their amorphous phase [29]. On the other hand, amorphous spray-dried drugs may have a smaller and more homogenous particle size and a higher respirable fraction than mechanically micronized microcrystalline particles [30]. Consequently, for drugs containing more than one excipient, the shell composition is fundamental for the efficacy of delivery [31-33]. In fact, in some cases, if the shell is crystalline or amorphous, the excipient contained can reach a different place in the respiratory tract. Crystal size, morphology and roughness are factors which may affect cohesion forces between two particles or adhesion between a particle and the respiratory tract [34-36]. Low cohesion forces between two microparticles prevent their coagulation and therefore increase the range of the locations at which they deposit in the respiratory tract of a patient. According to experimental measurements and theoretical models, the roughness is inversely proportional to the value of cohesion forces between two microparticles [35]. Thus, for amorphous and smooth particles, the cohesion forces are low.

Since individual breathing patterns vary widely, studies of drug impaction generally use a healthy adult as a reference case [37]. The most important parameter for impaction is the Stokes number, which compares the characteristic time of the falling particle and the characteristic time of a flow or an obstacle [38]. Consequently, the impaction of drug microparticles can be influenced by parameters other than their properties, for instance, the quality of air flow or the presence of an obstacle in the individual's respiratory tract. Another parameter worth mentioning is the viscosity of the gas, which varies with the kind of gas at the site of impaction. In the respiratory tract, whether the particles are inhaled from the nose or from the mouth, streamlines are present with different directions according to the location in the respiratory tract. As a result, deposition by impaction depends on the ratio between the microparticles' stopping distance, which in turn depends on the properties of the microparticles and airway dimensions. In case of microparticles, impaction is the most important deposition mechanism in the large airways [39]. The settling is defined as the speed rate at which particles deposit. This parameter indicates the velocity at which particles fall in a fluid, therefore, it is dependent on the morphology and the size of the particles [40]. In small sections of the lungs, settling becomes more important due to a change in dimension in airways and velocities [41]. Submicrometer-sized particles are most likely to deposit on the walls of smaller airways since they follow the Brownian diffusion [42]. The mechanism of diffusion is negligible for large particles but it becomes heavily influential for particles with

diameters lower than 1 μm [24]. The systems of interception and electrostatic deposition are only relevant in particular cases [43, 44]. For greater efficacy of delivery, it is preferable for the deposition of microparticles of drugs to occur in smaller airways [24].

The inhalation of drugs can be achieved using one of three different devices: a metered dose inhaler (MDI), a dry powder inhaler (DPI) or a nebulizer [45]. All of these devices are widely used, their use being strongly dependent on the production company and the delivery aims [46]. The MDI is one of the original inhalation devices, and its structure is quite simple: it contains a canister, a metered valve and an actuator [47]. These three components allow the release of a precise quantity of drug. This renders the device useful for self-administration and reduces the risk of improper administration of the drugs [48, 49]. The formulation contained in an MDI is composed of a drug, a propellant and in some cases an excipient [50]. Compared to MDIs, DPIs reduce the risk of oropharyngeal deposition [51]. Delivering dry powders reduces the risk of oropharyngeal deposition [52], but they often require greater inhalation effort [53], which may be problematic for patients with impaired lung function [54]. Both MDI and DPI drawback is poor delivery efficiency. The third option of inhalation device is the nebulizer, which delivers the drugs through an aerosol mist [55]. The advantage of this option is in the efficiency of the drug delivery [56]. The nebulizer, though, is an expensive device [57]. Nebulizers necessitate also a long time, more than an hour, to deliver the required dose [58]. For this reason, patient compliance is an issue for home care scenarios [59].

1.2 Generation of drug microparticles: Spray drying

Generally, microparticles used in inhalers are generated through various techniques: spray freeze-drying [60-62], supercritical fluid technology [63-65], micro-crystallization [66-68], micronization [69-71] and spray drying [72-74]. Spray freeze-drying is commonly used in the food and pharmaceutical industries, particularly for drying heat-sensitive material [75]. The initial solution or suspension is atomized and quickly frozen, with subsequent evaporation of the solvent occurring through low-pressure sublimation [76]. The process needs to be performed under the triple point of water, or of the solvent chosen [60]. Spray freeze-drying is recognized as one of the best methods for the production of microparticles of high quality [61]. It is an important technique for cases where the preservation of heat labile components is required. This task is achieved through a long and complex process. First, the material is frozen at a low temperature, creating ice

crystals [77]. These crystals are then sublimated from a solid to a vapor phase. Thus three main steps are involved in spray freeze drying: atomization, freezing and drying [78]. Because the drying rate depends on the vapor pressure, the drying time lasts at least one day or more, generating extra costs [62], over and above those related to expensive equipment, such as cryogenic and vacuum freeze dryers. Supercritical fluid technology is an alternative for the production of drug microparticles [65]. A fluid is considered supercritical when its pressure and temperature exceed their critical values. This kind of fluid has unique properties; an increase of the pressure results in an increase in gas mass without modifying the viscosity. In addition, during the process many solvents exhibit increased solvency as they approach and exceed the critical point [79]. As a consequence, an advantage of the supercritical fluid technology is that the solvation power can be controlled by changing temperature and pressure values [80]. The drawback of the technology is the conditions required to reach the supercritical state. For some solvents, the supercritical state is reached only at high temperatures not compatible with pharmaceutical compounds [81]. In addition, the choice of the gases that can be used is limited [65].

Micronization refers to the reduction of drug particles to a size smaller than 10 μm [82] through the impact between two particles or between a particle and a solid surface [83]. The typical device used to produce micronized particles is the jet mill [84]. The dried powders produced show an increase in surface area, bioavailability and activity [85]. On the other hand, micronization offers a poor control over the properties such as size, shape and morphology, of the dried particles [86]. In addition, it is difficult to control the size distribution of the particles or the homogeneity of the solid phase [86]. A technique similar to micronization is micro-crystallization, which involves a more precisely controlled nucleation process [87]. Micro-crystallization is commonly used for the production of protein crystals; the rate of evaporation is tuned to adjust the crystallization and prevent desiccation [88]. Another method for controlling the crystallization process is tuning the supersaturation [89]. Because of its complexity, micro-crystallization is used only when necessary.

The use of spray drying for the production of drug microparticles has constantly increased in the last decade [90-94]. Spray drying allows rapid drying of liquids using hot gas [95]. It is the method most commonly used in the food and pharmaceutical industries [96, 97] to produce dry powders from liquid solutions. In most cases, the drying medium is air; in cases where the solvent or powder is flammable or easily oxidized, nitrogen may be used [98]. Spray drying allows a broad range of solute and solvent to be used for the production of drug microparticles [99]. A main component of

a spray dryer is the atomizer or nozzle; the choice of atomizer type largely governs the throughput and the droplet diameter distribution, both of which directly influence the size distribution of the final dried particles [100]. Different types of nozzles can be found in spray drying applications: rotary disk, pneumatic, swirl or ultrasonic [99]. The drying of the solvent is commonly achieved in two or more steps to reduce dust and increase the flowability of the final particles; this happens at the back end of a spray dryer using a fluidized bed [101]. The produced microparticles are typically collected in a drum, filter, or cyclone [102]. An important advantage of spray drying is the production throughput, which is higher compared to the techniques previously mentioned [103]. In addition, the losses incurred in the drying process are fewer than those of other techniques. Furthermore, spray drying offers precise control over the properties of the final dried microparticles [104]. This control is achieved using insights from experimental and theoretical studies on the particle formation process.

1.3 Principles of particle formation

The particle formation process occurs during the transformation of a solution droplet into a dried microparticle. The work of Vehring et al. provides a starting point for describing particle formation process [2]. The model they created is named VFL, after the last names of the authors [2] utilizes theory to describe the particle formation process and experimentation to validate its predictions.

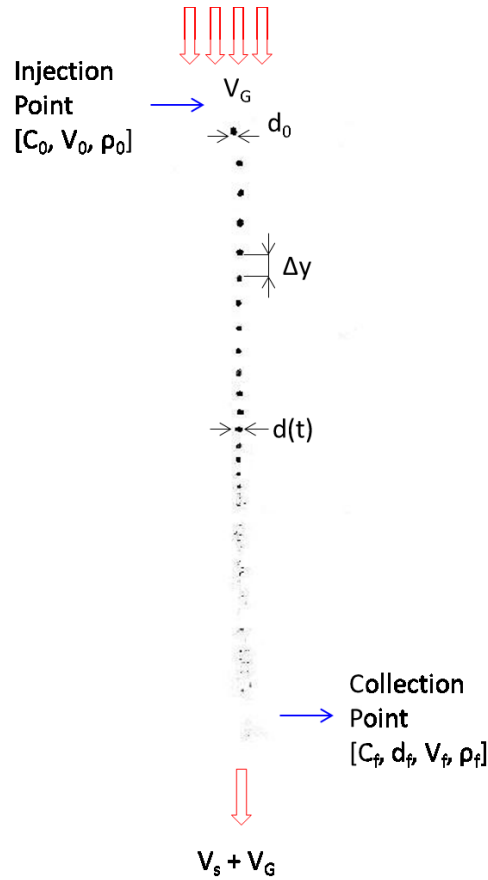


Figure 1.1 Example of a monodisperse droplet chain achieved in experiments shown in Chapter 2. A few theoretical parameters are shown: initial concentration C_0 , initial volume V_0 , initial density ρ_0 , initial diameter d_0 , spacing between two consecutive droplets or particles Δy , diameter of droplets or particles at a time step t $d(t)$, settling velocity v_s , gas velocity v_G , final concentration C_f , final volume V_f , final density ρ_f and final diameter d_f .

The process starts at the injection point, where the solution droplets are introduced into a drying gas flow, and ceases at the collection point, where the dried microparticles are collected. Injection and collection points are shown in Figure 1.1, together with important parameters. A droplet with initial diameter, d_0 , solute concentration, C_0 , volume, V_0 , and density, ρ_0 , is injected in a temperature and humidity controlled flow. The flow rate has an initial velocity, v_G , which increases when the droplets are injected. The droplets evaporation is governed by the diffusion between two events: the solvent evaporation and the solute distribution inside the droplet. Consequently, depending on the solute and solvent chosen and on the conditions of the evaporation process, the solute distributes on the surface and in the meantime the solvent leaves the droplet. When the solute reaches a critical amount on the surface, called supersaturation, the time of shell formation is imminent. The supersaturation state is strongly dependent on the solute and the evaporation

conditions chosen. The shell formation time identifies the moment in which the volume equivalent diameter of the droplets or particles is fixed. After this point, the diameter is fixed, since a shell has been formed. Other parameters, such as density or mass, can still change because of an evaporation of a possible solvent enclosed in the shell. In such cases, the enclosed solvent evaporates through the pores of a formed shell. Once the remaining solvent is null, the dried particles are collected and their properties, such as density, diameter, morphology, shell thickness and roughness, are analyzed.

As shown in Figure 1.1, different properties of the evaporation of the droplet can be measured using the VFL model. Droplets have a falling velocity called settling velocity, or v_s , which depends on the gravity and drag forces acting on the droplet. The equation governing the settling velocity is Equation 1.1, where, ρ_p , is the particle density, $d(t)$, is the diameter at the time step, t (shown in Figure 1.1), g , the gravitational acceleration and μ the dynamic viscosity of air.

$$v_s = \frac{\rho_p d(t)^2 g C_c}{18\mu} \quad \text{Equation 1.1}$$

C_c stays for the Cunningham factor. This factor is used for droplets with an aerodynamic diameter lower than 1 μm . C_c is used to account non continuum effects, when the Knudsen number is between the continuum regime and the free molecular path [105]. The diameter shown in Equation 1.1 is defined as the volume equivalent diameter, a variable introduced by the authors of the VFL model. This diameter consists of the diameter of a sphere with equivalent volume to the droplet or particle in question [106]. The volume equivalent diameter, d_v , differs from the aerodynamic diameter, d_a , which does not involve the density of the droplet or particle considered, ρ_p , [107]. Equation 1.2 shows the theoretical definition of the aerodynamic and volume equivalent diameters. As shown, the main difference between the two diameters is the consideration of the droplet density: the volume equivalent diameter contains information about the trend of the droplet density. In Equation 1.2, ρ^* , is the standard density of 1 g/cm^3 and χ the correction factor, lower or higher than 1 for non-spherical particles.

$$d_a = \sqrt{\frac{18\mu v_s}{\rho^* g}} \quad \text{Equation 1.2}$$

$$d_v = \sqrt{\frac{18\mu v_s}{\rho_p g \chi}}$$

The density of the droplets is an important parameter since it allows the derivation of other properties, such as mass or volume equivalent diameter. According to the VFL model and its implementation, the density is found using Equation 1.3. Equation 1.3 contains the assumption of a mostly liquid droplet. As a result, this equation cannot be used when the solute reaches a level of supersaturation. Equation 1.3 is used for time steps previous to the shell formation, where, m_l , is the mass of the solvent used, m_s , the mass of the solute, V_{tot} , the droplet total volume, $\rho_{t,l}$, the true density of the solvent, C_0 , the concentration of the initial solution, d_0 , the diameter of the initial injected droplet, and, $d(t)$, the diameter of the droplet at a time t . Equation 1.3 can be used only in case of a droplet mostly liquid.

$$\rho_p(t) = \frac{m_l + m_s}{V_{tot}} = \frac{\rho_{t,l}d(t)^3 + C_0d_0^3}{d(t)^3} = \rho_{t,l} + C_0 \left(\frac{d_0}{d(t)} \right)^3 \quad \text{Equation 1.3}$$

When the amount of solutes is becoming higher than the amount of the liquid, a different equation can be used to derive the density of droplets or particles. Equation 1.4 is used to determine the density of the particles after the point of shell formation.

$$\rho_p = \rho^* \left(\frac{d_a}{d_v} \right)^2 \quad \text{Equation 1.4}$$

After the density is determined, the mass of an evaporating droplet, $M(t)$, can be easily determined. Equation 1.5 defines the mass trend of an evaporating droplet.

$$M(t) = \frac{\pi\rho_p(t)d_v^3}{6} \quad \text{Equation 1.5}$$

The solvent evaporation is defined by the evaporation rate, κ , which is the velocity at which the liquid is leaving the droplet. Assuming a constant evaporation rate, Equation 1.6 can be used, where, f , is the frequency selected for the generation of each droplet. The assumption of a constant evaporation rate cannot be applied for several cases; the only case where this assumption can be used is when the trend of the evaporating volume equivalent diameter squared is linear. Otherwise, Equation 1.6 can be used only between two consecutive time steps.

$$\kappa = (d_0^2 - d(t)^2) \cdot f \quad \text{Equation 1.6}$$

The solute distribution is defined by the diffusion coefficient, D . The diffusion coefficient is derived by the Stokes-Einstein equation, Equation 1.7, where, T_w , is the wet bulb temperature, k_B , the Boltzmann constant and, r , is the droplet's radius.

$$D(t) = \frac{k_B T_w}{6\pi\mu(t)r} \quad \text{Equation 1.7}$$

The mutual tension of the solvent evaporation and the solute diffusivity is shown by the Peclet number, which is defined as the ratio between the evaporation rate and the diffusion coefficient of the solute. Previous studies have shown that, for cases with a constant evaporation rate, the Peclet number can predict the morphology of the final dried microparticles [2]. In this case, for instance, when the Peclet number is high, it is assumed that the evaporation rate is high and the diffusion coefficient low. As a result, the evaporation rate of the solvent is lower than the distribution of the solute on the surface; therefore, the final dried particles are expected to be solid and void free [2].

$$Pe(t) = \frac{\kappa(t)}{8D(t)} \quad \text{Equation 1.8}$$

Peclet number and Enrichment are two parameters of the VFL model used to predict the properties of final dried microparticles [2]. Enrichment is derived directly from the Peclet number and it can generate similar derivations for the properties of final dried particles. Enrichment can be considered as the ratio between the surface concentration and the medium concentration [2]. Equation 1.9 shows two methods to determine the Enrichment. The two methods differ from the applicable Peclet number. Boraey et al. observe that the trend of enrichment in time is considered to be in a steady state of low Peclet number. Therefore, they derived two companion equations to determine the enrichment number based on the value of the Peclet number, Equation 1.9 [1].

$$Pe < 20 \quad E = 1 + \frac{Pe}{5} + \frac{Pe^2}{100} - \frac{Pe^3}{4000} \quad \text{Equation 1.9}$$

$$Pe > 20 \quad E = \frac{Pe}{3} + \frac{4}{11}$$

Between the points of injection and collection, Figure 1.1, evaporation, saturation, nucleation, and crystallization may occur. The typical times associated with these mechanisms characterize the particle formation process; knowledge of them allows prediction of and control over the properties

of the final dried particles. The time of shell formation identifies the time at which a solute creates a shell; the final dry particle diameter may be established at this time. This process requires additional research in particle formation studies. In fact, the aerodynamic diameter becomes constant in the short phase between the time for shell formation and the drying time; this phase identifies the point when the solvent is completely evaporated [108]. For instance, the time to reach saturation normally happens close to the time for shell formation [36]. The time to reach saturation indicates the point at which the solutes distribute on the surface and saturate. This important time variable can be derived from the Enrichment, Equation 1.10. In Equation 1.10, S_0 , identifies the initial saturation, measured as the ratio between the initial concentration and the solubility of the solute in the solvent chosen. The difference between the time to reach saturation and the time to reach constant aerodynamic diameter, t_a , is called precipitation window, Δt_s .

$$t_s = \frac{d_0^2}{\kappa} \left(1 - (S_0 E)^{\frac{2}{3}} \right) \quad \text{Equation 1.10}$$

For cases where a solute with a tendency to crystallize is present in the evaporating droplet, additional time variables can be defined. The time of nucleation and time of crystallization, t_c , are important for the formation of particles from a crystalline solute. The time for nucleation identifies the moment in which the first nucleus is created. Further nuclei agglomerate until reaching a critical size, from which a crystal is formed and starts to grow; this point is called the time for crystallization. In this case, the particle formation process includes a sub-process called the crystallization process. The difference between the time for crystallization and the time to reach constant aerodynamic diameter, t_a , is called the crystallization window, Δt_c . According to crystallization theory, two phases are involved in the formation of crystals: nucleation and crystal growth [109]. Nucleation is the initial formation of solid crystal nuclei, upon which subsequent crystallization will proceed [110]. The process of nucleation can be identified as primary or secondary [111]. Primary nucleation occurs in the absence of other formed crystal in the solution [111]. Primary nucleation can also occur in cases when two or more crystals nucleate without interfering with each other [112]. If external impurities influence the process, the primary nucleation is described as induced; otherwise it is spontaneous [112]. Primary nucleation may cause secondary nucleation; secondary nucleation is activated when at least one existing crystal is present in the solution [113]. As previously mentioned, primary nucleation includes two main phases, the time of nucleation and the time of crystallization. The time of nucleation is the instant

at which the first nucleation occurs in a solution [114]. The time of crystallization is the instant at which the first crystal reaches a certain size, called a critical unit [115]. The critical unit identifies the limit at which the free energy of the system is decreased, determining whether the nucleus grows or dissolves [116]. The crystallization process is encountered in the production of drug microparticles [117-119]. This process is fundamental in understanding the relationship between the initial conditions of the particle formation process and the properties of the final dried particles. Boraey et al. [4] extended the VFL model to a larger range of Peclet number; additionally, variables describing particle morphology (shell thickness and the void fraction in the final dried particles) are predicted [1]. Equation 1.11 shows the prediction of the diameter of the voids possibly present in the generated dried microparticles.

$$d_s = d_f \sqrt[3]{1 - \frac{\rho_p}{\rho_T}} \quad \text{Equation 1.11}$$

In addition, the density of the final microparticles, ρ_f , can be derived. In Equation 1.12, d_f is the diameter of the final dried microparticles.

$$\rho_f = C_0 \left(\frac{d_0}{d_f} \right)^3 \quad \text{Equation 1.12}$$

The VFL model, containing its implementation, assumes that the main parameters are not affected by a change in time. Studies shown in Chapter 3 emphasize that, especially in cases of solutes prone to crystallization, the main variables, such as viscosity, diffusion coefficient, Peclet number, Enrichment and time to reach saturation, depend on time. These parameters change for every time step of the particle formation process. The dependence on time is due to the influence of the wet bulb temperature on the solubility limit and, especially, to the dependence of the viscosity on the mass fraction of solute. In these cases, a time-variable model is required to better predict the properties of the final dried microparticles. At every time step of the particle formation process, different values for the evaporation rate, Peclet number and Enrichment are calculated. In addition, a time-variable model is able to predict the main parameters between the shell formation and the collection point, a phase previously unknown. In these few milliseconds, the time to reach saturation, the time for nucleation and the time for crystallization are commonly reached.

1.4 Techniques used to experimentally produce droplets and analyze the droplet evaporation

Part of the studies of the particle formation process are based on the analysis of the evaporation process [120-122]. The formation of solid particles is dependent on the distribution of the solute inside the solvent and of the rate of evaporation of the solvent. The evaporation process can be observed experimentally using different techniques. The three main techniques involve droplets suspended on filaments [123-125], a single droplet [126-128] and a monodisperse droplet chain [129-131]. The technique involving droplets suspended on filaments is conducted as follows [132]. Millimeter sized droplets are suspended from filaments of a known material. Their weight and their size is recorded at several time increments [123]. This technique carries a few disadvantages. First, the size of the droplets used is in the millimeter range, a range not conducive to drug delivery, which are commonly in the micrometer range [133]. In addition, the experiments can be difficult to execute since placing a droplet on a filament is a challenging process. Moreover, the evaporation of such a droplet is influenced by the heat transfer between the droplet and the filament [133].

The single droplet method can be divided into two sub-methods: one involving a single droplet in a quiescent gas, and one a single droplet in a gas flow. Both of the two sub-methods involve the evaporation of one droplet; therefore, both methods present the drawback of a time limit. In fact, the evaporation of a single droplet in the millimeter range occurs in a few seconds; in common laboratory conditions, a droplet of 1 mm of H₂O takes about 2 seconds to evaporate [134]. The technique of evaporating a single droplet in a gas flow is rarely used due to its difficulties in the experimental process [135]. On the other hand, several researchers employ the method of a single droplet evaporating in a quiescent gas [136-138]. This method determines several important properties of droplets and particles and has enabled researchers to make several discoveries concerning the chemical reactivity, equilibrium size, composition and hygroscopicity of particles [139-142]. From the measurements obtained with this method, it is possible to describe the process that leads to the transformation of a particle through phase growth [139]. Different methods can be used to trap the droplet in a quiescent gas. One example is using radiation pressure. This method has an effect on the evaporating droplet; it accelerates in the direction of the applied radiation pressure [143]. Recently, several studies have used optical tweezers for the stabilization of a droplet in quiescent gas [144-146, 127]. The interest in this device has been growing also in the

field of aerosol science [147-149]. Optical tweezers focus the laser beam using a microscope objective lens forming a single beam gradient force; as a result, optical tweezers overcome the force balance problem encountered using radiation pressure [150]. A disadvantage of the device is the precision required to achieve reliable results. The droplet used has to remain homogenous, spherical or electrically charged [150].

1.5 Analysis of a droplet evaporation: The monodisperse droplet chain method

The third technique used to analyze the evaporation process involves the monodisperse droplet chain, as shown in Figure 1.2. The technique is used by researchers in diverse fields such as biology, MEMS, combustion and colloids chemistry [151-154]. The method entails the injection of uniform droplets into a gas flow. The injected droplets are of uniform diameter and composition. The temperature, humidity and flow rate of the gas flow are commonly controlled. Since the droplets and evaporation rate are uniform, the collected dried microparticles are expected to be homogeneous in their properties of diameter, density, morphology and chemical composition [155].

A monodisperse droplet chain can be produced using mainly three methods: a thermal dispenser, a vibrating orifice, or a piezoceramic dispenser [156-159]. Thermal dispensers take advantage of thermoelectric materials. When a voltage is applied, the thermoelectric material increases in temperature, generating bubbles of air inside the dispenser [160]. These air bubbles force the first droplet to be injected [161]. Thus, the number of air bubbles is directly proportional to the injection of the droplets and to the properties of the first injected droplet [162]. Another technique used for the production of monodisperse droplets is a vibrating orifice; this produces monodisperse droplets when voltage is applied, stimulating the orifice to vibrate. A vibrating orifice takes advantage of the piezoelectric properties of the material; when such material is supplied with voltage, it generates mechanical stress [163] by converting electrical energy to mechanical energy [164]. Piezoceramic materials yield large displacements relative to other piezoelectric materials. A commonly used piezoceramic is lead zirconate titanate (PZT) [165]. Normally, vibrating orifices are shaped as rings; therefore, when a voltage is applied, a shear stress is induced in the ring. The ring then shrinks and subsequently expands, allowing the emission of the solution contained in the dispenser [166]. Since vibrating orifices can generate consecutive droplets with a spacing on the

order of the droplet diameter [166], these devices have the disadvantage of a high chance of droplet coagulation. Consequently, piezoceramic dispensers are the most common technique used for the generation of monodisperse droplets [167-171].

Like vibrating orifices, piezoceramic dispensers take advantage of the piezoelectric effect. Piezoceramic dispensers typically consist of a tube-shaped piezoceramic element enclosing a micro-tube of glass [172]. When a voltage is applied, the piezoceramic element contracts. For each cycle of the piezoceramic element, a distortion to the glass micro-tube is caused. The minor distortion generates acoustic waves in the solution contained in the dispenser [173]. These acoustic waves divide the solution into two portions, one that moves forwards and one backwards. The forward portion is the injecting droplet [173], as shown in Figure 1.2. The injecting droplets have to overcome the capillary forces between the glass micro-tube and the solvent. Therefore, some applications require a slight positive pressure within the glass tube to expel droplets.

Additional information about the monodisperse droplet chain is reported in Appendix A.

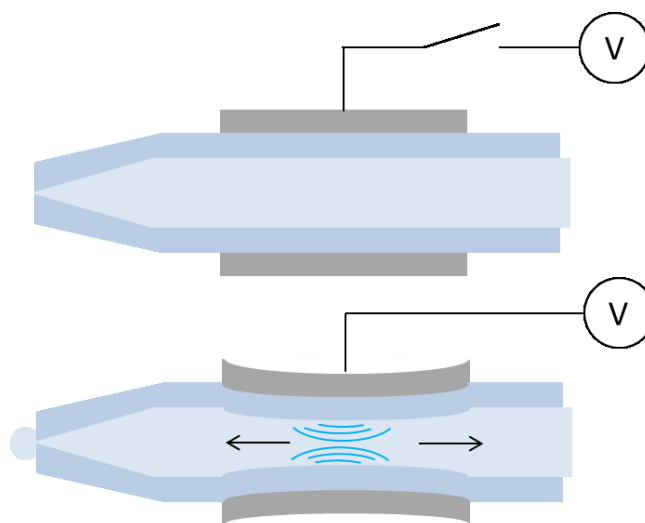


Figure 1.2 Diagram demonstrating the principle of operation of a piezoceramic dispenser. The voltage V causes compression of the piezoceramic. Consequently, the glass capillary is squeezed. Acoustic waves are created in the liquid contained. A portion of the liquid is pushed forwards and a second portion is pushed backwards. The forward portion generates a droplet.

1.6 Analysis of the properties of the final microparticles

A combination of experimental results and theoretical models can be used to describe the relationship between the initial conditions and the properties of the final dried particles. By

contrast, the properties of the produced dried microparticles are exclusively experimentally analyzed. Properties of final dried particles that influence the efficiency of the drug delivery are multiple; they include diameter, density, solid phase, distribution of the chemical compounds, crystal size, morphology, and roughness. All of these properties have a strong influence on the efficiency of drug delivery for respiratory diseases.

The diameter of the final dried microparticles is commonly analyzed using a Scanning Electron Microscope (SEM). SEM generates images of sample by scanning it with a focused electron beam [174]. The electrons interact with the sample surface and generate a signal that contains information about the topography of the sample [174]. SEM is the technique of choice for analyzing both the diameter and morphology of the final dried microparticle because it is affordable and familiar to the use. For the diameter analysis, a low magnification image is preferred in order to have an appreciable enough number of particles for a reliable standard deviation. For the morphology analysis, a high magnification is preferred in order to visualize the nano features on the surface of the microparticles. Final dried microparticles are collected onto a hollowed SEM stub. Subsequently, microparticles are gold sputtered with a layer of about 20 nm. Analysis of images obtained with the SEM allows the determination of the density of the final dried microparticles. The latter is obtained simply with a mass balance between the injection point and the collection point. SEM images can also provide clues to the crystal size of the final dried microparticles. Furthermore, SEM is the device used to determine the size distribution of the produced microparticles. Since the microparticles are monodisperse, the size distribution is narrow. The analysis of the particles size and their size distribution is reached using the software program ImageJ.

A better definition of the crystal size of final dried microparticles is achieved using an Atomic Force Microscope (AFM). AFM is a scanning probe microscopy that allows the determination and analysis of a small area of a sample. AFM focuses on the analysis of small forces, called Van der Waals forces. These forces are dominant at a short probe-sample distance. Different modes can be used in an AFM: tapping, contact and non-contact. The tapping mode is mostly used to analyze the morphology of the sample. In this mode, the cantilever, which is the probe, oscillates at a resonant frequency. The oscillation is kept at a constant amplitude and, therefore, the tip-sample interaction is maintained and an image of the sample is achieved [175]. This mode is useful for defining at a high resolution the morphology of the sample; on the other hand, imaging in liquid

is almost impossible [175]. The contact mode measures the repulsive Van der Waals forces. The cantilever deflection is constant and, thus, the forces between the surface and the cantilever are constant and the morphology of the particle is recorded. The contact mode is generally used to determine the forces between the cantilever and the surface. Furthermore, it is suggested for rough samples but not for fragile samples, since it could damage the morphology [176]. The last mode that AFM provides is the non-contact mode. This mode measures the attractive Van der Waals forces. The probe oscillates above the adsorbed fluid layer on the surface [176]. This method needs a feedback loop to understand any change in the amplitude and, thus, the surface topography is measured. This method is suitable for fragile samples since the cantilever never comes in contact with the sample. However, the measurement conditions are strict; an ultra-high vacuum environment is required in order to prevent the contaminant layer on the surface from interfering with the oscillations [176].

As previously mentioned, the AFM is used for measuring the forces between two materials; i.e the cantilever and the sample. The typical force curve of an AFM is well-known and it is shown in Figure 1.3. The cantilever is placed at a certain distance from the sample. The tip of the cantilever is then moved close to the sample, step 1. Once the cantilever is about 0.3 nm from the samples, forces attract it to the surface of the sample. These forces are called ‘snap in’ and are minor pull off forces. Subsequently, the cantilever is bended once in contact with the sample, step 2. Later, the cantilever starts detaching from the sample, step 3. At this point, stronger forces keep the cantilever attached to the sample, step 4. These forces are called ‘Maximum pull off forces’. Finally, the cantilever is removed from the sample and brought to its initial position, step 5.

The shell thickness and the density of the final dried microparticles are determined using two devices: Focus Ion Beam (FIB) and Helium Ion Microscopy (HIM). FIB has similar properties to SEM, previously introduced. The main difference is that FIB uses a ion beam focused on the sample [177]. The most common source used as ion beam is gallium. At high currents, high amount of material can be removed; this allows a precise milling. When the microparticles are cut, the shell thickness and the amount of voids can be recorded [177]. HIM is similar to FIB; the main difference is the kind of beam used. In HIM, a helium source is used. The high source of brightness and the short De Broglie wavelength of the helium ions, allow for qualitative data and images with higher resolution [178]. HIM allows imaging organic sample with a really low energy; thus the sample is less ruined compared when analyzed under an SEM.

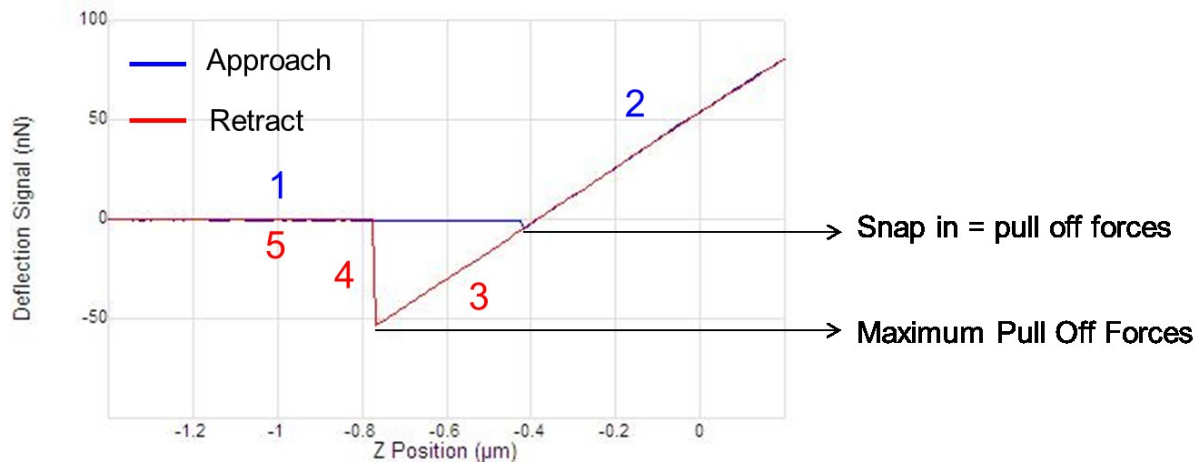


Figure 1.3 Example of force curve of a common AFM force measurements. Five steps define the approach and the retract part of an AFM force measurement.

Another property of the final monodisperse microparticles that has been widely analyzed is the solid phase. The solid phase has been analyzed using the technique of Raman spectroscopy, which is a spectroscopy technique commonly used in chemistry to understand the vibrational, rotational or other low frequency modes of each molecule [179]. Raman spectroscopy relies on an inelastic scattering of a monochromatic light source, commonly a laser. The laser interacts with molecular vibrations; thus, the photon energy is shifted up or down [179]. Electrons are moved temporally from their ground state to a vibrational state. The change in energy gives information about the vibrational mode of the molecule. If the energy of the emitted electron is higher than that of the scattered electron, the signal appears in the anti-Stokes region, otherwise in the Stokes region. The difficulty of this technique lies in separating the intense scattering light from the weak Raman signal [179]. Moreover, the Raman scattering has to be free of noise. For some material, the noise is mostly derived by fluorescence, which happens when an electron in an excited state emits energy returning to the ground state [179]. The Raman spectroscopy setup used to analyze the solid phase of final dried microparticles is a macro Raman spectroscopy. A macro Raman spectroscopy analyzes a bulk of particles. Macro Raman scattering is suitable to mostly all organic components, some used for the cure of pulmonary diseases, since most of the organic components are Raman active [180]. Furthermore, a micro Raman spectroscopy shows quantification errors. The sources of errors can be categorized into three types: instrument variations, errors introduced by the quantification methodology, and sample heterogeneity [181]. To decrease the error created by

sample inhomogeneity, the number of particle highlighted by the laser can be increased, as done in a macro Raman spectroscopy.

1.7 Objectives and Experimental Approach

Particle formation studies were achieved using a monodisperse droplet chain with a piezoceramic dispenser of an inner diameter of 30 μm . Initial droplet diameters varied from 70 to 100 μm for all the experiments. The generation frequency was constant at 50 Hz. Independent variables of interest included drying gas temperature and initial concentration of the solution. The range of the initial solutions varied from 5 mg/ml to 5×10^{-5} mg/ml. The range of gas temperatures varied from 25 to 150 $^{\circ}\text{C}$. Other input variables were maintained unmodified for the set of cases studied. The studies of the particle formation process can be categorized as follows:

1. Development of a time-variable model in which all the main parameters of the particle formation process are calculated at every time step.
2. Analysis of the particle formation process between the shell formation and the collection point.
3. Experimental measurement of a previously inaccessible parameter, the time for crystallization, and description of its relationship to the properties of final dried microparticles.
4. Development of correlations between the bulk properties of microparticles and values of the cohesion forces between two microparticles;
5. Description of the relationship between the evaporation rate of a multicomponent droplet and the distribution of species in residual particles.

1.8 Thesis structure

Two main systems are analyzed: non-crystallizing and crystallizing. Chapter 2 focuses on the first group; in this chapter, the mechanisms of the particle formation occurring between shell formation and cessation of drying are investigated. Because of the complexity of experimental tests and theoretical derivations, the physics occurring in this phase of particle formation are still sparsely studied. The relevant phenomena are studied using a combination of two methods: the “spacing” and the “imaging” method. The spacing method involves the determination of the distance between two consecutive droplets from images of the monodisperse droplet chain. By using results of a

steady-state constant evaporation model, key parameters governing the particle formation process are quantified. The imaging method uses a microscope lens to record images of each droplet of the monodisperse droplet chain. The volume equivalent diameter of every droplet of the chain is measured using the images. The volume equivalent diameter is compared with the aerodynamic diameter derived using the spacing method. The comparison allows the measurement of all droplet or particle density in the particle formation process. Experimental explorations of the part of the particle formation process between the shell formation and the collection point allow a deeper understanding of the morphology of the final dried microparticles.

The following chapters focus on crystallizing systems to investigate the crystallization sub-process of the particle formation process. Thus, in Chapter 3, the particle formation process of a crystalline solute, sodium nitrate, is analyzed theoretically and experimentally. The experiments allowed measurements of an important particle formation variable, the time for crystallization. This time variable is fundamental to predicting the properties of the final dried microparticles. To determine the time for crystallization, modifications of the steady-state model previously used are required. A time-variable model allowed key particle formation process variables to change at every time step, enabling a more complete description of the particle formation process. In order to determine the time to reach saturation and time for crystallization, the support of optical tweezers is required. The optical tweezers technique is used to record the bulk viscosity as a function of the mass fraction of sodium nitrate. Studies of the particle formation process of a solute that tends to crystallize show the impact of the time for crystallization on the properties of the final dried microparticles. High values of time for crystallization predict final microparticles with a smaller diameter, amorphous state, small quantities of voids and low roughness.

In Chapter 4, the relationship between the initial conditions of the particle formation process and the properties of the final dried microparticles is explored. The relationship between the initial conditions, environmental temperature and concentration and the cohesion forces between two microparticles are studied. The time to reach saturation and the time for crystallization are correlated with the roughness of the final microparticles. Experimental and theoretical methods are used to determine the cohesion forces between two microparticles. The experimental method involves the use of an Atomic Force Microscope (AFM), where one particle is placed on the cantilever and one on a flat surface. The theoretical method involves the derivation of the cohesion forces from the particle's physical properties (diameter, roughness, surface energy and asperities).

Different previously published theoretical models are evaluated. The comparison between experimental results and theoretical predictions determines the theoretical method that is the most consistent with the experimental results; the model most suitable can be used to analyze cohesion forces between two microparticles.

In Chapter 5, the particle formation process of a multicomponent solution is studied, and the relationships between the initial conditions and the radial distribution of the chemical components through the shell of the final dried microparticles are determined. Experimental tests of the distribution of the chemical components through the shell of final dried microparticles validate theoretical derivations achieved with a time-variable model, explained in previous chapters.

Chapter 6 summarizes the results and the key conclusions of the project and suggests possible directions for subsequent research.

2 Analysis of the Particle Formation Process of Structured Microparticles

The material shown in Chapter 2 has been previously published, [156]. The experiments have been personally conducted and the theory has been developed in previous publications, [1, 2]. The authors of this publication are me, my colleague Mohammed Boraey and my supervisor Reinhard Vehring. The material published is the following. Additional material is shown in Appendix B.

2.1 Abstract

The particle formation process for microparticles of cellulose acetate butyrate dried from an acetone solution was investigated experimentally and theoretically. A monodisperse droplet chain was used to produce solution microdroplets in a size range of 55-70 μm with solution concentrations of 0.37 and 10 mg/ml. While the droplets dried in a laminar air flow with temperatures of 30, 40 or 55°C the particle formation process was recorded by two independent optical methods. Dried particles in a size range of 10 to 30 μm were collected for morphology analysis, showing hollow, elongated particles whose structure was dependent on drying gas temperature and initial solution concentration. The setup allowed comprehensive measurements of the particle formation process, including the period after initial shell formation. The early particle formation process for this system was controlled by the diffusion of cellulose acetate butyrate in the liquid phase while later stages of the process were dominated by shell buckling and folding.

2.2 Nomenclature

C_0 , initial concentration of CAB in acetone [mg/ml];

D , diffusion coefficient of CAB in acetone [m^2/s];

$d(t)$, diameter of a droplet or particles at time t [μm];

d_a , aerodynamic diameter [μm];

d_0 , initial droplet diameter [μm];

d_T , diameter of the flow tube [m];

d_v , volume equivalent diameter [μm];
 E , surface enrichment;
 Δt , time step between two consecutive droplets in the droplet chain [μm];
 Δy , vertical spacing between two consecutive droplets in the droplet chain [μm];
 κ , droplet evaporation rate [$\mu\text{m}^2/\text{ms}$];
 f , droplet production frequency [Hz];
 g , gravitational acceleration [m^2/s];
 m_a , mass of acetone [kg];
 m_{CAB} , mass of cellulose acetate butyrate [kg];
 $M(t)$, mass of a droplet or particle at time t [kg];
 μ , drying gas dynamic viscosity [Pa s];
 Pe , Peclet number;
 ρ_0 , initial density of the solution droplet [kg/m^3];
 ρ_f , density of the dried microparticles [kg/m^3];
 ρ_p , density of droplets or particles in the monodisperse droplet chain [kg/m^3];
 $\rho_{t,a}$, true density of acetone [kg/m^3];
 ρ^* , standard density [kg/m^3];
 Q_G , drying gas flow rate [L/min];
 s_0 , initial solubility [mg/ml];
 S_0 , initial saturation;
 t , time [s];
 T_G ; temperature of gas flow [$^{\circ}\text{C}$];
 τ_D , droplet drying time [ms];
 τ_{sat} , saturation time [s];

V_0 , volume of the initial droplet of the droplet chain [m^3];

v_G , drying gas flow velocity [m^2/s];

v_s , droplet or particle settling velocity [m^2/s];

v_y , velocity of a falling droplet or particle [m^2/s];

χ , particle shape factor;

2.3 Introduction

Respiratory drug delivery is facilitated by aerosols whose dispersed phase consists of liquid or solid microparticles, typically in a size range of about 0.5 to 5 μm for pulmonary delivery, and sizes above 10 μm for nasal delivery applications [182]. Traditionally, many solid respirable dosage forms consisted of micronized active pharmaceutical ingredients in a crystalline form, optionally utilizing carrier particles, *e.g.*, consisting of lactose, to aid in the dispersion of a powder dose [183]. Lately, respiratory products have been marketed or are in development that rely on an expanded functionality of the delivered microparticles [184], providing, for example, reduced side effects via improved delivery efficiency [185], improved shelf life and environmental robustness via stabilization of labile or amorphous actives [186], including biologics, and controlled release or taste masking via encapsulation [187], etc. To accomplish these goals advanced pharmaceutical microparticles typically contain one or more excipients that address a specific design target and these microparticles are structured, *i.e.*, the particle surface and core have different composition, and, hence, may have different useful properties [188]. Furthermore, the particle density is frequently adjusted to improve aerosolization in dry powder inhalers, or achieve sufficient suspension stability in metered dose inhalers [189, 190].

Due to the complexity of the particle design task, a rational rather than empirical approach for dosage form development is needed. This rational approach is enabled by a rapidly growing discipline, particle engineering, which provides the required mechanistic understanding, improved process capabilities, and advanced analytical and experimental tools. A prerequisite for successful particle engineering is a fundamental comprehension of the process by which the microparticles are formed so that the process may be controlled to provide the desired particle properties [191, 192]. Many processing techniques for structured microparticles rely on drying of a droplet that comprises the active and the excipients in dissolved or suspended form. In this case the particle

formation process is the transition from a solution or suspension droplet to a dried solid particle [193]. During this process, the solvent evaporates and the solutes or suspended materials may remain either homogeneously mixed or may separate, *e.g.*, creating a core-shell morphology. For the latter particles the point in time during the drying process at which the shell is generated is called the “shell formation time” [194]. It is influenced by the physical and chemical properties of the solutes and the solvent and by the evaporation rate of the solvent [195].

Various techniques are used for the production of these microparticle drugs; examples include: spray freeze-drying [196-199], supercritical fluid technology [200-203], micro-crystallization [204-207] and spray drying [208, 95, 209, 210]. Evaporation of microdroplets is the underlying idea behind many of these techniques. At present, a common technique for the manufacture of structured microparticles is spray drying. Specifically for pharmaceutical applications, spray drying has several advantages: it can be conducted with minimal loss of activity of chemicals, a broad range of solutions or suspensions can be applied, and important properties of the final particles can be controlled [209]. In addition, interest in this technique is growing with the increase in the demand for smaller particles [101, 2] with more governable and defined properties.

A mechanistic understanding of the particle formation process is essential for the control and improvement of properties of pharmaceutical powders produced by spray drying [211]. As a result, in the last two decades, several studies have been conducted to investigate the particle formation process theoretically and experimentally [1, 212, 213, 193]. These studies focused mainly on the first part of the process which can be modeled as evaporation of a solution droplet. The solvent evaporation phase plays a key role in the particle formation process [214]. Four main techniques were used in these studies: observation of a single droplet in a quiescent gas, where one isolated droplet evaporates falling or while levitated, typically in a room temperature environment [215-218, 205, 159], analysis of droplets suspended from thin filaments, where several droplets evaporate while attached to a wire [219, 220, 124, 221], observation of a single droplet falling in a gas flow [222-225], where only one droplet evaporates in an air flow, and studies on monodisperse free falling droplets [129, 226-228], where a chain of droplets is injected into a gas flow. Several theoretical models have been developed that describe the process of evaporating single droplets falling in a gas flow [229-231, 224, 138], and evaporation of droplets in a monodisperse chain [232, 228, 233].

The droplet chain method has been demonstrated to be a good choice for the experimental study of evaporation processes, not only in spray drying, but also in other areas such as microfluidics, MEMS, combustion, and colloids chemistry [153, 154, 159, 234, 210]. This broad interest comes from its ability to overcome many of the drawbacks encountered in other techniques [235]. For droplet chain techniques evaporation measurements are feasible very shortly after generation of the droplet unlike in some single droplet techniques that require capture and stabilization of a droplet before measurements can commence. Particles do not need to remain homogenous, spherical, or electrically charged [233]. Techniques involving droplets suspended from thin filaments may bias evaporation rates by affecting heat conduction via the contact between the filament and the droplet. Also, filament techniques normally require droplets with diameters in the millimeter range, which undergo a different evaporation process compared to microdroplets relevant for inhalation applications [134].

A monodisperse droplet chain can be generated using a thermal dispenser, a vibrating orifice or a piezoceramic dispenser. The thermal dispenser has been used in several studies of inkjet printing [236-239], but rarely in the generation of monodisperse droplet chains [240, 241], because of bubble generation inside the dispenser. These bubbles interfere with the ejection of the droplets and the homogeneity of the droplet diameters in the chain [242]. The instrument most frequently used for the production of monodisperse droplet chains until the beginning of the last decade was the vibrating orifice generator [243-247]. The main benefit of this device is that it can produce monodisperse droplets in a broad size range. However, a vibrating orifice generates a very closely spaced droplet chain with a gap between two consecutive droplets on the order of only a few droplet diameters [235]. This can lead to droplet collisions and affects the mass transfer such that the evaporation rate is not representative of a single droplet. Piezoceramic dispensers provide a continuous and homogenous production of monodisperse droplets applying the piezoelectric effect [248]. The mechanical deformation of a piezoceramic tube in response to an electric signal creates acoustic waves in the liquid contained in the tube, expelling droplets in a reproducible manner, thus creating a monodisperse droplet chain with widely adjustable spacing.

The monodisperse chain technique has a fundamental role in particle formation studies. An analytical particle formation model was developed using experimental data from a droplet chain technique [2]. In this paper, Vehring et al. presented a partial theoretical description of the particle formation process, an experimental validation of different formation mechanisms for different

solutes and different process conditions, and a review of the most common techniques for manufacturing of microparticles. Boraey et al. [4, 1] refined the particle formation model adding new parameters to the theoretical derivations, *e.g.*, shell thickness of the dried particles. The two models, however, did not consider the particle formation process after the onset of shell formation and, thus, cannot describe an important part of the process: the evaporation of residual solvent contained by a shell.

The aim of the present work is to fill this gap by providing a more complete experimental analysis of the particle formation process, including the stage after the formation of a shell. The evaporation of acetone solution droplets of a polymer, cellulose butyrate acetate is investigated as a model case to demonstrate the capabilities of the new experimental approach. The choice of the solvent facilitates the experimental part. Acetone shows a relatively high evaporation rate at room temperature. A high evaporation rate encloses a short drying time, which ensures the drying of the droplet before the collection point. The choice of the solute relied on the properties of the CAB: its high solubility in acetone and its high molecular weight. The high solubility permits the inception of solutions with varying solute quantity, needed to study the effect of the initial concentration, and the high molecular weight promotes faster shell formation, leaving a reasonable period of time to investigate the evaporation process after shell formation. Besides, the use of CAB is of particular interest for this process because of its wide use in studies related to the improvement of the efficacy of drug delivery systems and controlled release applications [249-251].

2.4 Experimental section

2.4.1 Chemicals

Cellulose acetate butyrate (CAB) (catalog number 419044 – 500G, Sigma Aldrich, St Louis, MO, USA) was used; some of the properties analyzed and provided by the manufacturer are: molecular mass of about 65000 g/mol and true density of 1.25 g/ml at 25°C. Acetone (320110 – 1L ACS Reagent – 99.5% purity, Sigma Aldrich, St Louis, MO, USA) was used as the solvent, with a residual water content < 0.5%. The main physical properties of the acetone listed by the supplier are: vapor pressure of 24.4 kPa at 20°C and density of 0.791 g/ml at 25°C.

The solubility of CAB in acetone is a required input parameter for the particle formation model applied in this study. Therefore, the solubility was derived experimentally for three reference temperatures, which were the predicted steady state droplet temperatures for the chosen drying conditions. CAB was gradually added to 10 ml of acetone until the solution did not clear any more upon 3 hours of sonication and 1 hour of agitation on a wrist action shaker. The saturated solution stays in an environment at each reference temperature for 2 hours; undissolved mass was removed. The determined solubilities were 216 ± 2 mg/ml at 14 °C, 247 ± 2 mg/ml at 20.5 °C, and 258 ± 3 mg/ml at 27.5 °C. These droplet temperatures correspond to drying gas temperatures correspond to drying gas temperatures of 30, 40 and 55 °C, respectively [252].

To prepare CAB-acetone solutions, CAB was weighed out using an analytical balance (ME204E, Mettler Toledo, Mississauga, Ontario, Canada) and filled to volume with the solvent. The solution was closed with a paraffin film (PM992, Pechiney Plastic Packaging, Chicago, IL, U.S.) and agitated for 1.5 h on a wrist action shaker (Model 75, Burrell Scientific, Pittsburg, Pennsylvania, U.S.).

2.4.2 Experimental setup

An experimental system was developed to provide droplets -on-demand and consisted of three main systems: feeding, collection and optical, illustrated in Figure 2.1 and Figure 2.2. The feeding system was charged through filters (09-754-28, Corning PTFE 0.2 μ m, Fisher Scientific, Edmonton, AB, Canada) with a syringe (14-817-30, AirTite Norm-Jet Eccentric Luer Fisher Scientific, Edmonton, AB, Canada) filled with a solution. The solution was stored in an ‘S’-shaped reservoir with a volume of 2 ml, and entered a piezoceramic dispenser (MD-G-020K, Microdrop Technologies, Mühlenweg, Norderstedt, Germany) with an orifice diameter of 50 μ m. At the

initiation of droplet generation, it was necessary to apply additional pressure to overcome the capillary forces between the liquid and the glass tube of the droplet generator. For this purpose, the liquid feeding system was connected to a pressure regulated air supply (CDA) system.

The gas flow rate was measured with a flow meter (4000 Series, TSI, Shoreview, Minnesota, U.S.).

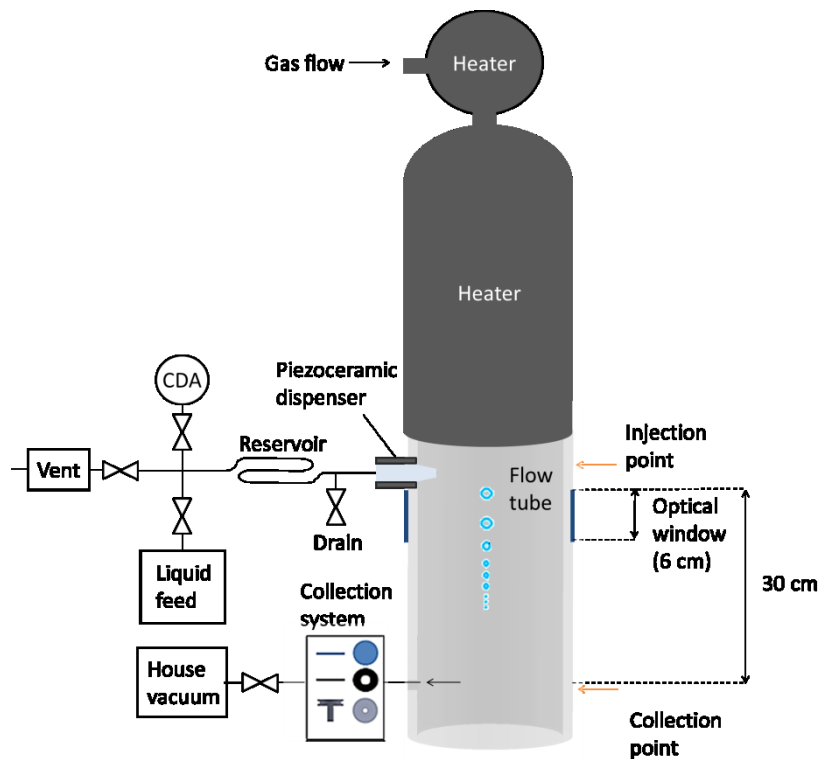


Figure 2.1 Schematic of the feeding and collection systems. The feeding system supplied the test solutions to the piezoceramic dispenser and consisted of valves, tubing, and a reservoir. The feeding system has the purpose to supply Clean Dry Air (CDA) and liquid to the piezoceramic dispenser. At the end of a flow tube dried microparticles were collected using hollowed SEM stubs onto which a filter was placed using a double-sided adhesive ring.

Two heaters were located on the top of the flow tube, warming the air to the required temperature. The temperature of the air was recorded at the droplet injection point and at a collection point at the end of the tube with two type K thermocouples (TFE-K-20, Omega Engineering, Laval, Quebec, Canada). The temperature difference between the two points ranged from 0°C, when the drying gas was at room temperature) to 10°C, when the drying gas was at 55°C. Temperature was monitored using a temperature controller (RK-89000-10, Digi-Sense, Cole Palmer, Laval, Quebec, Canada).

For the purpose of measuring the spacing between droplets, the droplet chain was illuminated with a diode laser (SNF-660 Lasiris, Coherent Co., Wilsonville, Oregon, U.S.) with a wavelength of

657 nm, entering through the bottom of the flow tube. The driver of the droplet generator controlled a pulse generator (4001, Global Specialties, Yorba Linda, California, U.S.) that triggered the laser pulses. Pulse width and spacing were adjusted to optimize stroboscopic illumination of the droplets. A digital camera (BM-500 GE GigE Vision, Pleora Technologies, Kanata, Ontario, Canada) recorded the droplet chain trajectory, including the spacing between the droplets. The camera was connected to a computer for capture and visualization of the images (JAI GigE Vision SDK and Control Tool, San Jose, California, U.S.). For calibration purposes images were recorded with a 1 mm resolution scale bar inserted in the center of the flow tube. The calibration process used a pixel resolution of $4.2 \times 10^{-2} \mu\text{m}/\text{pixel}$, a magnification of 3.5X, a field of view of 13.9° and a typical number of pixels across a nominal drop of 0.5.

As shown in Figure 2.1, the dried particles were collected for data analysis at the point labeled “Collection point”. The particles were considered to be completely dry at this point. Images recorded with a microscope lens showed that a constant droplet diameter was already reached within the period of time observable through the optical window, indicating that the drying process was nearly complete. As shown in Figure 1, particles continued to dry for a period of time at least 5 times longer than observable through the window. Dried particles were gathered for analysis by ultramicroscopy with a custom-built suction system, placed 30 cm downstream of the injection point. A hollowed-out Scanning Electron Microscope (SEM) sample stub was placed inside the flow tube at the collection point. The SEM stub was covered by double-sided adhesive tape with a central opening holding a membrane filter (GTTP 013 00, Millipore Isopore Polycarbonate, Darmstadt, Germany) in place. The suction flow rate was regulated with a ball valve and measured by a flow meter (4000 Series, TSI, Shoreview, Minnesota, U.S.). The collection flow rate was set to match the drying gas flow rate. Collected particles were gold sputter coated with a vacuum desk sputter coater (Desk II, Denton Vacuum LLC., Moorestown, New Jersey, U.S.) [253] and analyzed with a Scanning Electron Microscope (SEM LEO 1430, Zeiss, Jena, Germany) [254]. SEM stub samples were kept in SEM mount holders in a storage box (16709 Pelco 18 Pin mount storage holder, Ted Pella Inc., Redding, CA, USA) to avoid contamination of the particles. In addition, the interior of the samples was analyzed after cutting them with a Focused Ion Beam (FIB) (Hitachi NB 50000, Chiyoda, Tokyo, Japan) [255].

A microscope lens (1-60068, 12x Zoom System, Navitar, Rochester, New York, U.S.) was used to image individual droplets to measure their diameter and morphology. The microscope lens

recorded the droplets and particles from the ejection point to the collection point; the last image recorded before the collection point revealed the same diameter and morphology of the dried particles imaged with the SEM analysis. For this purpose the flow tube had two opposing optical windows. Droplets were illuminated using a strobe light (Mounted High Power LEDs M530L3, Thorlabs, Newton, New Jersey, U.S.) with a wavelength of 530 nm. The strobe light and the microscope lens were aligned and placed on a mounting stage which was attached to a stepping motor (VXM-2 Stepping Motor Controller, Velmex, Bloomfield, New York, U.S.), thus allowing the system to be moved vertically to follow the droplets along the chain while maintaining high magnification. To capture a steady droplet image, the strobe light and the camera were operated in pulse mode using a pulse generator, named “Pulse generator 1” in Figure 2.2, (BNC model 575 Pulse/delay generator, Berkeley Nucleonics, San Rafael, California, U.S.). This pulse generator had two outputs for the strobe light and the camera, and one input for the droplet generator driver MD-E-3000, relayed through another pulse generator (4001, Global Specialties, Yorba Linda, California, U.S.), named “Pulse generator 2” in Figure 2.2. The second pulse generator simplified the experiments that did not require the microscope lens.

The connection between the strobe light, camera, and pulse generator ensured a common frequency

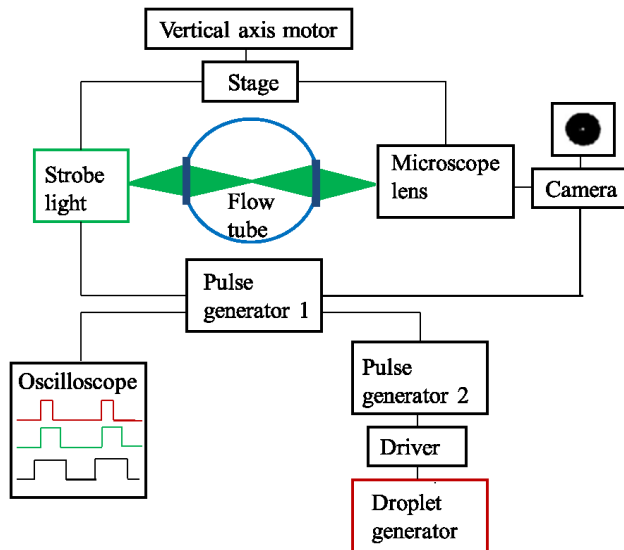


Figure 2.2 Schematic illustration of the imaging system.

for imaging and droplet generation. The first pulse generator allowed modification of the pulse delay and pulse width of the strobe light and camera, as shown in the connected oscilloscope (TDS 30143, Tektronix, Beaverton, Oregon, U.S.). To calibrate the imaging system, a calibration grid

(Mutifunctional Target DA029, Max Levy Co., Philadelphia, Pennsylvania, U.S.) was imaged for every test. The calibration process used a pixel resolution of $0.877 \mu\text{m}/\text{pixel}$ and a typical number of pixels across a nominal drop of 90. The magnification varied from 3 to 7 depending on the droplet size, providing respectively a depth of field of 0.049 and 0.114.

2.4.3 Measurement and derivation of the droplet or particle diameter

Two distinct methods, denoted “spacing” and “imaging”, were used to determine, aerodynamic and volume equivalent diameters of the droplets or particles. The volume equivalent diameter is the diameter of a sphere with the same volume as the droplet or particle considered. The aerodynamic diameter is the diameter of a sphere with a density of $1 \text{ g}/\text{cm}^3$ having the same settling velocity in air as the droplet or particle considered [24]. The spacing method derived the aerodynamic diameter of the droplets or particles from the distance between two consecutive droplets in the droplet chain (see Figure 2.3).

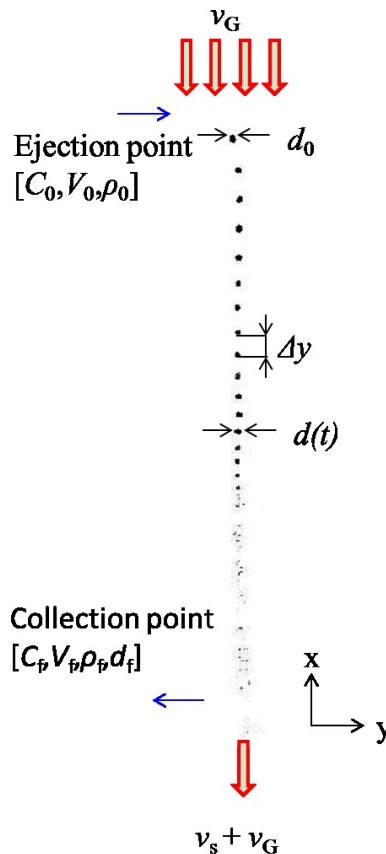


Figure 2.3 Annotated example of a typical droplet chain image. Δy is the spacing between two consecutive droplets, d_0 the initial droplet diameter, $d(t)$ the diameter of a droplet at time t , v_s the settling velocity and v_g the velocity of the gas flow.

For a given droplet generation frequency, f , the time step Δt between the generation of two droplets is simply the inverse of the frequency. Hence, the total droplet velocity, v_y , can be calculated from the spacing between droplets, Δy , as shown in Equation 2.1.

$$v_y = \frac{\Delta y}{\Delta t} = \Delta y f \quad \text{Equation 2.1}$$

Assuming the droplet reaches its terminal settling velocity, v_s , in the time step Δt , the droplet settling velocity can be calculated by subtracting the gas velocity, v_g , from the total droplet velocity as shown in Equation 2.2 [24], where Q_G is the gas flow rate and d_T is the flow tube diameter.

$$v_s = v_y - v_G = v_y - \frac{4\pi Q_G}{d_T^2} \quad \text{Equation 2.2}$$

Here, the gas velocity refers to the velocity at the center of the flow tube for a fully developed laminar flow. For microdroplets in Stokes flow the settling velocity is related to the droplet diameter as shown in Equation 2.3 [24]:

$$v_s = \frac{\rho_p d(t)^2 g}{18\mu} \quad \text{Equation 2.3}$$

where ρ_p is the density of the droplet.

For microparticles in general, the aerodynamic diameter can be derived from the settling velocity using Equation 2.3 in combination with the definition of the aerodynamic diameter. This results in Equation 2.4 where ρ^* is the standard density of 1 g/cm³, and the dynamic viscosity, μ , for air at 25°C is 1.846·10⁻⁵ Pa s [256]. The gravitational acceleration at the experiment's location [257] in Edmonton, Canada, was 9.81 m/s². Since the morphology of the solid particles differed for every case considered, the shape factor, χ , ranged from 1 for particles with spherical appearance to 1.09 [24] for particles that resemble a cylinder with an aspect ratio of 2.

$$d_a = \sqrt{\frac{18\mu v_s}{\rho^* g \chi}} \quad \text{Equation 2.4 *}$$

The imaging method derived the volume equivalent diameter, d_v , through image analysis (ImageJ, Imaging Processing and Analysis in Java, National Institute of Health, 1997, Bethesda, Maryland, USA) of the images of individual particles taken by the microscope lens at each point in the trajectory of the evaporating droplet. For the case of non-spherical particles, the main dimensions

of the shaped particles were derived. For oblate particles, the major and minor axes were determined and the particle volume was approximated as that of an oblate spheroid generated by rotating a corresponding ellipse about the major axis.

The aerodynamic diameter of the droplets prior to shell formation was also independently obtained through the imaging method by conversion from the volume equivalent diameter using the particle density. Assuming evaporation of a pure liquid droplet, a theoretical derivation of the droplet density can be attained [1]. Equation 2.5 provides the droplet density, ρ_p , as a function of time, where $\rho_{t,a}$ is the true density of acetone, C_0 is the CAB initial concentration, d_0 the initial diameter and $d(t)$ the droplet diameter as a function of time. Equation 2.5 is valid only for dilute solutions; therefore, this equation is valid only well before shell formation.

$$\rho_p(t) = \frac{m_a + m_{CAB}}{V_{tot}} = \frac{\rho_{t,a}d(t)^3 + C_0d_0^3}{d(t)^3} = \rho_{t,a} + C_0 \left(\frac{d_0}{d(t)} \right)^3 \quad \text{Equation 2.5}$$

* Equation 2.4 contains a mistake. The shape factor is not contained in the equation of an aerodynamic diameter.

results: firstly, validation of the theoretical derivations used and, secondly, determination of important parameters for the particle formation process that were previously inaccessible. The comparison between the aerodynamic diameter found with the spacing method and the volume equivalent diameter found with the imaging method provides the density for every phase of the particle formation, even after the shell formation.

2.4.4 Experimental determination of droplet or particle density and mass

The droplet or particle density was obtained through a comparison of the measured volume equivalent and aerodynamic diameters. In Equation 2.6, d_a , is the aerodynamic diameter, d_v the volume equivalent diameter and ρ^* standard density of 1 [g/cm³]. This equation permits the tracing of the particle density through the particle formation process.

$$\rho_p = \rho^* \left(\frac{d_a}{d_v} \right)^3 \quad \text{Equation 2.6 *}$$

Once the volume equivalent diameter of the particle no longer changes, the particles mass can still decrease due to solvent evaporation from the core of the particle. In this phase of the particle formation process the particle mass can be derived from the particle density using Equation 2.7, which can be used to assess mass loss due to solvent evaporation after shell formation.

$$M(t) = \frac{\pi \rho_p(t) d_v^3}{6} \quad \text{Equation 2.7}$$

Particle density was also derived via morphology analysis of the collected dried particles. After their diameter, d_f , was determined, the final dried particles density, ρ_f , was derived with Equation 2.8, where d_0 is the initial volume equivalent diameter and d_f is the final dried particle diameter.

$$\rho_f = C_0 \left(\frac{d_0}{d_f} \right)^3 \quad \text{Equation 2.8}$$

In summary, the density and the mass of the droplets or particles during the whole particle formation process were derived from the measured data without knowledge of any other material or particle properties. In contrast to many other sizing techniques the presented methods do not require input of any optical or electrical material properties.

2.4.5 Particle formation model

* Equation 2.6 contains a typographical error. The exponential is 2, not 3.

further refined by Boraey et al. [1]. The evaporation rate, κ , in this model is defined as the change of surface area over time and, using the experimental setup presented above, can be experimentally determined from the droplet diameter using Equation 2.9.

$$\kappa = (d_0^2 - d(t)^2) \cdot f \quad \text{Equation 2.9}$$

The model presented by Boraey et al. [1] can predict many of the final particle properties such as the volume equivalent diameter, density, aerodynamic diameter, and the time at which shell formation occurs based on the Péclet number of the evaporation process.

$$Pe = \frac{\kappa}{8D} \quad \text{Equation 2.10}$$

The diffusivity, D , of CAB in acetone strongly depends on the mass fraction of acetone in the solution [259]. However, the above mentioned model assumes a constant diffusivity. The diffusivity of CAB in acetone close to saturation was chosen, because this part of the evaporation process is most relevant for particle formation. The saturation point indicates the point at which no more solute dissolved in the remaining solvent. As a result, after this point the two processes happening are the distribution of the solute inside the droplet and the merely evaporation of the solvent[260]; these two phases are the key of the particle formation process. The mutual diffusivity

of CAB with 40000 g/mol molecular weight in acetone has been reported as $3.4 \pm 0.5 \times 10^{-11} \text{ m}^2/\text{s}$ [259]. It was adjusted for the higher molecular weight of the CAB in the present study using the Stokes-Einstein approximation [261].

The model further assumes a constant evaporation rate allowing an approximation of the droplet lifetime, or drying time, τ_D , as the ratio between the initial diameter squared and the evaporation rate, Equation 2.11.

$$\tau_D = \frac{d_0^2}{\kappa} \quad \text{Equation 2.11}$$

From the Péclet number, the surface enrichment can be obtained. The surface enrichment is defined as the ratio between the surface concentration of the solute and the average concentration in the droplet [258, 2]. Depending on the value of the Péclet number different relationships for the surface enrichment have been developed. For cases of Pe numbers between 25 and 200, which were encountered in this study Equation 2.12 is applicable [1].

$$E(t/\tau_D) = \frac{1}{32} \left[(15Pe - 4) - (15Pe - 36)e^{-\frac{5t}{4\tau_D}} \right] \quad \text{Equation 2.12}$$

Equation 2.12 is valid only up to $t < 0,75 \tau_D$. For times later in the evaporation process an analytical solution has not been developed yet, but Equation 2.12 can be extrapolated or the steady state approximation [1], Equation 2.13, can be used as approximation. In this range Equation 2.12 and Equation 2.13 differ by less than 20%, [1].

$$E = \frac{Pe}{3} + 0.363 \quad \text{Equation 2.13}$$

In the presented model, the surface enrichment can then be used to estimate the time to reach saturation, τ_{sat} , *i.e.*, the time for the solute to reach saturation at the surface (Equation 2.14 [1]). Here, S_0 indicates the initial saturation defined as the ratio between the CAB initial concentration and CAB solubility in acetone.

$$\tau_{sat} = \tau_D \left(1 - (S_0 E)^{\frac{2}{3}} \right) \quad \text{Equation 2.14}$$

2.4.6 Uncertainty analysis

Two types of uncertainty were considered, the precision derived from the measured data and the bias estimated from other sources, such as measurement devices [262]. The precision uncertainty

was derived from the repeatability of every experiment, which was repeated at least ten times. The bias was derived from the measurement errors of the spacing and imaging methods. For instance, the maximum total uncertainty derived for aerodynamic and volume equivalent diameter was 4.2 μm . For other properties, the uncertainty was propagated.

2.5 Result and discussion

2.5.1 Method suitability

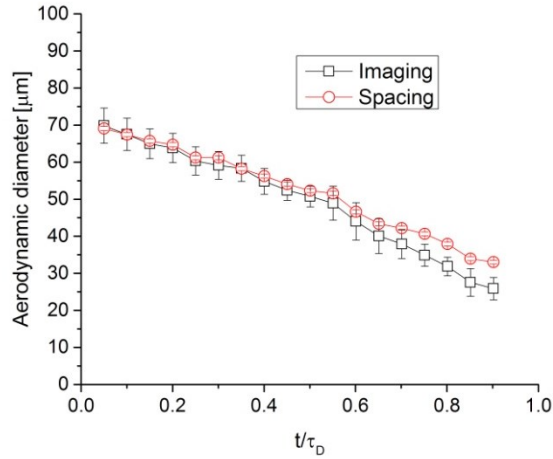


Figure 2.4 Comparison between the aerodynamic diameters obtained with the “Spacing” method and the “Imaging” method.

Figure 2.4 shows the results of a method suitability test for the “spacing” and “imaging” methods described above. The case considered for this test was the one with the lowest initial CAB concentration of 0.37 mg/ml, because the comparison between the aerodynamic diameter derived with the spacing method and the aerodynamic diameter derived with the imaging method relies on Equation 5, which is only valid for dilute solutions. In this case, shell formation was not reached during the observation window of the experiment. As is customary for evaporation experiments, the results were plotted as the square of the diameter as a function of time. The time for the n^{th} droplet in the chain was calculated as $n\Delta t = n/f$, and then normalized by the drying time, τ_D , defined in Equation 2.11. Figure 2.4 shows close agreement between the results of the two new methods, indicating their suitability for sizing of evaporating microdroplets. A linear fit to the imaging and spacing curve in Figure 2.4 show a difference in slope of 55 μm . Only for the last few data points, the results started to deviate from each other, indicating that the dilute solution assumption for Equation 5 was no longer valid.

2.5.2 Tracking of the particle formation process

Four cases were tested to investigate the effect of process parameters on the evaporation and particle formation processes and the properties of the final dry particles. For an initial CAB concentration of 10 mg/ml, drying gas temperatures of 30, 40, and 55°C were used. The effect of the CAB initial solution concentration was investigated by using two different concentrations of 0.37 and 10 mg/ml with a constant drying gas temperature of 30°C.

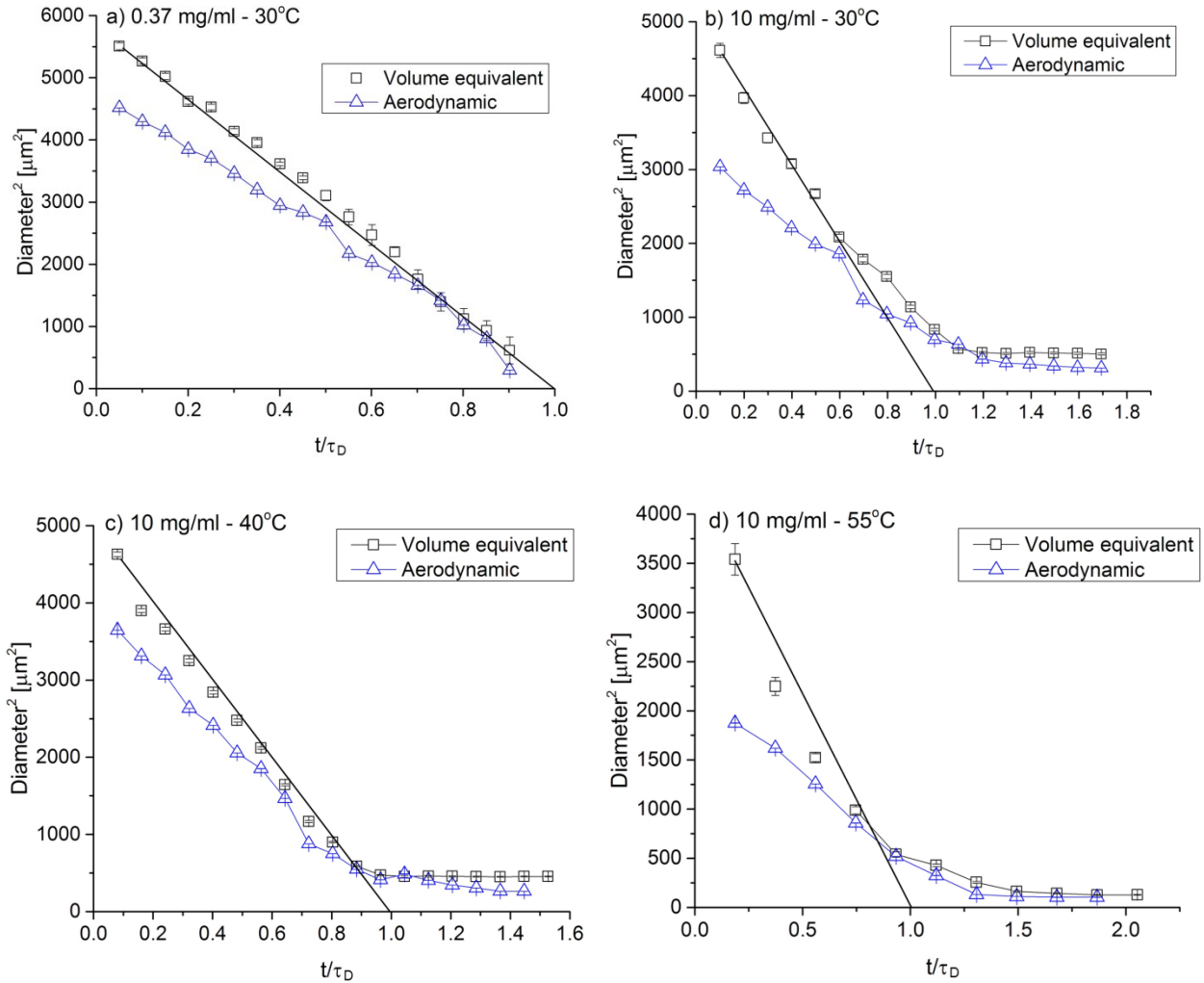


Figure 2.5 Comparison between the volume equivalent and the aerodynamic diameter for the cases considered: a) 0.37 mg/ml - 30°C, b) 10 mg/ml - 30°C, c) 10 mg/ml - 40°C and d) 10 mg/ml - 55°C. The first diameter ejected from the dispenser is omitted. The line indicates the linear fit to the first part of the volume equivalent diameter curve, indicating the initial evaporation rate

The particle formation process was evaluated through the analysis of three main properties: droplet and particle diameters, density, and mass. Figure 2.5 shows the results of the diameter measurements. Two diameters are represented: aerodynamic diameter, Equation 2.4, and the

volume equivalent diameter. Figure 2.5 shows the diameter squared trend with respect to the normalized time variable as described for Figure 2.4.

Table 2.1 Experimentally derived evaporation rate, initial droplet diameter, and droplet life time for the four cases considered

	κ [$\mu\text{m}^2/\text{ms}$]	d_0 [μm]	τ_D [ms]
30°C – 0.37 mg/ml	20.2 ± 1.4	89.3 ± 3.9	386 ± 86
30°C – 10 mg/ml	25.2 ± 1.1	87.4 ± 1.7	306 ± 39
40°C – 10 mg/ml	25.6 ± 0.4	86.3 ± 3.3	298 ± 45
55°C – 10 mg/ml	26.4 ± 0.3	73.7 ± 2.4	217 ± 71

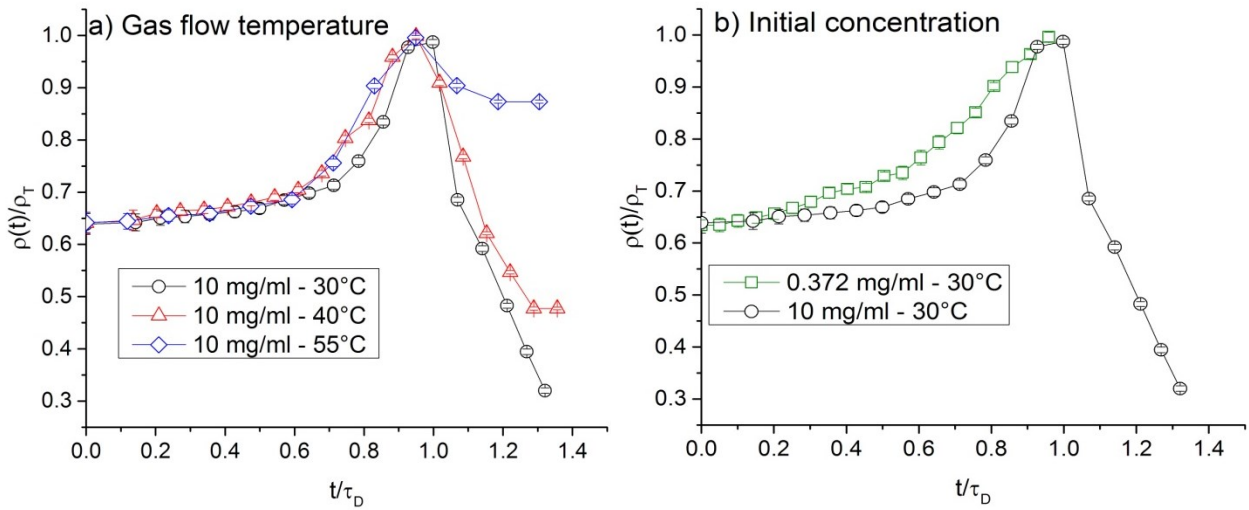


Figure 2.6 Droplet or particle density normalized by the true density of cellulose acetate butyrate as a function of time for different gas temperatures (a) and different initial concentrations (b).

As can be observed in Figure 2.5, the particle formation process can be described in two stages. In the first stage, the liquid solution droplet shrinks due to solvent evaporation. As expected, the square of volume equivalent diameter decreases linearly with time, following Equation 2.9. The slope of the closed lines fitted to this stage of the measurements provided the evaporation rates listed in the first column of Table 2.1. From the first data point followed the initial droplet diameter, reported in the second column of Table 2.1. The initial diameter decreased with both an increase in temperature and initial concentration.

The aerodynamic diameter in the first stage of the process was found to be lower than the volume equivalent diameter. This can be explained by the true density of acetone, which is lower than unit density. However, as the evaporation progresses, the true density of the solution increases according to Equation 2.5 and the gap between aerodynamic and volume equivalent diameter decreases, as shown in Figure 2.5. It becomes apparent, that by measuring both aerodynamic and volume equivalent diameters the concentration in the evaporating droplet can be derived at any point in time.

The second stage of the process begins with the deviation from the constant slope in Figure 2.5, which indicates a slowing of the evaporation rate. Shortly thereafter the volume equivalent diameter reached a plateau, which can be interpreted as the drying particles having achieved their final size. It is apparent, particularly in panels b) and c) of Figure 2.5, that the aerodynamic diameter still decreased in the second stage, while the volume equivalent diameter was already constant. This can be interpreted as continuing loss of mass, *i.e.*, solvent, from a particle with fixed size.

These trends become more obvious when the density is derived from the measured data using Equation 2.6. Figure 2.6 shows the trend of the density with respect to the normalized time variable. Here, the droplet or particle density was normalized by the true density of CAB. Figure 2.6(a) shows the results for variation of drying gas temperature. In all three cases the particle density decreased after reaching a common maximum close to the true density of CAB. At the end of the observation window the lowest particle densities were found for the case with the lowest drying temperature. For the 40 °C and 30 °C cases the particle density reached values much lower

than the true density of CAB; this can be interpreted as formation of dry particles with significant void space. Figure 2.6(b) shows the results for variation of initial CAB concentration. The volume equivalent diameter for the low concentration case did not reach a plateau during the observation window, so information about the shell formation phase could not be derived from the sizing data alone.

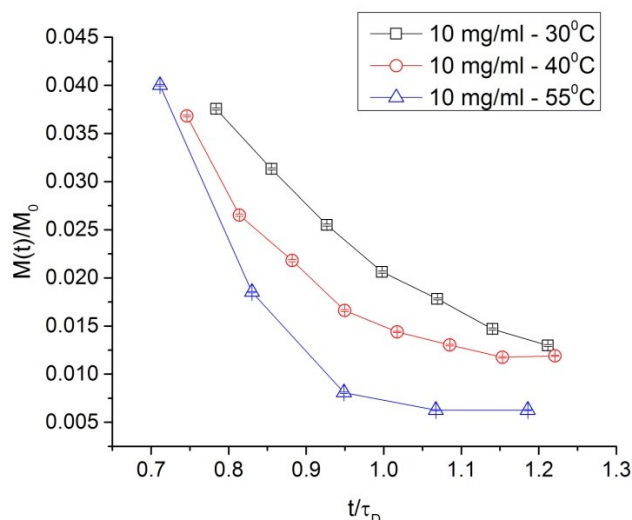


Figure 2.7 Change of the normalized droplet or particle mass for different drying temperatures.

The mass at every time step was derived from the density, as shown in Figure 2.7. In Figure 2.7, the mass was calculated with Equation 2.7 and normalized by the initial mass, *i.e.*, the mass at time step 0. The presented methods allow, for the first time, to our knowledge, direct observation of solvent mass loss rates in isolated microparticles drying in a carrier gas. The drying rate is the slope of the curves presented in Figure 2.7. Hence, the plateau in the profile for the particle mass indicates the completion of the solvent evaporation process.

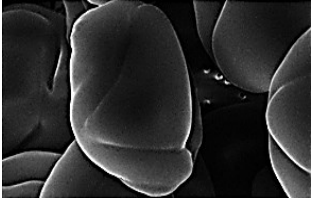
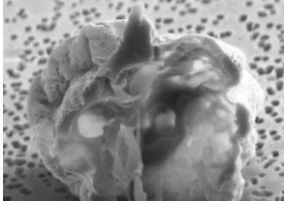
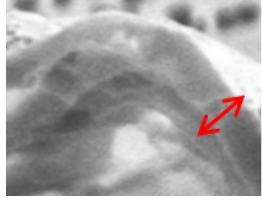
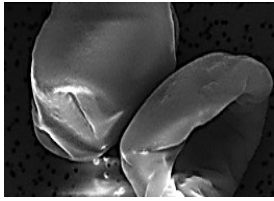
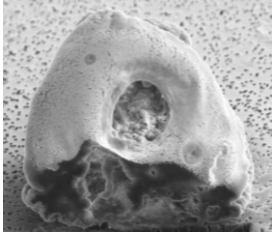
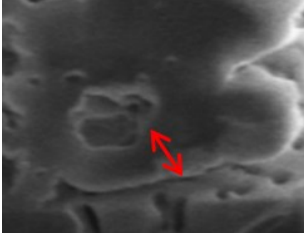
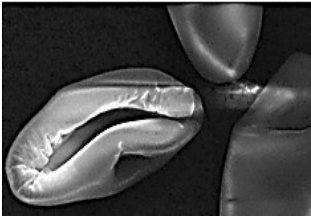
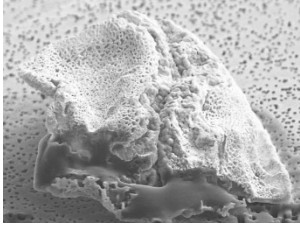
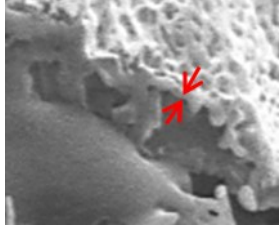
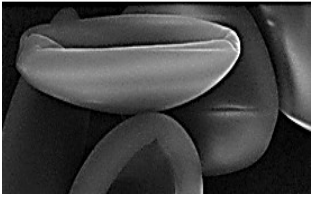
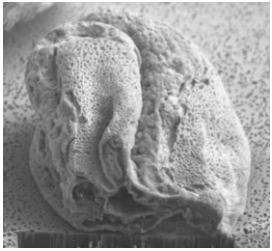
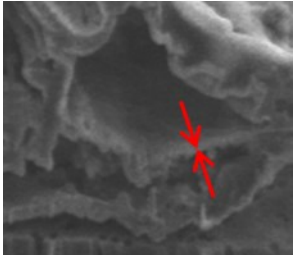
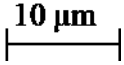
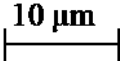
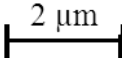
The results of the particle formation model, while only applicable to the first stage of the particle formation process, can provide insight into the underlying mechanism of the process: From the data shown in Figure 2.7, three important parameters were derived, the Péclet number, the surface enrichment, and the projected time to reach saturation on the surface. The results are reported in Table 2.2. The Péclet number is defined as the ratio between the evaporation rate and the diffusivity according to Equation 2.10. It was used to estimate the magnitude of the surface enrichment of CAB relative to the average concentration using Equation 2.12. For all four cases Pe was found to be large, see Table 2, predicting substantial radial de-mixing and surface enrichment during droplet

evaporation. The model results, therefore, support the hypothesis that a shell forms on the droplets, which is in agreement with the low particle densities derived from the sizing data. A shell cannot form prior to reaching saturation on the surface. The time at which saturation is reached was calculated by iteratively solving for τ_{sat} in Equation 2.12 and Equation 2.14.

Table 2.2 Theoretical derivations of Peclet number (Pe), Enrichment (E) and the ratio between the time to reach saturation (τ_{sat}) and the drying time (τ_{D}).

	Pe	E	$\tau_{\text{sat}}/\tau_{\text{D}}$
30°C – 0.37 mg/ml	46 ± 5	15 ± 3	0.99 ± 0.03
30°C – 10 mg/ml	63 ± 3	20 ± 1	0.99 ± 0.01
40°C – 10 mg/ml	63 ± 4	21 ± 1	0.95 ± 0.07
55°C – 10 mg/ml	77 ± 7	25 ± 2	0.94 ± 0.05

Table 2.3 Morphology analysis by SEM and FIB for the cases considered.

Cases	SEM	FIB	FIB shell thickness
0.37 mg/ml - 30°C			
10 mg/ml - 30°C			
10 mg/ml - 40°C			
10 mg/ml - 55°C			
Scales bars			









The results shown in Table 2.2 are in reasonably close agreement with the experimentally observed time at which the droplets stop shrinking, or at which the density curves reach their maximum. However, the particle formation model does not explain the trend in final particle density with drying gas temperature, which is unsurprising, given the fact the model cannot be applied to the phase after the shell is formed. Further elucidation of the particle formation process can be obtained

by a morphology analysis of the final dried particles. For each of the four cases considered the final dried particles were collected for the analysis of their morphology, Table 2.3.

Table 2.3 shows the morphologies associated with the results presented in Figure 2.6; highest temperatures relate to highest final particles density. Even though these particles show thinner walls, they appear to be folded into a more compact shape. The final dried particle shape was not spherical, but half oblate, as shown by their profiles in Table 2.4, which were schematically sketched based on observation of many particles; their ratios between the two oblate main dimensions, i.e., the aspect ratio are expressed in Table 2.4. The cross sections shown in Table 2.4 explain how the higher temperature cases can cause more compactly folded final particles, and hence a higher particle density.

For low initial concentration, the final dried particles appear almost as half sphere with a thicker shell, as shown in the first row in Table 2.4 or by the FIB images in Table 2.3; on the other hand, for high concentration, they have a ratio of almost two for the two main dimensions and they show a thinner shell.

Table 2.4 Sketch of the profiles for two main axes of the dried particles collected for the four cases analyzed.

Axis	0.37 mg/ml - 30°C	10 mg/ml - 30°C	10 mg/ml - 40°C	10 mg/ml - 55°C
<i>y</i>				
<i>x</i>				
Aspect ratio	1.0 ± 0.7	1.5 ± 0.9	1.9 ± 1.1	2.2 ± 1.3

These dimensions are important for the calculation of the volume of the final particles and for the derivation of their volume equivalent diameter. The final dried particles were assumed to be oblate spheroids; their volume was calculated using the equation shown in Table 2.5, where, *a*, denotes half of the longest side and, *b*, half of the shortest side. Table 2.5 lists the density of the final dried particles, attained with the use of Equation 2.8. In Table 2.5, the ratio between the final densities and the CAB true density is also presented, which allows an estimate of the void fraction in the particles.

Table 2.5 Densities of dry particles in kg/m³ and ratio between the final density and the CAB true density (1250 kg/m³) for all the cases studied

$V = \frac{3}{4}\pi a^2 b$	Final Density (ρ_f) [kg/m ³]	Final Density (ρ_f)/ True density (ρ_T)
30°C – 0.37 mg/ml	38.7 ± 1.7	0.031
30°C – 10 mg/ml	422±1.3	0.337
40°C – 10 mg/ml	728 ± 2	0.581
55°C – 10 mg/ml	930 ± 0.9	0.754

The normalized final particle densities derived from the morphology analysis, Table 2.5, were in good agreement with the results shown in Figure 2.6, providing another indication for the validity of the experimental methods. The morphology analysis shows that particles with shells were formed as predicted by the particle formation model. The trend in final particle density did not directly correlate to differences in the Péclet number or surface enrichment. The electron micrographs revealed that the shells buckled and folded upon further drying, a process which cannot be described by the particle formation model. Close inspection of the ion beam milled particles revealed that the shell thickness was slightly greater for the particles dried at lower temperatures. This finding can be explained by the theoretical model which predicts that for droplets which dry at lower temperatures saturation on the surface is reached later, see Figure 2.6 and Table 2.2. A later onset of shell formation on a smaller droplet is consistent with increased shell thickness. However, the final particle density is determined by the folding mechanism, which appeared to lead to less void fraction for the particles with lesser shell thickness, in agreement with a recent study on shell deformation [263].

2.6 Conclusion

The new approach presented in this study enables comprehensive experimental and theoretical analysis of the particle formation process of drying microparticles, here demonstrated on a model compound, cellulose acetate butyrate (CAB). The process can be tracked from the generation of the solution droplets to the collection of dried particles. Solvent evaporation rates can be assessed throughout the whole particle formation process, including the evaporation through the formed particle shell. The experimental approach relies on morphology analysis of the dried particles and,

additionally, on two optical methods that independently derive volume equivalent and aerodynamic diameters from the spacing of particles in a monodisperse droplet chain and from individual particle images respectively. From a comparison of the equivalent diameters, the particle density and particle mass can be derived at each point in time, which enables tracking of shell folding and solvent mass loss rates on partially dried particles, an area that is currently theoretically inaccessible. Given only the distance between two consecutive particles, the particle spacing method can provide an accurate prediction of final particle density. The method is also applicable to more complicated combinations of solutes and solvents, because it does not require knowledge of any optical or electrical material properties.

It can be shown by current particle formation models and verified by the presented experimental tools that the particle formation mechanism for solvent droplets dried in a high Péclet regime, as was the case for the current study, is strongly influenced by liquid phase diffusion of the solute. At high Péclet numbers radial de-mixing and subsequent surface enrichment of the solvent occurs, leading to the formation of a shell. However, the second phase of the process after the shell formation is outside of the scope of simple analytical particle formation models. The experimental results show that shell buckling and folding dominates this phase and determines the final particle properties. This provides a strong motivation to develop predictive theoretical models for this phase of the drying process as well.

2.7 Acknowledgements

Funding from the Natural Sciences and Engineering Research Council of Canada (NSERC) and the Alberta Innovates Technology Futures is gratefully acknowledged. The authors would also like to acknowledge Luis Augusto Ferraz Albani who supported the design of the optical components.

3 Effect of Crystallization Kinetics on the Properties of Spray Dried Microparticles

The material shown in Chapter 3 has been published in Journal of Aerosol Science and Technology. The experiments have been personally conducted; only the trend between viscosity and mass fraction has been provided by Prof. Reid's research group at the University of Bristol, U.K. The theory has been developed in previous publications, [1, 2] and personally implemented, as the calculation of the density and determination of time for crystallization. The authors of this publication are me, my supervisor Reinhard Vehring, and Rory M. Power, Rachael E. H. Miles, and Jonathan Reid from the University of Bristol. The material submitted is the following, [264]. Additional material is shown in Appendix C.

3.1 Abstract

A droplet chain technique was used to study the influence of the crystallization process on the morphology of spray dried microparticles. A piezoceramic dispenser produced a chain of monodisperse solution droplets with an initial diameter in the range of 60 to 80 μm . Aqueous solutions of sodium nitrate were prepared in concentrations ranging from 5 mg/ml to $5 \cdot 10^{-5}$ mg/ml. The solution droplets were injected into a laminar flow with gas temperatures varying from 25 to 150 $^{\circ}\text{C}$, affecting the droplet temperature and the evaporation rate, accordingly. Dried particles with diameters between 0.3 and 18 μm were collected. The properties of the collected microparticles were studied and correlated with a particle formation model which predicted the onset of saturation and crystallization. The model accounted for the dependence of the diffusion coefficient of sodium nitrate in water on droplet viscosity. The viscosity trend for sodium nitrate solutions was determined by studying the relaxation time observed during coalescence of two aqueous sodium nitrate droplets levitated in optical tweezers. The combination of theoretical derivations and experimental results showed that longer time available for crystallization correlates with larger crystal size and higher degrees of crystallinity in the final microparticles.

3.2 Introduction

Respiratory drug delivery allows solid microparticles, in the range of 0.1 to 5 μm , to be deposited in the patients' lungs [265, 266]. The advantages of delivering drugs via inhalation are multiple:

high concentration of the drugs delivered to the disease site, minimal risks of side effects, rapid clinical response, low drug loss during the delivery compared to other techniques, and non-invasive treatment [22]. Despite the strong interest in respiratory drug delivery, an understanding of the impacts of the properties of microparticles on delivery efficiency and efficacy is not well defined [267]. An example of important properties of microparticles is the diameter. The smaller the particles are, the deeper they can reach; the effect can change according to the type of microparticles involved [268]. Other properties can be considered relevant; morphology and crystallinity are main factors in the efficiency of the drug delivery [3, 269, 270]. It has been shown that particles with high roughness reduce cohesion forces and, therefore, improve powder dispersibility [33]. Drugs can exist in different solid phases: amorphous, crystalline, or a mixture of them. Each phase can present different properties fundamental for pharmaceutical studies; the relationship between the properties and the solid phase can vary accordingly to which chemical compound the microparticles are made of [271, 272]. For example, it has been found that crystalline proteins remain more stable during the delivery compared to amorphous proteins [29]. In addition, crystalline drugs are more commonly used due to their thermodynamic stability. On the other hand, amorphous spray-dried drugs may have a smaller and more homogenous particle size and a higher respirable fraction than mechanically micronized particles [30]. The dependence of the performance of pulmonary drugs on their solid phase highlights the need to understand particle formation and crystallization process. The main goal of particle engineering is to understand particle formation process in order to control the properties of the produced microparticles [273]. The particle formation process is the transition between solution droplets to dried particles [193]. During this process, one of two development options is encountered: the solvent and solute remain homogeneously mixed or they separate creating core-shell or solid particles [156]. If the chosen solute can crystallize, the particle formation process may also involve two sub-processes related to crystallization, i.e. crystal nucleation and crystal growth [274].

Studies on particle formation focus mainly on the first part of the process that can be modeled as evaporation of a solution droplet [1]. The solvent evaporation phase plays an important role in the particle formation process [214]. However, few experimental methods are currently available for the study and the evaluation of the particle formation process, and specifically, of the crystallization process of a solution droplet. The main three methods use: droplets suspended on a thin filament [123, 220, 221], single droplets [275, 136, 225, 276, 277, 134], or monodisperse

droplet chains [129, 130, 227]. The method of droplets suspended on a thin filament may influence the evaporation process by affecting the heat conduction via the contact between the filament and the droplet. Secondly, filament techniques normally require droplets with diameters in the millimeter range, which undergo a different evaporation process compared to microdroplets relevant for inhalation applications [134]. The single droplet method is based on droplets evaporating in either a falling gas flow [225, 278] or in a quiescent environment [279, 136, 280]. The method of a single droplet falling in a gas flow is difficult to apply for fast process such as the evaporation of a micro-droplet which lasts only a few milliseconds.

Single particle studies in a quiescent environment have led to important improvements in the understanding of concepts such as chemical reactivity, equilibrium particle size, and hygroscopicity [150]. Furthermore, the single droplet method provides detailed information on the mechanisms that lead to the evaporation of the solvent from a solution droplet and the physical transformation of a particle through phase transformation and growth [281]. The traditional technique to hold a droplet in a quiescent environment is using the effect of radiation pressure [282-284]. If levitated with radiation pressure, the droplets experience a force in the direction of the laser beam propagation [282]. A slight modification to this traditional technique is optical tweezers. Optical tweezers have been widely used in fields such as biology or colloidal science [285], but their utility in aerosol science has been emphasized by several recent studies [286, 281, 287, 288]. The use of optical tweezers or optical traps eliminates the force balance problem encountered with the traditional radiation pressure technique. Optical tweezers focus the laser beam using a microscope objective forming a single beam gradient force trap, where the particle is attracted toward the region of highest light intensity and confined in three dimensions [150]. A drawback of the single droplet method is the time required for the capture and the stabilization of the droplet. In addition, particles have to remain homogenous and spherical if cavity enhanced. Raman scattering is to be used to determine particle physical properties such as size and refractive index.

The droplet chain method is widely used in experimental studies of evaporation processes, not only in spray drying, but also in other areas such as microfluidics, MEMS, combustion, and colloids chemistry [228, 159, 234, 210]. A monodisperse droplet chain can be formed by injection of uniform droplets into a gas flow. Monodisperse droplets can be produced using a thermal dispenser, a vibrating orifice, or a piezoceramic dispenser. The piezoceramic dispenser is

commonly used in recent studies due to several advantages. It typically does not generate interfering air bubbles, which are common in thermal dispensers [240, 241]. It can produce droplets with a spacing larger than several droplet diameters unlike the more narrowly spaced droplets from vibrating orifices which may lead to droplets merging [289, 166].

Both monodisperse droplet chain and single droplet methods need a theoretical model to aid interpreting the experimental data. In this work, the theoretical particle formation model introduced by Vehring et al. [2] is modified and implemented. This model provides a partial description of particle formation for cases that are dominated by liquid phase diffusion [2]. The model was extended to cases with very slow diffusion by Boraey et al. [1]. These models require a constant droplet evaporation rate. In the work presented here the model was adapted to allow for a change in material properties and evaporation rate over time. The goal of the present work is to describe the crystallization part of the particle formation process in more detail.

3.3 Experimental section

3.3.1 Chemicals

Sodium nitrate (NaNO_3) (catalog number 221341-500G, Sigma Aldrich, St Louis, MO, USA) was used; its relevant properties, as listed by the manufacturer, are: true density of 2260 mg/ml, and purity greater than 99%. Glass transition temperature and melting point of NaNO_3 are 185 – 215°C and 306°C, respectively [217]. This solute was dissolved in deionized Water (DI H_2O) (catalog number 38796 – 1L, Sigma Aldrich, St Louis, MO, USA) with a residual content lower than 0.01%.

3.3.2 Experimental setup

Monodisperse droplet chain

The monodisperse droplet chain was generated using an experimental setup which has been described before [156]. Briefly, it consisted of three main parts: feeding system, collection device, and optical setup Figure 3.1. The feeding part consisted of a piezoceramic dispenser (MJ-ATP-01-30, MicroFab Technologies, Plano, Texas, USA) with an orifice diameter of 30 μm , a flow tube and minor components. The piezoceramic dispenser was controlled with a driver (MD-E-3000 Microdrop Technologies, Mühlenweg, Norderstedt, Germany), which allowed the applied voltage and frequency to be governed. Voltage and frequency influenced the speed of the first injected droplet and the number of droplets in the chain, respectively.

The flow tube had double walls with a partially evacuated gap for thermally insulating the internal gas flow. The square cross section of the flow tube improved the visualization of the whole particle formation process. Two heaters were located on the top of the flow tube to warm the air to a set temperature. The temperature values were recorded with two type K thermocouples (TFE-K-20, Omega Engineering, Laval, Quebec, Canada). The recording points were at the exit of the first heater and at the injection point. The gas flow rate was measured with a flow meter (4000 Series, TSI, Shoreview, Minnesota, U.S.). A low flow rate of 2 L/min was used to reduce the turbulence in the flow tube.

After the solution was filled into the dispenser, droplets were injected into a dry ($< 1\%$ RH) laminar flow with controlled temperature. The distance between the injection point and the collection point was about 1 meter. This length allowed the use of a broader range of liquids, including liquids with low evaporation rate at low wet bulb temperatures. The collection device allowed the dried microparticles to be sampled on a hollowed Scanning Electron Microscope (SEM) substrate. The hollowed SEM stub was covered with filters with $0.2\ \mu\text{m}$ pores (GTTP 013 00, Millipore Isopore Polycarbonate, Darmstadt, Germany). The microparticles were collected differently for the analysis of their solid phase by Raman spectroscopy [180]. The filters were substituted with metal frits (Catalog number 9446T31, McMaster Carr, Aurora, OH, USA) with pores of an average diameter of $0.2\ \mu\text{m}$. All samples were stored in a dry environment until further analysis. Due to the high glass transition temperature of NaNO_3 , solid phase transitions were unlikely to occur on the sample stubs. Collected particles were gold sputter coated with a vacuum desk sputter coater (Desk II, Denton Vacuum LLC., Moorestown, New Jersey, U.S.). The samples were then analyzed with an SEM (SEM LEO 1430, Zeiss, Jena, Germany) and a Focused Ion Beam Milling (FIB) (Hitachi NB 50000, Chiyoda, Tokyo, Japan) device. The images were analyzed using the software ImageJ, (ImageJ, Imaging Processing and Analysis in Java, National Institute of Health, 1997, Bethesda, Maryland, USA). The optical part consisted of a camera (BM-500 GE GigE Vision, Pleora Technologies, Kanata, Ontario, Canada) that recorded the droplet chain illuminated by a diode laser (SNF-660 Lasiris, Coherent Co., Wilsonville, Oregon, U.S.). In addition, the camera was free to move vertically from the injection to the collection point. For calibration purposes, a scale bar with a resolution of 1 mm was placed in the same plane as the monodisperse droplet chain.

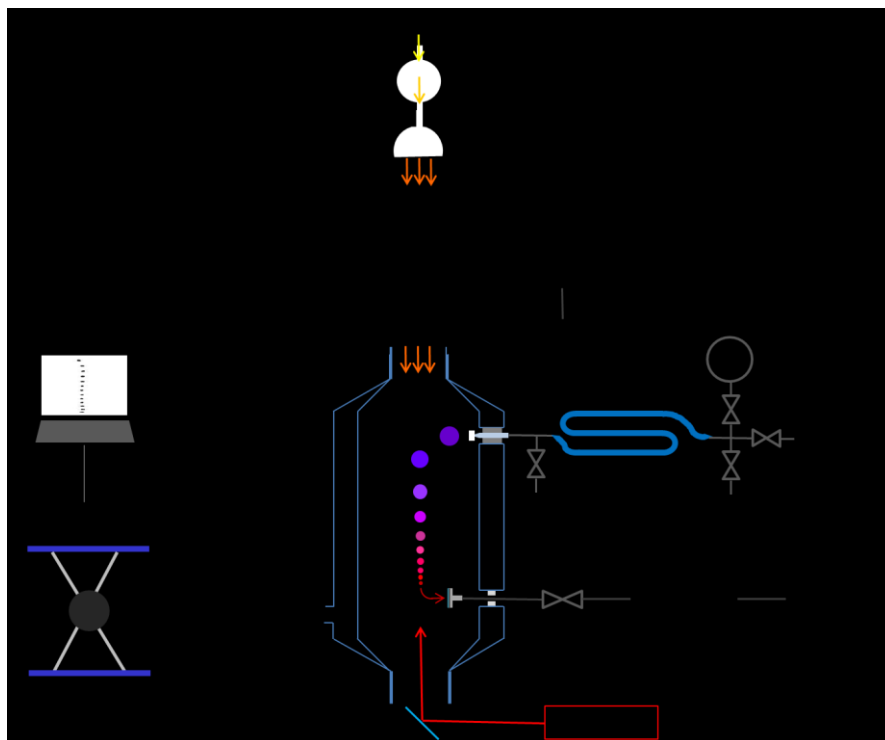


Figure 3.1 Main components of the experimental setup. Liquid is fed to a piezoceramic dispenser, which produces a monodisperse droplet chain. This chain follows the streamline of a temperature regulated gas flow. Dried microparticles are collected at the bottom of the flow tube onto a Scanning Electron Microscope sample stub. The flow tube is double walled for insulation. The flow tube has a square cross section facilitating the recording of images of the droplet chain. The images are recorded using a pulsed diode laser that highlights the chain of droplets and a camera that can be moved vertically to image all the droplets in the chain.

Determination of viscosity

The viscosities of aqueous solutions of sodium nitrate were determined as a function of mass fraction of solute by controllably inducing coalescence between two droplets held in holographic optical tweezers [290]. Details of the experimental technique are described in the supplementary information.

Figure 3.2 shows the trend of viscosity with sodium nitrate mass fraction, determined at 25°C. The viscosity trend is essential for the derivation of the diffusion coefficient dependence with sodium nitrate mass fraction. The trend line shown in Figure 3.2 is used to calculate viscosity also for mass fraction higher than 0.85, which is an experimental limit. Results shown in Figure 3.2 agree with measurements of the viscosities achieved using aqueous solutions [291].

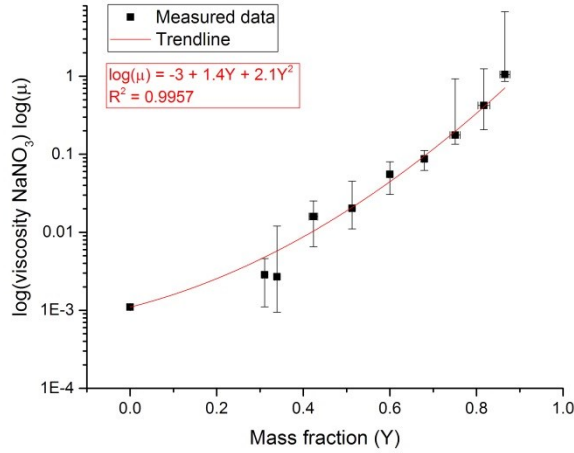


Figure 3.2 Viscosity as a function of mass fraction of sodium nitrate in an aqueous solution.

3.3.3 Measurement and derivation of the main parameters of the particle formation process

To describe the evaporation and particle formation process, aerodynamic diameter, volume equivalent diameter, particle density, and solute concentration are determined as a function of time. Images of the whole monodisperse droplet chain are analyzed to determine the distance between two consecutive droplets or particles. From the distance between two consecutive droplets their velocity can be obtained, because the production frequency of the droplets is known. Subtracting the velocity of the gas flow, which can be calculated from the volume flow rate and the geometry of the flow tube, yields the settling velocity, v_s of the droplets or particles as a function of position or time. The aerodynamic diameter, d_a , follows from the settling velocity. This method was introduced in a previous publication [156].

The volume equivalent diameter, d_v , as a function of time, t , can be determined if the particle density at every time step, i , is known. Depending on the phase of the particle formation process, the particle density, ρ_p , is approximated by different methods. Before any possible shell formation, it can be assumed that the particle is a sphere without internal voids. In this case, the mass fraction of the solute, Y_{sol} , in the particle is given by Equation 3.1.

$$Y_{sol}(t) = \frac{M_{sol}}{M(t)} = \frac{C_0 d_{v,0}^3}{\rho_P(t) d_{v,i}^3} = \frac{C_0 d_{a,0}^3}{\rho_P(t) d_{v,i}^3} \quad \text{Equation 3.1}$$

in which $d_{a,0}$ is the aerodynamic diameter at the initial time step, M_{sol} the mass of solute in the droplet, and $M(t)$ is the total mass of the droplet or particle. Under the assumption that the droplet initially consists of a dilute aqueous solution with concentration, C_0 , the particle density is close to 1 kg/L. Therefore, the initial aerodynamic diameter can be replaced by the initial volume equivalent diameter, $d_{v,0}$. For a sphere with a diameter large enough such that non-continuum effects can be neglected the volume equivalent diameter can be substituted with Equation 3.2.

$$\frac{\rho^*}{\rho_p(t)} d_{a,i}^2 = d_{v,i}^2 \quad \text{Equation 3.2}$$

where ρ^* is the standard density [1 kg/L]. Lastly, the density of a solution can be expressed as a function of the mass fraction of the solute based on measured data [292, 293] in the form shown in Equation 3.3.

$$Y_{\text{sol}}(t) = A\rho_p(t) - B \quad \text{Equation 3.3}$$

The parameters A and B vary according to the wet bulb temperatures of the evaporating droplet. Values of A range from 0.0018 to 0.0021 ml/mg and values of B range from -2.06 to -1.94 [292]. Equation 3.4 is obtained by combining Equation 3.1, 2 and 3. Equation 3.4 can be solved iteratively for the particle density at each time step.

$$\rho_p(t) = \left(\frac{C_0 \rho_p^{\frac{1}{2}} d_{a,0}^3}{\rho^{*\frac{3}{2}} d_{a,i}^3} + B \right) \frac{1}{A} \quad \text{Equation 3.4}$$

In the later phase of the particle formation a shell may have formed and the assumption of a sphere without voids is no longer valid. Also, the volume equivalent diameter of the particles cannot be smaller than the diameter of the final dried particles, d_f . In this phase the particle density can be approximated by a different method. Assuming that the volume equivalent diameter is now fixed at d_f , the particle density follows from Equation 3.5. The diameter of the final dried particles can be determined from an analysis of electromicrographs. Equation 3.5 is derived assuming that the volume equivalent diameter, after the shell formation, is constant and equal to the diameter of the final dried microparticles.

$$\rho_p(t) = \rho^* \left(\frac{d_{a,i}}{d_f} \right)^2 \quad \text{Equation 3.5}$$

The shell thickness can also be approximated from the final particle diameter and the ratio of particle density to true density of the solute, ρ_T , as shown in Equation 3.6 [1]. In Equation 3.6, d_s indicates the diameter of the inner void in the final dried microparticle.

$$d_s = d_f \sqrt[3]{1 - \frac{\rho_p}{\rho_T}} \quad \text{Equation 3.6}$$

Figure 3.3 shows a typical result for the aerodynamic diameter, measured using light scattering, as a function of time and the volume equivalent diameter derived using the methods described above. The next step in the analysis of the particle formation process requires knowledge of the evaporation rate of the droplets. The previously used steady-state particle formation model assumed that all variables are unaffected by a possible change of properties with time and assumed a constant evaporation rate [156]. The dot-dashed line in Figure 3.3 is drawn connecting the initial volume equivalent diameter squared and the first occurrence of the final aerodynamic diameter. It is apparent that assuming a constant evaporation rate for this case would produce a large error in the derivation of related properties. Therefore, a variable evaporation rate was used for further analysis.

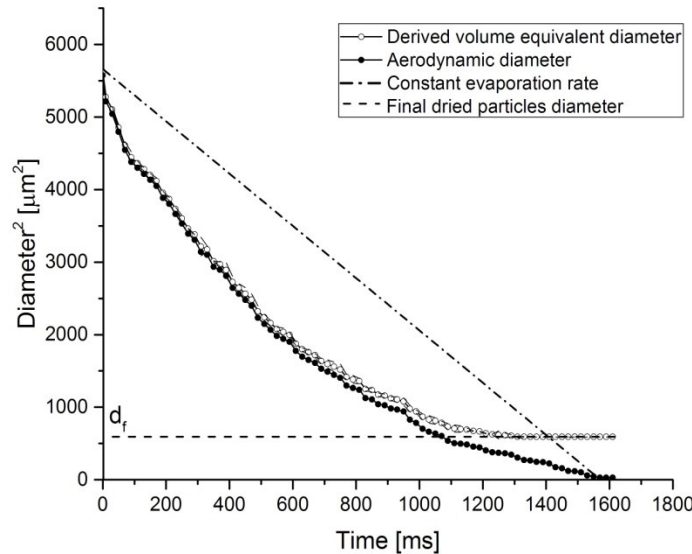


Figure 3.3 Determination of aerodynamic and volume equivalent diameter as a function of time in a droplet chain for a gas temperature of 25°C and an initial concentration of 5 mg/ml. The dashed line represents the final diameter of the dried particles. The dash-dot line is an approximation for a hypothetical constant evaporation rate case.

The evaporation rate, κ , as a function of time is calculated as the slope of the volume equivalent diameter squared according to Equation 3.7.

$$\kappa(t) = \frac{d_{v,i+1}^2 - d_{v,i}^2}{t_{i+1} - t_i} \quad \text{Equation 3.7}$$

Where $d_{v,i+1}$ and $d_{v,i}$ are the volume equivalent diameter at droplet $i+1$ and i , respectively. t_{i+1} and t_i are the time corresponding to droplet $i+1$ and i , respectively.

Previous publications have demonstrated that the Peclet number, Pe , is an indicator of the morphology of the final dried particles [294-296]. Larger Peclet numbers indicate low density particles, typically with a shell. Previously, the Peclet number was treated as constant. Here, the evaporation rate changes with time, Equation 3.8.

$$Pe(t) = \frac{\kappa(t)}{8D(t)} \quad \text{Equation 3.8}$$

Since the restriction of constant Peclet number no longer applies, we can also admit a diffusion coefficient, $D(t)$, that changes over time. The diffusion coefficient is obtained from the viscosity, μ , of the solution using the Stokes Einstein equation [297], as shown in Equation 3.9.

$$D(t) = \frac{k_B T_w}{6\pi\mu(t)r} \quad \text{Equation 3.9}$$

Where k_B is the Boltzmann's constant, T_w is the wet bulb temperature of the evaporating droplet and r the Stokes' radius of NaNO_3 , 0.309 nm [298].

The relationship between NaNO_3 mass fraction, Figure 3.2, and viscosity is provided from experimental results on coalescing droplets levitated in optical tweezers, described above. Power et al. [299] have confirmed for sucrose solutions that the Stokes Einstein equation provides a reasonable method for estimating diffusion constants from viscosities when the viscosity is in the range 10^{-3} to 10 Pa s. Over this range, the estimated diffusion constant may be expected to be within one order of magnitude of the correct value.

The surface enrichment E is another important parameter for the evaluation of the particle formation process. It is defined as the surface concentration of the solute relative to its average concentration in the droplet, c_m . [1]. Equation 3.10 shows the relationship used to determine E . This equation has negligible error for Peclet numbers lower than 0.5. For higher Peclet numbers,

the error related to the enrichment increases, but assuming a steady state system, Equation 3.10 can be used to approximate the enrichment for Peclet numbers up to 20. For higher Peclet numbers, encountered towards the end of the evaporation process, Equation 3.11 provides an approximation [1].

$$\text{Pe} < 20 \quad E = 1 + \frac{\text{Pe}}{5} + \frac{\text{Pe}^2}{100} - \frac{\text{Pe}^3}{4000} \quad \text{Equation 3.10}$$

$$\text{Pe} > 20 \quad E = \frac{\text{Pe}}{3} + \frac{4}{11} \quad \text{Equation 3.11}$$

The particle formation process cannot be fully explained without knowing the time required to reach saturation. The time to reach saturation is defined as the time at which the surface concentration reaches the solubility limit of the solute at a determined wet bulb temperature. The surface concentration is obtained using Equation 3.12.

$$c_s(t) = E(t) c_m(t) \quad \text{Equation 3.12}$$

However, it is known that crystallization does not start at saturation, but rather requires a certain level of supersaturation, depending on the nucleation mechanism. Hence, the time for crystallization defines the time at which the crystal starts to nucleate and subsequently grow. Tang and Munkelwitz [300] studied the evaporation of sodium nitrate and other inorganic components using a single droplet evaporating in an electrodynamic balance. These authors reported that nucleation commences at a concentration between 83% to 98% of NaNO_3 by weight [300]. Because of the fast kinetics encountered in the drying of microdroplets, the time for crystallization was defined here as the time at which the NaNO_3 weight percentage reaches the higher value of 98%.

For simplification, two time intervals are introduced: the precipitation window (Δt_p) and the crystallization window (Δt_c). These two time intervals simplify the understanding and the explanation of the relationship between the final dried particle properties and the crystallization process. The Δt_p and Δt_c are the time between the time to reach saturation or the time for crystallization, respectively, and the time to reach constant aerodynamic diameter. The time for constant aerodynamic diameter is the time at which the aerodynamic diameter stops to decrease. At this point, it is assumed that all the solvent is evaporated.

3.4 Results

For various initial conditions and the gas temperatures, Table 3.1 lists the predicted time intervals available for precipitation and crystallization, Δt_p and Δt_c , respectively. For the sake of brevity, further results are shown mostly for four or six representative cases, highlighted in Table 3.1. The four main cases are: 5 mg/ml at 50°C, $5 \cdot 10^{-1}$ mg/ml at 75°C, $5 \cdot 10^{-2}$ mg/ml at 100°C and $5 \cdot 10^{-4}$ mg/ml at 150°C. Two intermediate cases are added when a strong difference is highlighted; these two cases are $5 \cdot 10^{-3}$ mg/ml at 125°C and $5 \cdot 10^{-5}$ mg/ml at 150°C.

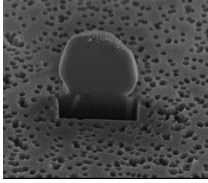
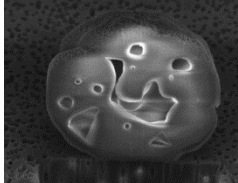
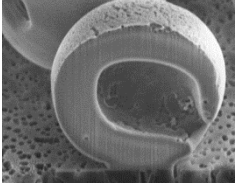
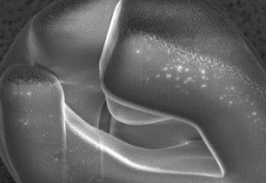
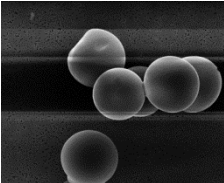
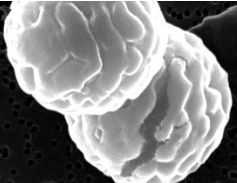
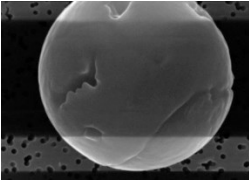
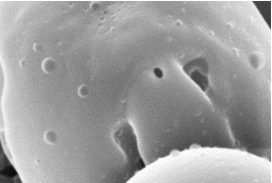
Table 3.1 Experimental matrix with the predicted precipitation window (Δt_p) and crystallization window (Δt_c). The cases are distinguished by initial solution concentration (C_0) and drying gas temperature (T). The indicated errors were obtained by uncertainty propagation of the imaging resolution error.

C_0 [mg/ml]	T	Δt_p [ms]	Δt_c [ms]	C_0	T	Δt_p [ms]	Δt_c [ms]
	[°C]			[mg/ml]	[°C]		
5	25	266 ± 2	265 ± 3	5×10^{-3}	25	132 ± 2	122 ± 5
	50	239 ± 2	221 ± 1		50	120 ± 1	110 ± 1
	75	221 ± 6	191 ± 3		75	101 ± 3	79 ± 1
	100	161 ± 4	122 ± 2		100	75 ± 2	73 ± 1
	125	119 ± 5	99 ± 2		125	37 ± 2	34 ± 2
	150	79 ± 14	60 ± 7		150	20 ± 1	16 ± 4
5×10^{-1}	25	190 ± 2	201 ± 1	5×10^{-4}	25	98 ± 2	82 ± 4
	50	181 ± 1	162 ± 17		50	80 ± 1	79 ± 2
	75	161 ± 3	151 ± 1		75	62 ± 5	49 ± 1
	100	119 ± 18	95 ± 4		100	56 ± 4	38 ± 2
	125	90 ± 5	68 ± 2		125	36 ± 1	22 ± 1
	150	62 ± 8	49 ± 12		150	16 ± 2	10 ± 8
5×10^{-2}	25	159 ± 1	144 ± 9	5×10^{-5}	25	78 ± 2	59 ± 1
	50	139 ± 7	138 ± 3		50	54 ± 2	36 ± 2

75	117 ± 2	115 ± 1	75	36 ± 1	26 ± 1
100	99 ± 9	92 ± 2	100	20 ± 1	19 ± 1
125	59 ± 3	58 ± 2	125	18 ± 2	10 ± 1
150	39 ± 1	31 ± 5	150	5 ± 1	4 ± 1

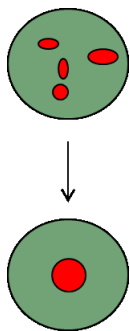
Table 3.2 shows the morphology of the final dried particles. The Scanning Electron Microscope (SEM) images show the dimensions and the external morphology of the final dried particles. The ion beam milled (FIB) particles show the shell thickness and the internal morphology. Table 3.2 also lists the crystallization window and the final particle density for these cases. The values of density shown in Table 3.2 were derived from an analysis of SEM and FIB images. The final dried microparticles were monodisperse; thus, their properties, such as density, amount of voids, morphology and diameter, were the same for each case.

Table 3.2 Focused Ion Beam (FIB) and Scanning Electron Microscope (SEM) images of the final dried microparticles. The cases are, from right to left, 5 mg/ml at 50°C, $5 \cdot 10^{-1}$ mg/ml at 75°C, $5 \cdot 10^{-2}$ mg/ml at 100°C and $5 \cdot 10^{-4}$ mg/ml at 150°C. Final particle density and crystallization window are shown for each case.

FIB				
SEM				
Scale bars	<u>1 μm</u>	<u>1 μm</u>	<u>1 μm</u>	<u>1 μm</u>
ρ_f [mg/ml]	1980	876	446	305
Δt_c [ms]	34	92	151	221

The FIB images show that the shell thickness changes with respect to the Δt_c . Table 3.3 shows the trend of Δt_c and amount of void space contained in the final dried particle. The void fraction was calculated using two methods: theoretical (Equation 3.6) and experimentally from the FIB images. If the final dried particles contained several voids, it was assumed that all the voids were equally distributed along all directions and were concentrated at the center of the microparticles. The void fraction is calculated as the difference between the diameters of the equally distributed voids and the diameter of the final dried particles, derived from three separate SEM images.

Table 3.3 Comparison between predicted and experimentally observed void fractions of the final particles.



Δt_c [ms]	Void fraction (theoretical) [%]	Void fraction (experimental) [%]
37	34 ± 2	28 ± 10
99	61 ± 3	67 ± 20
161	80 ± 3	78 ± 13
239	90 ± 4	96 ± 6

The particle density, derived using Equation 3.4 and Equation 3.5, is shown in Figure 3.5 for three selected cases. Figure 3.5 shows the difference between the two equations used to calculate the density of droplets or particles, Equation 3.4 and Equation 3.5. Equation 3.4 is based on the assumption of droplets or particles without internal or external voids. Equation 3.5 takes advantage of the SEM analysis on the properties of the final dried microparticles. The crossing point of the two methods identifies the point at which the derived volume equivalent diameter is equal to the diameter of the final dried particles. The exact point in time at which voids first occur is unknown. Therefore, both versions are provided after the crossing point.

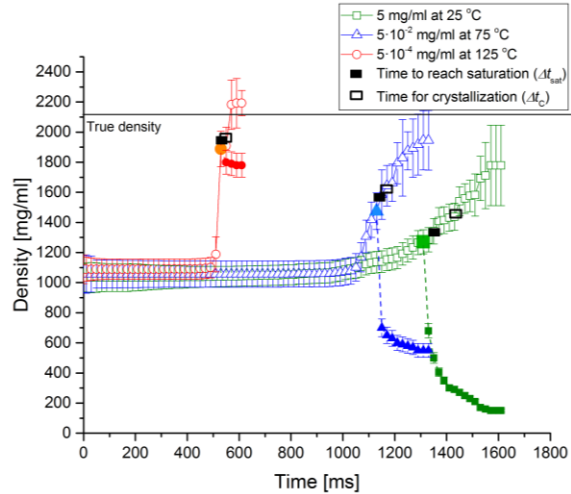


Figure 3.4 Particle density as a function of time during the particle formation process for three sample cases, 5 mg/ml at 25°C, 5×10^{-2} mg/ml at 75°C and 5×10^{-4} mg/ml at 125°C. The full black squares show the predicted time to reach saturation and the empty black squares the predicted time for onset of crystallization. The right part of each curve, described with full symbols, is obtained using Equation 3.5. The part of the curves, described with empty symbols, is obtained using Equation 3.4.

Figure 3.5 shows the predicted droplet surface concentration of sodium nitrate as a function of time. The plots are terminated at the saturation time point. The surface concentration curves allow determination of the time to reach saturation for every case considered. The dashed lines in Figure 3.5 indicate: horizontally, the solubility limit for the appropriate wet bulb temperature for each case and vertically, the time to reach saturation.

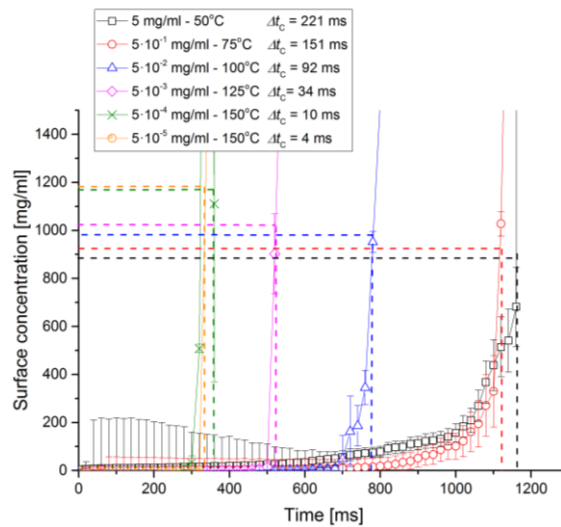


Figure 3.5 Predicted droplet surface concentration of NaNO₃ as a function of time during the evaporation process. The horizontal dashed lines indicate the solubility limit; the vertical dashed lines the time to reach saturation.

The trend of the normalized particle densities of the final dried microparticles as a function of crystallization window is shown in Figure 3.6. For larger crystallization windows, i.e. more time available for crystallization, the final particle densities are lower; for very small crystallization windows the normalized particle density approaches 1, indicating a solid particle without voids. This plot introduces the effect of the initial conditions to the crystallization window. Both initial solution concentration and temperatures of the external environment impact the properties of the final dried particles. Crystallization windows to the left of the dashed line labeled ‘experimental limit’ have large uncertainties due to the limited time resolution of the droplet chain method.

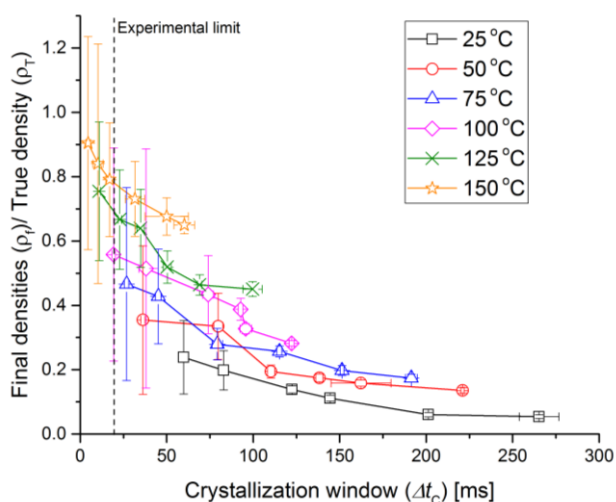


Figure 3.6 Relationship between the predicted time available for crystallization, Δt_c and the final particle density normalized by the true density of the solute. For each line, the six data points are obtained increasing the concentration in the initial solution.

Another instructive property of the final dried particles is the solid phase. As the other properties, the solid state is affected by the Δt_c of the cases considered. Figure 3.7 shows the relationship between the crystallinity of the final microparticles and Δt_c . It has been shown that sodium nitrate can be considered mostly amorphous when the peaks at Raman shifts of 96 and 185 cm^{-1} disappear [301, 302]. These two Raman peaks at 96 and 185 cm^{-1} are caused by long-wavelength librational and transitional crystal lattice modes. To the left, the Raman spectra of six typical cases are shown. The peak areas of both the 185 cm^{-1} lattice peak and the 96 cm^{-1} lattice peak normalized by the peak area of a reference peak at 1067 cm^{-1} , caused by an intramolecular vibrational mode, are shown for all studied cases to the right. The normalized peak area increases with Δt_c , indicating increasing order in the solid. The smallest Δt_c are correlated with mostly amorphous final dried particles.

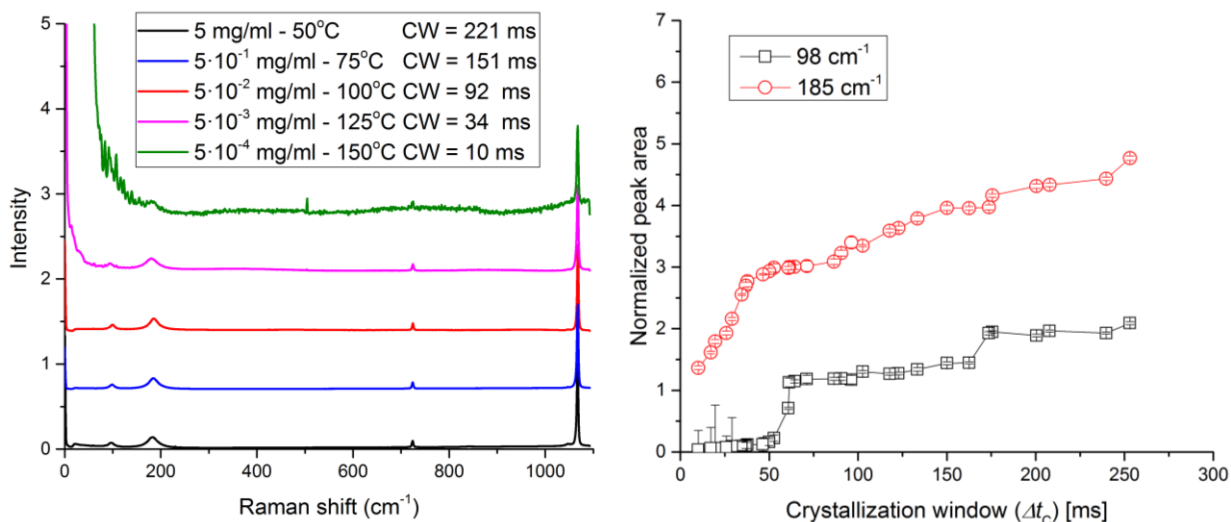


Figure 3.7 Crystallinity of the final particles as a function of crystallization window. Raman spectra of six typical cases are shown in the left panel. The right panel shows the normalized peak area of the crystal lattice mode at 96 and 185 cm^{-1} , a measure of order in the solid phase.

3.5 Discussion

The purpose of this project is to understand the role of crystallization on particle formation. The main properties of the particle formation process are assessed through a combination of experimental tests and theoretical predictions. A time-variable model is necessary for the prediction of the main parameters of the particle formation process of a crystalline solute. The evaporation rate obtained with a time-constant model does not approximate the slope of the squared volume equivalent diameter, Figure 3.3.

The combination of the time-variable model and experimental results determine several parameters of the particle formation process, such as diameter, both aerodynamic and volume equivalent, density, mass, and void amount. The trend of diameters and density with time indicates the main phases of the particle formation process, such as solvent evaporation, shell formation and solute saturation. When the droplet is dilute, the aerodynamic and the volume equivalent diameter have similar values, Figure 3.3. Subsequently, the density curve reaches a peak, which indicates the shell formation point, Figure 3.4. After shell formation the volume equivalent diameter is assumed to be constant, but the aerodynamic diameter keeps decreasing. This shows that the solvent trapped inside a formed shell is evaporating through the shell's pores. The density curve reaches a plateau only when the aerodynamic diameter becomes constant, Figure 3.4. The condition of

supersaturation is reached between the time step indicating the shell formation and the next time step, Figure 3.5. Between these two time steps the surface concentration rises strongly, Figure 3.5. The time for onset of crystallization and the remaining time available for crystallization, the crystallization window, are two variables that strongly influence the particle formation process. The initial process and formulation conditions of the particle formation process in turn influence the crystallization window. The largest values of the crystallization window are achieved in cases where the concentration of the initial solution is high and the temperature of the external environment is low. It is expected that increasing the relative humidity of the environment would have a similar effect. This would be the case for evaporation of ambient particles in the atmosphere. On the other hand, the smallest Δt_c is achieved for the combination of low concentration of the initial solution and high temperature of the external environment, Table 3.1. For the same temperature of the drying gas, the time for crystallization is reached later for lower initial concentration. For the same initial concentration, the time for crystallization is reached earlier for higher temperatures of the external environment. The temperature of the external environment influences the evaporation rate and thus surface saturation. The higher wet bulb temperature shortens the particle formation process. As a consequence, the crystallization window is also reduced. In addition, the surface concentration reaches saturation earlier in those cases, Figure 3.5. The crystallization window influences the properties of the final dried microparticles. Smaller values of Δt_c produce microparticles with a smaller diameter, smaller crystal size, smoother surface, lower crystalline content and smaller void volume, Table 3.2, Table 3.3 and Figure 3.7. A smaller crystallization window indicates less time for the solute to nucleate and for crystals to grow. As a consequence, for smaller crystallization windows, the final microparticles appear mostly amorphous, Figure 3.7. Furthermore, both theoretical derivations [1] and experimental results agree that for these cases the final dried microparticles have a smaller void fraction, Table 3.3. This agreement validates the theoretical derivations used.

For cases of high wet bulb temperatures and low concentration, the droplets show a high evaporation rate. The low solute mass fraction corresponds to low viscosity and a high diffusion coefficient. Previous publications on non-crystallizing systems show that for these conditions amorphous particles are expected to have a thin shell and a larger diameter [2]. The crystallization event causes a different result. Here, shell formation is induced by the crystallization event. At a

certain mass fraction, the solute starts to nucleate on the surface and subsequently generates a shell. This phase can be identified in a drastic drop in density curves, Figure 3.4. Close to this point in the evaporation process the theoretical model predicts that supersaturation is reached. Then, a long crystallization window allows these crystals to grow and form the shell of the final microparticles. The crystallization effect is emphasized by the gap between the density curves for time steps after the shell formation, Figure 3.4. For cases where the final dried particles are mostly amorphous, Table 3.2, the gap between the two methods is reduced, highlighting the impact of the crystallization on the particle formation process, mainly after the shell formation.

The methods used to analyze the particle formation process show limitations. These limitations are seen in both density curves and surface concentration curves, where the trend changes drastically between the time step of shell formation and the following one, Figure 3.4 and Figure 3.6. In these 20 milliseconds, time to reach saturation and time for crystallization are reached. Selecting a smaller time step might reduce these limitations.

3.6 Conclusion

This project demonstrates that the crystallization process influences the particle formation process in the case of substances that can crystallize within the same amount of time. The time gap between the onset of crystallization and the completion of drying contains the main steps in the particle formation process. Only during this time period may crystals nucleate and grow. Thus, the duration of the crystallization window determines the properties of the dried microparticles. Longer crystallization windows generate microparticles with higher crystallinity, larger crystal size, higher void fraction, and, consequently, lower density.

Understanding the relationship between the initial process conditions and the crystallization window, and thereby, the properties of the final dried particles is expected to improve control over the performance of microparticle based products. This may improve the efficiency of the delivery of drugs for respiratory diseases. The delivery efficiency of respiratory drugs, for example, depends on the diameter and the dispersibility of the spray dried microparticles. For instance, leucine, a much studied respiratory excipient, shows different properties according to its solid state. Leucine needs to be in crystalline form to improve powder dispersibility [303].

Limitations are found both on the experimental and on the theoretical approach. In the experiments, a time step of 20 milliseconds is chosen. A shorter time step might help with a better

definition of important time variables, such as the time to reach saturation and the time for crystallization. The theoretical approach yields only approximate results for the onset of the crystallization, due to limitations of the semi-analytical model. A fully numerical model seems more appropriate to describe particle formation processes that involve crystallization.

3.7 Acknowledgements

Funding from the Natural Sciences and Engineering Research Council of Canada (NSERC) and the Alberta Innovates Technology Futures is gratefully acknowledged. The authors thank Jason Dibbs for the fabrication of components of the setup used. JPR, RMP and REHM thank the EPSRC for financial support through a Leadership Fellowship awarded to JPR (grant reference EP/G007713/1) and grant EP/L010569/1.

3.8 Supplemental Information

3.8.1 Experimental details

Chemicals

The solubility of NaNO_3 in water at the droplet temperature, *i.e.*, the wet bulb temperature, is needed for the theoretical model. Wet bulb temperatures depend on the temperatures of the external environment and the evaporation rate [2]. Assuming a constant wet bulb temperature through the process, at the temperatures of 10, 20, 25, 30, 35 and 40°C, the solubilities are 870, 930, 970, 1020 and 1070 mg/ml, respectively [304]. However, vapor pressures are influenced by the percentage of solute contained in the evaporating droplet. Since the weight percentage of NaNO_3 increases due to the evaporation of water, the evaporation rate decreases and the wet bulb temperature increases during the particle formation process [305]. As a consequence, the solubility increases according to the weight percentage of NaNO_3 in DI H_2O .

Solution preparation began by weighing out NaNO_3 on an analytical balance (ME204E, Mettler Toledo, Mississauga, Ontario, Canada) and adding it to the solvent within a volumetric flask. The solution was closed with a paraffin film (PM992, Pechiney Plastic Packaging, Chicago, IL, U.S.) and agitated for 15 minutes using a wrist action shaker (Model 75, Burrell Scientific, Pittsburg, Pennsylvania, U.S.).

3.8.2 Experimental setup

Determination of viscosity

The composite particle underwent relaxation to a single spherical droplet, governed by the balance of surface and bulk viscous forces. A detailed description of the aerosol optical tweezers technique and its use in studying particle coalescence has been presented previously [306, 299]. Frequency doubled light from a Nd:YVO₄ laser at 532 nm was incident on a liquid-crystal-on-silicon spatial light modulator (LC-R 2500, Holoeye Photonics AG, Berlin-Adlershof, Germany), conjugated to the back focal plane of an inverted microscope objective (ACH oil, 100 x, NA 1.25, Olympus Niko, Chiyoda Tokyo, Japan) to form a tightly focused optical trap within a custom built aerosol trapping cell. The spatial light modulator imparted a phase-only modulation on the profile of the Gaussian beam, allowing the creation of two gradient-force optical traps within the trapping chamber. The axial and lateral trap positions were determined by the modulation pattern applied to the spatial light modulator by user-controlled software, allowing spatial manipulation of the optical traps to initiate particle coalescence.

Two particles, 3 to 6 μm in radius, were trapped from a plume of aqueous sodium nitrate aerosol introduced into the trapping cell using a medical nebulizer (NE U22, Omron, Kyoto, Japan), with particles passing through the focal point of each optical trap caught and confined in three dimensions by the strong gradient force. Particles were trapped within a relative humidity (RH) controlled environment, maintained by a constant gas flow (< 0.2 l/min), and generated by mixing different proportions of dry and humidified nitrogen. The gas flow RH was measured after the trapping cell using a calibrated capacitance probe (Honeywell 500, Honeywell, Morristown, New Jersey, USA). By varying the gas phase RH, different sodium nitrate solute mass fractions, and thus viscosities, could be accessed in the trapped particles.

Inelastically back-scattered light from each particle was collected by the same objective and dispersed using a spectrograph onto a Peltier-cooled CCD camera (SpectraPro SP550i, Pixis 256, Acton, Princeton Instruments, Buckinghamshire, UK). Raman active species within the trapped particles were excited by the 532nm laser light, leading to spontaneous Raman emission at Stokes shifted wavelengths characteristic of the molecular species present. At wavelengths commensurate with whispering gallery modes, the trapped particles acted as optical cavities, enhancing Raman scattering at discrete wavelengths and leading to a superposition of narrow stimulated Raman peaks on the broad spontaneous Raman bands. Measurement of the whispering gallery mode wavelengths through cavity enhanced Raman spectroscopy (CERS) and subsequent comparison

with Mie theory calculations allows the radius and refractive index of a particle to be determined with accuracy ± 2 nm and ± 0.0006 , respectively. Trapped particles were imaged using brightfield microscopy, with a maximum camera frame rate of 1000 frames per second. Elastically back-scattered light from one of the particles was isolated and collected by a silicon photodetector (Thorlabs DET110, Thorlabs, Ely, UK).

Following capture, the two particles were left to equilibrate with the humidity in the gas phase until no further change in either particle's size was observed over a period of 30 minutes. Once equilibrated, the two droplets were positioned such that the separation between the surfaces of the two particles was lower than $1 \mu\text{m}$ before removing one of the optical traps. The optical field of the remaining trap extended over sufficient range to draw the free particle in to the remaining trap, initiating particle coalescence. Depending on particle viscosity, the timescale for coalescence could be monitored using elastic light scattering, brightfield imaging or Raman spectroscopy. The viscosity range accessible by each technique depended on their maximum rate of data acquisition: higher than 100 MHz for elastic light scattering, 1 kHz for brightfield imaging and 1 Hz for Raman spectroscopy. In the work presented here, the relaxation in particle shape following coalescence was monitored using elastic light scattering as all relaxation times were shorter than 10 ms with viscosities lower than 10 Pa s [299, 307].

The intensity of elastically back-scattered light from a particle is a function of its scattering cross-section, dependent on the particle size and shape, and its position within the optical trap. As the second optical trap is removed and the coalescence of the particles begins within the optical field of the remaining trap, an increase in the elastically scattered light intensity recorded by the photodetector is observed due to the increase in size of the composite scattering body within the sampling volume. The back-scattered light intensity then decreases to a constant final value as the coalesced particle relaxes to a spherical shape driven by capillary forces. Motion of the composite particle due to trapping forces is negligible over the time scales studied, likewise the optical forces are many orders of magnitude weaker than the restoring capillary forces and play no part in determining the dynamics. For particles with a viscosity below the critical damping threshold (~ 20 mPa s for the particle sizes considered here), the relaxation is accompanied by shape oscillations and corresponding oscillations in backscattering intensity, which takes the form of a damped harmonic oscillator. The oscillation frequency and the damping time can be used to estimate the

surface tension and viscosity of the droplet, respectively. For particles of higher viscosity, the time dependence can be fit to a single exponential decay whose characteristic relaxation time can be determined. This is equivalent to the time taken for the elastically back-scattered light intensity to fall to $1/e$ (37%) of its initial value, and can be used to determine the particle viscosity. Correspondence between the elastic light scattering signature and the change in particle shape has been discussed in detail in our previous work, including a detailed comparison of light scattering calculations for an oscillating sphere with the measured signal, and we refer the reader to this earlier work for more information [308, 299].

To estimate the particle viscosity from the relaxation time, it is necessary to know the radius and true density of the coalesced particle. The radius of the coalesced particle is calculated from fitting the CERS spectra, and the true density is determined from the Extended Aerosol Inorganics Model using the RH as measured by the capacitance probe to determine the particle water activity [309, 310].

Seventeen sodium nitrate particle coalescence events were observed at RHs in the range 86.5% to 24.2%. The uncertainty associated with the capacitance probe RH measurement increases with increasing humidity, reaching values higher than 3% at humidities approaching 90% RH. To mitigate this uncertainty, the sodium nitrate mass fraction of solute in all coalesced particles equilibrated above 50% RH was calculated from the refractive index determined from the Raman spectra rather than from the RH measurement, employing the parameterization shown in previous literature [311]. The dispersion in refractive index (i.e., variation in refractive index with wavelength) retrieved from fitting the Raman spectra was used to compensate for the differences in refractive index measured using CERS (at a wavelength of 650 nm) and the model treatment (at a wavelength of 632.8 nm) [311]. For coalescence measurements performed on particles equilibrated below 50% RH, the uncertainty in the water activity was observed to be less than the variation between successive measurements and thus the probe RH was used directly to calculate the mass fraction of sodium nitrate in the coalesced particles using a second parameterization [300]. Measured data points were binned in to water activity ranges, with viscosities reported as an average and standard deviation.

4 Analysis of Cohesion Forces between Monodisperse Microparticles with Rough Surfaces

The material shown in Chapter 4 has been submitted in Colloids and Surfaces a Physicochemical and Engineering Aspects. All the experiments have been personally conducted. The theory has been developed in previous publications, [312-314]. The authors of this publication are me and my supervisor Reinhard Vehring. Additional material is shown in Appendix D.

4.1 Abstract

This project investigated the impact of roughness, morphology and crystal size on the cohesion forces between microparticles of different size and shape. A chain of droplets with an initial diameter of about 70 μm was used for the production of monodisperse and monomorph microparticles in a diameter range of 0.7 to 17 μm . Droplets were composed of sodium nitrate and deionized water. Initial conditions of the process differed in temperature of the external environment, from 50 to 150°C, and in solution concentration, from 5 to $5 \cdot 10^{-4}$ mg/ml. By varying these initial conditions, microparticles with different diameter and morphology were generated. Their root mean squared roughness was in a range from 2 to $6 \cdot 10^{-5}$ μm . Pull-off forces between particles of the same morphology and of different morphology were determined using colloidal probe microscopy. A wide range of cohesion forces were measured and were found to be affected primarily by the microparticle roughness. The utility of several theoretical cohesion models in predicting the experimental results was tested.

4.2 Nomenclature

A , Hamaker constant [J];

α , adhesiveness [N/m^2];

E , Young's modulus [Pa];

ϵ_i , dielectric constant for solvent or solute;

F , cohesion force [N];

ν , Poisson's ratio;

h , Planck's constant;

H_0 , minimum distance between two microparticles [m];

γ , surface tension [N/m];

γ_s , surface tension of a solid smooth surface [N/m];

γ_l , surface tension of a liquid [N/m];

k , Boltzmann's constant [$\text{m}^2\text{kg}/\text{s}^2\text{K}$];

L , load normal force [N];

λ , peak to peak distance [m];

μ , dimensionless coefficient used to choose between DMT or JKR model;

n_i , refractive index of solute or solvent;

θ_a , advancing contact angle [$^\circ$];

θ_r , receding contact angle [$^\circ$];

r , radius of asperities [m];

R , radius of microparticles [m];

R_q , root mean square roughness [m];

$R_{q,i}$, root mean square roughness for different scanning area i [m];

S , contact area between two particles [m^2];

T , temperature [K];

Δt_c , crystallization window [s];

ω ; absorption frequency [rad/s];

4.3 Introduction

Pulmonary drug delivery is an area of constant growth for research studies [315-317, 19, 318]. These studies focus on two main methods of delivery: inhalation and instillation. Drugs are most commonly delivered to the lungs through inhalation [21, 20] due to its multiple advantages. The risks involved in inhalation are minimal compared to other techniques, such as liquid instillation

[22]. In addition, inhalation is a non-invasive and often self-applied treatment [22, 319]. The main disadvantage of drug inhalation, however, is inefficiency; a large portion of the drugs commonly does not reach the lungs [320, 321]. This issue can be improved by using calculations and predictions to refine the delivery process. The predictions are based on the influence of the properties of drugs on their delivery location inside the respiratory tract.

Studies on pulmonary drug delivery have recently focused on the control of the main properties of drugs to improve the quality and the efficiency of their delivery [322]. Pulmonary drugs are commonly delivered to the lungs using microparticles [323]. The diameter of the microparticles is important for their deposition in the lungs; a range of 0.1 to 5 μm is suggested to allow the microparticles to reach the lungs [324]. While smaller particles easily reach the lungs and their alveoli [325], they may be exhaled again to some extent. Large particles may also reach the lungs and alveoli, if they have a suitable morphology [326].

Morphology is, thus, a property of the microparticles that can influence their delivery. Several studies improve the knowledge of the relationship between morphology and delivery efficiency [327, 265, 328]. Morphology describes the shape and structure of the particle interface and interior; it includes parameters such as crystal size for particles composed of smaller crystals, and measures of surface roughness. The crystal size of composite microparticles is directly connected to their roughness; smaller crystal size tends to generate greater roughness [329]. This relationship depends on the material of which the microparticles are composed. The roughness can affect the delivery of the microparticles to the lung primarily by reducing the strength of cohesion between microparticles [326, 318], thereby causing improved powder dispersibility and better aerosol properties [39, 330].

The determination of cohesion forces between two microparticles is quite complicated. Firstly, interlocking of rough microparticles can occur randomly between any possible points of contact on the interface [331], increasing measurement variability. Secondly, it is more difficult to measure cohesion forces between two microparticles than between a microparticle and a flat surface [332, 34].

Studies addressing the relationship between the properties of microparticles and their cohesion forces can be seen as a sub-discipline of particle engineering [2]. The main goal of particle engineering is to improve the properties of the microparticles. To achieve this, the process of

producing the microparticles is studied. The microparticles used for pulmonary drug delivery are commonly produced via spray drying [182], a process that has the following advantages among others: low manufacturing cost, low loss of activity of chemicals, broad choice of solutions or suspensions, and control over fundamental properties of the final particles [99].

The process by which pulmonary drug microparticles are generated from solution or suspension droplets is called particle formation [156, 333]. Two possible outcomes may result from the particle formation process: homogenous or core shell particles. In systems with crystallizing excipients or drugs the time at which the solute reaches saturation on the surface of the evaporating droplet is one of the critical time variables for the prediction of the particle formation process. A late time to reach saturation may produce solid particles [156, 2], because not enough time is left in the evaporation process for nucleation and crystallization. Another similar variable is the time for crystallization. This time variable indicates, for solutes with a tendency to crystallize, the moment at which sufficient supersaturation is reached such that one or more crystal nuclei may start to grow. The knowledge of this time variable facilitates the prediction of the morphology of final dried microparticles; if the time for crystallization occurs late in the evaporation process, particles smooth, amorphous and with a small crystal size may result.

The basis for the theoretical description of particle formation was provided by Vehring et al. [2] using an approach based on liquid phase diffusion in droplets evaporating with a constant evaporation rate. Different types of formation mechanisms were considered, depending on the nature of the solutes or suspended materials in the droplets. Boraey et al. [1] included new variables into the analysis, for example shell thickness or the void volume of the dried particles. The particle formation process for solutes undergoing crystallization is a topic of current investigations [334].

In order to describe the particle formation process, the evaporation sub-process [335] has to be studied. The evaporation of the solvent is the main part of the particle formation process [122]. Several experimental methods are available for understanding the evaporation process. Recent studies have focused on the monodisperse droplet chain method [336, 131] because it overcomes many disadvantages of other commonly used methods. The monodisperse droplet chain is not affected by heat conduction through the support wire encountered in the method of suspending droplets on filaments. In addition, the monodisperse droplet chain is less affected by time constraints, encountered in the method involving a single levitated droplet evaporating in a

quiescent environment or in a gas flow [337]. The piezoceramic dispenser is the most suitable choice for the production of microparticles with high homogeneity in their properties. In response to an input voltage pulse, the piezoceramic dispenser expands and then contracts to its normal size. Thus, acoustic waves are produced in the solution contained in the piezoceramic dispenser and droplets are generated with consistent ejection velocity and diameter [218].

Monodisperse and monomorph microparticles facilitate measurements using the colloidal probe technique, which can be used to determine the forces between two microparticles. Commonly, the colloidal probe technique makes use of an Atomic Force Microscope (AFM) to obtain values of cohesion forces between one microparticle and a flat surface or between two microparticles [338]. In this technique, a microparticle is attached to the tip of an AFM cantilever. The measurement process can be divided into two main parts: approach and retraction. The approach has two sub-steps. Firstly, the functionalized cantilever is moved downward towards the sample particle. Secondly, once the cantilever is close enough to the sample, it is attracted to it and accelerated into contact. The forces involved in this step are called 'snap in'. The cantilever is further pushed downward and deflected until the retraction starts. The third step simply follows the retraction of the cantilever along the same path during the approach. At some point, the adhesion forces that keep the cantilever in contact with the sample are overcome and determined as maximum pull off forces. Lastly, the cantilever is brought back to the start point. Results can be influenced by the type of cantilever chosen [339]. It is known that cohesion between particles is affected by particle radius and surface roughness. Therefore, a large number of particles from a powder with polydisperse size distribution and variable particle morphology would have to be measured to obtain a representative mean cohesion value. This is not easy to accomplish using this technique, because it is quite time consuming. Thus, if monodisperse and monomorph particles can be used, like in the study presented here, the utility of the technique is enhanced.

The main goal of this study is to demonstrate the connection between surface roughness and crystal size and the cohesion forces between two spray dried microparticles. The cohesion forces are measured experimentally and described theoretically. Theoretical descriptions of cohesion between two realistic microparticles are limited. A number of theoretical models regarding the contact forces between elastic solids, such as a sphere and a plate, have been published [340-345, 314]. In this paper the experimental results will be compared to several existing models to identify the one most applicable to this case.

4.4 Materials and methods

4.4.1 Chemicals

The solute present in the dried microparticles is sodium nitrate (NaNO_3) (catalog number 221341-500G, Sigma Aldrich, St Louis, MO, USA). Its main properties, listed by the manufacturer, are as follows: molecular weight of 84.99 g/mol and true density of 2260 mg/ml. Its purity is greater than 99%; the impurities are chloride, iodate, nitrite, phosphate and sulfate. Other important properties of NaNO_3 are its glass transition temperature range between 185°C and 215°C and melting point of 306°C [217].

The Hamaker constant is used in some theoretical cohesion models to represent van der Waals interactions. The Hamaker constant for interaction of two sodium nitrate particles in air was approximated using Equation 4.1 [346].

$$A_{131} = \frac{3kT}{4} \left(\frac{\varepsilon_1 - \varepsilon_3}{\varepsilon_1 + \varepsilon_3} \right)^2 + \frac{3h\omega}{32\pi\sqrt{2}} \frac{(n_1^2 - n_3^2)^2}{(n_1^2 + n_3^2)^{\frac{3}{2}}} \quad \text{Equation 4.1}$$

The required properties of crystalline sodium nitrate are as follows: refractive index, n_1 , of 1.633 [311] and dielectric constant, ε_1 , of 5.2 [347]. The properties of air are well known: refractive index, n_3 , of 1.00023 [348] and the dielectric constant, ε_3 , of 1.00059 [349]. The other terms shown in Equation 4.1 are Planck's constant, h , Boltzmann's constant, k , and the absorption frequency, ω , of 9.4×10^{15} rad/s, derived from the absorption wavelength of sodium nitrate in UV/visible light of about 200 nm [350, 351]. Equation 4.1 yields an approximate Hamaker constant between two sodium nitrate microparticles in air of $5.3 \cdot 10^{-20}$ J. This value is close to the Hamaker constant of similar salts [346].

The Young's modulus for sodium nitrate is required for some theoretical models. It was calculated from the main elastic constant, the shear stress and bulk stress of sodium nitrate [352]. Young's modulus, E , and Poisson's ratio, ν , are found using their well-known definitions [353] and are 34.9 GPa and 0.41, respectively. The values of these two variables are close to the ones of a similar salt, NaCl [354].

The solvent used to generate the dried microparticles is deionized water (catalog number 38796 – 1L, Sigma Aldrich, St Louis, MO, USA), with a residual content lower than 0.01%. Other solvents are used to determine the surface energy of sodium nitrate powder: chloroform (528730, Sigma

Aldrich, Oakville, Ontario, Canada), perfluorooctyl bromide (PFOB) (383648, Sigma Aldrich, Oakville, Ontario, Canada), and silicon oil (84049, Sigma Aldrich, Oakville, Ontario, Canada). These solvents are selected for their inability to dissolve sodium nitrate and for their high surface tension, which prevent penetration of the liquid into pores in the flat surface made of sodium nitrate, as described below. In air and at 20°C, the surface tension of chloroform, PFOB and silicon oil are 26.7, 30 and 20 N/m, respectively [355].

4.4.2 Methods

4.4.2.1 Generation of monodisperse microparticles

The production of monodisperse and monomorph microparticles was explained in detail in a previous publication [356, 156, 1, 2]. Here, only a brief description is provided. NaNO₃ was weighed out on an analytical balance and added to water within a volumetric flask. The vial containing the solution was closed with paraffin film and agitated for 15 minutes using a wrist action shaker. A monodisperse chain of sodium nitrate solution droplets was generated using a piezoceramic droplet dispenser with an inner diameter of 30 μm. The droplets were injected into a gas flow enclosed in a double-walled, square flow tube. The temperature of the gas was set using two heaters placed at the top of the flow tube. The temperature was recorded at the droplet injection point and at the point at which dried particles were collected on a hollow SEM stub for further analysis. The monodisperse droplet chain was recorded with a digital camera. From the images, the changing aerodynamic diameter of the droplets during the drying process was derived. Then, with the help of particle formation models, the surface concentration of the solute, here sodium nitrate, was calculated as described in more detail elsewhere [156]. This allowed determining the point in time at which sodium nitrate reached sufficient supersaturation at the surface for crystallization to commence. The difference between this time and the time at which all solvent is evaporated, *i.e.*, the time at which the aerodynamic diameter stops to decrease, is the period of time that is available for crystal growth. This time difference, termed crystallization window, Δt_c , was derived for all types of particles generated.

4.4.2.2 Microparticle characterization: SEM and FIB

The diameter and the morphology of the final dried microparticles were analyzed using a Scanning Electron Microscope (SEM) (LEO 1430, Zeiss, Jena, Germany). The images collected with the SEM were analyzed with image processing software (ImageJ, Imaging Processing and Analysis in

Java, National Institute of Health, 1997, Bethesda, Maryland, USA). The morphology of the interior of the microparticles was evaluated by using a Focused Ion Beam (FIB) (Hitachi NB 50000, Chiyoda, Tokyo, Japan) to section the particles.

4.4.2.3 *AFM analyses*

An atomic force microscope (AFM) (DimensionEdge Bruker, Billerica, MA, USA) was used for two purposes: analysis of the morphology of microparticles and determination of cohesion forces between two spray dried microparticles. For the first purpose, tapping mode was used to measure roughness and morphology of the produced microparticles. The tapping mode was selected to avoid any damage to the fragile microparticles and it was retained the most common technique to measure the roughness of microparticles [357]. A common AFM cantilever was purchased: three tips AFM cantilever with aluminum coating (HQ:NSC15/Al BS, Mikro Mash, Lady's Island, SC, USA). This probe was chosen for its broad range of bulk resistivity, rendering it applicable to a variety of cases.

Depending on the size of the microparticles, different scanning areas were selected: 100, 25, 1, 0.25, and 0.0625 μm^2 . The following roughness parameters were determined: primary root mean squared roughness, $R_{q,1}$, secondary root mean squared roughness, $R_{q,2}$, the radius of asperities, r , the peak to peak distance for primary peaks, λ_1 , and for secondary peaks, λ_2 . $R_{q,1}$ and λ_1 were measured using a scanning area with both sides of at least half the diameter of the particle. $R_{q,2}$ and λ_2 were measured using a scanning area with both sides smaller than the radius of the particle. The radius of asperities, r , was obtained as the average of the radius of highest peaks, analyzed using a scanning area with both side half the diameter of the particle, and the radius of the lowest peaks, analyzed using a scanning area smaller than the radius of the particle. For example, for a particle with a diameter of about 18 μm , $R_{q,1}$ and λ_1 were calculated using a scanning area of 100 μm^2 . $R_{q,2}$ and λ_2 were obtained using a scanning area of 25 μm^2 . If the diameter of the particle was lower than 1 μm , an additional scanning area was measured, i.e., 0.01 μm^2 .

For the second purpose, contact mode was used to measure the cohesion forces between two microparticles. A three lever tipless AFM cantilever (HQ:CS38/tipless/AL BS, Mikro Mash, Lady's Island, SC, USA) was chosen to facilitate attachment of a microparticle to the tip. The three lever AFM probe allowed selection of different low force constants. Among the three levers, the

one with a lower force constant was selected for its geometry; its length facilitated the visualization of both particles and the cantilever tip under a microscope.

Samples were prepared using the same method for both purposes. Thin, smooth glass slides (12-548-5P Fisher finest, Fisher Scientific, Edmonton, AB, Canada) were purchased. In order to fix the microparticles on the glass slide, glue was required (04004, Hardman Double/bubble water-clear epoxy, Royal Adhesives and Sealants, South Bend, IN, USA). The glue was selected for its medium viscosity, 14000 mPa·s, and for its long working time, 1 hour. A medium-high viscosity is ideal for microparticles composed of organic materials. Glues too liquid would embed the microparticles and glues too hard would not hold the microparticles tightly. A long working time allows sufficient time for placing of the microparticles and their stabilization. A drop of about 20 μ l was placed on the glass slide. A clean glass slide was then squeezed against the glass slide carrying the drop of glue, flattening the drop of glue and removing the excess of glue.

A modified optical microscope (Olympus IX70 Fluorescence Microscope, Olympus Corporation, Shinjuku, Japan) was used for attaching the microparticles to the tip of the AFM tipless cantilever. The modifications to the microscope were described in a previous publication [358]. The rotational stage of the microscope held tweezers in which the cantilever was attached. The rotational stage allowed the movement of the cantilever in three directions. The cantilever was placed at an angle with respect to the sample. Previous studies verified that the best angle for a successful attachment of a microparticle to the cantilever was 30° [358]. Figure 1 shows the steps taken to place one microparticle on a tipless AFM cantilever: 1) the AFM cantilever was aligned with a drop of glue. The cantilever was dipped into the drop, carefully ensuring that only one side of the cantilever tip was in contact with the glue. 2) The excess glue was removed by dragging the cantilever on a clean area of the glass microscope slide. 3) The correct amount of glue on the cantilever was verified using a Confocal Scanning Microscope (Zeiss LMS 700, Jena, Germany). 4) The cantilever was then aligned with a microparticle placed on a clean glass microscope slide. 5) The cantilever was moved until touching the microparticle. 6) The microparticle was verified to be attached to the cantilever using two methods: first, the spot on the glass slide where the microparticle was lying was visualized under the microscope and second, the cantilever was visualized under the confocal scanning microscope.

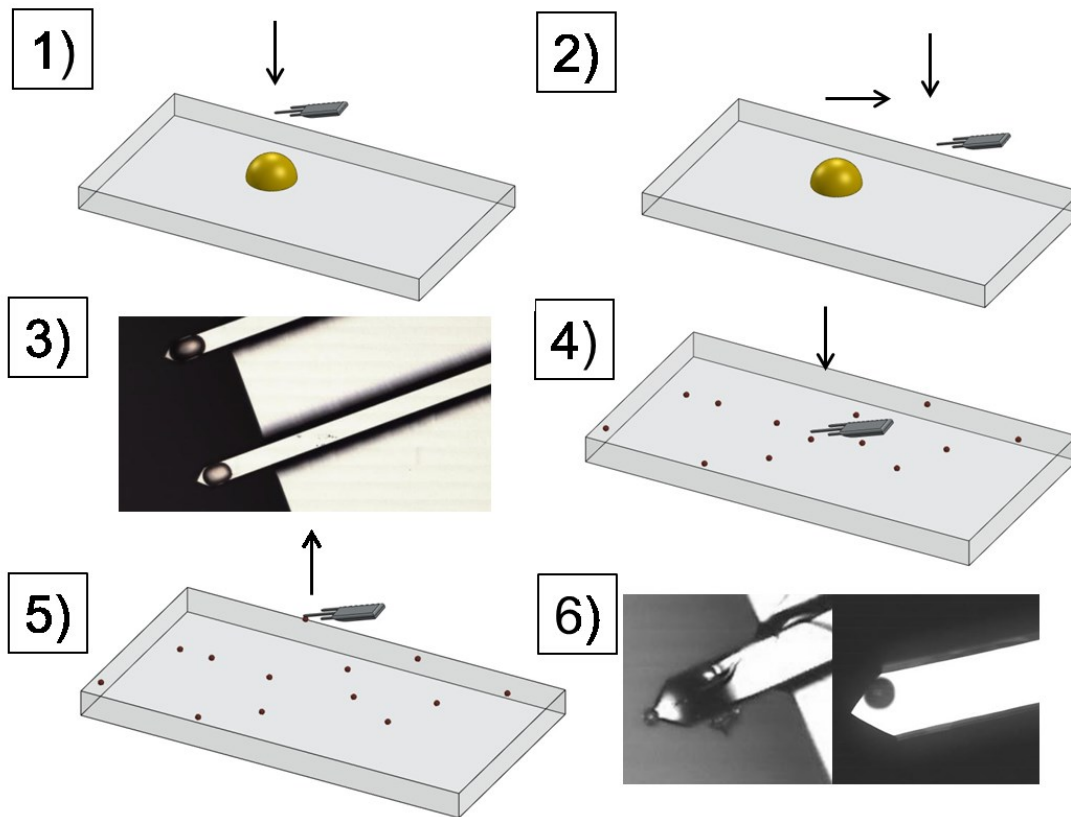


Figure 4.1 Procedure to attach a microparticle on an AFM tipless cantilever: 1) dipping the cantilever into the glue , 2) removing excess glue, 3) verifying under a Confocal Scanning Microscope the glue amount, 4) pushing the cantilever downwards until the microparticle is contacted, 5) picking up the microparticle and 6) verifying that the microparticle is attached to the cantilever.

4.4.2.4 *Surface energy analysis*

The surface tension of sodium nitrate needed to be measured, because it was necessary for the theoretical determination of cohesion forces. The sessile droplet method, a method that determined the contact angle between a flat, smooth surface of sodium nitrate and a liquid drop, was used for this purpose. A flat surface of sodium nitrate was achieved using the steps indicated in Figure 4.2. Powder of sodium nitrate, about 20 mg, was placed on a glass microscope slide. The sodium nitrate was heated above its melting point using a heat gun. The melted sodium nitrate was then squeezed in between two glass microscope slides. Once solidified, it was transferred to a glass microscope slide with double side tape (3M VHB Foam tape, 3M, London, Ontario, Canada). The smoothness of the sodium nitrate substrate was verified under the confocal scanning microscope, as Figure 4.2 illustrates. Sodium nitrate substrates with root mean squared roughness larger than 1 μm were discarded.

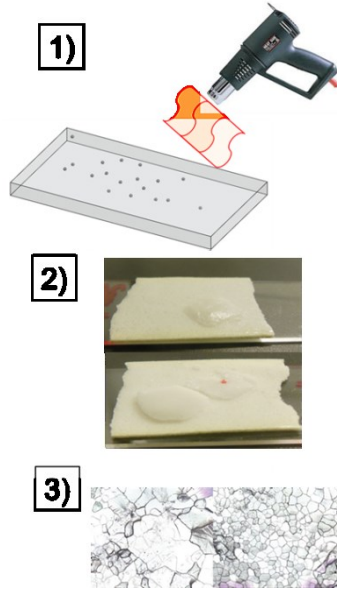


Figure 4.2 Production steps of a flat and smooth substrate of sodium nitrate: 1) melting of sodium nitrate powder, 2) squeezing the molten sodium nitrate in between two glass microscope slides, 3) verifying the smoothness with a Confocal Scanning Microscope. The image shown has a magnification of 20x.

The contact angle device (FTA 200, First Ten Angstroms, Portsmouth, Vancouver, Canada) comprised a syringe, a needle and a liquid. The syringe was filled with the selected liquid and inserted in the contact angle device. The glass microscope slide supporting the melted sodium nitrate substrate was placed under the syringe. The liquid was released in close proximity to the substrate. After contact with the surface, the liquid drop was further released and an image was recorded every three seconds. Recording at the same camera speed, the drop was subsequently retracted. The images recorded were then analyzed using the software ImageJ (ImageJ, Imaging Processing and Analysis in Java, National Institute of Health, 1997, Bethesda, Maryland, USA), to obtain the average advancing and receding contact angles. The sessile droplet method is based on the contact angle hysteresis, which is the difference between the advancing, θ_a , and the receding, θ_r , contact angles. Equation 4.2 determines the surface tension of a solid, γ_s , knowing the surface tension of the liquid considered, γ_l , [359].

$$\gamma_s = \gamma_l(\cos \theta_r - \cos \theta_a) \left\{ \frac{(1 + \cos \theta_a)^2}{[(1 + \cos \theta_r)^2 - (1 + \cos \theta_a)^2]} \right\} \quad \text{Equation 4.2}$$

The value of surface tension for sodium nitrate, found with Equation 4.2 from measurements with three probe liquids, chloroform, PFOB, and silicon oil, was 23.5 ± 4.4 mN/m. The use of different probe liquids contributes to the error. This value of surface energy applies to crystalline sodium

nitrate. Even though sodium nitrate was melted to create a flat surface, it was found to recrystallize in a very short time. The surface tension of molten NaNO₃ was reported to be larger, with a value of 119 mN/m [360], as can be expected for the more disordered liquid state.

4.4.3 Theory and Calculations

Several theoretical cohesion models were considered for comparison with the experimental results:

The *Hamaker contact force model* is based on the Hamaker constant. Since cohesion forces were measured between two microparticles with potentially dissimilar radius, R_2 and R_1 , an intermediate radius, R , was obtained as shown in Equation 4.3 [361]. This reduced radius was used for all theoretical models.

$$R = \frac{2R_2R_1}{(R_2 + R_1)} \quad \text{Equation 4.3}$$

The cohesion forces are then calculated using Equation 4.4. A represents the Hamaker constant, and H_0 is the minimum distance between the two surfaces. The minimum distance achieved using AFM in contact mode was reported as 0.3 nm [362].

$$F = \frac{AR}{12H_0^2} \quad \text{Equation 4.4}$$

Several *surface energy based cohesion models* have been presented, e.g., the Johnson, Kendall and Roberts (JKR) [341] and Derjaguin, Muller and Toporov (DMT) [343] models. These models are based on the surface tension, γ , of the solid and the dimensions of the contact surfaces. A dimensionless parameter, μ , has been introduced to determine which model is most applicable for a given case [363, 364].

$$\mu = \left(\frac{4R\gamma^2}{\pi E^2 H_0^3} \right)^{\frac{1}{3}} \quad \text{Equation 4.5}$$

E is the Young's modulus and H_0 is the equilibrium separation distance derived from the Lennard Jones potential, which is similar to the separation distance used in equation 4. The use of H_0 for Equation 4.5 is justified by its similarity with the distance between two ions of sodium chloride for a minimum potential energy [365]. If this dimensionless parameter is lower than 0.1, the use of the DMT model is recommended. Since this was the case for all studied conditions, the DMT method was used to predict the pull off force according to Equation 4.6 [343].

$$F = 2\pi\gamma R \quad \text{Equation 4.6}$$

Several models include the effect of *contact surface roughness*. The Rumpf model [314] takes into account both noncontact and contact interactions. The influence of irregularities in the morphology of both particles is evaluated using Equation 4.7 [314].

$$F = \frac{A}{6H_0^2} \left[\frac{rR}{r+R} + \frac{R}{\left(1 + \frac{r}{H_0}\right)^2} \right] \quad \text{Equation 4.7}$$

In Equation 4.7, r stands for the radius of asperities on the particles. The variable r introduces the impact of the roughness on cohesion forces between a particle and a flat surface.

Instead of asperity radius the *modified Rumpf model* uses the root mean squared roughness, R_q , derived from AFM measurements, as Equation 4.8 [366] illustrates:

$$F = \frac{AR}{6H_0^2} \left[\frac{1}{1 + \frac{R}{1.48 R_q}} + \frac{1}{\left(1 + \frac{1.48 R_q}{H_0}\right)^2} \right] \quad \text{Equation 4.8}$$

Rabinovich developed an alternative method for the derivation of the cohesion forces between a particle and a flat surface, including different variables related to the surface morphology of the particle considered. The *Rabinovich model* requires the root mean squared roughness at different length scales, $R_{q,1}$ (primary roughness), and, $R_{q,2}$, the peak to peak distance, λ_1 , for primary peaks and, λ_2 , for secondary peaks, as shown in Equation 4.9 [366]. A peak is considered primary or secondary according to the peak height distribution. The two values of R_q are derived from the analysis of AFM measurements obtained with different scanning windows: wider for $R_{q,1}$ to contain the highest peaks.

$$F = \frac{AR}{6H_0^2} \left[\frac{1}{1 + \frac{58R R_{q,2}}{\lambda_2^2}} + \frac{1}{\left(1 + \frac{58R R_{q,1}}{\lambda_1^2}\right) \left(1 + \frac{1.82R_{q,2}}{H_0}\right)^2} \right] \quad \text{Equation 4.9}$$

Equation 4.9 has been further developed by introducing the effect of the surface energy on the cohesion forces between rough surfaces. Equation 4.9 is applicable for contacts between particles with radius of asperities not much smaller than the radius of the particles [345]. In the *surface*

energy Rabinovich model, the first term in the sum in Equation 4.9 is replaced by the DMT contact interaction [366], assuming that the contact is between a sphere of reduced radius, R , and an asperity, r . which can be replaced by Equation 4.10 [55].

$$r = \frac{\lambda_2^2}{58R_{q,2}} \quad \text{Equation 4.10}$$

Equation 4.10 is applied in the first term of Equation 4.11, which describes the surface energy Rabinovich model.

$$F = \frac{2\pi\gamma Rr}{(r+R)} + \frac{\frac{AR}{6H_0^2}}{\left(1 + \frac{58R R_{q,1}}{\lambda_1^2}\right) \left(1 + \frac{1.82 R_{q,2}}{H_0}\right)^2} \quad \text{Equation 4.11}$$

In the previous decade, Li et al. [342] developed a different method which describes cohesion forces as a product of intrinsic adhesiveness, α , and contact surface area, S .

$$S = \pi \left[\frac{3LR(1-\nu^2)}{4E} \right]^{\frac{2}{3}} \quad \text{Equation 4.12}$$

Equation 4.12 shows the contact area between two particles according to the Hertzian model of contact [367]. Here, L indicates the normal load force used in AFM contact mode experiments. The normal load force was 0.27 nN, found as the product of the spring constant of the cantilever, the average deflection sensitivity, and the voltage of the detector in AFM contact mode analysis [368]. Equation 4.12 was used here to approximate the effective contact area. The intrinsic adhesiveness based on the DMT theory is expressed in Equation 4.13 [342].

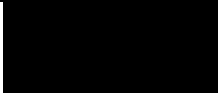
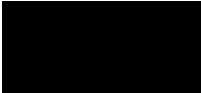



$$\alpha = \frac{4}{\sqrt[3]{9\pi^2 r \frac{(1-\nu^2)^2}{E^2}}} \gamma^{\frac{1}{3}} \quad \text{Equation 4.13}$$

It can be understood as a material property that captures the combined effects of surface energy, γ , Young's modulus, E , Poisson ratio, ν , and surface roughness as expressed by asperity radius, r , found with AFM measurements.

4.5 Results

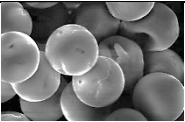
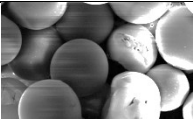
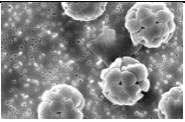
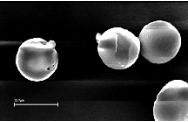
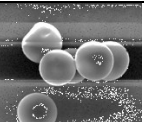
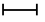
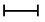

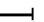


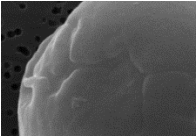
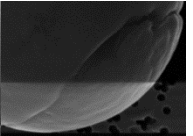
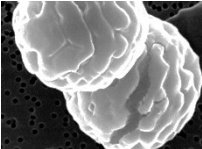
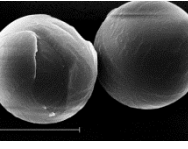
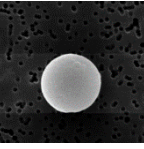
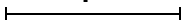
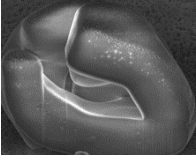
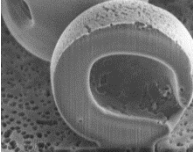
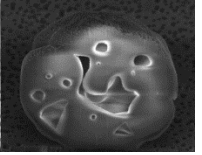
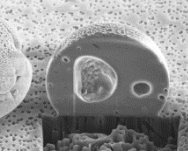
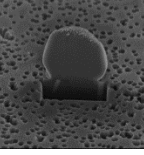
Five particle types with different morphologies were chosen according to their differences in initial conditions, *i.e.*, solution concentration and drying gas temperature. The cases selected are shown in Table 4.1. The measured crystallization window (Δt_c), the difference between time for onset of crystallization at the surface and time to reach constant aerodynamic diameter [156], is also listed. It is strongly dependent on the initial conditions of the particle formation process. In Table 4.1, the sketched profiles of microparticles emphasize the differences between microparticles obtained with different particle formation processes.

Table 4.1 List of the five morphology types considered. Initial solution concentration, drying gas temperature, profile, particle diameter and crystallization window are shown for every case.

Case	Conditions	Profile	Diameter [μm]	Δt_c [ms]
A	5 mg/ml at 50°C		17.7 ± 0.7	221 ± 1
B	$5 \cdot 10^{-1}$ mg/ml at 75°C		7.8 ± 0.5	151 ± 1
C	$5 \cdot 10^{-2}$ mg/ml at 100°C		3.8 ± 0.7	92 ± 2
D	$5 \cdot 10^{-3}$ mg/ml at 125°C		1.1 ± 0.2	34 ± 2
E	$5 \cdot 10^{-4}$ mg/ml at 150°C		0.7 ± 0.2	10 ± 8

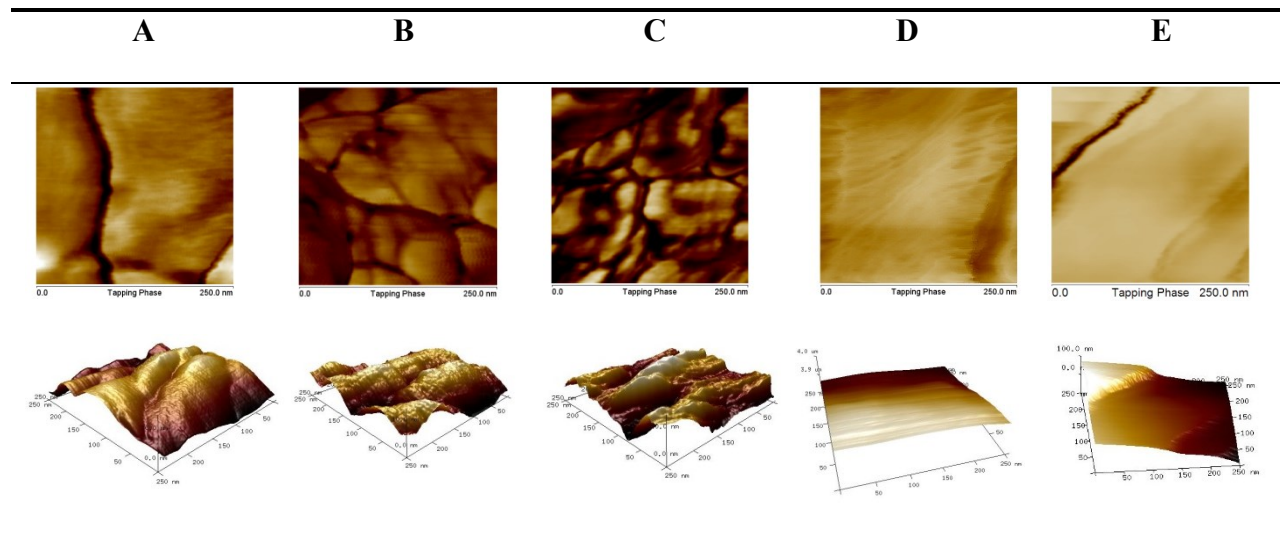
The images, derived with SEM and FIB for the five morphology types are shown in Table 4.2. Table 4.2 confirms that the monodisperse droplet chain generated final microparticles with the same diameter and morphology.

Table 4.2 Illustration of the morphology of the five types of microparticles. The morphology is analyzed with SEM, for the outside of the shell, and with FIB, for the inner side of the shell. Images of more than one microparticle are shown to demonstrate their similarity.

Cases	Scale	A	B	C	D	E
						
SEM		20 μm 	10 μm 	5 μm 	1 μm 	1 μm 
	2 μm 					
FIB	2 μm 					

An AFM analysis in tapping mode for different scanning areas was used to study the trend of roughness and crystal size in microparticles created by different particle formation processes. Since the particle size varied from 17.7 to 0.7 μm , scanning areas of 400, 100, 25, 1, 0.25, 0.0625 and 0.01 μm^2 were selected. Examples of crystal sizes are shown in Table 4.3.

Table 4.3 Tapping mode AFM analysis of the surface morphology of the microparticles. The AFM images are shown in two and three dimensions using a scanning area of 0.0625 μm^2 .



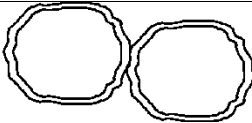

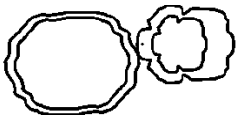

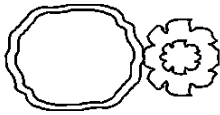
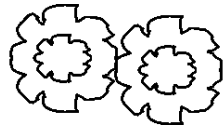
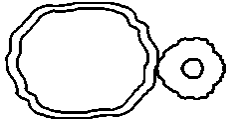








The root mean squared roughness, R_q , for the different cases is shown in Table 4.4. The primary roughness, $R_{q,1}$, of the cases considered is bolded in Table 4.4. Square scanning areas with side length larger than the radius of the microparticles showed a larger standard deviation. This means that the scan might have covered other microparticles or the glue. For scanning areas with side length smaller than the radius of the microparticles, the roughness decreased, indicating that an individual crystal on the surface might have been scanned.

Table 4.4 Root mean squared roughness, R_q , in nm for the cases studied as a function of scanning area. The bolded cases are selected as $R_{q,1}$ in Equation 4.9.

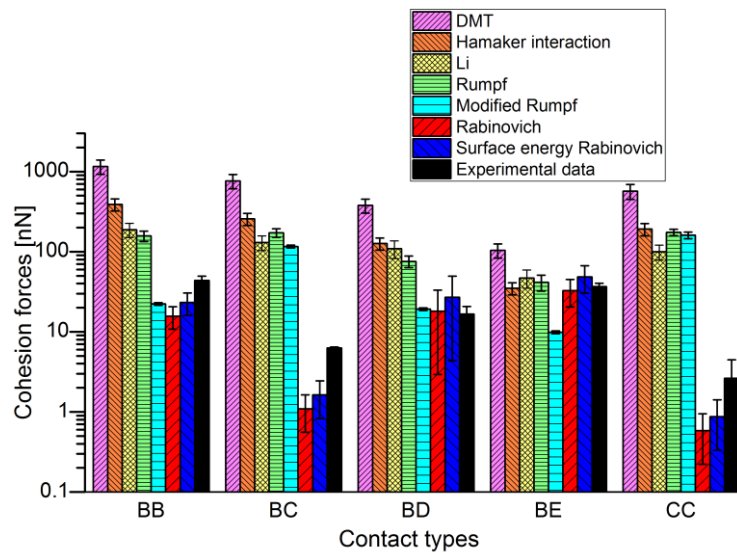
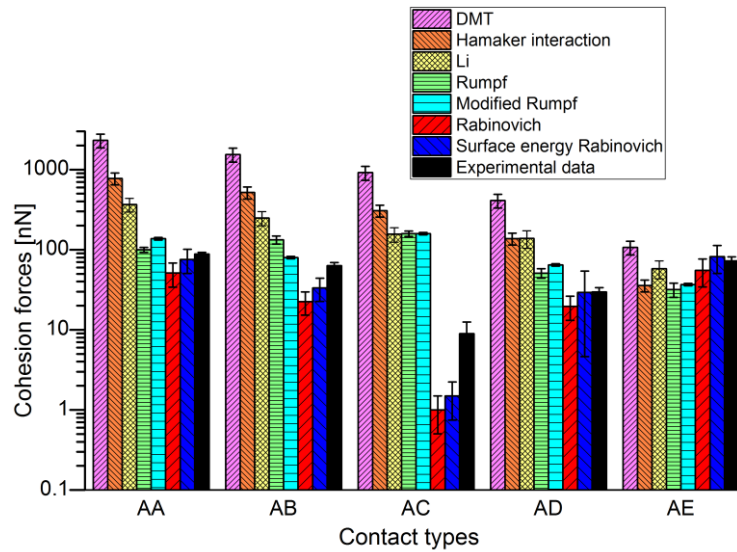
Scanning area [μm^2]	A	B	C	D	E
0.01					0.06 ± 0.003
0.0625	0.04 ± 0.01	0.09 ± 0.03	17.2 ± 2.22	36.2 ± 12.2	2 ± 0.1
0.25	4.11 ± 0.98	10.4 ± 3.42	19.3 ± 4.73	58.6 ± 20.1	65.2 ± 24.5
1	27.7 ± 11.3	65.5 ± 20.1	1078 ± 17.5	134 ± 38.7	
25	32.5 ± 13.2	156 ± 20.2	355 ± 34.4		
100	97 ± 22.3	696 ± 91.4			
20	1710 ± 47.6				

Table 4.5 shows the cohesion forces between two microparticles produced with the same and with a different particle formation process. In Table 4.5 only the maximum pull off forces are shown. The snap-in forces for the cases AA, BB, CC, DD and EE were 1.3 ± 0.7 , 0.6 ± 0.2 , 0.3 ± 0.1 , 0.3 ± 0.1 and 0.2 ± 0.1 nN respectively. Similarly, the case of average Δt_c and high R_q showed the lowest value of snap in forces.

Table 4.5 Cohesion forces between pairs of microparticles of similar (bold) and dissimilar morphology. For selected cases, the comparison of adhesion forces between a microparticle and a glue drop is shown.

Contact profile	Contact name	Max pull off forces [nN]	Contact profile	Contact name	Max pull off forces [nN]
	AA	88 ± 4.7		BD	16.7 ± 4.1
	A-glue	167 ± 122			
	AB	63.5 ± 6.4		BE	36.7 ± 3.6
	AC	8.9 ± 3.5		CC	2.6 ± 1.8
				C-glue	32 ± 23
	AD	29.7 ± 3.8		CD	3.7 ± 1.8
	AE	72.6 ± 8.7		CE	3.5 ± 0.2
	BB	43 ± 5.6		DD	10 ± 3.5
	B-glue	102 ± 76		D-glue	61 ± 40
	BC	6.2 ± 0.2		DE	12.6 ± 6.1
				EE	127 ± 3.5
				E-glue	257 ± 111

The comparison between experimental and theoretical cohesion results is shown in Figure 4.3. The theoretical models used are: Hamaker interaction, and DMT, Rumpf, Modified Rumpf, Rabinovich, Surface energy Rabinovich, and Li models. Solid black columns indicate the experimental data.



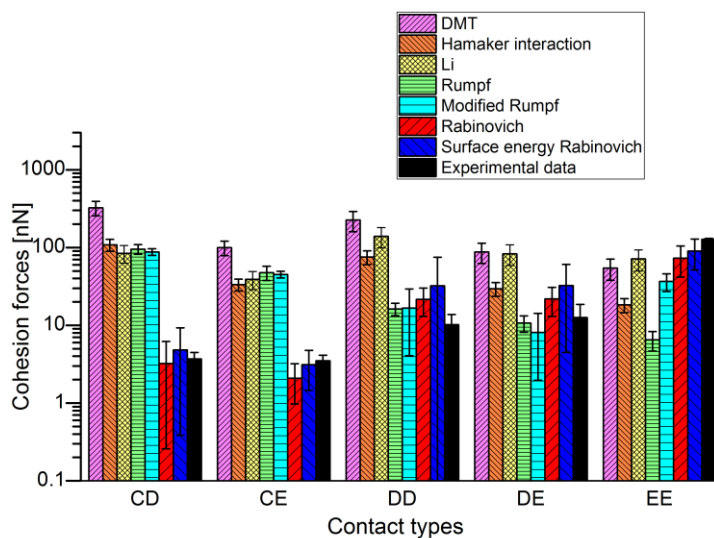


Figure 4.3 Comparison between experimental results and theoretical predictions of the cohesion forces between two microparticles. The solid black columns indicate the experimental data.

4.6 Discussion

Five kinds of microparticles are studied for two purposes: controlling the relationship between initial conditions of the particle formation process and the properties of dried microparticles and understanding the trend of cohesion forces between two microparticles and the properties of dried microparticles. Table 4.1 shows that larger Δt_c were achieved with lower external temperatures and higher initial concentrations. Since lower drying gas temperatures lead to lower evaporation rates, the drying process takes longer and, thus, more time is available for crystallization. With higher initial concentrations, less time is required to reach sufficient supersaturation and to commence crystallization upon drying, allowing for a longer crystal growth time before the solvent is completely evaporated. Analysis of the microparticles with low-frequency shift Raman spectroscopy (results not shown) revealed the nature of their solid phase [180]. In this project, Δt_c affected the crystalline fraction of the final dried microparticles; low Δt_c (case E) indicated low crystallinity.

The morphology changed along with the time available for crystallization. For high Δt_c , the microparticles had more internal void volume and apparently smooth surfaces. In this case crystallization commences early in the evaporation process and sufficient time is available to form a shell composed of large crystals. Once the shell is formed the particle can no longer shrink and

internal voids are created. For average Δt_c , the surface of the microparticles was rough and with distinguishable crystals of intermediate size. Compared to the first case, there is now less time available to grow large crystals and a composite shell of smaller crystals is formed on a smaller droplet. Therefore, the void volume is reduced. For still lower Δt_c individual crystals were hardly discernible, but still present, evidenced by the Raman results. For the lowest Δt_c the particles did not have discernable crystal boundaries, no void space, and the Raman results showed increasing disorder, indicating that in this case sufficient time for crystallization was not available and a shell was no longer formed. Consequently, in this regime, the roughness decreased with a decrease of the time allowed for crystallization.

Analysis of AFM images shows that microparticles with less time available for crystallization have, as expected, a smaller crystal size, if considering the same scanning area, Table 4.3. The profile sketches of the dried microparticles summarize and clarify the roughness and the crystal size information obtained from the different microparticles, Table 4.2. Case C, which has an average Δt_c , shows the highest roughness, Table 4.4. It is apparent that crystal size influences the roughness of the particles, with intermediate crystal size producing the roughest surfaces.

The AFM was used in contact mode to detect cohesion forces between two microparticles. Confirming the results of Adi et al [356], pull off forces, both maximum and the snap in, are dependent on the roughness of the microparticles, Table 4.5. For contacts of microparticles with the same morphology, case CC with an intermediate Δt_c , shows the lowest pull off force. These particles have the largest roughness. Most cohesive were case AA, which had large diameter, crystalline, smooth particles, and case EE, very smooth and partially amorphous particles. Experimental results were checked against possible glue contamination by comparison with pull off forces between a microparticle and a glue drop. The pull off forces between a glue drop and a microparticle were always much larger and more variable than for contact between two particles. The cohesion forces between dissimilar microparticles also demonstrate the importance of roughness for cohesion forces. If at least one of the microparticles had a rough profile, then the cohesion forces were low. If both microparticles had a high roughness, the cohesion forces were further reduced.

The Hamaker interaction only considers the Hamaker constant and the dimension of the particles, which are considered to have perfectly smooth surfaces Equation 4.4. The limitations of this model

are obvious; the actual cohesion forces on rough particles were orders of magnitude smaller than predicted by the Hamaker model. The DMT model is very similar to the Hamaker model but uses surface tension instead of the Hamaker coefficient, Equation 4.6. Since the surface tension is the same for all the cases considered, the DMT model is influenced only by the diameter of the microparticles and the results can be converted into those of the Hamaker model using a fixed factor. Hence the results do not match the actual cohesion forces any better. The Rumpf and the modified Rumpf model, Equation 4.7 and Equation 4.8, introduce a single roughness parameter, either the radius of asperities or the root mean squared roughness in the calculation of cohesion forces. This leads to an improvement relative to the Hamaker and DMT models in some cases, but in others, the theoretical predictions are still not close to the experimental results, Table 4.1. Despite the fact that the Li model is the most recent and incorporates the roughness of the microparticles, Equation 4.12 and Equation 4.13, it does not match most of the experimental results. A possible reason is that the roughness is also described by one parameter only, the asperity radius. The Rabinovich models describe the roughness of the particles in more detail. The root mean squared roughness and asperities are divided into two variables which depend on the size of the respective scanning areas, Equation 4.9 and Equation 4.11. This approach generates values of cohesion forces closer to experimental data. Of the two, the surface energy Rabinovich model was slightly superior to the Rabinovich model in most tested cases. The importance of roughness and its appropriate incorporation in cohesion models is clearly shown here. This emphasizes the dominating impact of roughness and, therefore, crystal size in the particles tested here, on the cohesion forces between two microparticles.

4.7 Conclusions

Production of monodisperse and monomorph particles facilitates systematic studies of cohesion between particles of different morphologies using colloidal probe microscopy. The strong impact of microparticle morphology, specifically roughness, on cohesion forces is verified. In cases of contact between microparticles with similar morphology, microparticles with higher roughness generate lower cohesion forces. In cases where microparticles have different morphologies, cohesion forces are reduced when at least one of the microparticles has a high root mean squared roughness. Intermediate crystal size in relation to the particle size generates the highest value of roughness and, therefore, the lowest cohesion force. The crystal size depends on the time available

for crystallization during the particle formation process. The time available for crystallization in turn depends on processing and formulation parameters. The best approximation to the experimental results is achieved using the Surface Energy Rabinovich model, which considers both properties of the material, such as surface tension, and morphology, such as diameter, and roughness parameters.

Spray drying, the most common technique used to produce drugs for pulmonary delivery, generates microparticles in a broad range of size. As demonstrated in this publication, the diameter of the microparticles is not as influential as their roughness on the cohesion forces in spray dried powders. During process and formulation design and during potential changes to the process, e.g. on scale up, the effect on crystallization kinetics must be carefully considered to avoid changes in roughness, which could lead to altered powder dispersibility and, thus, could negatively affect product performance.

4.8 Acknowledgements

Funding from the Natural Sciences and Engineering Research Council of Canada (NSERC) and the Alberta Innovates Technology Futures is gratefully acknowledged. The authors would also like to acknowledge Shiau-Yin Wu for assistance with the attachment of the microparticles on AFM cantilevers and Dexter D'Sa for the advice on the measurement of cohesion forces between two microparticles.

5 Control of the Radial Distribution of Chemical Components in Spray Dried Crystalline Microparticles

The material shown in Chapter 5 has been submitted in Aerosol Science and Technology. All the experiments have been personally conducted. The theory has been developed in previous chapter, 2 and 3. The authors of this publication are me and my supervisor Reinhard Vehring. Additional material is shown in Appendix E.

5.1 Abstract

The particle formation process from evaporating droplets containing more than one solute has been studied. Two-component microparticles were produced using a piezoceramic dispenser with an inner diameter of 30 μm . Initial droplets had a diameter in the range of 70 to 85 μm and contained sodium nitrate and potassium nitrate in different molar ratios of 30:70, 50:50, and 70:30 or weight ratios of 26.5:73.5, 45.7:54.3, or 66.2:33.8 in the form of aqueous solutions with initial concentrations of 1 or 10 mg/mL. The monodisperse droplets were dried in a dry laminar gas flow with temperatures of 50 or 100 $^{\circ}\text{C}$. Different initial conditions affected the particle formation process and the particle morphology. The diameter of the final dried microparticles ranged from 4 to 10 μm . Their density varied from 1250 to 1950 mg/mL. The formulation and process conditions determined the distribution of chemical components in the dried microparticles, especially their surface composition as determined by energy-dispersive X-ray spectroscopy. The distribution of the chemical components was theoretically explained using characteristic times for the crystallization kinetics of the drying process. It was shown that the solute which reached supersaturation first formed most of the outer shell of the microparticles.

5.2 Introduction

The role of respiratory drug delivery in effective interventions for lung diseases continues to attract much interest [369, 33, 370, 20]. The diameter of drug containing particles delivered to the lung is commonly in the micrometer range [371, 372]. Particles with diameters between 1 to 5 μm tend to reach the lung upon delivery and can release the drug at the desired location [372]. Another

important property of medicinal microparticles is their morphology [373]. Microparticles with rough surfaces decrease cohesion forces [374, 375]. The solid phase is another parameter with impact on the performance of respiratory dosage forms [269]. For example, some amorphous materials may show a low storage stability and higher reactivity [376].

The area of research describing and controlling the particle formation process of respiratory drugs is called particle engineering [7]. The particle formation process represents the transformation of a solution droplet into a dry particle [193]. Several qualities render spray drying the most used technique for the production of microparticles for respiratory drug delivery: minimal loss of activity of chemicals, compatibility with a wide range of solutions or suspensions, and control over important properties of the final particles [99]. For a fundamental understanding of the microdroplet drying process in a spray dryer experimental observations on model systems have been fruitful. In particular, the experimental method using a free falling, monodisperse droplet chain has several favorable qualities for analyzing the particle formation process: ability to study fast processes, representative droplet dimension in the micrometer range, and representative heat and mass transfer on isolated droplets [2]. A piezoceramic dispenser is generally used to produce such a monodisperse droplet chain, because it is capable of producing monodisperse droplets with high precision. [218].

The particle formation process for single-component solution droplets has been investigated quite thoroughly [156, 4, 377, 158, 11, 2, 378, 379]. On the other hand, few researchers have investigated particle formation from evaporating droplets with more than one chemical component [33, 380, 381], which is the more relevant case for most formulations in respiratory drug delivery. The characteristics of multicomponent particles are strongly dependent on the composition of their surface or shell [382]. Surface properties are fundamental for the delivery of respiratory drugs [383, 384], since they can influence both the location at which the drugs are delivered and the release profile of the drugs [385]. As a consequence, particle formation studies that provide a reliable prediction of which components form the surface of microparticles are important for improving particulate dosage forms for respiratory drug delivery.

Previous particle formation studies [156, 294, 193] have focussed on non-crystallizing systems, where the solute precipitates into an amorphous solid during the process. Such systems are relatively well understood [1, 33, 2, 193]. In this case, many properties of the final dried

microparticles can be predicted from an analysis of the Peclet number [193]. The Peclet number is the ratio of the evaporation rate, indicating the speed at which the droplet shrinks, and the diffusion coefficient, indicating the speed at which the solute diffuses away from the surface [4]. It has been shown that low Peclet numbers predict solid microparticles, typically with a smooth surface and spherical shape [2]. This prediction is valid only for non-crystalline systems [386], because the Peclet number does not capture the impact of crystallization kinetics on particle formation. However, it is known from electron micrographs that crystals may grow on the surface of droplets, eventually forming a crystalline shell. Several respiratory drugs have a known tendency to crystallize or have been formulated with crystallizing excipients [33, 387-389]. In this case, the particle formation process includes a crystallization sub-process. The effect of crystallization on the particle formation process is still mostly unknown. The main reasons are the complexity of the crystallization theory [390] and the fast kinetics involved in the drying of microdroplets. In order to predict the properties of spray dried crystalline microparticles, theoretical approaches for the nucleation and crystallization processes will have to be incorporated in models describing the particle formation process. Furthermore, it has been difficult to experimentally determine crystallization kinetics in drying microdroplets, e.g. the time at which nucleation commences and the time at which crystals starts to grow. Thus, further studies on the formation process of crystalline particles are needed to gain a better understanding of these important systems.

In this paper a comprehensive evaluation of the particle formation process for a crystallizing system is achieved by combining an experimental and a theoretical approach. The experimental approach uses a monodisperse droplet chain as a model system. The theoretical approach applies a relatively simple model which can predict the internal distribution of components in an evaporating droplet, the time they reach saturation on the surface, and the shell thickness of the resulting particle [1]. While this model has not been fully validated for crystallizing multi-component systems, it predicts that the time to reach saturation on the surface is the main variable that determines the sequence in which components can form a shell [156]. In case of evaporating droplets composed of more than one solute, it was hypothesized that the solute with the shorter time to reach saturation has a higher probability to nucleate and crystallize first on the surface, thus forming the shell [1].

5.3 Experimental section

5.3.1 Chemicals

The chemical components chosen are sodium nitrate (NaNO_3), potassium nitrate (KNO_3), and deionized water (catalog number 38796 – 1L, Sigma Aldrich, St Louis, MO, USA). The properties of NaNO_3 (catalog number 221341-500G, Sigma Aldrich, St Louis, MO, USA) which are important for this study are molecular weight of 84.99 g/mol, true density of 2260 mg/ml, glass transition temperature of 185 – 215°C, melting point of 306°C [217], and aqueous solubility of 740 mg/ml and 860 mg/ml [304] at temperatures of 18.7 and 31.9°C, respectively. The corresponding properties of KNO_3 (catalog number 221295-500G, Sigma Aldrich, St Louis, MO, USA) are molecular weight of 101.1 g/mol, true density of 2109 mg/ml, glass transition temperature of 128°C, melting point of 334°C, and aqueous solubility of 320 mg/ml and 570 mg/ml [391], at temperatures of 18.7 and 31.9°C, respectively. Since the evaporation rate, and, consequently, the wet bulb temperature is almost constant during each droplet evaporation process prior to shell formation, the solubility is assumed to be constant for each drying gas temperature.

5.4 Experimental approach

5.4.1.1 *Monodisperse droplet chain*

Binary solutions of NaNO_3 and KNO_3 were generated that differed in the molar percentage of NaNO_3 , i.e., 30, 50, and 70%. The production of monodisperse microparticles was explained in detail in a previous publication [156]. Briefly, the monodisperse droplet chain was generated using a piezoceramic dispenser with an inner diameter of 30 μm . The initial droplet diameter was in the range of 70 to 75 μm . The droplets were injected in a flow tube with a temperature regulated gas flow. The monodisperse droplet chain was illuminated with a diode laser and images were recorded with a digital camera to determine the distance between two consecutive droplets. From the distance the aerodynamic diameter could be derived as a function of time as described below. The resulting dry microparticles were collected on a filter for further ultramicroscopy and Raman spectroscopic analysis.

5.4.1.2 *Microparticles characterization: final properties*

An important property of the dried microparticles is the spatial distribution of the two chemical components on the surface and in the shell. The analysis of the near-surface component distribution

was achieved using Scanning Electron Microscopy with X-ray spectroscopy (SEM/EDX) (Zeiss Sigma FESEM with EDX & EBSD, Zeiss, Jena, Germany). In general EDX is not a surface specific technique, but it can be adapted to preferentially provide information about elemental composition near the surface. To do so, the interaction volume was kept as small as possible by selecting minimal overvoltage. In this study the highest x-ray energy used was 3.59 keV (potassium, K β). To provide reliable excitation, all samples were irradiated with electron beams with an energy of 5 keV (with one exception: 10 keV was used in the case with drying temperature of 50°C, 10 mg/mL initial concentration and 1:1 molar ratio of the components). For this electron energy the penetration depth into a sample coated with a 20 nm gold layer is on the order of 100 nm and the x-ray signal is strongly weighted towards the surface [392]. The diameters of the dry microparticles were in the range of 4 to 10 μm with a shell thickness larger than 0.1 μm in all cases. SEM/EDX measures characteristic x-ray intensity. Furthermore, every element has a standard intensity, provided by calibration measurements performed by the instrument manufacturer. The ratio between the measured intensity and the standard intensity is equivalent to the ratio of the mass or weight fractions [393], which can be converted to mole fraction using the molar mass of each component.

To measure the distribution of the components across the shell of the microparticles with higher spatial resolution, Transmission Electron Microscopy with X-ray spectroscopy (S/TEM) (CM 20 FEG, TEM S/TEM, Philips, Amsterdam, Netherlands) was used. In bio-techniques the characteristic X-ray lines were K α and K β with an emission energy of 1.041 keV and 1.071 keV for Na, and 3.312 keV and 3.59 keV for K, respectively [394].

Other properties analyzed were diameter, morphology, and solid phase. The diameter and the morphology of the final dried microparticles were measured using a Scanning Electron Microscope (SEM) (SEM LEO 1430, Zeiss, Jena, Germany). The images derived from the SEM were analyzed with the software ImageJ (ImageJ, Imaging Processing and Analysis in Java, National Institute of Health, 1997, Bethesda, Maryland, USA). To determine shell thickness and interior morphology the microparticles were cut and imaged using a Helium Ion Microscope (HiM) (Zeiss Orion Helium Ion Microscope, Zeiss, Jena, Germany). The solid phase of the particles was analyzed using a custom macro Raman spectroscopy system with low frequency shift capability. Details of this instrument and the associated methodology have been described previously.[180].

5.4.1.3 Samples used for the TEM analysis

Microparticles were collected on a frit placed on a hollow Scanning Electron Microscopy (SEM) stub. A small amount, about 1 mg, was transferred into a pencil-shaped mold (Catalog number 70902, flat embedding mold, Electron Microscopy Sciences, Hatfield, PA, USA). The microparticles were pushed with a sharp tweezer (SS140-A Dumont, Ted Pella, Redding, CA, USA) to the tip of the pencil-shaped mold. The mold was then filled with an embedding medium (Catalog number 14300, Low Viscosity Embedding Media Spurr's Kit, Electron Microscopy Sciences, Hatfield, PA, USA). The embedding medium was composed of four components: epoxy ERL 4221, diglycidyl ether of polypropylene glycol (DER 736), hardener nonenyl succinic anhydride (NSA), and accelerator dimethylaminoethanol (DMAE). The embedding medium was cured in an oven (VWR 140, VWR, Radnor, PA, USA) at 70 °C for 16 to 20 hours. A section of the tip of the dried mold was chopped every 90 nm with an ultramicrotome (Ultracut E, Reichert-Jung, Leica Biosystems, Wetzlar, Germany) and the sectioned material was collected on a Transmission Electron Microscopy (TEM) grid.

5.5 Theoretical approach

A theoretical particle formation model was described in detail in previous publications [156, 1, 2]. For crystallizing multi-component systems the parameters that can predict the onset and kinetics of the crystallization process are most important. Boraey et al. [4] introduced a description for the particle formation process of a droplet composed by more than one solute. The concentration of all solutes increases during the evaporation due to loss of solvent. It is assumed that the solute that saturates first during the particle formation process forms a crystalline shell on the microparticle. Equation 5.1 shows the expression for the time, $t_{s,j}$ at which each component, j , reaches saturation on the surface of the evaporating droplet. d_0 is the initial diameter, $C_{0,j}$, the initial concentration, $C_{sol,j}$, the solubility, and E_j , the enrichment of solute j on the surface of the droplet, relative to its average concentration. The surface enrichment is caused by the limited speed of solute diffusion away from the receding droplet surface. Expressions for E have been reported before [1].

$$t_{s,j} = \frac{d_0^2}{\kappa} \left[1 - \left(\frac{C_{0,j} E_j}{C_{sol,j}} \right)^{\frac{2}{3}} \right] \quad \text{Equation 5.1}$$

From Equation 5.1, it can be derived that, all else equal, the solute with lower solubility tends to precipitate earlier than the others. The surface enrichment is dependent on the diffusion coefficient of the solute in the liquid phase and the evaporation rate of the droplet. Both of these two parameters are strongly affected by the wet bulb temperature of the droplet. In addition, the time to reach saturation depends on the initial concentration of the solute in the solution, Equation 5.1. The theoretical model used to derive Equation 5.1 assumes a constant evaporation rate [156, 1, 2] but can be improved by applying it stepwise, assuming a constant evaporation rate for each time step only. This allows a correction for material properties and other parameters that change as a function of time [156]. In this case, the time to saturation is reached when the surface concentration of a solute reaches the solubility of the solute at the present conditions. A second parameter, important for the kinetics of the crystallization process is the precipitation window, Δt_s , which is the difference between the time when the evaporation process is complete and the time to reach saturation. The evaporation process is assumed to be complete when the measured aerodynamic diameter no longer decreases. A related parameter, the crystallization window, Δt_c , is the difference between the time to reach constant aerodynamic diameter and the time for earliest possible onset of crystallization, t_c . The time for crystallization defines the point in time when the surface concentration reaches sufficient supersaturation such that crystals can nucleate and grow. Previous publications determined the required supersaturation level in aqueous solutions at which crystals start to grow [395, 300]. This level of supersaturation also changes according to the wet bulb temperature of the solution. For wet bulb temperatures of 18.7 and 31.8 °C, which correspond to the experimental conditions of this study, sodium nitrate starts to crystallize at a supersaturation of 15.7 and 17.1 molar percentages or 97 (720 mg/ml) and 99 (850 mg/ml) weight percentages, respectively. For the same wet bulb temperatures, potassium nitrate starts to crystallize at a supersaturation of 8.2 and 9.1 molar percentages, respectively [395]. Since both sodium and potassium nitrate needs a condition of supersaturation to crystallize, the effect of latent heat of crystallization can be considered negligible. At the supersaturation state, a minor amount of solvent is left and, thus, the latent heat of crystallization effect on the wet bulb temperature is negligible.

From an analysis of images of the monodisperse droplet chains, the distance between two consecutive droplets was obtained. This data was processed as follows: Knowing the frequency at which each droplet was injected in the flow tube, the velocity of each droplet was obtained from the distance. The settling velocity of the droplets or particles was found by subtracting the velocity

of the gas flow from the total velocity of each droplet. Using Stokes law, the aerodynamic diameter for each droplet position was derived from the settling velocity [156]. Once the aerodynamic diameter was known as a function of time, the evaporation rate, and the droplet or particle mass, solute concentrations and overall particle density were derived from a mass balance. Diffusion coefficient and viscosity were then adjusted considering the instantaneous concentrations and droplet temperature. With this, the instantaneous Peclet number was calculated [2] and surface enrichment and finally surface concentration resulted as a function of time.

The density was calculated using two different methods depending on the phase of the drying process, specifically the time at which a shell forms. Shell formation was assumed to occur when the volume equivalent diameter of the evaporating droplets was equal to the diameter of the final dried particle. . Before shell formation, Equation 3.4 was used, where $d_{a,0}$ is the initial aerodynamic diameter of the droplet, $d_{a,j}$, the aerodynamic diameter at time step j , and ρ^* , the standard density [1 g/cm³]. A and B are parameters derived from the trend of the mass fraction and viscosity for the solutes used [292, 293]. Both values of A and B depends on the wet bulb temperature. Values of A vary from 0.0019 to 0.002 mL/mg for NaNO₃ and 0.0027 and 0.0031 mL/mg for KNO₃ at 18.7°C and 31.8°C as wet bulb temperatures. Values of B vary from -2.03 to -1.98 for NaNO₃ and -2.76 and -3.01 for KNO₃ at 18.7°C and 31.8°C as wet bulb temperatures [292]. This method is obtained from a mass balance assuming that the particles lack in internal and external voids. For each time step, I , Equation 5.2 provides the particle density assuming only one component, j , is present. In Equation 5.2, the droplet or particle density ρ_P is equal to the true density, ρ_T , since no internal or external voids are involved.

$$\rho_{P,j}(t) = \rho_{T,j}(t) = \left(\frac{C_{0,j} d_{a,0}^3 \rho_P^{\frac{1}{2}}}{\rho^{*\frac{3}{2}} d_{a,i}^3} + B_j \right) \frac{1}{A_j} \quad \text{Equation 5.2}$$

Subsequently, the total particle density of the multicomponent droplet is approximated using Equation 5.3, where Y_j is the mass fraction of each component.

$$\rho_{P,tot} = \rho_{T,tot} = \frac{1}{\sum_j \frac{Y_j}{\rho_{T,j}}} \quad \text{Equation 5.3}$$

After the shell formation, Equation 5.4 was used to determine the density of the droplets or particles. In Equation 5.4, $d_{v,f}$, is the diameter of the final dried particles.

$$\rho_p(t) = \frac{d_{a,t}^2}{d_{v,t}^2} \rho^* \quad \text{Equation 5.4}$$

The instantaneous diffusion coefficient, which was necessary to calculate Peclet number and surface enrichment, was derived as a function of viscosity using the Stokes-Einstein equation [396, 397]. The viscosity for each component, η_j , was approximated using Equation 5.5 [398]. In Equation 5.5, $\alpha_1, \alpha_2, \alpha_3, \alpha_4, \alpha_5$, and α_6 , are constants [398], different for NaNO_3 and KNO_3 , while, w_w , is the water content, and T_w , is the wet bulb temperature.

$$\eta_j = \exp\left(\frac{\alpha_1(1 - w_w)^{\alpha_2} + \alpha_3}{(\alpha_4(T_w) + 1)(\alpha_5(1 - w_w)^{\alpha_6} + 1)}\right) \quad \text{Equation 5.5}$$


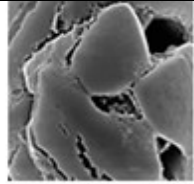
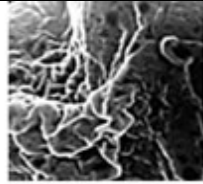
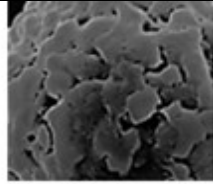

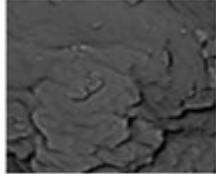
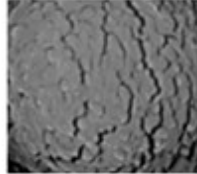
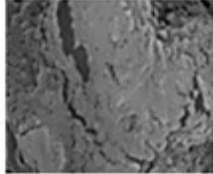
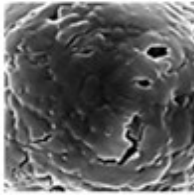
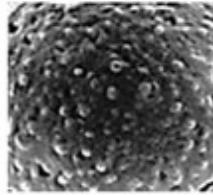
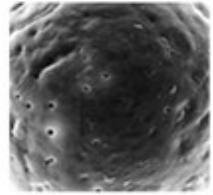
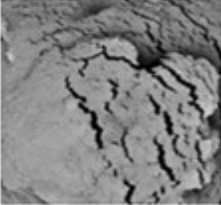
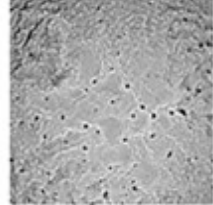
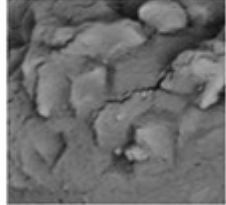
The total viscosity, η , was then obtained using the Gambill equation for a mixture of liquids, [399].

5.6 Results and Discussion

Twelve cases, shown in Table 5.1, were studied to understand the influence of the initial conditions on the distribution of chemical components in the final dried particles. The initial total solution concentration, C_0 , was either 1 or 10 mg/ml and the drying gas temperature, T_{Gas} , was either 50 or 100°C. Furthermore, the twelve cases differed in composition, i.e., the molar percentages of NaNO_3 and KNO_3 were 30:70, 50:50, or 70:30, respectively. The weight percentages were thus 26.5:73.5, 45.7:54.3, or 66.2:33.8, respectively.

NaNO_3 and KNO_3 were chosen for their strong tendency to crystallize. Any material that tends to crystallize and has well-known properties, as solubility, viscosity and supersaturation state, at which it starts to crystallize, can be used. In the experimental design of this study, it was assumed that these materials would likely crystallize even during a fast microdroplet evaporation process. It was hypothesized that the crystallization would commence on or near the surface and then lead to the formation of a shell and of interior voids in the particles. For some of the produced microparticles the crystalline nature is obvious from their morphology, shown in Table 5.1. In three of the cases (left and right in top row and bottom row, right) well defined domains with a size of a few hundred nanometers are clearly recognizable on the surface. These domains are very likely individual crystals. For the other cases, discerning individual crystals is challenging. If present, they could be either too small to be clearly observable or could have merged to form a continuous crystalline shell.

Table 5.1 SEM images showing surface morphology, including crystal size, of the dried microparticles.

C_0	T_{Gas}	Scale	mol%: 30 NaNO ₃ - 70 KNO ₃	50 NaNO ₃ - 50 KNO ₃	70 NaNO ₃ - 30 KNO ₃
mg/ml	°C		wt%: 26.5 NaNO ₃ - 73.5 KNO ₃	45.7 NaNO ₃ - 54.3 KNO ₃	66.2 NaNO ₃ - 33.7 KNO ₃
1	50				
	100				
10	50	<u>2 μm</u>			
	100	<u>2 μm</u>			

Further evidence for the proposed particle formation mechanism is provided in Figure 5.1, which shows the particle density as a function of time during the particle formation process for four selected cases with equal molar percentage of the two components. In the first drying phase (full symbol curves) the density of the solution droplet increases as the water evaporates. These results are achieved using the data processing method assuming that there are no voids in the particles, Equation 3.4. Since the exact point when a void first appears is unknown, the calculation was carried on until the true densities of the solutes were reached. This extrapolation represents the case of a hypothetical, non-crystallizing system. However, this calculation predicts unrealistically small final particle diameters, inconsistent with the size of the dry particles determined by SEM. Therefore, a shell and, subsequently, voids must have formed. In Figure 5.1, the larger and brighter

data point approximates the time of shell formation, i.e., the point in time when the diameter of the droplet equals the final volume equivalent diameter of the dry particle. After this point, it is increasingly likely that the density trend follows Equation 5.4 (open symbols), which is based on the properties of the final particles. For all the curves shown, the predicted point of shell formation is at a density below the true density of the solutes used, indicating the presence of voids or solvent trapped in the formed shell in the evaporating microparticles. After shell formation, the trapped solvent continues to evaporate without a further change in the droplet diameter, which explains the observed drop in particle density.

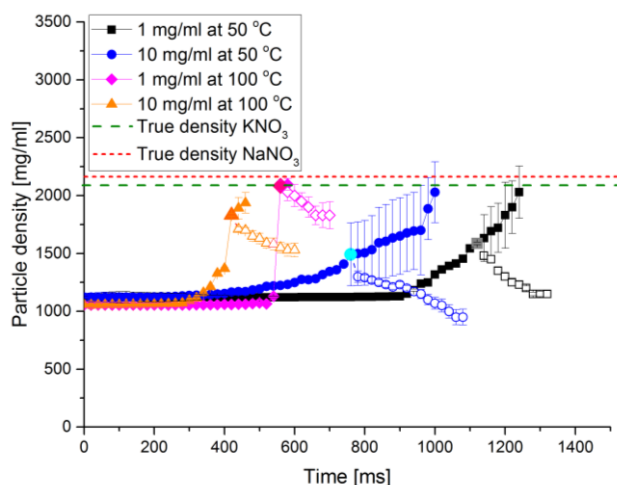


Figure 5.1 The particle density as a function of time during evaporation and particle formation for droplets with equal molar amounts of NaNO_3 and KNO_3 . The full symbol curves were calculated assuming no voids in the particle, i.e. a non-crystallizing system. The open symbol curves were calculated using the final diameter of the actual dry particles. The larger data point approximates the onset of shell formation.

It is known that some non-crystallizing systems can also form hollow, low density particles [156]. In these systems a shell is formed due to a very large surface enrichment, which correlates with large Peclet numbers. On the other hand, all twelve cases studied here show a small Peclet number for most of the evaporation process which indicates comparatively little enrichment on the surface. According to previous studies [4, 2] microparticles with a high density and without voids would result in this case. This is not observed here, ruling out this mechanism.

This interpretation is consistent with the HiM images of cut particles shown in Table 5.2. All the microparticles shown in Table 5.2 have varying amounts of voids. The voids in the particle shown in the lower left position are difficult to see, because they are quite small. A comparison of the

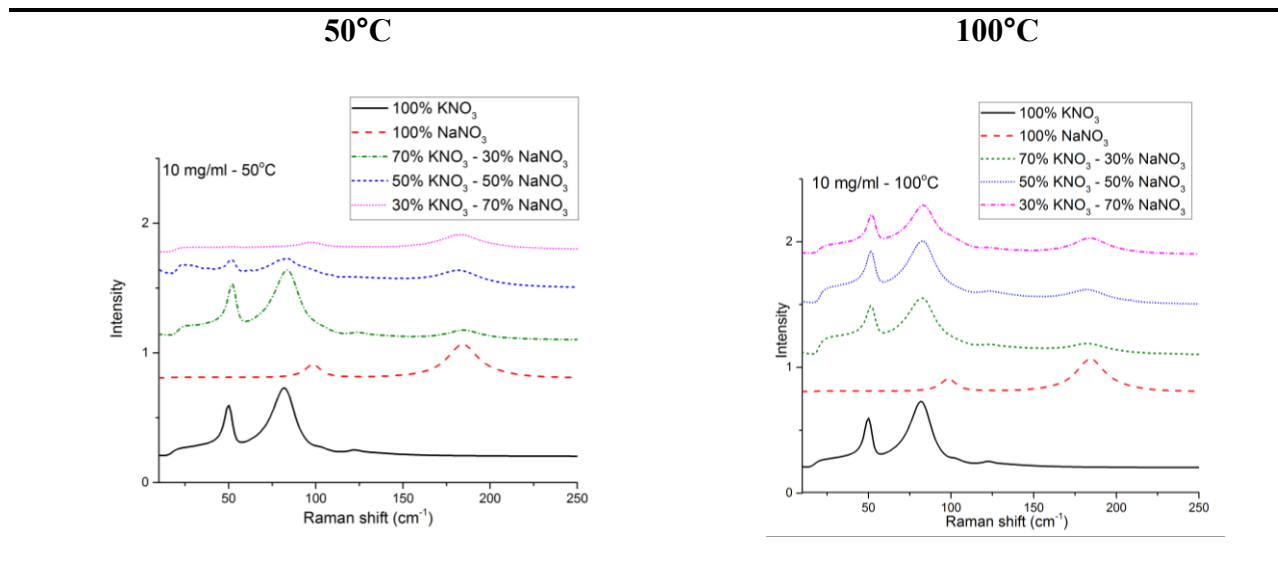
particles in the top row, which were dried at 50°C, with the ones in the bottom row, dried with higher evaporation rate at 100°C drying gas temperature yields a result that is consistent with the trend shown in Figure 5.1: Higher evaporation rates cause more dense particles with less void volume. For non-crystallizing systems the opposite effect is expected: In these systems higher evaporation rates would lead to higher Peclet numbers, higher surface enrichment, and decreased particle density [156]. Two peculiar features of the particles in Table 2 require an explanation. Firstly, the surface morphology of the microparticles shown in Table 5.2 seems to differ from that shown in Table 5.1. This is an artifact caused by the HiM coating requirements. For HIM, the microparticles were sputtered with a gold layer of about 100 nm thickness to securely attach the microparticles to the stub. When an ion beam is used to cut a microparticle, the high beam energy can remove microparticles if they are not strongly attached. On the other hand, the microparticles were sputtered with a much thinner gold layer of 20 nm for SEM experiments; thus, the structure and the details of the surface were better recorded. Secondly, for the case with molar percentages of 50 NaNO₃ and 50 KNO₃ at 50°C (middle particle, top row), the microparticle appears different than in the other cases. This section was probably not at the center of the microparticle; as a consequence, part of the crystal structure in the microparticle may have collapsed.

Table 5.2 Helium Ion Microscope images of sectioned microparticles dried from droplets with an initial concentration of 10 mg/ml.

Temperature	Scale	mol%: 30 NaNO ₃ - 70 KNO ₃ wt%: 26.5 NaNO ₃ - 73.5 KNO ₃	50 NaNO ₃ - 50 KNO ₃ 45.7 NaNO ₃ - 54.3 KNO ₃	70 NaNO ₃ - 30 KNO ₃ 66.2 NaNO ₃ - 33.7 KNO ₃
50°C	5 μm			
100°C	5 μm			

The analysis of the solid phase of the dried microparticles, shown in Table 5.3, verifies the previous assumptions unambiguously. Table 5.3 lists the low-frequency shift Raman spectra of the produced microparticles together with the reference spectra of the crystalline raw materials. Both NaNO₃ and KNO₃ have characteristic lattice peaks in the low frequency area of their Raman spectrum. NaNO₃ has its vibrational lattice modes at 98 and 195 cm⁻¹ and KNO₃ at 57 and 85 cm⁻¹ [400, 302]. These modes are absent in amorphous material which lacks an ordered crystal lattice. The selected cases shown in Table 5.3 all show strong crystalline marker peaks. For all twelve cases crystallinity indicating peaks for at least one component were detected (data not shown). It can be concluded from the results discussed so far that NaNO₃ and KNO₃ can indeed crystallize within a few hundred milliseconds (compare Figure 1) and that the crystallization kinetics dominate the particle formation process.

Table 5.3 Low frequency shift Raman spectra of dried microparticles compared with the reference spectra of crystalline NaNO_3 and crystalline KNO_3 . Cases with initial concentration of 10 mg/ml are shown. Molar percentages are shown as a reference.



Can a drying process that is dominated by crystallization kinetics be controlled and how do characteristic parameters affect the properties of the final dried microparticles? A key parameter is the time available for crystallization, called precipitation window, spanning the time from reaching supersaturation on the surface until complete evaporation of solvent. The precipitation window has been shown to be the main parameter controlling crystal size and particle density in a single component system, [386]. For multi-component systems each component has a different precipitation window. The particle formation process should be dominated by the component with the longest precipitation window, because it may crystallize first. Hence, in Figure 5.2, the particle density of the dry particles was plotted as a function of the longer of the two precipitation windows for all tested cases. Longer precipitation windows correlate with lower particle density of the dried microparticles, as predicted. The lower particle density is caused by a larger amount of voids. A long precipitation window indicates that the time to reach saturation is reached early. Thus, a shell can be formed earlier on a droplet that still has a large diameter which corresponds to the larger diameter of the final dried microparticle. In addition, a longer precipitation window indicates that the crystals have more time to nucleate and grow to a larger size on the surface, a tendency that should generate more internal voids, Table 5.2. It can be concluded that managing the time to reach saturation, and thus the precipitation window, allows control over the properties of the final dried

microparticles, such as their density. The precipitation window can be predicted using an adaptation of Equation 5.1. Subtracting the droplet lifetime [1] yields

$$\Delta t_{s,j} = \frac{d_0^2}{\kappa} \left(\frac{C_{0,j} E_j}{C_{sol,j}} \right)^{\frac{2}{3}} \quad \text{Equation 5.6}$$

Equation 5.6 is useful to discuss which process and formulation parameters must be controlled to affect the precipitation window. Three main factors can be discerned: Firstly, the precipitation window is strongly dependent on initial droplet diameter, d_0 , which indicates that control of the atomizer in spray drying of crystalline systems is important. Secondly, the crystallization window increases with the initial concentration, C_0 , of a component in relation to its solubility, C_{sol} . This can be affected by the total concentration of the formulation and by adjusting the mass fraction of a component in the formulation, but is also dependent on the temperature of the droplet which affects the solubility of the components. The droplet temperature and evaporation rate, which is the third factor, are both dependent on the drying gas temperature. According to this model, none of the listed process and formulation parameters can be varied freely without affecting the crystallization window and with it the morphology of the resulting particles.

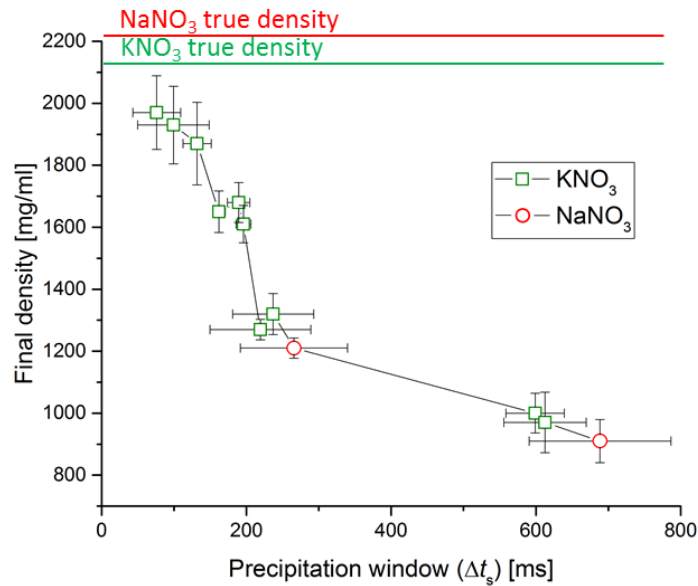


Figure 5.2 Particle density of the final dried microparticles as a function of the precipitation window for the component that first saturates on the surface. The continue lines indicate the true densities of KNO_3 and NaNO_3 .

From the Raman results, it can be concluded that both crystals of NaNO_3 and KNO_3 are present in most dried microparticles. The particle densities in Figure 5.2 show that most of these particles are hollow. Therefore, one can conclude that they have a mixed crystalline shell, which is in agreement with the morphology of the sectioned particles shown in Table 5.2. Is it possible to control the radial distribution of the components in the shell? In other words, is it possible to design particles such that they have a specific component on the surface of the shell to affect, e.g. cohesion between particles? Based on the previous discussion we hypothesize that the parameter that can be used to control the surface composition is the time to reach saturation (Equation 5.1). Specifically, we postulate that a component can be brought to the surface by shortening its time to reach saturation relative to the other component. This hypothesis is illustrated in Figure 5.3, which shows the surface concentration for the two solutes as a function of time during the late phase of the evaporation. The cases for 1 mg/ml initial solution concentration at 50°C drying gas temperature and two different molar ratios, 30:70 and 70:30, are plotted. The time to reach saturation for each component is indicated when the solute reaches its solubility. It can be seen that the ratio of KNO_3 and NaNO_3 affects the sequence of events. The two materials have a different solubility for the same wet bulb temperature; for KNO_3 it is easier to reach saturation, due to its lower solubility. In the case of 30:70 molar ratio of NaNO_3 to KNO_3 , the latter is predicted to reach saturation about 90 ms earlier than NaNO_3 . If the molar ratio is reversed to 70:30, saturation is also reached in a reversed sequence; with NaNO_3 now leading by about 20 ms. According to the hypothesis the latter case should show an increased amount of sodium on the surface.

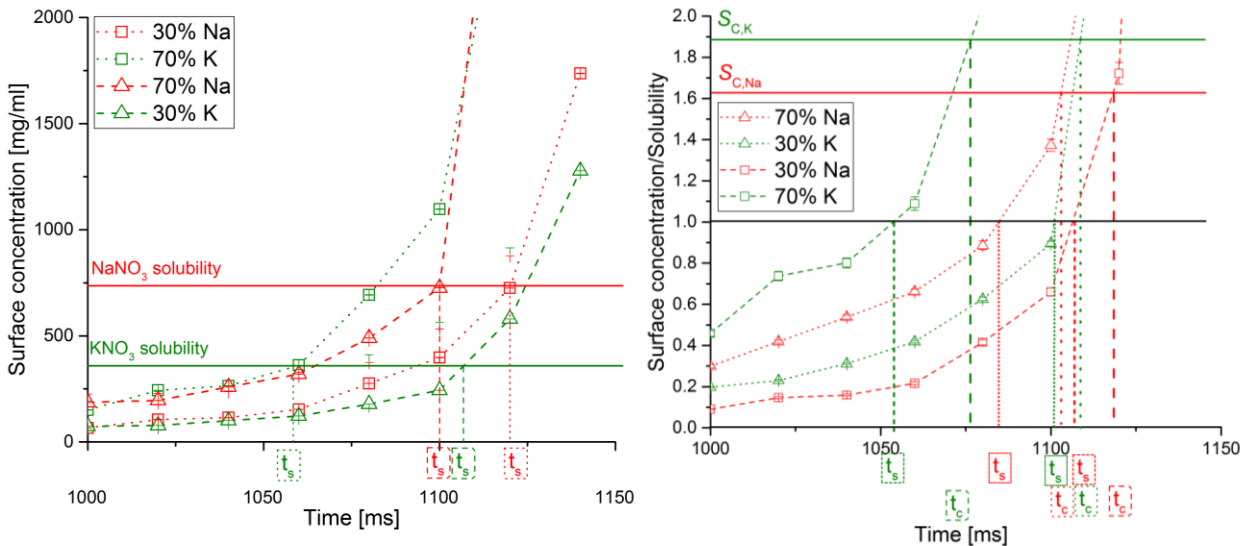


Figure 5.3 Surface concentrations of NaNO_3 and KNO_3 in evaporating droplets as a function of time for the cases with initial concentration of 1 mg/ml at 50°C drying gas temperature and molar percentage of NaNO_3 of 30% or 70% or weight percentages of NaNO_3 of 26.5% or 66.2%. t_s indicates the time to reach saturation. On the right hand side, the plot of normalized surface saturation with the solubility of each solute is shown. The time to reach saturation is simply obtained when the ratio between surface concentration and solubility is equal to 1. The time for crystallization is reached in a supersaturation level, around 1.6 for NaNO_3 and 1.9 for KNO_3 . The time for crystallization is all reached for a further ratio between the surface concentration and solubility.


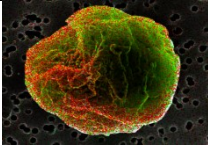
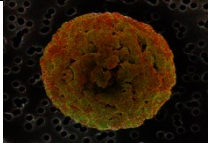

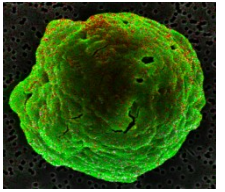
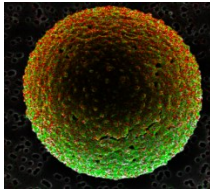
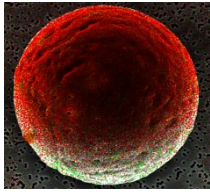
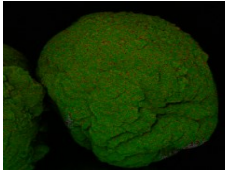
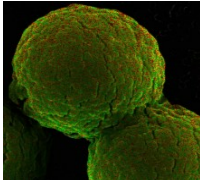
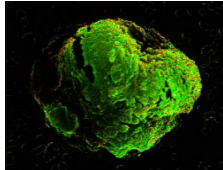
To test the hypothesis that the sequence of the times to reach saturation or crystallization can predict the radial distribution of the chemical components in the final dried microparticles, the times to reach saturation, $t_{s,j}$, and the times for onset of crystallization, $t_{c,j}$, were calculated for all twelve cases. To express the relative timing of the saturation and crystallization event for the two components these times were subtracted from each other according to $\Delta t_{\text{seq},s} = t_{s,\text{NaNO}_3} - t_{s,\text{KNO}_3}$ and $\Delta t_{\text{seq},c} = t_{c,\text{NaNO}_3} - t_{c,\text{KNO}_3}$. These time differences, shown in Table 4, quantify how much earlier KNO_3 reaches saturation and onset of crystallization on the surface than NaNO_3 . If the values become negative, the sequence is reversed, i.e., NaNO_3 reaches these events first. In Table 5.4, the cases are grouped according to their initial conditions, such as total solution concentration, temperature of the drying gas, and molar ratio of NaNO_3 and KNO_3 . It is apparent that KNO_3 reaches saturation and onset of crystallization earlier than NaNO_3 in almost all cases studied. This is caused by the higher solubility of NaNO_3 . Moreover, NaNO_3 nucleates and commences crystal

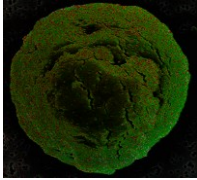
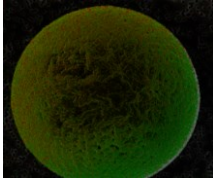
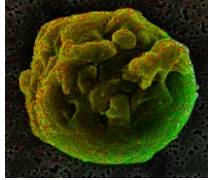
growth only after reaching a molar percentage of 20.7% or a weight percentage of 97% in water at a wet bulb temperature of 18.7°C. As a result, the conditions necessary for NaNO₃ to nucleate are of high supersaturation [300]. KNO₃, on the contrary, crystallizes already at a molar percentage of 8.3% or weight percentage of 47% at the same temperature. Due to the temperature dependence of the solubilities, an increase of the drying gas temperature and, consequently, an increase in wet bulb temperature favors KNO₃ to saturate first. Hence, the only cases that allowed NaNO₃ to saturate first were the ones with 70/30 NaNO₃/KNO₃ molar ratio or 66.2/33.8 NaNO₃/KNO₃ weight ratio at the lower drying gas temperature.

The hypothesis that the sequence in which the components reach saturation or onset of crystallization determines the radial distribution of chemical components in final dried microparticles was verified by comparison with the experimentally determined composition near the surface of the particles. In Table 5.4, the elemental maps from the SEM/EDX analysis for all twelve cases are shown. Green color indicates potassium and red indicates sodium. Also listed are the measured molar ratios of the components in the EDX interaction volume near the surface. These results are semi-quantitative due to the difference in overvoltage for the characteristic X-ray peaks in the EDX spectrum.

The only case that has clearly more sodium than potassium on the surface (molar ratio 93/7, second row, right), is also the one that has the largest negative values for $\Delta t_{\text{seq,c}}$ and $\Delta t_{\text{seq,s}}$, i.e., sodium nitrate reaches saturation 68 ms earlier and onset of crystallization 86 ms earlier than potassium nitrate. The only other case with negative values for $\Delta t_{\text{seq,c}}$ and $\Delta t_{\text{seq,s}}$ also shows a measured enrichment, albeit smaller, of sodium relative to the nominal ratio. On the other hand, the cases that have the highest surface coverage of potassium (molar ratio 14/86, top row left, and molar ratio 12/88, second row, left) also have the largest positive values for $\Delta t_{\text{seq,c}}$ and $\Delta t_{\text{seq,s}}$. In these cases KNO₃ has a head start of more than 150 ms over NaNO₃ for the onset of crystallization. In the other cases, both components reach saturation at about the same time and the near surface composition does not differ by much from the nominal composition. In summary, the measured near surface composition is in very good agreement with the predictions, providing strong support for the tested hypothesis.


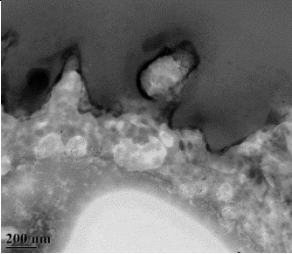
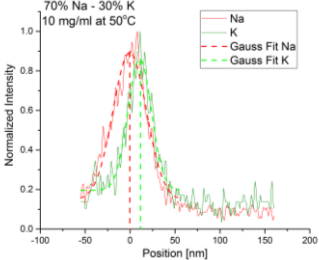

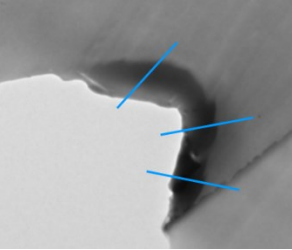
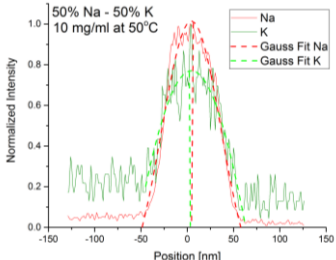
Table 5.4 SEM/EDX maps of the chemical components near the surface of the dried particles. Below each map the measured molar ratio of NaNO₃ to KNO₃ is listed together with the time differences between saturation and crystallization events for the components. Positive values indicate earlier saturation and crystallization for KNO₃.

T_{Gas}	C_0	Molar ratio (nominal)	NaNO ₃ /KNO ₃		NaNO ₃ /KNO ₃		NaNO ₃ /KNO ₃			
			30/70		50/50		70/30			
		Weight ratio	26.5/73.5		45.7/54.3		66.2/33.8			
°C	mg/ml		Na	K	Na	K	Na	K		
50	1	<u>2 μm</u>								
		Molar ratio (EDX)	14/86	47/52	58/42					
		Weight ratio (EDX)	12/87	44/56	54/46					
		$\Delta t_{\text{seq,s}}$ ($\Delta t_{\text{seq,c}}$), [ms]	+ 91 (+ 150)	+ 55 (+ 36)	- 19 (- 11)					
	10									
		Molar ratio (EDX)	12/88	50/50	93/7					
		Weight ratio (EDX)	10/90	45/55	92/8					
		$\Delta t_{\text{seq,s}}$ ($\Delta t_{\text{seq,c}}$), [ms]	+ 183 (+ 273)	+ 36 (+ 9)	- 68 (- 86)					
		100	1	<u>2 μm</u>						
				Molar ratio (EDX)	31/69	43/57	37/62			
Weight ratio (EDX)	28/72			39/61	34/66					

	$\Delta t_{\text{seq},s} (\Delta t_{\text{seq},c}), [\text{ms}]$	+ 53 (+ 39)	+ 22 (+ 9)	+ 2 (+ 1)
10	<u>5 μm</u>			
	Molar ratio (EDX)	30/70	46/54	47/53
	Weight ratio (EDX)	26/74	42/58	43/57
	$\Delta t_{\text{seq},s} (\Delta t_{\text{seq},c}), [\text{ms}]$	+ 58 (+ 101)	+ 28 (+ 12)	+ 31 (+ 95)

One disadvantage of the SEM/EDX technique is its limited depth resolution. Therefore, for selected cases the elemental composition in the inner part of the microparticles was analyzed using S-TEM. Table 5.5 shows microtome cuts across the shell of the particles and the elemental composition across the shell as determined by S-TEM. The elemental composition is shown qualitatively as normalized X-ray intensity as a function of position on a scan line across the shell. Peaks shifted more to the left on the x axis (negative position values) are shifted in the direction of the surface. The zero position was chosen arbitrarily in the middle of the shell. An average curve obtained with a Gaussian fit and its center indicated with a vertical line are also shown. Table 5.5 shows in the top row the case with surface enrichment of sodium (C_0 , 10 mg/ml at T_{Gas} of 50°C for 70% of NaNO_3 and 30% of KNO_3) and as comparison a case with close to nominal EDX composition (C_0 , 10 mg/ml at T_{Gas} of 50°C for 50% of NaNO_3 and 50% of KNO_3). The results are in agreement with the SEM/EDX findings. In the case where SEM/EDX measures near surface enrichment of sodium, S-TEM shows a sodium maximum shifted towards the surface relative to the potassium maximum, indicating that sodium crystallized earlier, as predicted. In the other case both components seem well mixed, indicating that they have crystallized at about the same time.

Table 5.5 Elemental composition across the shell of sectioned microparticles determined by S-TEM. Peaks shifted to the left represent the chemical components present on the surface. Cases with solution concentration of 10 mg/ml dried at 50°C for molar percentages of 70% of NaNO₃ and 30% of KNO₃ and 50% of NaNO₃ and 50% of KNO₃ .are shown.

Particle sections	Elemental composition
200 nm  	
1 μm  	

5.7 Conclusions

This study clarifies the particle formation process of a multicomponent droplet with crystallizing solutes. The properties of the dried microparticles can be linked to characteristic times describing the crystallization sub-process, specifically the time at which components reach supersaturation and onset of crystallization and the time available for crystallization. Morphological features of the dried particles, like particle density and radial distribution of components in the shell, can be affected by changing these characteristic times. These particle features can be predicted to some extent, and the influence of process and formulation variables can be evaluated. For example, both the theoretical model and the experimental results indicate that the chemical element that saturates first is mostly distributed on the surface.

Drugs for pulmonary disease can be combined in structure spray dried particles that are composed of a crystalline shell encapsulating the drug and excipients. It can be inferred from this study that in this case many formulation and process parameters can affect the particle morphology of crystallizing systems. Among these parameters are atomized droplet diameter, drying gas

temperature, feed concentration, and formulation composition. Therefore, these parameters need to be carefully controlled to ensure consistent particle morphology, which may affect the stability and aerosol efficiency of spray dried particles for inhalation.

The conclusions of this study were drawn from a simple binary system. Further work is necessary to refine the mechanistic understanding of the particle formation process in multicomponent systems with crystallizing and non-crystallizing components.

5.8 Acknowledgements

Funding from the Natural Sciences and Engineering Research Council of Canada (NSERC), the Alberta Innovates Technology Futures, and the George Ford chair endowment is gratefully acknowledged. The authors would also like to acknowledge Arlene Oatway for the help provided to section the microparticles and Anqiang He for the support in teaching the use of the S/TEM.

6 Conclusions

6.1 Main results

6.1.1 Theoretical developments

This thesis has shown that the particle formation process can be predicted and understood using parameters such as the Peclet number or Enrichment. In the foregoing chapters it has been demonstrated that these two parameters are related to the properties of the dried microparticles. In cases of high Peclet numbers, the shell is formed early in the particle formation process, generating microparticles with thin shells. After the point at which a shell is formed, the remaining solvent is released through the pores of the shell, leading to folding or buckling. These results show that the steady-state model cannot predict the properties of the final dried microparticles in the case of a non-constant evaporation rate.

As a consequence, a non-steady model was introduced. This model involves the measurement of the main parameters of the particle formation process at each time step. These parameters are, for instance, aerodynamic diameter, volume equivalent diameter, density, viscosity, diffusion coefficient, Peclet number, and Enrichment. Theoretical implementations relate also to the introduction of innovative equations. For example, the density is found in relationship with the solute amount contained in the evaporating droplet at every time step. More precisely, the density is obtained using two methods. Before the shell formation, a method that considers a liquid droplet is used. After the shell formation, a method that considers internal and external voids in the microparticles is used.

6.1.2 Experimental implementations

The setup used for the production of monodisperse microparticles was built in previous studies but did not function properly. Therefore, first of all, an innovative “Spacing” method was introduced. This method allowed the derivation of the main properties of the particle formation process by measuring only the distance between two consecutive droplets. The whole chain was simply highlighted with a pulse diode laser and images of the chain recorded with a camera. This method made possible the achievement of important results and a better understanding of the particle formation process. Along with the “Spacing” method, a so called “Imaging” method was used. This method needed the addition to the setup of a few devices, such as a strobe light, an

oscilloscope, and a microscope. These additions facilitated the derivation of the volume equivalent diameter, and thus of the density, at every time step in the particle formation process.

Moreover, the setup required implementations to simplify the experimental procedure. For example, the flow tube was modified from a rounded to a squared section. A squared section allows the recording of the droplets up to a meter far from the injection point. Furthermore, double sided walls were inserted into the flow tube. This modification allowed a vacuum layer to keep the flow temperature almost constant from the injection to the collection point.

Experimental implementations also involved the characterization of the final dried microparticles. The produced microparticles were innovatively analyzed with a Focused Ion Beam (FIB) and a Helium Ion Microscope (HIM). These techniques helped determine the shell thickness and the void amount contained in the produced microparticles. For the first time, monodisperse microparticles were used in a colloidal probe microscope. This innovation introduced an easy methodology to measure the cohesion forces between two microparticles.

6.1.3 Particle formation analysis

Important discoveries were achieved through the analysis of the particle formation process, of which the control and understanding is the main goal of this project. First, particle formation processes of non-crystallizing systems were studied. These systems have been partially analyzed in previous studies, but high Peclet number cases had not been investigated. It has now been verified that a high Peclet number generates a large diameter and a thin shell. In addition, these studies involved a previously unknown phase of the particle formation process: that between the shell formation and the collection point. It is in this phase that the most important steps of the particle formation process occur: shell formation, surface saturation and drying of the solvent.

Particle formation processes of crystallizing systems had never previously been studied. Compared to non-crystallizing systems, these systems were found to contain additional time steps: the time of nucleation and the time for crystallization. Changing these time variables was shown to affect the properties of the final microparticles. Small crystallization windows generated microparticles with a smaller crystal size, amount of crystallinity, void fraction and diameter. Also, the values of surface roughness were found to be proportional to the crystallization window. The roughness, though, was inversely proportional to cohesion forces between two microparticles. In drug delivery, coagulation of two drug microparticles results in a coarser effective particle size

distribution. As a result, coarser powders may have lower delivery efficiency from a DPI device. Therefore, coarser particle size distribution will generally result in decreased drug delivery efficiency to the lung. Studies of these systems are fundamental to improving pulmonary drug delivery.

Another system not previously analyzed is the particle formation process of crystallizing systems of a multicomponent evaporating droplet. The radial distribution of chemical components in a drug microparticle was found to be an important factor in the efficiency and the efficacy of drug delivery. Particles for sustained release or targeted delivery commonly consist of a thin shell composed by a carrier and an inner part composed by the excipient. It was demonstrated that the composition of spray dried microparticles can be predicted using the definition of time for saturation. The component of the particle formation process that first reaches the time for saturation dominates the external composition of the shell of spray dried microparticles. This finding, which had previously only been theorized, was experimentally validated. Furthermore, it was demonstrated that the chemical composition on the surface can be managed by changing the initial conditions of the particle formation process.

This thesis improves existing methodologies and develops novel techniques that enhance our understanding of the relationship between the initial conditions and the properties of produced microparticles. This work should benefit particle engineers working on drug delivery by enabling quantitative predictions related to the efficiency and efficacy of delivery of drugs for respiratory diseases. Even though the time-variable method predicts innovative time variables, such as the time for crystallization, and requires only one parameter as input, it presents limitations: time steps too extended to accurately predict time variables, lengthy time-frames for some of the techniques used, and inadequacies in practical application to drugs used for respiratory disease.

6.2 Future recommendations

In closing, some recommendations for future studies in this area are provided. Improvements can be made to both the experimental and the theoretical sides. On the experimental side, further implementations can improve drug delivery for pulmonary diseases: for instance, the decrease of turbulence in the flow tube, the analysis of the evaporation of a multi-solvent droplet, the recording of the volume equivalent diameter at every time step of the particle formation process, control over the temperature in the piezoceramic dispenser, the management of the pressure in the piezoceramic

dispenser, studies of the particle formation process of respiratory drugs, evaluation of the solid state composition of spray dried microparticles, and analysis of the properties of the final dried microparticles.

6.2.1 Experimental future developments

For the studies shown in all chapters, a low flow rate has been used. This decision was due to the use of water as a solvent. Since water has a low evaporation rate, droplets risk coagulating unless the spacing between two consecutive droplets is much higher than the volume equivalent diameter of a droplet. In cases of solvents with a higher evaporation rate, a higher flow rate might improve the quality of each experiment. However, a high flow rate entails a slight turbulence in the flow tube because of the change in section in the flow tube from a circular to a squared section. Eliminating the turbulence should reduce the errors involved in determining the properties of the droplets in the monodisperse droplet chain. Therefore, the flow tube could still benefit from a redesign: the distance between the change in section shape and the injection point could be increased to achieve a fully developed, laminar flow at the injection point. Alternatively, both the flow tube and the heater could be modified into a squared section so that no change in section would occur.

A microscope lens was used to record volume equivalent diameter in only some of the studies outlined here. Using the microscope for all the experiments would have facilitated the derivation of the properties of the particle formation process. Moreover, the use of a microscope with high magnification would clarify the crystallization process by recording images of the droplets or particles during the formation of each crystal. Consistent use of high-magnification microscopy would in turn improve the determination of the time for crystallization.

Greater control over the temperature inside the piezoceramic dispenser would be useful in cases of high temperature flow rate. A high external temperature also increases the temperature inside the tip of the piezoceramic dispenser, thus interfering with the droplet's injection. This problem could be solved by improving the insulation of the tip of the piezoceramic dispenser with spray coatings or by enclosing the whole piezoceramic dispenser in a cooling system.

Another problem related to the piezoceramic dispenser is control of its pressure. The stage where the piezoceramic dispenser was placed could be moved vertically, thus slightly modifying the internal pressure. A more precise method could involve connecting the vent valve to a container

with a fixed volume. The container could have a gauge and a metering valve to manage minor changes in the pressure inside the piezoceramic dispenser.

The distribution of the solid phase of the produced microparticles is of great interest for companies producing pulmonary drugs. Some excipients release faster or have different properties if amorphous respect than crystalline. Determination of the radial solid phase distribution of microparticles might be facilitated with the use of silver nanoparticles and Surface Enhanced Raman Spectroscopy (SERS). The use of silver nanoparticle would enhance the Raman signal of the surface of the microparticles.

Further improvements in particle characterization are possible. For instance, the production of samples for Raman analysis can generate high losses. The microparticles are collected on a frit that is inserted into a hollow SEM stub. The frit is then removed to place it on a holder for Raman analysis. The process of transferring the microparticles generates losses. Furthermore, the microparticles are often damaged when chopped for TEM analysis. The microparticles have been cut using a glass tip; the force on the microparticles during the cut can be too high and damage them. The damage seems to be more likely in cases where the shell is thin. A better method might involve using a diamond tip, which is thinner and sharper and can reduce the forces in the impact.

6.2.2 Theoretical future implementations

On the theoretical side, the main improvement regards the model used to determine all the properties of the droplets or particles in the particle formation process. A computation model could greatly reduce the time constraints caused by manual calculations. This model could have as input the images of each droplet, recorded using a microscope lens, and images of the droplet chain, recorded and highlighted with a diode laser, to produce a trend of all the main properties of the particle formation process: aerodynamic diameter, volume equivalent diameter, density, mass, evaporation rate, viscosity, diffusion coefficient, Peclet number and enrichment. All of these parameters have to be dependent on time, especially for a particle formation process involving a solute with a tendency to crystallize. In addition, the model could provide a better determination of the enrichment for a non-steady situation. The computational model might consider a smaller time step than 20 milliseconds, used in the studies outlined in this thesis. This computational model could easily and quickly provide a more precise value of important time variables, such as time for crystallization and time to reach saturation.

6.2.3 Particle formation future studies

Analysis of the evaporation of a multi-solvent droplet, even though complex and time consuming, is strongly appealing because of its multiple potential applications, such as increasing the solubility of certain respiratory drugs. Using the setup presented here, only the change in properties of the final dried microparticles can be analyzed. A Raman spectroscopy of the evaporating droplet could determine the evaporation path of each solvent contained in the droplet. This analysis might enable observation of critical transitions in the particle formation process (e.g. crystallization), and might allow detailed studies of the evolving composition of an evaporating multi-solvent droplet.

Studies of the particle formation process of respiratory drugs could be simply achieved by injecting into the flow tube a droplet composed of a solvent and the selected respiratory drugs. This approach would allow the evaluation of the evaporation process and the properties of the final dried particles. Afterwards, the properties of the final dried particles could be related to the initial conditions of the particle formation process. Studying an appropriately selected active pharmaceutical ingredient might provoke stronger interest from respiratory drugs companies. Moreover, the knowledge of the relationship between the properties of final dried microparticles and the initial conditions of the droplet drying could be beneficial for real applications, such as spray drying process development or drug delivery from solution metered dose inhalers.

References

1. Boraey, M.A. and R. Vehring, *Diffusion Controlled Formation of Microparticles*. Journal of Aerosol Science, 2014. **67**: p. 131-143.
2. Vehring, R., W.R. Foss, and D. Lechuga-Ballesteros, *Particle Formation in Spray Drying*. Journal of Aerosol Science, 2007. **38**(7): p. 728-746.
3. Beck-Broichsitter, M., O.M. Merkel, and T. Kissel, *Controlled Pulmonary Drug and Gene Delivery Using Polymeric Nano-Carriers*. Journal of Controlled Release, 2012. **161**(2): p. 214-224.
4. Boraey, M.A., et al., *Improvement of the Dispersibility of Spray-Dried Budesonide Powders Using Leucine in an Ethanol–Water Cosolvent System*. Powder Technology, 2013. **236**: p. 171-178.
5. Goldberg, M., R. Langer, and X. Jia, *Nanostructured Materials for Applications in Drug Delivery and Tissue Engineering*. Journal of Biomaterials Science, Polymer Edition, 2007. **18**(3): p. 241-268.
6. Gupta, R.B. and U.B. Kompella, *Nanoparticle Technology for Drug Delivery*. 2006: Taylor & Francis New York.
7. Ragab, D.M. and S. Rohani, *Particle Engineering Strategies Via Crystallization for Pulmonary Drug Delivery*. Organic Process Research & Development, 2009. **13**(6): p. 1215-1223.
8. Yan, Y., et al., *Engineering Particles for Therapeutic Delivery: Prospects and Challenges*. ACS nano, 2012. **6**(5): p. 3663-3669.
9. Kim, S., C. Wei, and S. Kiang, *Crystallization Process Development of an Active Pharmaceutical Ingredient and Particle Engineering Via the Use of Ultrasonics and Temperature Cycling*. Organic Process Research & Development, 2003. **7**(6): p. 997-1001.
10. Rogers, T.L., et al., *A Novel Particle Engineering Technology: Spray-Freezing into Liquid*. International Journal of Pharmaceutics, 2002. **242**(1): p. 93-100.
11. Shoyele, S.A. and S. Cawthorne, *Particle Engineering Techniques for Inhaled Biopharmaceuticals*. Advanced Drug Delivery Reviews, 2006. **58**(9): p. 1009-1029.
12. Smola, M., T. Vandamme, and A. Sokolowski, *Nanocarriers as Pulmonary Drug Delivery Systems to Treat and to Diagnose Respiratory and Non Respiratory Diseases*. International journal of nanomedicine, 2008. **3**(1): p. 1.
13. Harris, D. and J.R. Robinson, *Drug Delivery Via the Mucous Membranes of the Oral Cavity*. Journal of Pharmaceutical Sciences, 1992. **81**(1): p. 1-10.
14. Türker, S., E. Onur, and Y. Ózer, *Nasal Route and Drug Delivery Systems*. Pharmacy World and Science, 2004. **26**(3): p. 137-142.
15. Allen, T.M. and P.R. Cullis, *Drug Delivery Systems: Entering the Mainstream*. Science, 2004. **303**(5665): p. 1818-1822.
16. D'Addio, S.M., et al., *Spray Freeze Dried Large Porous Particles for Nano Drug Delivery by Inhalation*. Respiratory Drug Delivery 2012, 2012. **3**: p. 695-698.
17. Lim, J. and E.E. Simanek, *Triazine Dendrimers as Drug Delivery Systems: From Synthesis to Therapy*. Advanced Drug Delivery Reviews, 2012. **64**(9): p. 826-835.
18. Cohen, M.H., et al., *Fda Drug Approval Summary: Pemetrexed for Injection (Alimta®) for the Treatment of Non-Small Cell Lung Cancer*. The Oncologist, 2005. **10**(6): p. 363-368.

19. Pham, D.-D., E. Fattal, and N. Tsapis, *Pulmonary Drug Delivery Systems for Tuberculosis Treatment*. International Journal of Pharmaceutics, 2015. **478**(2): p. 517-529.
20. Zhou, Q.T., et al., *Inhaled Formulations and Pulmonary Drug Delivery Systems for Respiratory Infections*. Advanced drug delivery reviews, 2015. **85**: p. 83-99.
21. d'Angelo, I., et al., *Improving the Efficacy of Inhaled Drugs in Cystic Fibrosis: Challenges and Emerging Drug Delivery Strategies*. Advanced Drug Delivery Reviews, 2014. **75**: p. 92-111.
22. Courier, H., N. Butz, and T.F. Vandamme, *Pulmonary Drug Delivery Systems: Recent Developments and Prospects*. Critical Reviews™ in Therapeutic Drug Carrier Systems, 2002. **19**(4-5): p. 425-498.
23. Kulkarni, P., P.A. Baron, and K. Willeke, *Aerosol Measurement: Principles, Techniques, and Applications*. 2011: John Wiley & Sons.
24. Hinds, W.C., *Aerosol Technology: Properties, Behavior, and Measurement of Airborne Particles*. 2012: John Wiley & Sons.
25. Patton, J.S., *Practical Considerations for Drug Delivery to the Respiratory Tract*. Nanoparticles in the Lung: Environmental Exposure and Drug Delivery, 2014: p. 211.
26. Garcia-Contreras, L., et al., *Pharmacokinetics of Inhaled Rifampicin Porous Particles for Tuberculosis Treatment: Insight into Rifampicin Absorption from the Lungs of Guinea Pigs*. Molecular Pharmaceutics, 2015.
27. Vehring, R., et al., *Cosuspensions of Microcrystals and Engineered Microparticles for Uniform and Efficient Delivery of Respiratory Therapeutics from Pressurized Metered Dose Inhalers*. Langmuir, 2012. **28**(42): p. 15015-15023.
28. Sarafraz-Yazdi, A., et al., *Determination of Non-Steroidal Anti-Inflammatory Drugs in Water Samples by Solid-Phase Microextraction Based Sol–Gel Technique Using Poly (Ethylene Glycol) Grafted Multi-Walled Carbon Nanotubes Coated Fiber*. Analytica Chimica Acta, 2012. **720**: p. 134-141.
29. Elkordy, A.A., R.T. Forbes, and B.W. Barry, *Stability of Crystallised and Spray-Dried Lysozyme*. International Journal of Pharmaceutics, 2004. **278**(2): p. 209-219.
30. Steckel, H., N. Rasenack, and B.W. Müller, *In-Situ-Micronization of Disodium Cromoglycate for Pulmonary Delivery*. European Journal of Pharmaceutics and Biopharmaceutics, 2003. **55**(2): p. 173-180.
31. Al-Tabakha, M.M., et al., *Influence of Capsule Shell Composition on the Performance Indicators of Hypromellose Capsule in Comparison to Hard Gelatin Capsules*. Drug Development and Industrial Pharmacy, 2015(0): p. 1-12.
32. Forsberg, F., et al., *Effect of Shell Type on the in Vivo Backscatter from Polymer-Encapsulated Microbubbles*. Ultrasound in Medicine & Biology, 2004. **30**(10): p. 1281-1287.
33. Hoe, S., et al., *Use of a Fundamental Approach to Spray-Drying Formulation Design to Facilitate the Development of Multi-Component Dry Powder Aerosols for Respiratory Drug Delivery*. Pharmaceutical Research, 2014. **31**(2): p. 449-465.
34. D'Sa, D.J., H.-K. Chan, and W. Chrzanowski, *Attachment of Micro-and Nano-Particles on Tipless Cantilevers for Colloidal Probe Microscopy*. Journal of Colloid and Interface Science, 2014. **426**: p. 190-198.
35. Zhang, F., et al., *Roughness-Controlled Self-Assembly of Mannitol/Lb Agar Microparticles by Polymorphic Transformation for Pulmonary Drug Delivery*. Molecular Pharmaceutics, 2014. **12**(1): p. 223-231.

36. Zhang, X., et al., *Experimental Study on the Surface Characteristics of Pd-Based Bulk Metallic Glass*. Applied Surface Science, 2014. **321**: p. 420-425.
37. Kanakidou, M., *Atmospheric Aerosols and Climate Impacts*. Aerosol Science: Technology and Applications, 2013: p. 181-206.
38. Rubinstein, G.J., J. Derksen, and S. Sundaresan, *Lattice Boltzmann Simulations of Low-Reynolds-Number Flow Past Fluidized Spheres: Effect of Stokes Number on Drag Force*. Journal of Fluid Mechanics, 2016. **788**: p. 576-601.
39. Adi, S., et al., *Effects of Mechanical Impaction on Aerosol Performance of Particles with Different Surface Roughness*. Powder Technology, 2013. **236**: p. 164-170.
40. Ueyama, K., *Virtual Force Term Based on the Velocity Distribution Surrounding a Spherical Particle Settling in a Simple Shear Flow*. Chemical Engineering & Technology, 2015. **38**(11): p. 1933-1939.
41. Colbeck, I., *Aerosol Science: Technology and Applications*. 2014: John Wiley & Sons.
42. Gopalakrishnan, R., et al., *The Unipolar Diffusion Charging of Arbitrary Shaped Aerosol Particles*. Journal of Aerosol Science, 2013. **64**: p. 60-80.
43. Gen, M., et al., *Simultaneous Deposition of Submicron Aerosols onto Both Surfaces of a Plate Substrate by Electrostatic Forces*. e-Journal of Surface Science and Nanotechnology, 2014. **12**(0): p. 238-241.
44. Xie, M., Q. He, and W. Wang, *Interception Efficiency of Particle Laden Flow over a Finite Flat Plate in Potential Flow Regimes*. Thermal Science, 2013. **17**(5): p. 1343-1348.
45. Zhou, Q.T., et al., *Emerging Inhalation Aerosol Devices and Strategies: Where Are We Headed?* Advanced Drug Delivery Reviews, 2014. **75**: p. 3-17.
46. Dolovich, M.B. and R. Dhand, *Aerosol Drug Delivery: Developments in Device Design and Clinical Use*. The Lancet, 2011. **377**(9770): p. 1032-1045.
47. Wyatt, E.L., et al., *Metered-Dose Inhaler Ipratropium Bromide in Moderate Acute Asthma in Children: A Single-Blinded Randomised Controlled Trial*. Journal of Paediatrics and Child Health, 2015. **51**(2): p. 192-198.
48. Buchmann, N.A., et al., *A Novel High-Speed Imaging Technique to Predict the Macroscopic Spray Characteristics of Solution Based Pressurised Metered Dose Inhalers*. Pharmaceutical Research, 2014. **31**(11): p. 2963-2974.
49. Paggiaro, P., et al., *High Dose Extrafine Beclomethasone/Formoterol Via Metered Dose Inhaler Is Effective and Safe in Asthmatics Not Controlled on Medium-High Dose of Inhaled Corticosteroids*. European Respiratory Journal, 2014. **44**(Suppl 58): p. P901.
50. Chen, Y., et al., *The Influence of Actuator Materials and Nozzle Designs on Electrostatic Charge of Pressurised Metered Dose Inhaler (PMDI) Formulations*. Pharmaceutical Research, 2014. **31**(5): p. 1325-1337.
51. Chen, Y., et al., *The Effect of Actuator Nozzle Designs on the Electrostatic Charge Generated in Pressurised Metered Dose Inhaler Aerosols*. Pharmaceutical Research, 2015. **32**(4): p. 1237-1248.
52. Ziffels, S., et al., *In Vitro Dry Powder Inhaler Formulation Performance Considerations*. Journal of Controlled Release, 2015. **199**: p. 45-52.
53. Lin, Y., et al., *Powder Production and Particle Engineering for Dry Powder Inhaler Formulations*. Current Pharmaceutical Design, 2015.
54. Al-Showair, R.A., et al., *Can All Patients with Copd Use the Correct Inhalation Flow with All Inhalers and Does Training Help?* Respiratory Medicine, 2007. **101**(11): p. 2395-2401.

55. Ivanova, M. and A. Glazova. *Nebulizer Improvement for Children Suffering from Bronchial Asthma*. in *Young Researchers in Electrical and Electronic Engineering Conference (EIconRusNW), 2015 IEEE NW Russia*. 2015: IEEE.
56. Jarvas, G., et al., *Simulation-Based Design of a Microfabricated Pneumatic Electrospray Nebulizer*. *Electrophoresis*, 2015. **36**(3): p. 386-392.
57. Latthe, S.S., et al., *Self-Cleaning and Superhydrophobic CuO Coating by Jet-Nebulizer Spray Pyrolysis Technique*. *CrystEngComm*, 2015. **17**(13): p. 2624-2628.
58. Idris, A.H., et al., *Emergency Department Treatment of Severe Asthma. Metered-Dose Inhaler Plus Holding Chamber Is Equivalent in Effectiveness to Nebulizer*. *CHEST Journal*, 1993. **103**(3): p. 665-672.
59. Corden, Z.M., et al., *Home Nebulized Therapy for Patients with Copd: Patient Compliance with Treatment and Its Relation to Quality of Life*. *CHEST Journal*, 1997. **112**(5): p. 1278-1282.
60. Bruttini, R. and A. Liapis, *The Drying Rates of Spray Freeze Drying Systems Increase through the Use of Stratified Packed Bed Structures*. *International Journal of Heat and Mass Transfer*, 2015. **90**: p. 515-522.
61. Her, J.-Y., M.S. Kim, and K.-G. Lee, *Preparation of Probiotic Powder by the Spray Freeze-Drying Method*. *Journal of Food Engineering*, 2015. **150**: p. 70-74.
62. Wanning, S., R. Süverkrüp, and A. Lamprecht, *Pharmaceutical Spray Freeze Drying*. *International Journal of Pharmaceutics*, 2015. **488**(1): p. 136-153.
63. Huang, X., et al., *Tumor-Targeted Paclitaxel-Loaded Folate Conjugated Poly (Ethylene Glycol)-Poly (L-Lactide) Microparticles Produced by Supercritical Fluid Technology*. *Journal of Materials Science: Materials in Medicine*, 2015. **26**(2): p. 1-14.
64. Obaidat, R.M., et al., *Drying Using Supercritical Fluid Technology as a Potential Method for Preparation of Chitosan Aerogel Microparticles*. *AAPS PharmSciTech*, 2015: p. 1-10.
65. Rodríguez-Meizoso, I. and M. Plaza, *Particle Formation of Food Ingredients by Supercritical Fluid Technology*, in *High Pressure Fluid Technology for Green Food Processing*. 2015, Springer. p. 155-183.
66. Ganesh, M., et al., *Chitosan Cocrystals Embedded Alginate Beads for Enhancing the Solubility and Bioavailability of Aceclofenac*. *International Journal of Biological Macromolecules*, 2015. **74**: p. 310-317.
67. Javadzadeh, Y., S. Hamedeyzdan, and S. Asnaashari, *Recrystallization of Drugs: Significance on Pharmaceutical Processing*. 2012: INTECH Open Access Publisher.
68. Lawrence, R.M., et al., *Serial Femtosecond X-Ray Diffraction of Enveloped Virus Microcrystals*. *Structural Dynamics*, 2015. **2**(4): p. 041720.
69. Mao, A., et al., *Recycling Polyurethane Materials: A Comparison of Polyol from Glycolysis with Micronized Polyurethane Powder in Particleboard Applications*. *BioResources*, 2014. **9**(3): p. 4253-4265.
70. Uttekar, P. and P. Chaudhari, *Formulation and Evaluation of Engineered Pharmaceutical Fine Particles of Budesonide for Dry Powder Inhalation (Dpi) Produced by Amphiphilic Crystallization Technique: Optimization of Process Parameters*. *International Journal of Pharmaceutical Sciences and Research*, 2013. **4**(12): p. 4656.
71. Ye, F., et al., *Effect of Micronization on the Physicochemical Properties of Insoluble Dietary Fiber from Citrus (Citrus Junos Sieb. Ex Tanaka) Pomace*. *Food Science and Technology International*, 2015: p. 1082013215593394.

72. Beck-Broichsitter, M., et al., *Modified Vibrating-Mesh Nozzles for Advanced Spray-Drying Applications*. European Journal of Pharmaceutics and Biopharmaceutics, 2015. **92**: p. 96-101.
73. Porras-Saavedra, J., et al., *Microstructural Properties and Distribution of Components in Microparticles Obtained by Spray-Drying*. Journal of Food Engineering, 2015. **152**: p. 105-112.
74. Wang, Z., et al., *Lanthanide–Organic Framework Nanothermometers Prepared by Spray-Drying*. Advanced Functional Materials, 2015. **25**(19): p. 2824-2830.
75. Wang, Z., et al., *Powder Formation by Atmospheric Spray-Freeze-Drying*. Powder Technology, 2006. **170**(1): p. 45-52.
76. Ishwarya, S.P., C. Anandharamakrishnan, and A.G. Stapley, *Spray-Freeze-Drying: A Novel Process for the Drying of Foods and Bioproducts*. Trends in Food Science & Technology, 2015. **41**(2): p. 161-181.
77. Ali, M.E. and A. Lamprecht, *Spray Freeze Drying for Dry Powder Inhalation of Nanoparticles*. European Journal of Pharmaceutics and Biopharmaceutics, 2014. **87**(3): p. 510-517.
78. Karthik, P. and C. Anandharamakrishnan, *Microencapsulation of Docosahexaenoic Acid by Spray-Freeze-Drying Method and Comparison of Its Stability with Spray-Drying and Freeze-Drying Methods*. Food and Bioprocess Technology, 2013. **6**(10): p. 2780-2790.
79. Yener, M.E., *Supercritical Fluid Processing for the Recovery of Bioactive Compounds from Food Industry by-Products*, in *High Pressure Fluid Technology for Green Food Processing*. 2015, Springer. p. 305-355.
80. Temelli, F. and O.N. Ciftci, *Developing an Integrated Supercritical Fluid Biorefinery for the Processing of Grains*. The Journal of Supercritical Fluids, 2015. **96**: p. 77-85.
81. Parhi, R. and P. Suresh, *Supercritical Fluid Technology: A Review*. 2013.
82. Joshi, J.T., *A Review on Micronization Techniques*. Journal of Pharmaceutical Sciences and Research, 2011. **3**(7): p. 651-681.
83. Mathiowitz, E., C. Thanos, and Z. Liu, *Methods for Micronization of Hydrophobic Drugs*. 2013, Google Patents.
84. Protonotariou, S., et al., *Sieving Fractionation and Jet Mill Micronization Affect the Functional Properties of Wheat Flour*. Journal of Food Engineering, 2014. **134**: p. 24-29.
85. Santos, D.T. and M.A.A. Meireles, *Micronization and Encapsulation of Functional Pigments Using Supercritical Carbon Dioxide*. Journal of Food Process Engineering, 2013. **36**(1): p. 36-49.
86. Seville, P.C., H.-y. Li, and T.P. Learoyd, *Spray-Dried Powders for Pulmonary Drug Delivery*. Critical Reviews™ in Therapeutic Drug Carrier Systems, 2007. **24**(4).
87. Fan, C., *Contribution to Nano or Micro Crystallization Induction in Silica-Based Glass by Femtosecond Laser Irradiation*. 2012, Université Paris Sud-Paris XI; East China University of Science and Technology.
88. Brumshstein, B., et al., *Control of the Rate of Evaporation in Protein Crystallization by Themicrobatch under Oil'method*. Journal of Applied Crystallography, 2008. **41**(5): p. 969-971.
89. Lin, H.-x., et al., *Supersaturation-Dependent Surface Structure Evolution: From Ionic, Molecular to Metallic Micro/Nanocrystals*. Journal of the American Chemical Society, 2013. **135**(25): p. 9311-9314.

90. Amstad, E., et al., *Production of Amorphous Nanoparticles by Supersonic Spray-Drying with a Microfluidic Nebulator*. Science, 2015. **349**(6251): p. 956-960.
91. Dijkstra, A.R., et al., *Diversity in Robustness of Lactococcus Lactis Strains During Heat Stress, Oxidative Stress, and Spray Drying Stress*. Applied and Environmental Microbiology, 2014. **80**(2): p. 603-611.
92. Paireau, C., et al., *Si/C Composites Prepared by Spray Drying from Cross-Linked Polyvinyl Alcohol as Li-Ion Batteries Anodes*. Electrochimica Acta, 2015. **174**: p. 361-368.
93. Sinkiewicz-Enggren, G., A. Skurzynska, and T. Sandberg, *Stabilization of Lactobacillus Reuteri by Encapsulation of Bacterial Cells through Spray Drying*. American Society of BioMedicine, 2015, **3**: p 432-443.
94. Stocke, N.A., et al., *Formulation and Characterization of Inhalable Magnetic Nanocomposite Microparticles (Mnms) for Targeted Pulmonary Delivery Via Spray Drying*. International Journal of Pharmaceutics, 2015. **479**(2): p. 320-328.
95. Masters, K., *Spray Drying*. 1972.
96. Gharsallaoui, A., et al., *Applications of Spray-Drying in Microencapsulation of Food Ingredients: An Overview*. Food Research International, 2007. **40**(9): p. 1107-1121.
97. He, P., S.S. Davis, and L. Illum, *Chitosan Microspheres Prepared by Spray Drying*. International Journal of Pharmaceutics, 1999. **187**(1): p. 53-65.
98. Li, X., et al., *Large-Scale Synthesis of Mesoporous Carbon Microspheres with Controllable Structure and Nitrogen Doping Using a Spray Drying Method*. RSC Advances, 2014. **4**(107): p. 62662-62665.
99. Filková, I., L.X. Huang, and A.S. Mujumdar, *9 Industrial Spray Drying Systems*. Handbook of Industrial Drying, 2014: p. 191.
100. Shemirani, F.M., et al., *Onset of Flash Atomization in a Propellant Microjet*. Journal of Fluids Engineering, 2015. **137**(9): p. 091101.
101. Donz, E., P. Boiron, and J.-L. Courthaudon, *Characterization of Industrial Dried Whey Emulsions at Different Stages of Spray-Drying*. Journal of Food Engineering, 2014. **126**: p. 190-197.
102. Mujumdar, A.S., *Handbook of Industrial Drying*. 2014: CRC Press.
103. Nagy, Z.K., et al., *High Speed Electrospinning for Scaled-up Production of Amorphous Solid Dispersion of Itraconazole*. International Journal of Pharmaceutics, 2015. **480**(1): p. 137-142.
104. Durli, T., et al., *Innovative Approach to Produce Submicron Drug Particles by Vibrational Atomization Spray Drying: Influence of the Type of Solvent and Surfactant*. Drug Development and Industrial Pharmacy, 2014. **40**(8): p. 1011-1020.
105. Rader, D.J., *Momentum Slip Correction Factor for Small Particles in Nine Common Gases*. Journal of Aerosol Science, 1990. **21**(2): p. 161-168.
106. Tumolva, L., J.Y. Park, and K. Park, *Combination of Transmission Electron and Atomic Force Microscopy Techniques to Determine Volume Equivalent Diameter of Submicrometer Particles*. Microscopy Research and Technique, 2012. **75**(4): p. 505-512.
107. Shapiro, M., et al., *Characterization of Agglomerates by Simultaneous Measurement of Mobility, Vacuum Aerodynamic Diameter and Mass*. Journal of Aerosol Science, 2012. **44**: p. 24-45.
108. Deegan, R.D., *Pattern Formation in Drying Drops*. Physical Review E, 2000. **61**(1): p. 475.

109. Kats, E., V.V. Lebedev, and A. Muratov, *Weak Crystallization Theory*. Physics Reports, 1993. **228**(1): p. 1-91.
110. Gránásy, L., T. Börzsönyi, and T. Pusztai, *Nucleation and Bulk Crystallization in Binary Phase Field Theory*. Physical Review Letters, 2002. **88**(20): p. 206105.
111. Price, F.P., *A Phenomenological Theory of Spherulitic Crystallization: Primary and Secondary Crystallization Processes*. Journal of Polymer Science Part A: General Papers, 1965. **3**(9): p. 3079-3086.
112. Lenka, M. and D. Sarkar, *Determination of Metastable Zone Width, Induction Period and Primary Nucleation Kinetics for Cooling Crystallization of L-Asparaginenohydrate*. Journal of Crystal Growth, 2014. **408**: p. 85-90.
113. Anwar, J., S. Khan, and L. Lindfors, *Secondary Crystal Nucleation: Nuclei Breeding Factory Uncovered*. Angewandte Chemie, 2015. **127**(49): p. 14894-14897.
114. Sear, R.P., *Nucleation of a New Phase on a Surface That Is Changing Irreversibly with Time*. Physical Review E, 2014. **89**(2): p. 022405.
115. Beekmans, L. and G. Vancso, *Real-Time Crystallization Study of Poly (ϵ -Caprolactone) by Hot-Stage Atomic Force Microscopy*. Polymer, 2000. **41**(25): p. 8975-8981.
116. De Yoreo, J.J. and P.G. Vekilov, *Principles of Crystal Nucleation and Growth*. Reviews in Mineralogy and Geochemistry, 2003. **54**(1): p. 57-93.
117. Costantino, H.R., et al., *Effect of Mannitol Crystallization on the Stability and Aerosol Performance of a Spray-Dried Pharmaceutical Protein, Recombinant Humanized Anti-Ige Monoclonal Antibody*. Journal of Pharmaceutical Sciences, 1998. **87**(11): p. 1406-1411.
118. Maa, Y.-F., et al., *Protein Inhalation Powders: Spray Drying Vs Spray Freeze Drying*. Pharmaceutical Research, 1999. **16**(2): p. 249-254.
119. Yu, L. and K. Ng, *Glycine Crystallization During Spray Drying: The Ph Effect on Salt and Polymorphic Forms*. Journal of Pharmaceutical Sciences, 2002. **91**(11): p. 2367-2375.
120. Abianeh, O.S., C. Chen, and S. Mahalingam, *Numerical Modeling of Multi-Component Fuel Spray Evaporation Process*. International Journal of Heat and Mass Transfer, 2014. **69**: p. 44-53.
121. Maas, S.G., et al., *The Impact of Spray Drying Outlet Temperature on the Particle Morphology of Mannitol*. Powder Technology, 2011. **213**(1): p. 27-35.
122. Vaden, T.D., et al., *Evaporation Kinetics and Phase of Laboratory and Ambient Secondary Organic Aerosol*. Proceedings of the National Academy of Sciences, 2011. **108**(6): p. 2190-2195.
123. Al Zaitone, B.A. and C. Tropea, *Evaporation of Pure Liquid Droplets: Comparison of Droplet Evaporation in an Acoustic Field Versus Glass-Filament*. Chemical Engineering Science, 2011. **66**(17): p. 3914-3921.
124. Shih, A.T. and C.M. Megaridis, *Suspended Droplet Evaporation Modeling in a Laminar Convective Environment*. Combustion and Flame, 1995. **102**(3): p. 256-270.
125. Walton, D., *The Evaporation of Water Droplets. A Single Droplet Drying Experiment*. Drying Technology, 2004. **22**(3): p. 431-456.
126. Cotterell, M.I., et al. *Extinction Cross Section Measurements for a Single Optically Trapped Particle*. in *SPIE Nanoscience+ Engineering*. 2015: International Society for Optics and Photonics.
127. Preston, T.C., et al., *Size-Dependent Position of a Single Aerosol Droplet in a Bessel Beam Trap*. Journal of Optics, 2014. **16**(2): p. 025702.

128. Stewart, D., et al., *Liquid-Liquid Phase Separation in Mixed Organic/Inorganic Single Aqueous Aerosol Droplets*. The Journal of Physical Chemistry A, 2015. **119**(18): p. 4177-4190.
129. Azhdarzadeh, M., et al., *Effect of Electrostatic Charge on Oral-Extrathoracic Deposition for Uniformly Charged Monodisperse Aerosols*. Journal of Aerosol Science, 2014. **68**: p. 38-45.
130. Gebel, G., et al., *Laser-Induced Blast Waves in Air and Their Effect on Monodisperse Droplet Chains of Ethanol and Kerosene*. Shock Waves, 2015: p. 1-15.
131. Tanaka, H., et al., *Hands-Off Preparation of Monodisperse Emulsion Droplets Using a Poly (Dimethylsiloxane) Microfluidic Chip for Droplet Digital Pcr*. Analytical chemistry, 2015. **87**(8): p. 4134-4143.
132. Fuchs, N.A., *Evaporation and Droplet Growth in Gaseous Media*. 2013: Elsevier.
133. Dambach, E.M., et al., *Temperature Estimations in the near-Flame Field Resulting from Hypergolic Ignition Using Thin Filament Pyrometry*. Combustion Science and Technology, 2012. **184**(2): p. 205-223.
134. Schutyser, M.A., J. Perdana, and R.M. Boom, *Single Droplet Drying for Optimal Spray Drying of Enzymes and Probiotics*. Trends in Food Science & Technology, 2012. **27**(2): p. 73-82.
135. Aggarwal, S.K., *Single Droplet Ignition: Theoretical Analyses and Experimental Findings*. Progress in Energy and Combustion Science, 2014. **45**: p. 79-107.
136. Davies, J.F., et al., *Bulk, Surface, and Gas-Phase Limited Water Transport in Aerosol*. The Journal of Physical Chemistry A, 2012. **116**(45): p. 10987-10998.
137. Haddrell, A., et al. *A Detailed Understanding of Physicochemical Properties of Pharmaceutical Containing Aerosol Can Be Used to Improve Targeted Drug Delivery in the Lung*. in Journal of Aerosol Medicine and Pulmonary Drug Delivery. 2015.
138. Subramaniam, V. and S. Garimella, *Numerical Study of Heat and Mass Transfer in Lithium Bromide-Water Falling Films and Droplets*. International Journal of Refrigeration, 2014. **40**: p. 211-226.
139. Cotterell, M.I., et al., *Measurements of the Evaporation and Hygroscopic Response of Single Fine-Mode Aerosol Particles Using a Bessel Beam Optical Trap*. Physical Chemistry Chemical Physics, 2014. **16**(5): p. 2118-2128.
140. Crowe, C.T., et al., *Multiphase Flows with Droplets and Particles*. 2011: CRC press.
141. Seinfeld, J.H. and S.N. Pandis, *Atmospheric Chemistry and Physics: From Air Pollution to Climate Change*. 2012: John Wiley & Sons.
142. Shemesh, J., et al., *Coalescence-Assisted Generation of Single Nanoliter Droplets with Predefined Composition*. Lab on a chip, 2011. **11**(19): p. 3225-3230.
143. Yang, S., et al., *Integration of a Discrete Multi-Component Fuel Evaporation Model with a G-Equation Flame Propagation Combustion Model and Its Validation*. International Journal of Engine Research, 2012. **13**(4): p. 370-384.
144. Galinskiy, I., et al., *Measurement of Particle Motion in Optical Tweezers Embedded in a Sagnac Interferometer*. arXiv preprint arXiv:1507.05321, 2015.
145. Huang, K.-W., et al., *Microfluidic Integrated Optoelectronic Tweezers for Single-Cell Preparation and Analysis*. Lab on a Chip, 2013. **13**(18): p. 3721-3727.
146. Jin, Y., et al., *Measuring the Pressures across Microfluidic Droplets with an Optical Tweezer*. Optics express, 2012. **20**(22): p. 24450-24464.

147. Anand, S., et al., *Aerosol Droplet Optical Trap Loading Using Surface Acoustic Wave Nebulization*. Optics Express, 2013. **21**(25): p. 30148-30155.
148. Corsetti, S., et al. *Studying Biofuel Aerosol Evaporation Rates with Single Particle Manipulation*. in *SPIE NanoScience+ Engineering*. 2014: International Society for Optics and Photonics.
149. Horstmann, M., K. Probst, and C. Fallnich, *Towards an Integrated Optical Single Aerosol Particle Lab*. Lab on a Chip, 2012. **12**(2): p. 295-301.
150. Wills, J.B., K.J. Knox, and J.P. Reid, *Optical Control and Characterisation of Aerosol*. Chemical Physics Letters, 2009. **481**(4): p. 153-165.
151. Albani, L.A.F., *Estimation of the Evaporation Rate of an Isolated Water Microdroplet Subjected to Infrared Radiative Heating*. 2014, University of Alberta.
152. Choi, C.H., et al., *Synthesis of Monodispersed Microspheres from Laplace Pressure Induced Droplets in Micromolds*. Advanced Materials, 2012. **24**(37): p. 5078-5082.
153. Roger, K., R. Botet, and B. Cabane, *Coalescence of Repelling Colloidal Droplets: A Route to Monodisperse Populations*. Langmuir, 2013. **29**(19): p. 5689-5700.
154. Seemann, R., et al., *Droplet Based Microfluidics*. Reports on Progress in Physics, 2012. **75**(1): p. 016601.
155. Azhdarzadeh, M., et al., *An Atomizer to Generate Monodisperse Droplets from High Vapor Pressure Liquids*. Atomization and Sprays, 2016. **26**(2).
156. Baldelli, A., et al., *Analysis of the Particle Formation Process of Structured Microparticles*. Molecular Pharmaceutics, 2015. **12**(8): p. 2562-2573.
157. Minov, S.V., et al., *Droplet Generation and Characterization Using a Piezoelectric Droplet Generator and High Speed Imaging Techniques*. Crop Protection, 2015. **69**: p. 18-27.
158. Shekunov, B.Y. and P. York, *Crystallization Processes in Pharmaceutical Technology and Drug Delivery Design*. Journal of Crystal Growth, 2000. **211**(1): p. 122-136.
159. Verboket, P.E., et al., *A New Microfluidics Based Droplet Dispenser for Icp-Ms*. Analytical Chemistry, 2014.
160. Snyder, G.J. *Complex Thermoelectric Materials*. in *Frontiers in Electronic Materials: A Collection of Extended Abstracts of the Nature Conference Frontiers in Electronic Materials, June 17 to 20 2012, Aachen, Germany*. 2015: Wiley Online Library.
161. Jia, Q., C. Miers, and A. Marconnet, *3d Printing Nanostructured Thermoelectric Device*. 2015.
162. Koltay, P. and R. Zengerle. *Non-Contact Nanoliter & Picoliter Liquid Dispensing*. in *Solid-State Sensors, Actuators and Microsystems Conference, 2007*. Transducers 2007. International. 2007: IEEE.
163. Komijani, M., J. Reddy, and M. Eslami, *Nonlinear Analysis of Microstructure-Dependent Functionally Graded Piezoelectric Material Actuators*. Journal of the Mechanics and Physics of Solids, 2014. **63**: p. 214-227.
164. Jaffe, B., *Piezoelectric Ceramics*. Vol. 3. 2012: Elsevier.
165. Mohammadi, M., et al., *Synthesis and Crystallization of Lead-Zirconium-Titanate (Pzt) Nanotubes at the Low Temperature Using Carbon Nanotubes (Cnts) as Sacrificial Templates*. Advanced Powder Technology, 2012. **23**(5): p. 647-654.
166. Kosch, S. and N. Ashgriz, *Note: A Simple Vibrating Orifice Monodisperse Droplet Generator Using a Hard Drive Actuator Arm*. Review of Scientific Instruments, 2015. **86**(4): p. 046101.

167. Aliño, V.J., et al., *Inkjet Printing and Release of Monodisperse Liquid Crystal Droplets from Solid Surfaces*. *Langmuir*, 2012. **28**(41): p. 14540-14546.
168. Kishi, T., et al., *Microdroplet Generation Using an Ultrasonic Torsional Transducer Which Has a Micropore with a Tapered Nozzle*. *Archive of Applied Mechanics*, 2015: p. 1-12.
169. Lu, S., et al., *Nozzle and Needle During High Viscosity Adhesive Jetting Based on Piezoelectric Jet Dispensing*. *Smart Materials and Structures*, 2015. **24**(10): p. 105023.
170. Raman, I., et al. *Viscosity Effect on Piezoelectric Actuated Nozzle in Generating Micro Droplet*. in *Advanced Materials Research*. 2013: Trans Tech Publ.
171. Zhang, A.L. and Q.J. Han. *The Generation of Droplets with Micro-Liter Volume Using Surface Acoustic Wave*. in *Advanced Materials Research*. 2012: Trans Tech Publ.
172. Wen, Y., G. Deng, and C. Zhou. *Simulation Analysis of Jet Dispenser Based on Piezoelectric Actuators*. in *Electronic Packaging Technology (ICEPT), 2014 15th International Conference on*. 2014: IEEE.
173. Chahal, D., A. Ahmadi, and K.C. Cheung, *Improving Piezoelectric Cell Printing Accuracy and Reliability through Neutral Buoyancy of Suspensions*. *Biotechnology and Bioengineering*, 2012. **109**(11): p. 2932-2940.
174. Trimby, P.W., *Orientation Mapping of Nanostructured Materials Using Transmission Kikuchi Diffraction in the Scanning Electron Microscope*. *Ultramicroscopy*, 2012. **120**: p. 16-24.
175. Cubillas, P. and M.W. Anderson, *Atomic Force Microscopy*. *Multi Length-Scale Characterisation*, 2013: p. 121-193.
176. Bhushan, B. and M.L. Palacio, *Atomic Force Microscopy*, in *Encyclopedia of Nanotechnology*. 2012, Springer. p. 146-160.
177. Rigort, A., et al., *Focused Ion Beam Micromachining of Eukaryotic Cells for Cryoelectron Tomography*. *Proceedings of the National Academy of Sciences*, 2012. **109**(12): p. 4449-4454.
178. Fox, D., et al., *Helium Ion Microscopy of Graphene: Beam Damage, Image Quality and Edge Contrast*. *Nanotechnology*, 2013. **24**(33): p. 335702.
179. Ferrari, A.C. and D.M. Basko, *Raman Spectroscopy as a Versatile Tool for Studying the Properties of Graphene*. *Nature Nanotechnology*, 2013. **8**(4): p. 235-246.
180. Wang, H., et al., *Low-Frequency Shift Dispersive Raman Spectroscopy for the Analysis of Respirable Dosage Forms*. *International Journal of Pharmaceutics*, 2014. **469**(1): p. 197-205.
181. Wang, H., et al., *Quantitative Macro-Raman Spectroscopy on Microparticle-Based Pharmaceutical Dosage Forms*. *Applied Spectroscopy*, 2015. **69**(7): p. 823-833.
182. Beck-Broichsitter, M., et al., *Characterization of Novel Spray-Dried Polymeric Particles for Controlled Pulmonary Drug Delivery*. *Journal of Controlled Release*, 2012. **158**(2): p. 329-335.
183. Zhou, Q.T. and D.A. Morton, *Drug–Lactose Binding Aspects in Adhesive Mixtures: Controlling Performance in Dry Powder Inhaler Formulations by Altering Lactose Carrier Surfaces*. *Advanced Drug Delivery Reviews*, 2012. **64**(3): p. 275-284.
184. Geller, D.E., J. Weers, and S. Heuerding, *Development of an Inhaled Dry-Powder Formulation of Tobramycin Using Pulmosphere™ Technology*. *Journal of Aerosol Medicine and Pulmonary Drug Delivery*, 2011. **24**(4): p. 175-182.

185. Liu, L., et al., *Curcumin Loaded Polymeric Micelles Inhibit Breast Tumor Growth and Spontaneous Pulmonary Metastasis*. International Journal of Pharmaceutics, 2013. **443**(1): p. 175-182.
186. Raftery, T.D., et al., *Discrete Nanoparticles Induce Loss of Legionella Pneumophila Biofilms from Surfaces*. Nanotoxicology, 2014. **8**(5): p. 477-484.
187. Cipolla, D., I. Gonda, and H.-K. Chan, *Liposomal Formulations for Inhalation*. Therapeutic delivery, 2013. **4**(8): p. 1047-1072.
188. Mandal, B., et al., *Core-Shell-Type Lipid-Polymer Hybrid Nanoparticles as a Drug Delivery Platform*. Nanomedicine: Nanotechnology, Biology and Medicine, 2013. **9**(4): p. 474-491.
189. Ling, T.Y., J. Wang, and D.Y. Pui, *Measurement of Retention Efficiency of Filters against Nanoparticles in Liquids Using an Aerosolization Technique*. Environmental Science & Technology, 2009. **44**(2): p. 774-779.
190. Son, Y.-J., P. Worth Longest, and M. Hindle, *Aerosolization Characteristics of Dry Powder Inhaler Formulations for the Excipient Enhanced Growth (Eeg) Application: Effect of Spray Drying Process Conditions on Aerosol Performance*. International Journal of Pharmaceutics, 2013. **443**(1): p. 137-145.
191. Dennehy, R.D., *Particle Engineering Using Power Ultrasound I*. Organic Process Research & Development, 2003. **7**(6): p. 1002-1006.
192. Schafroth, N., et al., *Nano and Microparticle Engineering of Water Insoluble Drugs Using a Novel Spray-Drying Process*. Colloids and Surfaces B: Biointerfaces, 2012. **90**: p. 8-15.
193. Vicente, J., et al., *Fundamental Analysis of Particle Formation in Spray Drying*. Powder Technology, 2013. **247**: p. 1-7.
194. Handscomb, C., M. Kraft, and A. Bayly, *A New Model for the Drying of Droplets Containing Suspended Solids after Shell Formation*. Chemical Engineering Science, 2009. **64**(2): p. 228-246.
195. Nandiyanto, A.B.D. and K. Okuyama, *Progress in Developing Spray-Drying Methods for the Production of Controlled Morphology Particles: From the Nanometer to Submicrometer Size Ranges*. Advanced Powder Technology, 2011. **22**(1): p. 1-19.
196. Anwar, S.H. and B. Kunz, *The Influence of Drying Methods on the Stabilization of Fish Oil Microcapsules: Comparison of Spray Granulation, Spray Drying, and Freeze Drying*. Journal of Food Engineering, 2011. **105**(2): p. 367-378.
197. Cabane, B., S. Blanchon, and C. Neves, *Recombination of Nanometric Vesicles During Freeze-Drying*. Langmuir, 2006. **22**(5): p. 1982-1990.
198. Mumenthaler, M. and H. Leuenberger, *Atmospheric Spray-Freeze Drying: A Suitable Alternative in Freeze-Drying Technology*. International Journal of Pharmaceutics, 1991. **72**(2): p. 97-110.
199. Parsian, A.R., et al., *Inhalable Budesonide Porous Microparticles Tailored by Spray Freeze Drying Technique*. Powder Technology, 2014. **260**: p. 36-41.
200. García-González, C. and I. Smirnova, *Use of Supercritical Fluid Technology for the Production of Tailor-Made Aerogel Particles for Delivery Systems*. The Journal of Supercritical Fluids, 2013. **79**: p. 152-158.
201. Matson, D.W. and R.D. Smith, *Supercritical Fluid Technologies for Ceramic-Processing Applications*. Journal of the American Ceramic Society, 1989. **72**(6): p. 871-881.
202. Philippot, G., et al., *Supercritical Fluid Technology: A Reliable Process for High Quality Batio< Sub> 3</Sub> Based Nanomaterials*. Advanced Powder Technology, 2014.

203. Yoon, S.-D. and H.-S. Byun, *Molecularly Imprinted Polymers for Selective Separation of Acetaminophen and Aspirin by Using Supercritical Fluid Technology*. Chemical Engineering Journal, 2013. **226**: p. 171-180.
204. Liu, X., et al., *Study on Micro-Crystallization, Growth, Optical Properties and Defects of a Nonlinear Optical Crystal: MnHg (Scn)₄*. Journal of Crystal Growth, 2011. **317**(1): p. 92-97.
205. Redinova, T., [*Microcrystallization of the Saliva in Children Following Carbohydrate Intake and the Performance of Caries Prophylactic Measures*]. Stomatologia, 1988. **68**(4): p. 62-63.
206. Sun, G., et al., *Nucleation Kinetics, Micro-Crystallization and Etching Studies of L-Histidine Trifluoroacetate Crystal*. Journal of Crystal Growth, 2011. **316**(1): p. 132-136.
207. Wang, H., et al., *Micro-Crystallization of the Infrared Transmitting Chalcogenide Glass in GeSe₂-as₂Se₃-Pbse System*. Ceramics International, 2009. **35**(1): p. 83-86.
208. Kumar, S., R. Gokhale, and D.J. Burgess, *Quality by Design Approach to Spray Drying Processing of Crystalline Nanosuspensions*. International Journal of Pharmaceutics, 2014. **464**(1): p. 234-242.
209. Saffari, M. and T. Langrish, *Effect of Lactic Acid in-Process Crystallization of Lactose/Protein Powders During Spray Drying*. Journal of Food Engineering, 2014. **137**: p. 88-94.
210. Waldron, K., et al., *Formation of Monodisperse Mesoporous Silica Microparticles Via Spray-Drying*. Journal of Colloid and Interface Science, 2014. **418**: p. 225-233.
211. Odziomek, M., T.R. Sosnowski, and L. Gradoń, *Conception, Preparation and Properties of Functional Carrier Particles for Pulmonary Drug Delivery*. International Journal of Pharmaceutics, 2012. **433**(1): p. 51-59.
212. Bück, A., S. Palis, and E. Tsotsas, *Model-Based Control of Particle Properties in Fluidised Bed Spray Granulation*. Powder Technology, 2014.
213. Gradon, L. and T.R. Sosnowski, *Formation of Particles for Dry Powder Inhalers*. Advanced Powder Technology, 2014. **25**(1): p. 43-55.
214. Paudel, A., et al., *Manufacturing of Solid Dispersions of Poorly Water Soluble Drugs by Spray Drying: Formulation and Process Considerations*. International Journal of Pharmaceutics, 2013. **453**(1): p. 253-284.
215. Chen, W.-H., S.-M. Chen, and C.-I. Hung, *Carbon Dioxide Capture by Single Droplet Using Selexol, Rectisol and Water as Absorbents: A Theoretical Approach*. Applied Energy, 2013. **111**: p. 731-741.
216. Davies, J.F., et al., *Influence of Organic Films on the Evaporation and Condensation of Water in Aerosol*. Proceedings of the National Academy of Sciences, 2013. **110**(22): p. 8807-8812.
217. Kracek, F., E. Posnjak, and S. Hendricks, *Gradual Transition in Sodium Nitrate. Ii. The Structure at Various Temperatures and Its Bearing on Molecular Rotation*. Journal of the American Chemical Society, 1931. **53**(9): p. 3339-3348.
218. Pechkova, E., et al., *Nanoprobe Nappa Arrays for the Nanoconductimetric Analysis of Ultra-Low-Volume Protein Samples Using Piezoelectric Liquid Dispensing Technology*. NanoWorld J, 2015. **1**(1): p. 26-31.

219. Ali Al Zaitone, B. and C. Tropea, *Evaporation of Pure Liquid Droplets: Comparison of Droplet Evaporation in an Acoustic Field Versus Glass-Filament*. Chemical Engineering Science, 2011. **66**(17): p. 3914-3921.
220. Duprat, C., et al., *Evaporation of Drops on Two Parallel Fibers: Influence of the Liquid Morphology and Fiber Elasticity*. Langmuir, 2013. **29**(25): p. 7857-7863.
221. Tóth, T., et al., *Suspension of Water Droplets on Individual Pillars*. Langmuir, 2011. **27**(8): p. 4742-4748.
222. Chen, W.-H., M.-H. Tsai, and C.-I. Hung, *Numerical Prediction of Coagulation Capture Process by a Single Droplet in Alkaline Spray*. Applied Energy, 2013. **109**: p. 125-134.
223. Crowe, C.T., M. Sharma, and D.E. Stock, *The Particle-Source-in Cell (Psi-Cell) Model for Gas-Droplet Flows*. Journal of Fluids Engineering, 1977. **99**(2): p. 325-332.
224. Fakhari, A. and T. Lee, *Multiple-Relaxation-Time Lattice Boltzmann Method for Immiscible Fluids at High Reynolds Numbers*. Physical Review E, 2013. **87**(2): p. 023304.
225. Jalaal, M. and K. Mehrvaran, *Fragmentation of Falling Liquid Droplets in Bag Breakup Mode*. International Journal of Multiphase Flow, 2012. **47**: p. 115-132.
226. Berglund, R.N. and B.Y. Liu, *Generation of Monodisperse Aerosol Standards*. Environmental Science & Technology, 1973. **7**(2): p. 147-153.
227. Li, Y., S. Zhang, and J. Li, *Indirect-Mode Jet Pulse Spray System Design and Monodisperse Droplets Generation*. Chemical Engineering Science, 2012. **68**(1): p. 461-468.
228. Rogers, S., et al., *Particle Shrinkage and Morphology of Milk Powder Made with a Monodisperse Spray Dryer*. Biochemical Engineering Journal, 2012. **62**: p. 92-100.
229. Bararnia, H., et al., *Numerical Investigation of the Coalescence and Breakup of Falling Multi-Droplets*. Colloids and Surfaces A: Physicochemical and Engineering Aspects, 2013. **424**: p. 40-51.
230. Caiazza, G., et al., *Seawater Scrubbing Desulfurization: A Model for So₂ Absorption in Fall-Down Droplets*. Environmental Progress & Sustainable Energy, 2012. **31**(2): p. 277-287.
231. Elperin, T., A. Fominykh, and B. Krasovitev, *Non-Isothermal Scavenging of Highly Soluble Gaseous Pollutants by Rain in the Atmosphere with Non-Uniform Vertical Concentration and Temperature Distributions*. Meteorology and Atmospheric Physics, 2014: p. 1-15.
232. Frackowiak, B., et al., *Numerical Analysis of the Interactions between Evaporating Droplets in a Monodisperse Stream*. International Journal of Heat and Mass Transfer, 2010. **53**(7): p. 1392-1401.
233. Sazhin, S., *Heating and Evaporation of Monocomponent Droplets*, in *Droplets and Sprays*. 2014, Springer. p. 97-142.
234. Vladisavljević, G., I. Kobayashi, and M. Nakajima, *Production of Uniform Droplets Using Membrane, Microchannel and Microfluidic Emulsification Devices*. Microfluidics and Nanofluidics, 2012. **13**(1): p. 151-178.
235. Rogers, S., et al., *A Monodisperse Spray Dryer for Milk Powder: Modelling the Formation of Insoluble Material*. Chemical Engineering Science, 2012. **71**: p. 75-84.
236. Frederickson, C.J., et al. *Applications of Fluid Microjets to Medical and Dental Laser Procedures*. in *Photonics West'95*. 1995: International Society for Optics and Photonics.

237. Parsa, S., et al., *Effects of Surfactant and Gentle Agitation on Inkjet Dispensing of Living Cells*. Biofabrication, 2010. **2**(2): p. 025003.
238. Scoutaris, N., et al., *Inkjet Printing as a Novel Medicine Formulation Technique*. Journal of Controlled Release, 2011. **156**(2): p. 179-185.
239. Velichko, Y.S., P.G. Khalatur, and A.R. Khokhlov, *Molecular Dispenser: Conformation-Dependent Design Approach*. Macromolecules, 2003. **36**(14): p. 5047-5050.
240. Sgro, A.E., P.B. Allen, and D.T. Chiu, *Thermoelectric Manipulation of Aqueous Droplets in Microfluidic Devices*. Analytical chemistry, 2007. **79**(13): p. 4845-4851.
241. Zhu, Y. and B.E. Power, *Lab-on-a-Chip in Vitro Compartmentalization Technologies for Protein Studies*, in *Protein-Protein Interaction*. 2008, Springer. p. 81-114.
242. Riefler, N. and T. Wriedt, *Generation of Monodisperse Micron-Sized Droplets Using Free Adjustable Signals*. Particle & Particle Systems Characterization, 2008. **25**(2): p. 176-182.
243. Lind, T., S. Danner, and S. Guentay, *Monodisperse Fine Aerosol Generation Using Fluidized Bed*. Powder Technology, 2010. **199**(3): p. 232-237.
244. Liu, B.Y. and J.K. Agarwal, *Experimental Observation of Aerosol Deposition in Turbulent Flow*. Journal of Aerosol Science, 1974. **5**(2): p. 145-155.
245. Rajagopalan, V., E. Grulke, and A. Ray, *Generation of Multicomponent Polymer Particles Using Microdroplet Evaporation Technique*. Chemical Engineering, 2011. **24**.
246. Shemirani, F.M., et al., *A Continuous, Monodisperse Propellant Microdroplet Stream as a Model System for Laser Analysis of Mass Transfer in Metered Dose Inhaler Sprays*.
247. Tracey, P.J., et al., *Rapid Profiling of Laser-Induced Photochemistry in Single Microdroplets Using Mass Spectrometry*. Analytical Chemistry, 2014. **86**(6): p. 2895-2899.
248. Ashgriz, N. and S. Yao, *Development of a Controlled Spray Generator*. Review of Scientific Instruments, 1987. **58**(7): p. 1291-1296.
249. Huang, C., et al., *A Controlled Release System of Biomacromolecules by Encapsulating Nanoparticles in Electrospun Cellulose Acetate Butyrate Nanofibers*. Journal of Controlled Release: Official Journal of the Controlled Release Society, 2013. **172**(1): p. e99.
250. Keraliya, R.A., et al., *Osmotic Drug Delivery System as a Part of Modified Release Dosage Form*. ISRN Pharmaceutics, 2012. **2012**.
251. Nibha, K.P. and S. Pancholi, *An Overview On: Sublingual Route for Systemic Drug Delivery*. Int. J. Res. Pharmaceut. Biomed. Sci., 2012. **3**: p. 913-923.
252. Vehring, R., *Berechnung Des Verdunstungsprozesses Von Monodispersen Aerosolpartikeln*, in *Diplomarbeit (diploma thesis), Universität Gesamthochschule Duisburg*. 1989, Universität Gesamthochschule: Duisburg, Germany.
253. Lee, K., et al., *Sem/Eds Evaluation of Porcelain Adherence to Gold-Coated Cast Titanium*. Journal of Biomedical Materials Research Part B: Applied Biomaterials, 2004. **68**(2): p. 165-173.
254. Everhart, T.E. and T.L. Hayes, *Scanning Electron Microscope*. 1973: The Council.
255. Watkins, R., et al., *Focused Ion Beam Milling*. Vacuum, 1986. **36**(11): p. 961-967.
256. Watson, J.T.R., R. Basu, and J.V. Sengers, *An Improved Representative Equation for the Dynamic Viscosity of Water Substance*. Journal of Physical and Chemical Reference Data, 1980. **9**(4): p. 1255-1290.
257. Lightman, A.P., *Problem Book in Relativity and Gravitation*. 1975: Princeton University Press.

258. Vehring, R., *Pharmaceutical Particle Engineering Via Spray Drying*. Pharmaceutical Research, 2008. **25**(5): p. 999-1022.
259. Verros, G. and N. Malamataris, *Estimation of Diffusion Coefficients in Acetone-Cellulose Acetate Solutions*. Industrial & Engineering Chemistry Research, 1999. **38**(9): p. 3572-3580.
260. Petit, C., T. Zemb, and M. Pileni, *Structural Study of Microemulsion-Based Gels at the Saturation Point*. Langmuir, 1991. **7**(2): p. 223-231.
261. Edward, J.T., *Molecular Volumes and the Stokes-Einstein Equation*. Journal of Chemical Education, 1970. **47**(4): p. 261.
262. Beckwith, T.G., R.D. Marangoni, and J.H. Lienhard, *Mechanical Measurements*. 2007: Pearson Prentice Hall.
263. Meng, F., M. Doi, and Z. Ouyang, *Cavitation in Drying Droplets of Soft Matter Solutions*. Physical Review Letters, 2014. **113**(9): p. 098301.
264. Baldelli, A., et al., *Effect of Crystallization Kinetics on the Properties of Spray Dried Microparticles*. Aerosol Science and Technology, 2016(just-accepted): p. 00-00.
265. Garcia, A., et al., *Microfabricated Engineered Particle Systems for Respiratory Drug Delivery and Other Pharmaceutical Applications*. Journal of Drug Delivery, 2012. **2012**.
266. Wachtel, H., *Respiratory Drug Delivery*, in *Microsystems for Pharmatechnology*. 2016, Springer. p. 257-274.
267. Labiris, N. and M. Dolovich, *Pulmonary Drug Delivery. Part I: Physiological Factors Affecting Therapeutic Effectiveness of Aerosolized Medications*. British Journal of Clinical Pharmacology, 2003. **56**(6): p. 588-599.
268. Everard, M.L., A.R. Clark, and A.D. Milner, *Drug Delivery from Jet Nebulisers*. Archives of Disease in Childhood, 1992. **67**(5): p. 586-591.
269. Park, C.-W., et al., *Advanced Spray-Dried Design, Physicochemical Characterization, and Aerosol Dispersion Performance of Vancomycin and Clarithromycin Multifunctional Controlled Release Particles for Targeted Respiratory Delivery as Dry Powder Inhalation Aerosols*. International Journal of Pharmaceutics, 2013. **455**(1): p. 374-392.
270. Zhu, B., et al., *The Solid-State and Morphological Characteristics of Particles Generated from Solution-Based Metered Dose Inhalers: Influence of Ethanol Concentration and Intrinsic Drug Properties*. Colloids and Surfaces A: Physicochemical and Engineering Aspects, 2014. **443**: p. 345-355.
271. Byrn, S., et al., *Solid-State Pharmaceutical Chemistry*. Chemistry of Materials, 1994. **6**(8): p. 1148-1158.
272. Sou, T., et al., *The Effect of Amino Acid Excipients on Morphology and Solid-State Properties of Multi-Component Spray-Dried Formulations for Pulmonary Delivery of Biomacromolecules*. European Journal of Pharmaceutics and Biopharmaceutics, 2013. **83**(2): p. 234-243.
273. Ticehurst, M.D. and I. Marziano, *Integration of Active Pharmaceutical Ingredient Solid Form Selection and Particle Engineering into Drug Product Design*. Journal of Pharmacy and Pharmacology, 2015. **67**(6): p. 782-802.
274. Ye, X., et al., *In Situ Microscopic Observation of the Crystallization Process of Molecular Microparticles by Fluorescence Switching*. Angewandte Chemie, 2015. **127**(127): p. 8087-8091.
275. Al Zaitone, B. and A. Lamprecht, *Single Droplet Drying Step Characterization in Microsphere Preparation*. Colloids and Surfaces B: Biointerfaces, 2013. **105**: p. 328-334.

276. Liu, W., et al., *A Single Step Assembly of Uniform Microparticles for Controlled Release Applications*. *Soft Matter*, 2011. **7**(7): p. 3323-3330.
277. Liu, W., et al., *Facile Spray-Drying Assembly of Uniform Microencapsulates with Tunable Core-Shell Structures and Controlled Release Properties*. *Langmuir*, 2011. **27**(21): p. 12910-12915.
278. Lehmann, S., et al., *Experimental Analysis and Semicontinuous Simulation of Low-Temperature Droplet Evaporation of Multicomponent Fuels*. *Experiments in Fluids*, 2015. **56**(1): p. 1-12.
279. Chen, W.-H., Y.-L. Hou, and C.-I. Hung, *A Theoretical Analysis of the Capture of Greenhouse Gases by Single Water Droplet at Atmospheric and Elevated Pressures*. *Applied Energy*, 2011. **88**(12): p. 5120-5130.
280. Wegener, M., N. Paul, and M. Kraume, *Fluid Dynamics and Mass Transfer at Single Droplets in Liquid/Liquid Systems*. *International Journal of Heat and Mass Transfer*, 2014. **71**: p. 475-495.
281. Hopkins, R.J., et al., *Control and Characterisation of a Single Aerosol Droplet in a Single-Beam Gradient-Force Optical Trap*. *Physical Chemistry Chemical Physics*, 2004. **6**(21): p. 4924-4927.
282. Ashkin, A. and J. Dziedzic, *Optical Levitation of Liquid Drops by Radiation Pressure*. *Science*, 1975. **187**(4181): p. 1073-1075.
283. Davis, E.J., *A History of Single Aerosol Particle Levitation*. *Aerosol Science and Technology*, 1997. **26**(3): p. 212-254.
284. Schweiger, G., *Raman Scattering on Single Aerosol Particles and on Flowing Aerosols: A Review*. *Journal of Aerosol Science*, 1990. **21**(4): p. 483-509.
285. McGloin, D., *Optical Tweezers: 20 Years On*. *Philosophical Transactions of the Royal Society of London A: Mathematical, Physical and Engineering Sciences*, 2006. **364**(1849): p. 3521-3537.
286. Hargreaves, G., et al., *Measurements of the Equilibrium Size of Supersaturated Aqueous Sodium Chloride Droplets at Low Relative Humidity Using Aerosol Optical Tweezers and an Electrodynamic Balance*. *The Journal of Physical Chemistry A*, 2010. **114**(4): p. 1806-1815.
287. Knox, K.J., et al., *Observation of Bistability of Trapping Position in Aerosol Optical Tweezers*. *JOSA B*, 2010. **27**(3): p. 582-591.
288. Miles, R.E., et al., *Retrieval of the Complex Refractive Index of Aerosol Droplets from Optical Tweezers Measurements*. *Physical Chemistry Chemical Physics*, 2012. **14**(9): p. 3037-3047.
289. Iida, K., et al., *Inkjet Aerosol Generator as Monodisperse Particle Number Standard*. *Aerosol Science and Technology*, 2014. **48**(8): p. 789-802.
290. Zheng, X.-S., et al., *Laser Power Dependent Surface-Enhanced Raman Spectroscopic Study of 4-Mercaptopyridine on Uniform Gold Nanoparticle-Assembled Substrates*. *The Journal of Physical Chemistry C*, 2014. **118**(7): p. 3750-3757.
291. Doan, T.H. and J. Sangster, *Viscosities of Concentrated Aqueous Solutions of Some 1: 1, 2: 1, and 3: 1 Nitrates at 25. Degree. C*. *Journal of Chemical and Engineering Data*, 1981. **26**(2): p. 141-144.
292. Isono, T., *Density, Viscosity, and Electrolytic Conductivity of Concentrated Aqueous Electrolyte Solutions at Several Temperatures. Alkaline-Earth Chlorides, Lanthanum Chloride, Sodium Chloride, Sodium Nitrate, Sodium Bromide, Potassium Nitrate,*

- Potassium Bromide, and Cadmium Nitrate*. Journal of Chemical and Engineering Data, 1984. **29**(1): p. 45-52.
293. Mahiuddin, S. and K. Ismail, *Temperature and Concentration Dependence of the Viscosity of Aqueous Sodium Nitrate and Sodium Thiosulphate Electrolytic Systems*. Fluid Phase Equilibria, 1996. **123**(1): p. 231-243.
294. Belotti, S., et al., *Spray-Dried Amikacin Sulphate Powder for Inhalation in Cystic Fibrosis Patients: The Role of Ethanol in Particle Formation*. European Journal of Pharmaceutics and Biopharmaceutics, 2015. **93**: p. 165-172.
295. Castillo, J.L., et al., *Morphology and Nanostructure of Granular Materials Built from Nanoparticles*. Kona Powder and Particle Journal, 2014(31): p. 214-233.
296. Nuzzo, M., et al., *Surface Composition and Morphology of Particles Dried Individually and by Spray Drying*. Drying Technology, 2014. **33**(6): p. 757-767.
297. Ohtori, N. and Y. Ishii, *Explicit Expression for the Stokes-Einstein Relation for Pure Lennard-Jones Liquids*. Physical Review E, 2015. **91**(1): p. 012111.
298. Sata, T., *Studies on Anion Exchange Membranes Having Permselectivity for Specific Anions in Electrodialysis—Effect of Hydrophilicity of Anion Exchange Membranes on Permselectivity of Anions*. Journal of Membrane Science, 2000. **167**(1): p. 1-31.
299. Power, R., et al., *The Transition from Liquid to Solid-Like Behaviour in Ultrahigh Viscosity Aerosol Particles*. Chemical Science, 2013. **4**(6): p. 2597-2604.
300. Tang, I. and H. Munkelwitz, *Water Activities, Densities, and Refractive Indices of Aqueous Sulfates and Sodium Nitrate Droplets of Atmospheric Importance*. Journal of Geophysical Research: Atmospheres (1984–2012), 1994. **99**(D9): p. 18801-18808.
301. Payne, S., et al., *A Neutron Diffraction Study of the Order-Disorder Phase Transition in Sodium Nitrate*. Journal of Physics: Condensed Matter, 1997. **9**(11): p. 2423.
302. Shen, T., et al., *Order-Disorder Phenomenon in Sodium Nitrate Studied by Low-Frequency Raman Scattering*. Physical Review B, 1975. **12**(10): p. 4530.
303. Feng, A., et al., *Mechanistic Models Facilitate Efficient Development of Leucine Containing Microparticles for Pulmonary Drug Delivery*. International Journal of Pharmaceutics, 2011. **409**(1): p. 156-163.
304. Holden, A. and P. Morrison, *Crystals and Crystal Growing*. 1982: MIT press.
305. Sadafi, M., et al., *A Theoretical Model with Experimental Verification for Heat and Mass Transfer of Saline Water Droplets*. International Journal of Heat and Mass Transfer, 2015. **81**: p. 1-9.
306. Power, R., et al., *Observation of the Binary Coalescence and Equilibration of Micrometer-Sized Droplets of Aqueous Aerosol in a Single-Beam Gradient-Force Optical Trap*. The Journal of Physical Chemistry A, 2012. **116**(35): p. 8873-8884.
307. Power, R.M. and J.P. Reid, *Probing the Micro-Rheological Properties of Aerosol Particles Using Optical Tweezers*. Reports on Progress in Physics, 2014. **77**(7): p. 074601.
308. Bzdek, B.R., et al., *Precise, Contactless Measurements of the Surface Tension of Picolitre Aerosol Droplets*. Chemical Science, 2015(7): p. 274-285.
309. Clegg, S.B.P. *Extended Aim Aerosol Thermodynamics Model*. 2014.
310. Clegg, W., et al., *Publications: W. Clegg 1998*. Chem. Commun, 1998. **23**: p. 24.
311. Tang, I. and H. Munkelwitz, *Simultaneous Determination of Refractive Index and Density of an Evaporating Aqueous Solution Droplet*. Aerosol Science and Technology, 1991. **15**(3): p. 201-207.

312. Prokopovich, P. and S. Perni, *Comparison of Jkr-and Dmt-Based Multi-Asperity Adhesion Model: Theory and Experiment*. Colloids and Surfaces A: Physicochemical and Engineering Aspects, 2011. **383**(1): p. 95-101.
313. Rabinovitch, O., *An Extended High Order Cohesive Interface Approach to the Debonding Analysis of Frp Strengthened Beams*. International Journal of Mechanical Sciences, 2014. **81**: p. 1-16.
314. Rumpf, H. and H. Schubert, *Adhesion Forces in Agglomeration Processes*. Onada & Hench: Ceramic Processing Before Firing, J. Wiley a. Sons, Inc., London, 1978.
315. d'Angelo, I., et al., *Pulmonary Drug Delivery: A Role for Polymeric Nanoparticles?* Current Topics in Medicinal Chemistry, 2015. **15**(4): p. 386-400.
316. de Boer, A.H. and P. Hagedoorn, *The Role of Disposable Inhalers in Pulmonary Drug Delivery*. Expert Opinion on Drug Delivery, 2015. **12**(1): p. 143-157.
317. Kim, S.Y., et al., *The Future Perspectives of Natural Materials for Pulmonary Drug Delivery and Lung Tissue Engineering*. Expert Opinion on Drug Delivery, 2015(0): p. 1-19.
318. Yang, M.Y., J.G.Y. Chan, and H.-K. Chan, *Pulmonary Drug Delivery by Powder Aerosols*. Journal of Controlled Release, 2014. **193**: p. 228-240.
319. Kuzmov, A. and T. Minko, *Nanotechnology Approaches for Inhalation Treatment of Lung Diseases*. Journal of Controlled Release, 2015(219): p. 500-518.
320. Bertrand, N. and J.-C. Leroux, *The Journey of a Drug-Carrier in the Body: An Anatomico-Physiological Perspective*. Journal of Controlled Release, 2012. **161**(2): p. 152-163.
321. Hein, S., et al., *A New Pharmaceutical Aerosol Deposition Device on Cell Cultures (Paddoc) to Evaluate Pulmonary Drug Absorption for Metered Dose Dry Powder Formulations*. European Journal of Pharmaceutics and Biopharmaceutics, 2011. **77**(1): p. 132-138.
322. Liang, Z., et al., *Recent Advances in Controlled Pulmonary Drug Delivery*. Drug Discovery Today, 2015. **20**(3): p. 380-389.
323. Secret, E., et al., *Matrix Metalloproteinase-Sensitive Hydrogel Microparticles for Pulmonary Drug Delivery of Small Molecule Drugs or Proteins*. Journal of Materials Chemistry B, 2015. **3**(27): p. 5629-5634.
324. Kaialy, W. and A. Nokhodchi, *Freeze-Dried Mannitol for Superior Pulmonary Drug Delivery Via Dry Powder Inhaler*. Pharmaceutical Research, 2013. **30**(2): p. 458-477.
325. Ernsting, M.J., et al., *Factors Controlling the Pharmacokinetics, Biodistribution and Intratumoral Penetration of Nanoparticles*. Journal of Controlled Release, 2013. **172**(3): p. 782-794.
326. Edwards, D.A., et al., *Large Porous Particles for Pulmonary Drug Delivery*. Science, 1997. **276**(5320): p. 1868-1872.
327. Crowder, T.M., et al., *Fundamental Effects of Particle Morphology on Lung Delivery: Predictions of Stokes' Law and the Particular Relevance to Dry Powder Inhaler Formulation and Development*. Pharmaceutical Research, 2002. **19**(3): p. 239-245.
328. Lee, H. and J. Lee, *Confined Crystallization of Drug in Directionally Freeze-Dried Water-Soluble Template*. Journal of Industrial and Engineering Chemistry, 2015. **21**: p. 1183-1190.
329. Puurunen, R.L., et al., *Controlling the Crystallinity and Roughness of Atomic Layer Deposited Titanium Dioxide Films*. Journal of Nanoscience and Nanotechnology, 2011. **11**(9): p. 8101-8107.

330. Salama, R., et al., *Preparation and Characterisation of Controlled Release Co-Spray Dried Drug-Polymer Microparticles for Inhalation I: Influence of Polymer Concentration on Physical and in Vitro Characteristics*. European Journal of Pharmaceutics and Biopharmaceutics, 2008. **69**(2): p. 486-495.
331. Hickey, A.J., *Controlled Delivery of Inhaled Therapeutic Agents*. Journal of Controlled Release, 2014. **190**: p. 182-188.
332. D'Sa, D., H.-K. Chan, and W. Chrzanowski, *Predicting Physical Stability in Pressurized Metered Dose Inhalers Via Dwell and Instantaneous Force Colloidal Probe Microscopy*. European Journal of Pharmaceutics and Biopharmaceutics, 2014. **88**(1): p. 129-135.
333. Elzoghby, A.O., W.M. Samy, and N.A. Elgindy, *Albumin-Based Nanoparticles as Potential Controlled Release Drug Delivery Systems*. Journal of Controlled Release, 2012. **157**(2): p. 168-182.
334. Muhammad, S.A.F.a.S., et al., *A Novel Method for the Production of Crystalline Micronised Particles*. International Journal of Pharmaceutics, 2010. **388**(1): p. 114-122.
335. Vehkamäki, H. and I. Riipinen, *Thermodynamics and Kinetics of Atmospheric Aerosol Particle Formation and Growth*. Chemical Society Reviews, 2012. **41**(15): p. 5160-5173.
336. Carver, K.M. and R.C. Snyder, *Unexpected Polymorphism and Unique Particle Morphologies from Monodisperse Droplet Evaporation*. Industrial & Engineering Chemistry Research, 2012. **51**(48): p. 15720-15728.
337. Davies, J.F., A.E. Haddrell, and J.P. Reid, *Time-Resolved Measurements of the Evaporation of Volatile Components from Single Aerosol Droplets*. Aerosol Science and Technology, 2012. **46**(6): p. 666-677.
338. Nanayakkara, S.U., J. van de Lagemaat, and J.M. Luther, *Scanning Probe Characterization of Heterostructured Colloidal Nanomaterials*. Chemical Reviews, 2015. **115**(16): p. 8157-8181.
339. Butt, H.-J., B. Cappella, and M. Kappl, *Force Measurements with the Atomic Force Microscope: Technique, Interpretation and Applications*. Surface Science Reports, 2005. **59**(1): p. 1-152.
340. French, R.H., *Origins and Applications of London Dispersion Forces and Hamaker Constants in Ceramics*. Journal of the American Ceramic Society, 2000. **83**(9): p. 2117-2146.
341. Johnson, K., K. Kendall, and A. Roberts. *Surface Energy and the Contact of Elastic Solids*. in *Proceedings of the Royal Society of London A: Mathematical, Physical and Engineering Sciences*. 1971: The Royal Society.
342. Li, Q., V. Rudolph, and W. Peukert, *London-Van Der Waals Adhesiveness of Rough Particles*. Powder Technology, 2006. **161**(3): p. 248-255.
343. Muller, V., B. Derjaguin, and Y.P. Toporov, *On Two Methods of Calculation of the Force of Sticking of an Elastic Sphere to a Rigid Plane*. Colloids and Surfaces, 1983. **7**(3): p. 251-259.
344. Prokopovich, P. and V. Starov, *Adhesion Models: From Single to Multiple Asperity Contacts*. Advances in Colloid and Interface Science, 2011. **168**(1): p. 210-222.
345. Rabinovich, Y.I., et al., *Capillary Forces between Surfaces with Nanoscale Roughness*. Advances in colloid and interface science, 2002. **96**(1): p. 213-230.
346. Bergström, L., *Hamaker Constants of Inorganic Materials*. Advances in Colloid and Interface Science, 1997. **70**: p. 125-169.
347. Palik, E.D., *Handbook of Optical Constants of Solids*. Vol. 3. 1998: Academic Press.

348. Murray, J.M., et al., *Measuring Refractive Index Using the Focal Displacement Method*. Applied Optics, 2014. **53**(17): p. 3748-3752.
349. Hector, L. and H. Schultz, *The Dielectric Constant of Air at Radiofrequencies*. Journal of Applied Physics, 1936. **7**(4): p. 133-136.
350. Otten, D.E., P.B. Petersen, and R.J. Saykally, *Observation of Nitrate Ions at the Air/Water Interface by Uv-Second Harmonic Generation*. Chemical Physics Letters, 2007. **449**(4): p. 261-265.
351. Ramdas, A. *The Infra-Red Absorption Spectra of Sodium Nitrate and Calcite*. in *Proceedings of the Indian Academy of Sciences-Section A*. 1953: Springer.
352. Ramachandran, V., et al., *Elastic Constants of Sodium Nitrate from 77 to 300 K*. Physica Status Solidi (a), 1982. **69**(1): p. 407-411.
353. Giovannini, D., et al., *Photons That Travel in Free Space Slower Than the Speed of Light*. arXiv preprint arXiv:1411.3987, 2014.
354. Kelly, A., W. Tyson, and A. Cottrell, *Ductile and Brittle Crystals*. Philosophical Magazine, 1967. **15**(135): p. 567-586.
355. Khan, M.I. and M.M. Nasef, *Spreading Behaviour of Silicone Oil and Glycerol Drops on Coated Papers*. Leonardo Journal of Sciences, 2009(14): p. 18-30.
356. Adi, S., et al., *Micro-Particle Corrugation, Adhesion and Inhalation Aerosol Efficiency*. European Journal of Pharmaceutical Sciences, 2008. **35**(1): p. 12-18.
357. Adi, S., et al., *Scanning White-Light Interferometry as a Novel Technique to Quantify the Surface Roughness of Micron-Sized Particles for Inhalation*. Langmuir, 2008. **24**(19): p. 11307-11312.
358. Feng, X., et al., *Mechanistic Study on Demulsification of Water-in-Diluted Bitumen Emulsions by Ethylcellulose*. Langmuir, 2009. **26**(5): p. 3050-3057.
359. Bachmann, J. and G. McHale, *Superhydrophobic Surfaces: A Model Approach to Predict Contact Angle and Surface Energy of Soil Particles*. European Journal of Soil Science, 2009. **60**(3): p. 420-430.
360. Nissen, D.A., *Thermophysical Properties of the Equimolar Mixture Sodium Nitrate-Potassium Nitrate from 300 to 600°C*. Journal of Chemical and Engineering Data, 1982. **27**(3): p. 269-273.
361. Batchelor, G. and J.-T. Green, *The Hydrodynamic Interaction of Two Small Freely-Moving Spheres in a Linear Flow Field*. Journal of Fluid Mechanics, 1972. **56**(02): p. 375-400.
362. Knoll, A., R. Magerle, and G. Krausch, *Tapping Mode Atomic Force Microscopy on Polymers: Where Is the True Sample Surface?* Macromolecules, 2001. **34**(12): p. 4159-4165.
363. Maugis, D. and B. Gauthier-Manuel, *Jkr-Dmt Transition in the Presence of a Liquid Meniscus*. Journal of Adhesion Science and Technology, 1994. **8**(11): p. 1311-1322.
364. Shi, X. and Y.-P. Zhao, *Comparison of Various Adhesion Contact Theories and the Influence of Dimensionless Load Parameter*. Journal of Adhesion Science and Technology, 2004. **18**(1): p. 55-68.
365. Badger, R.M., *A Relation between Internuclear Distances and Bond Force Constants*. The Journal of Chemical Physics, 1934. **2**(3): p. 128-131.
366. Rabinovich, Y.I., et al., *Adhesion between Nanoscale Rough Surfaces: Ii. Measurement and Comparison with Theory*. Journal of Colloid and Interface Science, 2000. **232**(1): p. 17-24.

367. Johnson, K., *L. 1985 Contact Mechanics*. Cambridge: Longman) Cambridge University Press) and references therein *Phys. Rev. Lett*, 1987. **50**: p. 120.
368. Liu, Y., et al., *A New Afm Nanotribology Method Using a T-Shape Cantilever with an Off-Axis Tip for Friction Coefficient Measurement with Minimized Abbé Error*. *Tribology Letters*, 2011. **41**(1): p. 313-318.
369. Beck-Broichsitter, M., et al., *Polymer Nanoparticle-Based Controlled Pulmonary Drug Delivery*, in *Drug Delivery System*. 2014, Springer. p. 133-145.
370. Lechuga-Ballesteros, D. and D.P. Miller, *Advances in Respiratory and Nasal Drug Delivery*. *Molecular Pharmaceutics*, 2015. **12**(8): p. 2561-2561.
371. Islan, G., et al., *Development and Characterization of New Enzymatic Modified Hybrid Calcium Carbonate Microparticles to Obtain Nano-Architected Surfaces for Enhanced Drug Loading*. *Journal of Colloid and Interface Science*, 2015. **439**: p. 76-87.
372. Longest, P.W., et al., *Production of Inhalable Submicrometer Aerosols from Conventional Mesh Nebulizers for Improved Respiratory Drug Delivery*. *Journal of Aerosol Science*, 2012. **51**: p. 66-80.
373. Ko, J., et al., *Preparation and Characterization of Chitosan Microparticles Intended for Controlled Drug Delivery*. *International Journal of Pharmaceutics*, 2002. **249**(1): p. 165-174.
374. Aman, Z.M., et al., *Micromechanical Cohesion Force Measurements to Determine Cyclopentane Hydrate Interfacial Properties*. *Journal of Colloid and Interface Science*, 2012. **376**(1): p. 283-288.
375. Pilcer, G. and K. Amighi, *Formulation Strategy and Use of Excipients in Pulmonary Drug Delivery*. *International Journal of Pharmaceutics*, 2010. **392**(1): p. 1-19.
376. Pasquali, I., R. Bettini, and F. Giordano, *Solid-State Chemistry and Particle Engineering with Supercritical Fluids in Pharmaceutics*. *European Journal of Pharmaceutical Sciences*, 2006. **27**(4): p. 299-310.
377. Hakuta, Y., H. Hayashi, and K. Arai, *Fine Particle Formation Using Supercritical Fluids*. *Current Opinion in Solid State and Materials Science*, 2003. **7**(4): p. 341-351.
378. Vladislavljević, G.T., et al., *Glass Capillary Microfluidics for Production of Monodispersed Poly (DL-Lactic Acid) and Polycaprolactone Microparticles: Experiments and Numerical Simulations*. *Journal of Colloid and Interface Science*, 2014. **418**: p. 163-170.
379. Zhang, J., et al., *Formation, Characterization, and Fate of Inhaled Drug Nanoparticles*. *Advanced Drug Delivery Reviews*, 2011. **63**(6): p. 441-455.
380. Zhang, Y. and G.C. Stangle, *Preparation of Fine Multicomponent Oxide Ceramic Powder by a Combustion Synthesis Process*. *Journal of Materials Research*, 1994. **9**(08): p. 1997-2004.
381. Zhu, J. and R.C. Hayward, *Interfacial Tension of Evaporating Emulsion Droplets Containing Amphiphilic Block Copolymers: Effects of Solvent and Polymer Composition*. *Journal of Colloid and Interface Science*, 2012. **365**(1): p. 275-279.
382. De Villiers, S., et al., *Active Immunization against Nicotine Suppresses Nicotine-Induced Dopamine Release in the Rat Nucleus Accumbens Shell*. *Respiration*, 2002. **69**(3): p. 247-253.
383. Gonzalez, R., et al., *Identification of Soybean Proteins Responsible for Respiratory Allergies*. *International Archives of Allergy and Immunology*, 1991. **95**(1): p. 53-57.

384. Sung, J.C., B.L. Pulliam, and D.A. Edwards, *Nanoparticles for Drug Delivery to the Lungs*. Trends in Biotechnology, 2007. **25**(12): p. 563-570.
385. Ai, H., et al., *Interactions between Self-Assembled Polyelectrolyte Shells and Tumor Cells*. Journal of Biomedical Materials Research Part A, 2005. **73**(3): p. 303-312.
386. Baldelli, A., et al., *Effect of Crystallization Kinetics on the Properties of Spray Dried Microparticles*. Aerosol Science and Technology, 2016. **Submitted**.
387. Niwa, T., D. Mizutani, and K. Danjo, *Spray Freeze-Dried Porous Microparticles of a Poorly Water-Soluble Drug for Respiratory Delivery*. Chemical and Pharmaceutical Bulletin, 2012. **60**(7): p. 870-876.
388. Patravale, V. and R. Kulkarni, *Nanosuspensions: A Promising Drug Delivery Strategy*. Journal of Pharmacy and Pharmacology, 2004. **56**(7): p. 827-840.
389. Young, P.M., et al., *Multi-Breath Dry Powder Inhaler for Delivery of Cohesive Powders in the Treatment of Bronchiectasis*. Drug Development and Industrial Pharmacy, 2015. **41**(5): p. 859-865.
390. Zhang, Q.-N., et al., *In Situ Observation on the Dynamic Process of Evaporation and Crystallization of Sodium Nitrate Droplets on a Znse Substrate by Ftir-Atr*. The Journal of Physical Chemistry A, 2014. **118**(15): p. 2728-2737.
391. Oriakhi, C.O., *Chemistry in Quantitative Language: Fundamentals of General Chemistry Calculations*. 2009: Oxford University Press, USA.
392. Robinson, J.W., *Practical Handbook of Spectroscopy*. 1991: CRC press.
393. Goldstein, J., et al., *Scanning Electron Microscopy and X-Ray Microanalysis: A Text for Biologists, Materials Scientists, and Geologists*. 2012: Springer Science & Business Media.
394. Sharma, S.K., *Atomic and Nuclear Physics*. 2008: Pearson Education India.
395. Graber, T., et al., *Determination of Mass Transfer Coefficients for Crystal Growth of Nitrate Salts*. Crystal Research and Technology, 1999. **34**(10): p. 1269-1277.
396. Evans, R., et al., *Quantitative Interpretation of Diffusion-Ordered Nmr Spectra: Can We Rationalize Small Molecule Diffusion Coefficients?* Angewandte Chemie International Edition, 2013. **52**(11): p. 3199-3202.
397. Slominski, C.G., A.M. Kraynik, and J.F. Brady, *The Einstein Shear Viscosity Correction for Non No-Slip Hyperspheres*. Journal of Colloid and Interface Science, 2014. **430**: p. 302-304.
398. Laliberté, M., *Model for Calculating the Viscosity of Aqueous Solutions*. Journal of Chemical & Engineering Data, 2007. **52**(2): p. 321-335.
399. Gambill, W., *How to Estimate Mixtures Viscosities*. Chemical Engineering, 1959. **66**: p. 151-152.
400. Brooker, M., *Raman Spectroscopic Investigations of Structural Aspects of the Different Phases of Lithium Sodium and Potassium Nitrate*. Journal of Physics and Chemistry of Solids, 1978. **39**(6): p. 657-667.

Appendix A. Generation and monitoring size change of monodisperse droplets in a conditioned flow tube

This appendix introduces additional material for the description of the setup used for experiments shown in all chapters. The monodisperse droplet chain setup, also called dropmeter, has been discussed in Chapter 1, 2, and 3. In Appendix A, a guideline for future users is shown. The process used to properly operate the monodisperse droplet chain can be divided into three phases: 1) generating the first injected droplet, 2) recording the distance between two consecutive droplets and 3) collecting dried microparticles.

The generation of the first injected droplet focuses on an appropriate use of the piezoceramic dispenser. The piezoceramic dispenser is the main component of the monodisperse droplet chain. It is connected to a liquid and gas feed systems. These two systems connect a solution and the clean air to the piezoceramic dispenser, respectively. The purpose of the liquid system is merely to fulfill the piezoceramic dispenser with the solution. On the other hand, the purpose of the gas feed system is firstly to flush the system after each usage and secondly to win the high surface tension between the first injectable droplet and the glass tip of the piezoceramic dispenser. Figure A. 1 shows the components used to produce the monodisperse droplet chain.

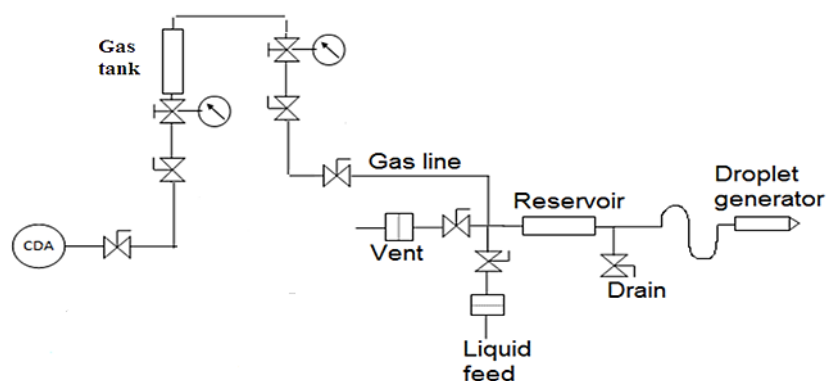


Figure A. 1 Components of the system used to generate a monodisperse droplet chain.

The recording of images of the monodisperse droplet chain is necessary to determine the main properties of each droplet or particle. On the other hand, collecting the final dried microparticles

allow to determine the main properties of the produced particles. For examples, a Scanning Electron Microscope (SEM) determines the morphology and the diameter, an Helium Ion Microscope (HIM) or a Focused Ion Beam (FIB) the void fraction and a Raman Spectroscopy the solid phase. The following list remarks the main steps that a user should take for properly generating and recording a monodisperse droplet chain and collecting its products:

1. Verify that all the valves present in the system are close;
2. Check that the diode laser is perfectly aligned with the centerline of the flow tube. If not, adjust the optical mirrors to direct the laser light to the center of the flow tube;
3. Verify that the hollow stubs with a paper based filter of 0.2 μm pores size (SEM stub) and with a metallic frit of 0.2 μm pore sizes (Raman stub) are ready to be used to collect dried microparticles for further analysis;
4. Ensure that the piezoceramic dispenser is connected to the voltage generator (Microdrop MD-E-3000, Microdrop Technologies GmbH, Norderstedt, Germany);
5. Set an appreciate value for the flow rate [L/min]. To avoid any turbulence, a value lower than 3 L/min is acceptable in the current setup;
6. Open the valve that connects the clean air general system to the flow tube;
7. If the temperature of the flow tube is set to be higher than 20°C, room temperature, turn on the heaters at the desired temperatures. In addition, place the thermocouple connected to the lower heater at the injection point. Connect the flow tube to a vacuum pump. Turn on the vacuum pump and wait until a stable temperature is reached. For temperatures higher than 100°C, record the temperature at the collection point to verify the temperature gap between injection and collection point;
8. Fulfill a syringe with the solution chosen, commonly 2 to 3 ml would be enough to run one test;
9. Connect the syringe to the system. Two filters purify the solution when entering in the system. If water is the solvent used for the solution chosen, then any hydrophilic filter would be appropriate. If other solvents are selected, as ethanol or acetone, a filter made of nylon or teflon can be used. Both kinds of filters are Millex filter units from EMD Millipore;

10. Open the valve connected to the liquid feed;
11. Fulfill the system with the solution until the liquid visibly reaches the glass tip of the dispenser. When the liquid reaches exactly the tip of the glass microtubes of the piezoceramic dispenser, turn on the voltage generator;
12. Verify the injecting droplet using the diode laser. If it is noticeable only a straight jet, then the voltage needs to be decreased. If necessary, decrease the voltage by 5 V until a falling chain is noticed. Afterwards, decrease of 1 V until the chain is placed at the center of the flow tube. If nor jet neither chain are visible, then the voltage needs to be increased or the experiment to start over. A third alternative can be to open the gas feed until a jet is visible present in the flow tube, close the gas feed system and open the release valve. Subsequently, repeat step 11 until a stable monodisperse chain is placed close to the center of the flow tube;
13. Turn on the pulse generator. If necessary, modify pulse width and pulse delay to improve the quality of the recording monodisperse droplet chain. The best situation would be the visualization of each droplet as a clear, bright dot. For a better definition, turn off the lights of the laboratory. Examples of well-defined images are shown in the following appendixes;
14. Connect the camera to the computer;
15. Open the program Jai Vision;
16. Start to record, at least 20 pictures for each recording window;
17. If the whole chain cannot be recorded in one optical window, then the camera can be move downward using the lab-jack on which it is placed;
18. If necessary, move downward the camera by each couple of droplets. As a consequence, when moving the camera downward, it would be useful to keep checking the recording images;
19. Save the images recorded and use ImageJ to derive the position of each point in the chain;
20. Open the valve that connected the vacuum system to the collection system. The collecting rate should be higher than the flow rate present in the flow tube;
21. Connect the SEM hollow stub to the collection system and place it at the collection point. Observe if the particles follow the streamline created between the centerline

of the flow tube and the SEM hollow stub. Hold the collection system in the same position for approximately 2 minutes;

22. Substitute the SEM stub with the Raman stub. Place it in the same position and fix the collection system by inserting a cotton ball or a tissue in the collection point. To accelerate the collection process, increase the production frequency of the piezoceramic dispenser up to 200 Hz. Collect until a white powder is visible present on the Raman stub. To analyze the solid phase of collected microparticles, Raman spectroscopy requires at least 1 mg for precise results;
23. Once the experiments is finished, turn off the voltage generator, the pulse generator, the diode laser and the heaters;
24. Before turning off the camera, turn on the lights of the laboratory and place a ruler beside one of the wall of the flow tube until focused. Record some images. These images will provide the ratio pixel/mm required for further studies;
25. Turn off the camera and the program JaiVision;
26. Close the valve that connect the vacuum to the collection system;
27. Turn off the heaters;
28. Turn off the flow when the temperature at the injection point reaches values below 50°C.

As previously mentioned, the images collected are analyzed using ImageJ. This program allows determining the central position of each dot in the image. The standard deviation of the position in pixel of the dots relates to half of their size. Using the same program, the scaling images, recorded using a ruler beside the flow tube, can be analyzed. The ratio between pixels and millimeters can be determined. The values of the position of each dot-droplet and the related standard deviation can be transferred in an excel file. At this point, the model extensively explained in previous publications and in Chapter 2 and 3 can be used to determine settling velocity, aerodynamic diameter, density, volume equivalent diameter, diffusion coefficient, Enrichment, and Peclet number.

In Chapter 2, few additional steps for the use of the monodisperse droplet chain setup were used. In this chapter, a strobe light, microscope lens and a second camera were used to record the volume equivalent diameter of each droplet or particle. The following steps were taken:

1. Place a motorized vertical stage close to the flow tube without blocking any side view;
2. Design and build a holder that can handle the weight of the strobe light, the second camera and the microscope lens;
3. Connect the camera to the computer using the program JaiVision;
4. Set correct values of pulse width and pulse spacing for the second camera, strobe light and piezoceramic dispenser. Adjusting these values allows the recording of a stable floating droplet or particle;
5. Move the vertical stage downward until recording every droplet in the monodisperse droplet chain;
6. Analyze the image collected with ImageJ.

Appendix B. Particle formation process with a constant higher Peclet number

This appendix shows additional material about the results shown in Chapter 2. The project shown in Chapter 2 focused on particle formation processes with a high constant Peclet number. In order to reach a situation of high Peclet number, a solute with a high molecular weight has been chosen. In this case, it was chosen cellulose acetate butyrate (CAB). CAB has a high solubility in acetone; thus acetone was the chosen solvent. The publication shown in Chapter 2 does not include all the experimental derivations. As a consequence, additional plots and parameters are shown as follow. In the publication shown in Chapter 2, some of the input parameters are not introduced. As a result, few of the important parameters selected for the conditions of the experiments are the following:

- Distance between injection point and collection point = $3 \cdot 10^{-1}$ [m];
- Air flow in the flow tube = 1 [L/min];
- Inner diameter of the flow tube = $3.48 \cdot 10^{-2}$ [m];
- Inner diameter of the piezoceramic dispenser = 50 [μm].

In addition, acetone evaporation rate trend is obtained as shown in Figure B. 1. A polynomial is shown and it is an approximation to the trend of evaporation rate and wet bulb temperature. This equation facilitates the derivation of the evaporation rate for different wet bulb temperatures.

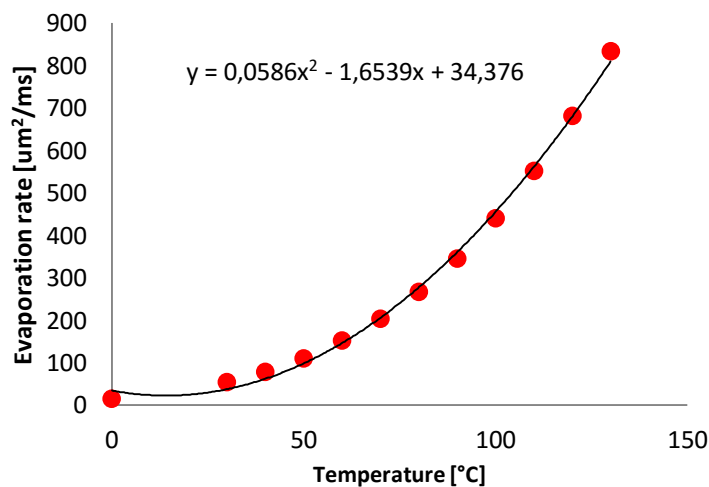


Figure B. 1 Trend of the evaporation rate of acetone respect the wet bulb temperature. The polynomial equation is used to easily calculate the evaporation rate for different wet bulb temperatures.

Before showing any additional results, the Spacing method introduced in Chapter 2 uses images of the monodisperse droplet chain. Chapter 2 lacks in monodisperse droplet chain images; therefore Figure B. 2 shows the monodisperse droplet chain produced using different frequencies of the piezoceramic dispenser. The monodisperse droplet chains shown in Figure B. 2 are achieved using pure deionized water.

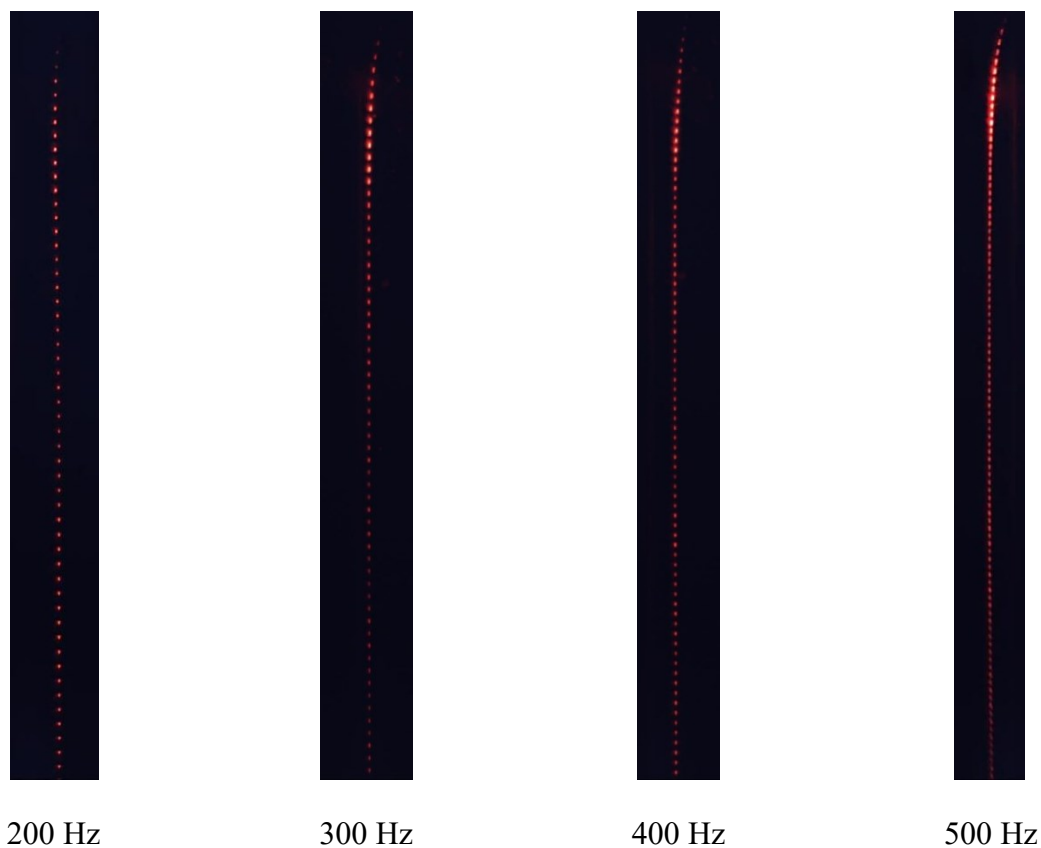


Figure B. 2 Images of the monodisperse droplet chain for different frequencies of the piezoceramic dispenser. The droplets are composed of deionized water.

For the cases shown in Chapter 2, the monodisperse droplet chain images are not as clear as the ones shown in Figure B. 2. The reason is due to the strong instability of a chain produced with acetone. The piezoceramic dispensers are tested with water. Acetone surface tension is strongly lower than water increasing the tendency of the injected droplet to stick on the glass of the piezoceramic dispenser. Experimental difficulties are increased when the initial solution contained CAB. CAB strongly increases the viscosity of the initial solution rendering the injection of the monodisperse droplet chain harder. Examples of few stable images are shown in Figure B. 3. For each case, about 30 pictures are used to calculate the distance between two consecutive droplets.

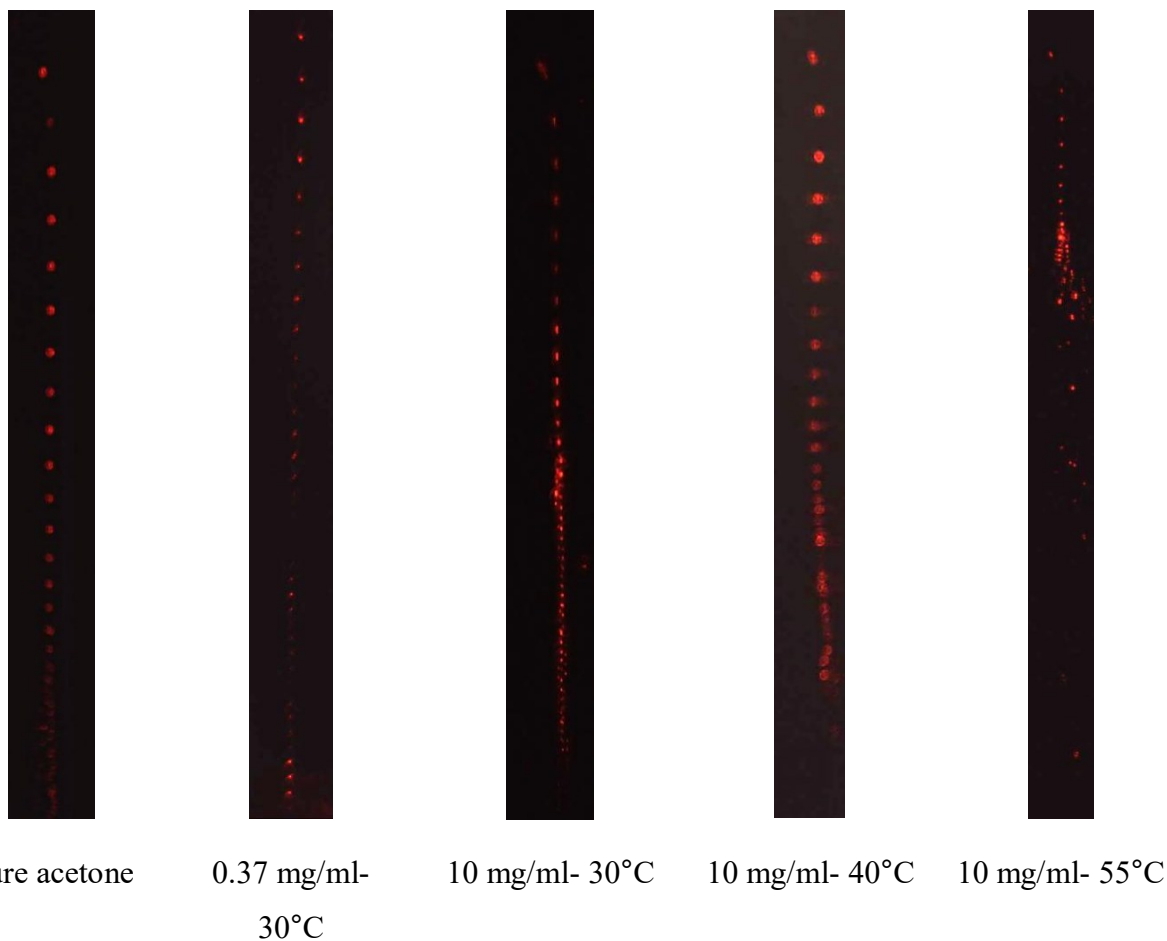


Figure B. 3 Images of the monodisperse droplet chain for the cases studies. In addition, a monodisperse droplet chain composed by pure acetone is shown for comparison purposes.

As a consequence, a sequel of images has been recorded in order to locate the position of each droplet. The Spacing technique is supported by the Microscope technique. Therefore, few pictures of each chain are recorded with a microscope lens, as described in Chapter 2. Figure B. 4 shows three images taken with a microscope lens; these images refer to different time steps of the particle formation process. In addition, Figure B. 4 shows an SEM image of the final dried microparticles.

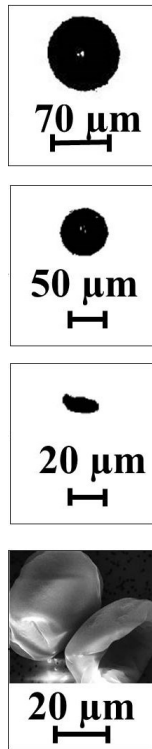


Figure B. 4 Microscope images of droplets or particles at different time steps of the particle formation process.

In the publication shown in Chapter 2, only the main results are shown due to limitations in number of pages. In this appendix, all the results achieved are shown. First of all, Figure 2.4 shows the trend of aerodynamic diameter only for one case studied. In particular, the case shown is 10 mg/ml at 30°C. The trend of aerodynamic diameter can be achieved through two methods, the “Imaging” and “Spacing” methods. Figure B. 5 shows the trend of aerodynamic diameter and the differences between the two methods used.

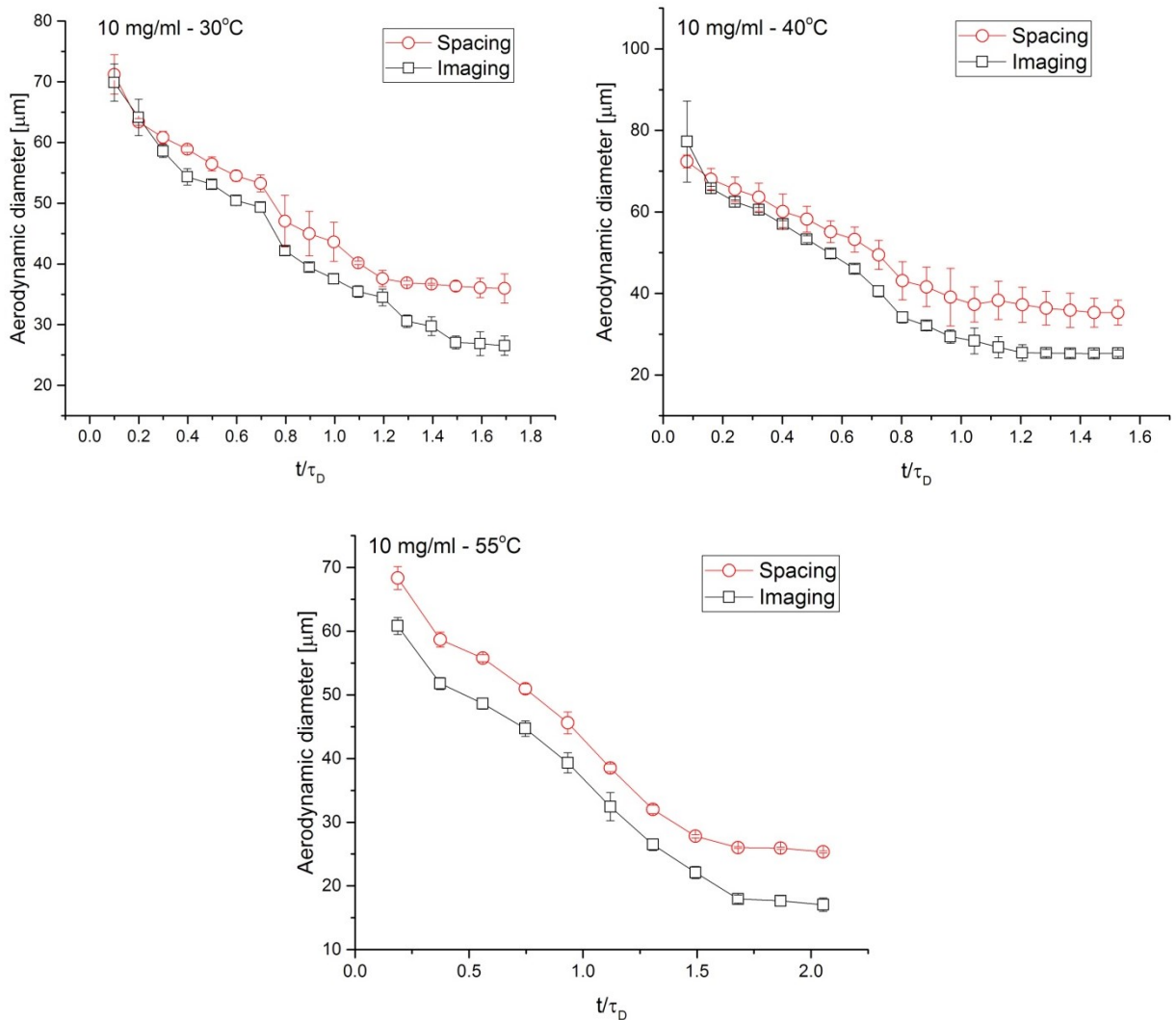


Figure B. 5 Aerodynamic diameter calculated with both Spacing and Imaging methods for the cases: 10 mg/ml at 30°C, 10 mg/ml at 40°C and 10 mg/ml at 55°C.

Other values are missing in Chapter 2. An example is the mass and density trends. Both of them are shown only for the cases with an initial concentration of 10 mg/ml. Figure B. 6 shows the trend of mass for the cases of 0.37 mg/ml at 30°C and 10 mg/ml at 30°C. The comparison between these two cases can show the impact of the initial concentration on the particle formation process.

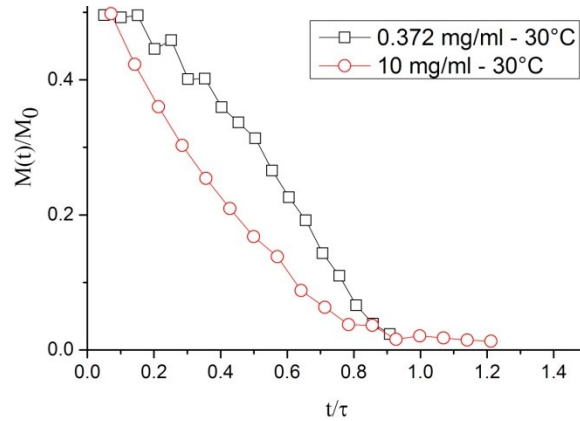


Figure B. 6 Trend of density and mass for the cases of 0.37 mg/ml at 30°C and 10 mg/ml at 30°C. The picture refers to the density curves. The comparison between the two cases shows the impact of the initial concentration on the particle formation process.

Another parameter not shown in Chapter 2 is the velocity during the particle formation process. This parameter has not been shown because it is implied in both mass and density trends. As a support for the understanding, Figure B. 7 shows the trend of settling velocity for all the cases analyzed.

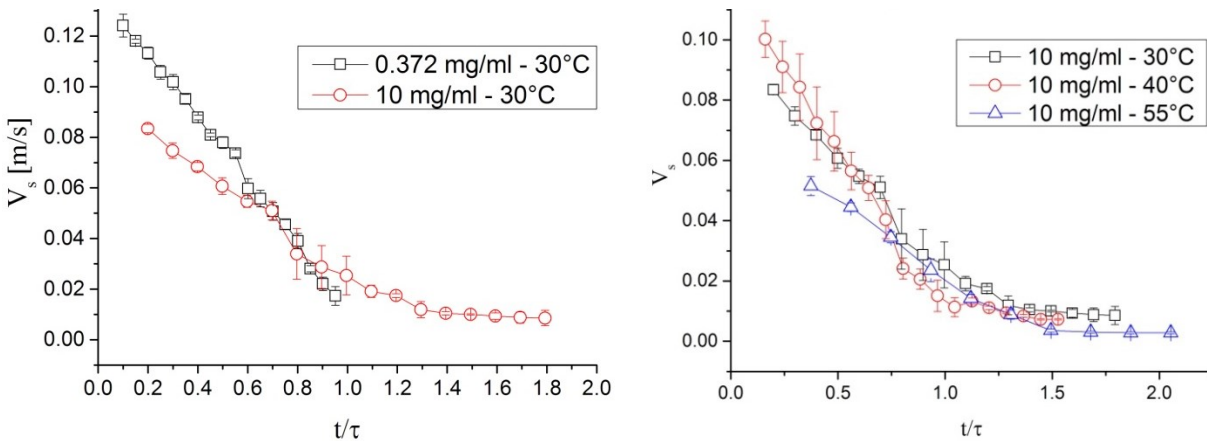


Figure B. 7 Trend of velocity in time for all the cases analyzed.

Time to reach saturation and drying time show the difference between calculations achieved through the theory and experiments, both explained in Chapter 2. Figure B. 8 shows the differences between experimental results and theoretical derivations for the parameters of drying time and time to reach saturation.

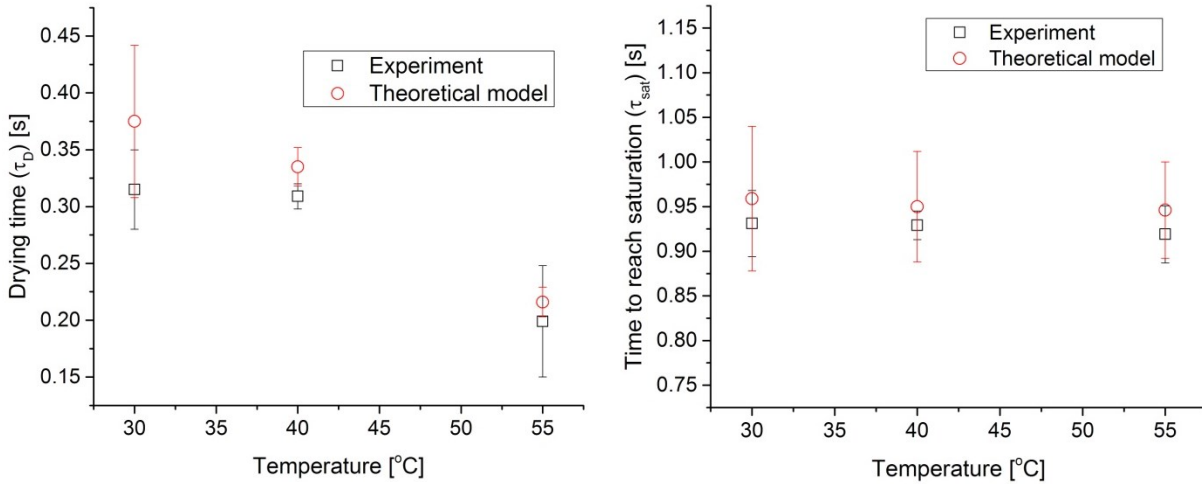
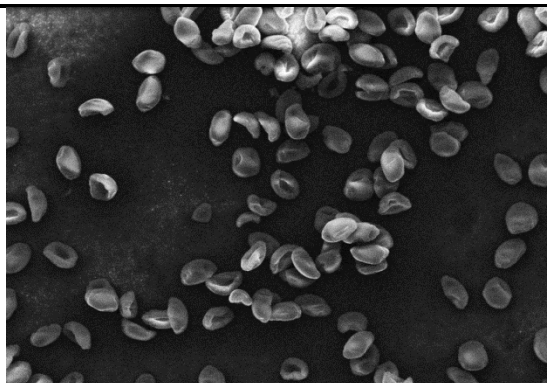


Figure B. 8 Differences between the theoretical method and experimental derivations. On the left hand side, the drying time is shown; on the right hand side, the time to reach saturation is shown. The results are shown for the cases of 10 mg/ml at the temperatures of 30, 40 and 55°C.

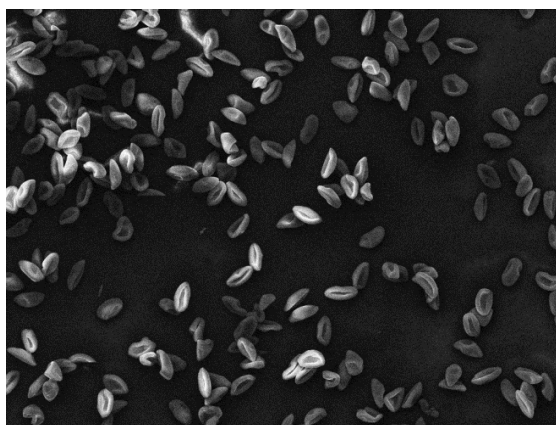
Scanning Electron Microscope (SEM) images are shown in Chapter 2. On the other hand, only few images are selected, especially with high magnification to focus the attention on a desired particle. Table B. 1 shows some SEM images of high magnification for the cases of 10 mg/ml at 30, 40 and 55°C.

Table B. 1 SEM images of a high magnification for the cases analyzed.

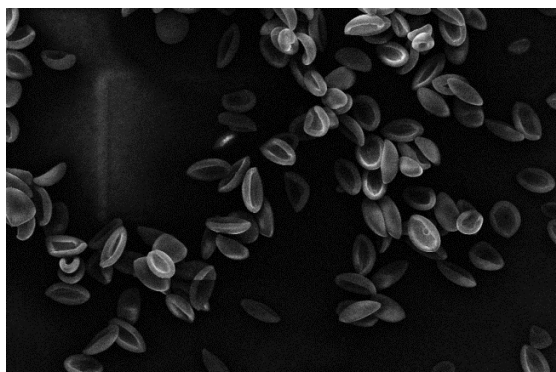
10 mg/ml at 30°C



10 mg/ml at 40°C



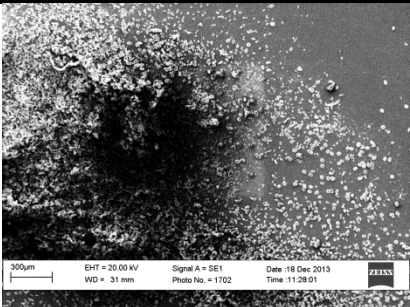
10 mg/ml at 55°C



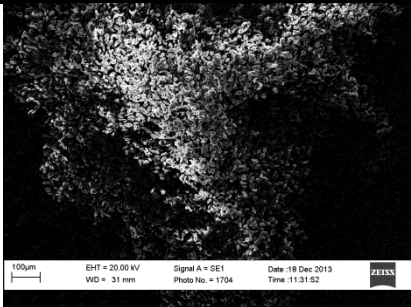
20 μ m

Another case is studied in Chapter 2, 0.37 mg/ml at 30°C. Table B. 2 shows three images obtained with 100, 200 and 500x.

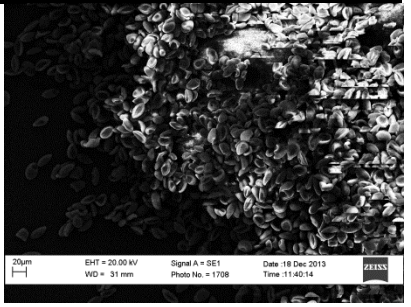
Table B. 2 SEM images for the cases 0.37 mg/ml at 30°C. Different magnifications are reported.



100x



200x



500x

Appendix C. Impact of the Crystallization Window on Properties of Spray Dried Microparticles

This appendix introduces additional material to the results shown in Chapter 3. In the publication shown in Chapter 3, the project relates to the crystallization kinetics in the particle formation process, Figure C. 1. Some of the input parameters are not introduced. As a result, few of the important parameters selected for the conditions of the experiments are the following:

- Distance between injection point and collection point = 1 [m];
- Air flow in the flow tube = 2 [L/min];
- Inner diameter of the flow tube = $4 \cdot 10^{-2}$ [m];
- Inner diameter of the piezoceramic dispenser = 30 [μm].

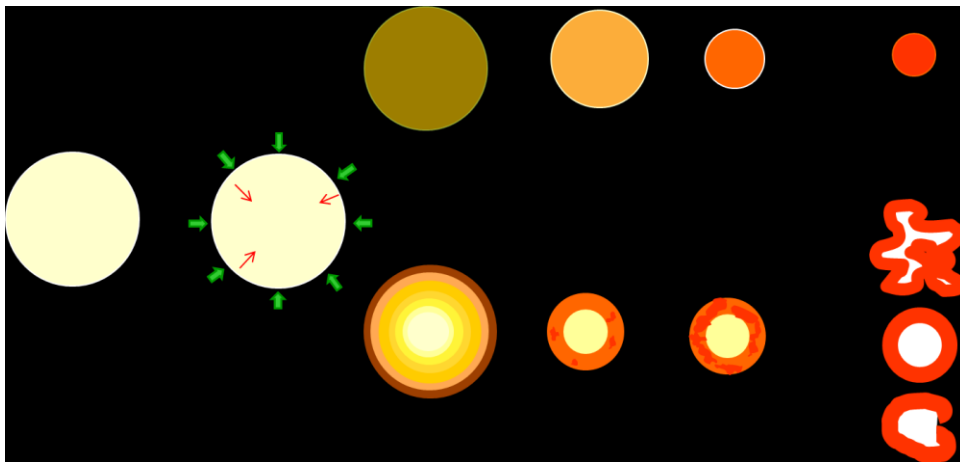


Figure C. 1 Graphical abstract of the main concept of this project. The solute distributes in the droplet during the particle formation process. According to the time allowed for crystallization the final dried microparticle changes in morphology.

The publication shown in Chapter 3 contains only a small portion of the material achieved through experimental results. In this appendix, additional material is shown. First of all, a flow chart of the parameters found in the particle formation process is shown in Figure C. 2. This flow chart can simplify the understanding of the descriptions shown in Chapter 3.

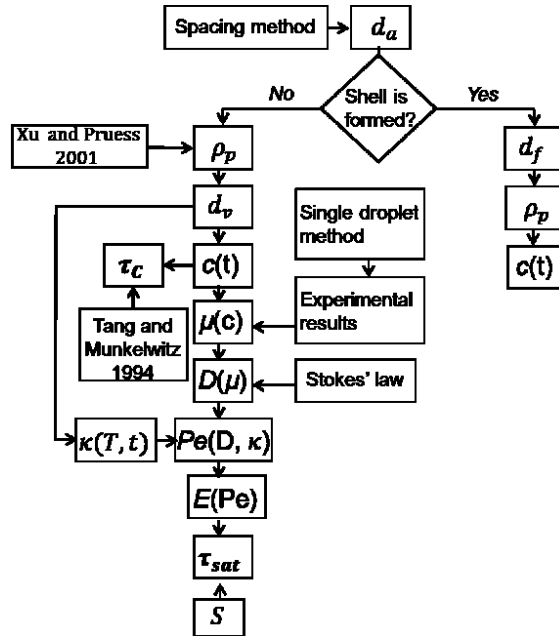


Figure C. 2 Flow chart of the methods used and main parameters of the particle formation process found.

In Chapter 2, a simple scheme of the setup is shown. Here, a section of the double wall and squared sectioned flow tube is shown in Figure C. 3. Main dimensions along with the distance between the injection and collection points are shown.

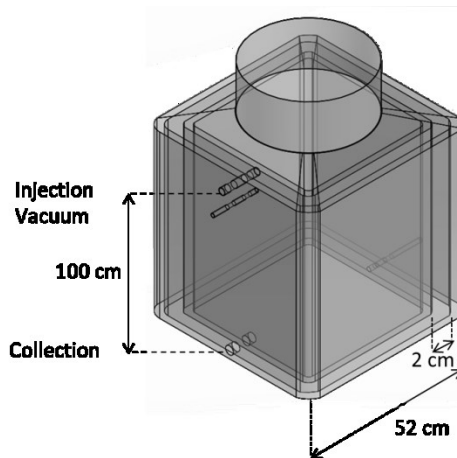


Figure C. 3 Drawing of the flow tube in the experiments to identify the impact of crystallization kinetics on the particle formation process. Few dimensions of the flow tube are shown.

As shown in Appendix B, the monodisperse droplet chain has been highlighted with a diode laser and its images recorded. The difference with previous experiments is the length of the flow tube. In the new version of the flow tube, the distance between injection and collection point is 1 meter; therefore, longer droplet chain can be produced and recorded. The drawback is that the optical

window of the camera in the conditions used is about 10 cm. As a result, consecutive images of the droplet chain are recorded. As an example, Figure C. 4 shows the initial part of the monodisperse droplet chain for five cases studied. As seen from the images of Figure C. 4, the flow tube still shows some drawback. The monodisperse droplet chain can become instable with a little turbulence created in the flow tube by the drastic change in shape of cross section area.

Figure C. 4 Images of the highlighted monodisperse droplet chain for five reference cases.



In the publication shown in Chapter 3 the trend of aerodynamic and volume equivalent diameter are shown. In particular, the case shown has initial conditions of 5 mg/ml and 25°C. Plots of other cases are shown in Figure C. 5.

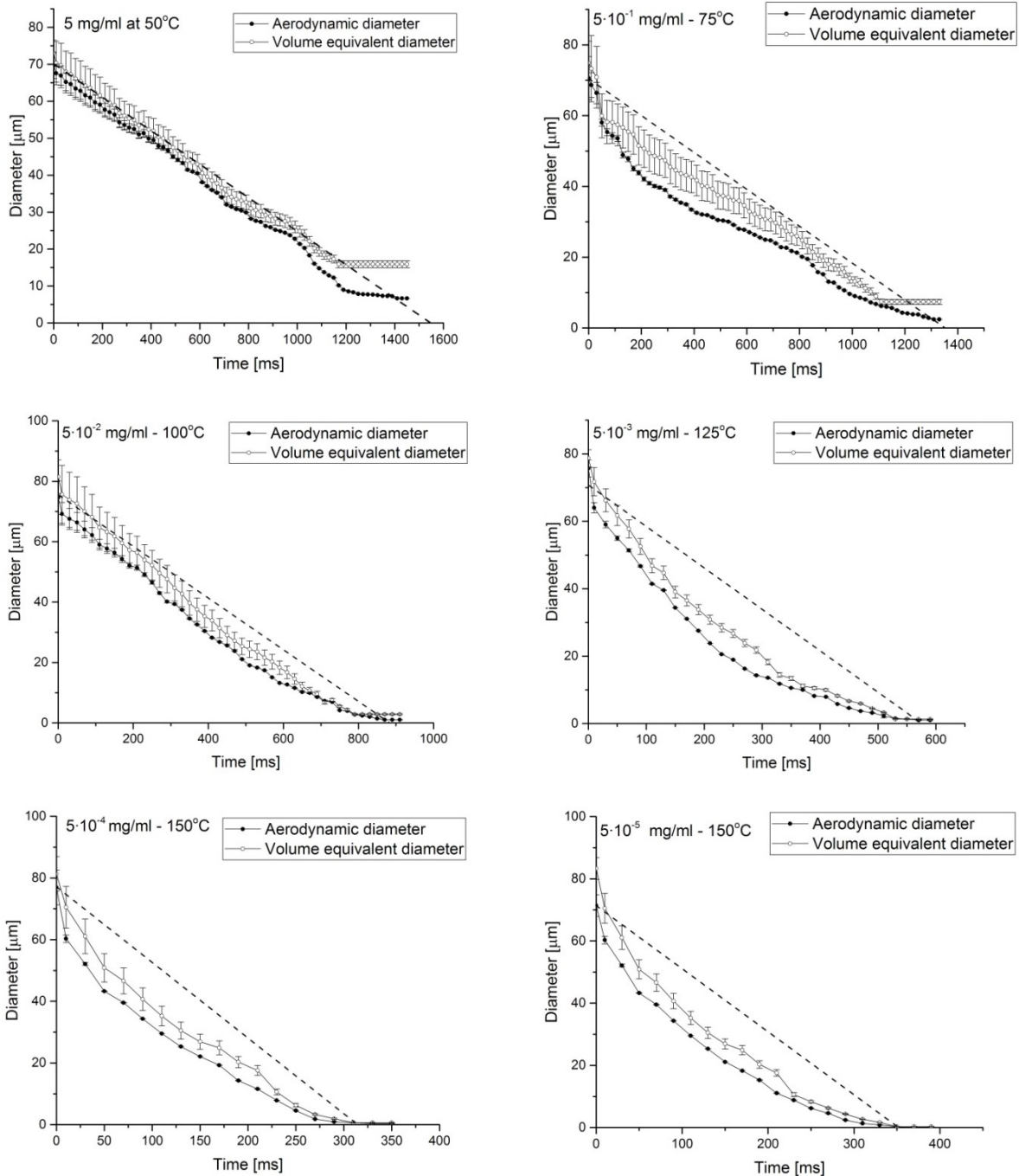


Figure C. 5 Comparison between time-constant and time-variable models. The dashed line identifies the evaporation rate achieved with a time-constant model. The aerodynamic and volume equivalent diameter are obtained with a time-variable model.

Figure C. 6 shows the trend of final diameters of the microparticles collected and the crystallization windows. For four cases, Scanning Electron Microscope (SEM) and Focused Ion Beam (FIB) images are shown.

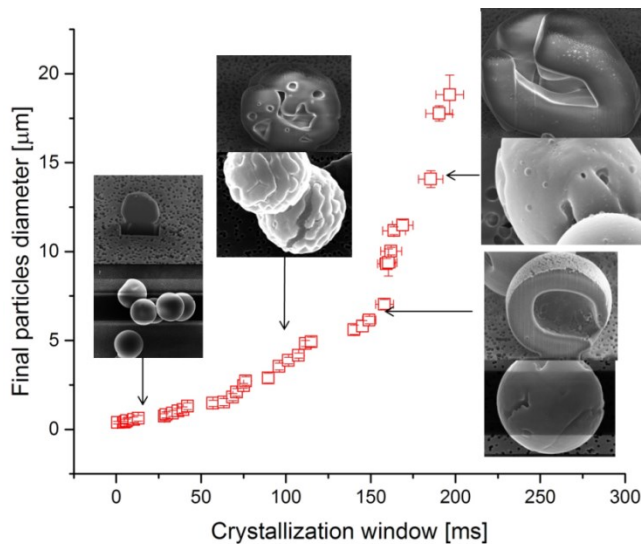
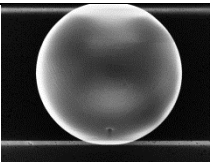
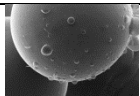
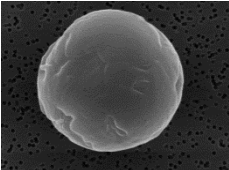
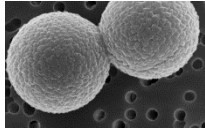
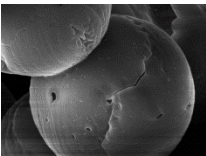

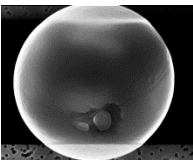
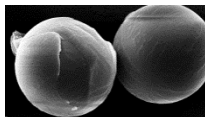
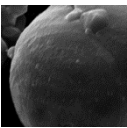
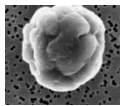
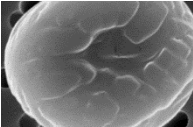
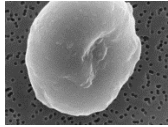
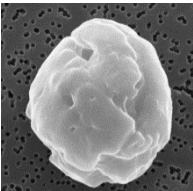
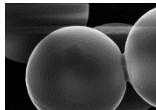
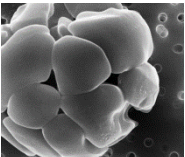
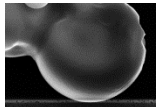
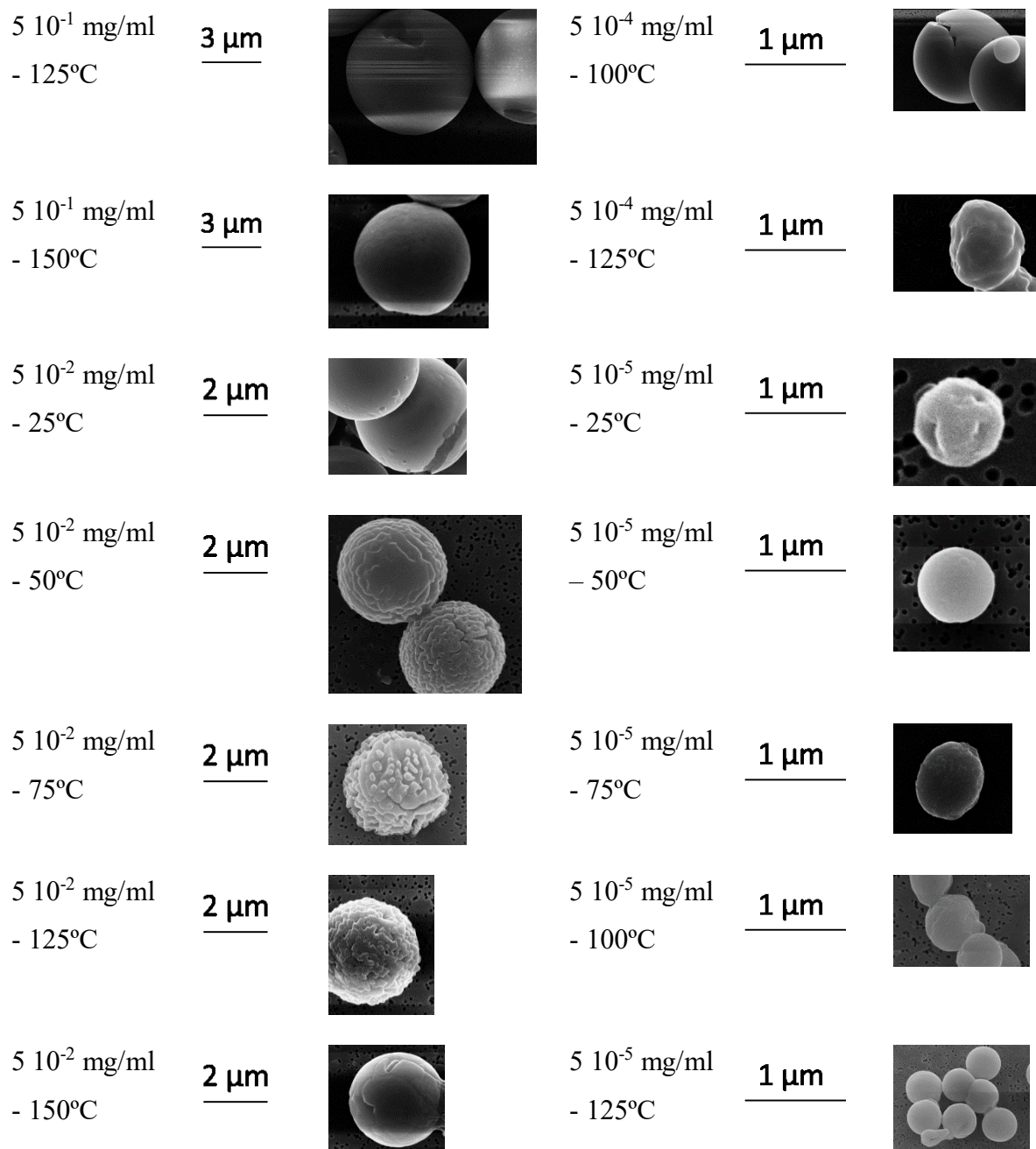


Figure C. 6 Trend of final diameter and crystallization window. In addition, few main SEM images are connected with their respective cases.

While FIB images have been achieved only for few cases due to cost efforts, SEM images are achieved for all the cases studied, Table C. 1. SEM images are used to analyze the morphology and the diameter of the monodisperse and monomorph microparticles.

Table C. 1 Additional SEM images for each case studied. A scale bar is shown for each case.

Case	Scale	SEM	Case	Scale	SEM
5 mg/ml - 25°C	<u>10 μm</u>		5 10 ⁻³ mg/ml - 25°C	<u>1 μm</u>	
5 mg/ml - 75°C	<u>8 μm</u>		5 10 ⁻³ mg/ml - 50°C	<u>1 μm</u>	
5 mg/ml - 100°C	<u>7 μm</u>		5 10 ⁻³ mg/ml - 75°C	<u>1 μm</u>	
5 mg/ml - 125°C	<u>5 μm</u>		5 10 ⁻³ mg/ml - 100°C	<u>1 μm</u>	
5 mg/ml - 150°C	<u>5 μm</u>		5 10 ⁻³ mg/ml - 150°C	<u>1 μm</u>	
5 10 ⁻¹ mg/ml - 25°C	<u>5 μm</u>		5 10 ⁻⁴ mg/ml - 25°C	<u>1 μm</u>	
5 10 ⁻¹ mg/ml - 50°C	<u>5 μm</u>		5 10 ⁻⁴ mg/ml - 50°C	<u>1 μm</u>	
5 10 ⁻¹ mg/ml - 100°C	<u>3 μm</u>		5 10 ⁻⁴ mg/ml - 75°C	<u>1 μm</u>	



Other properties of the spray dried microparticles have been analyzed. For example, in the publication the density trend during the particle formation process is shown. The density and the mass trend are shown for few cases, Figure C. 7.

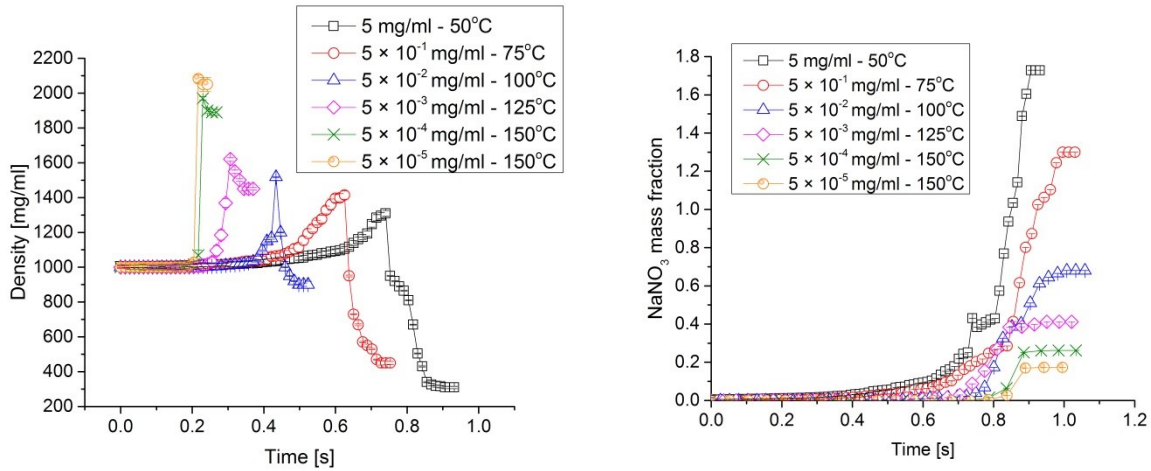


Figure C. 7 On the left hand side, the trend of the density for each case is shown. Only the method concerning the voids in the forming particle is used. On the right hand side, the trend of mass for the same cases is shown.

In the publication shown in Chapter 3, the trend in time for crystallization is shown for few cases studied. Similarly, the time to reach saturation is calculated for the same cases.

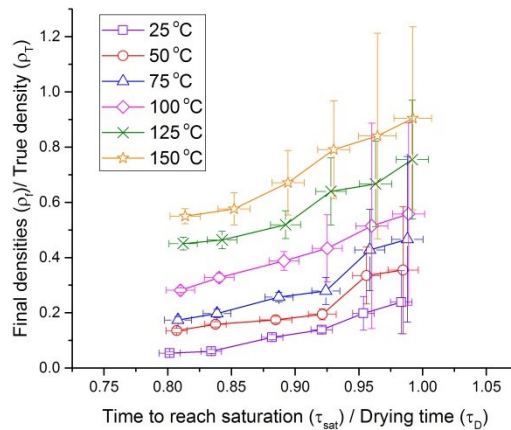


Figure C. 8 Trend of time to reach saturation and density of the final dried microparticles. The cases shown are the main six sample cases shown in Chapter 3.

An additional properties of the final dried microparticles studied is their solid phase. The solid phase is achieved using Raman spectroscopy.

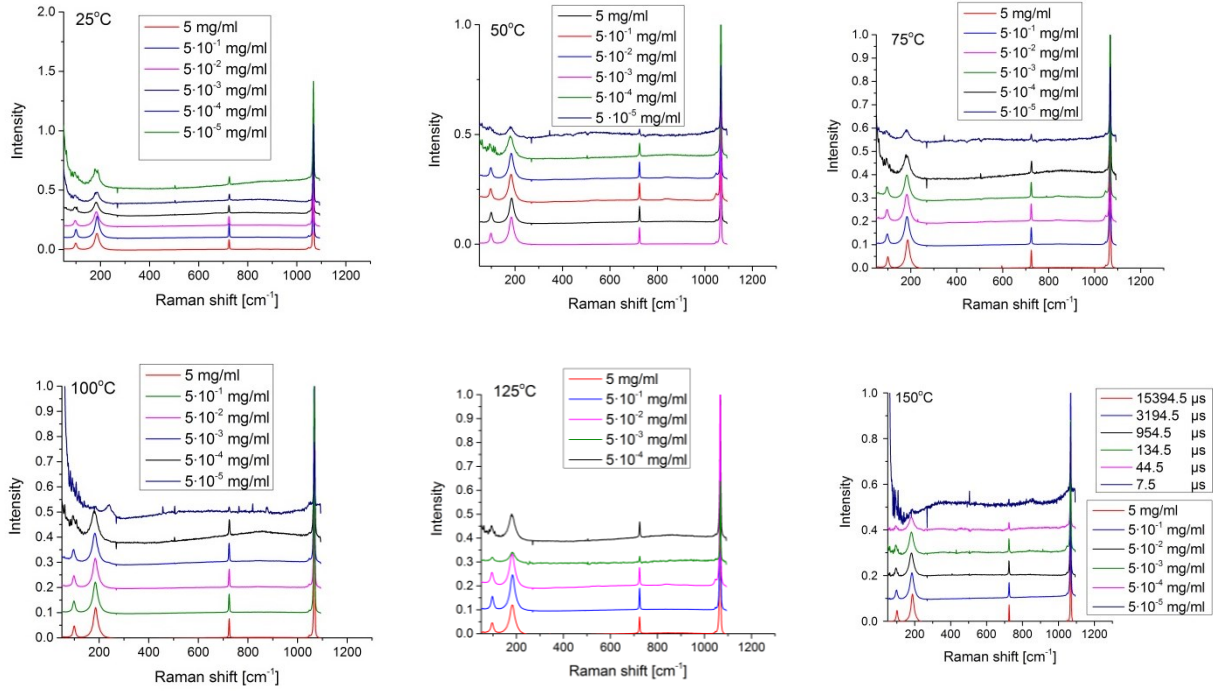


Figure C. 9 Raman spectroscopy of all the cases studied. The plots are separated according to the temperature of the external environment.

In addition, in Chapter 3 only the trend of peak area is shown. The trends of peak width and height have been similarly calculated, Figure C. 10.

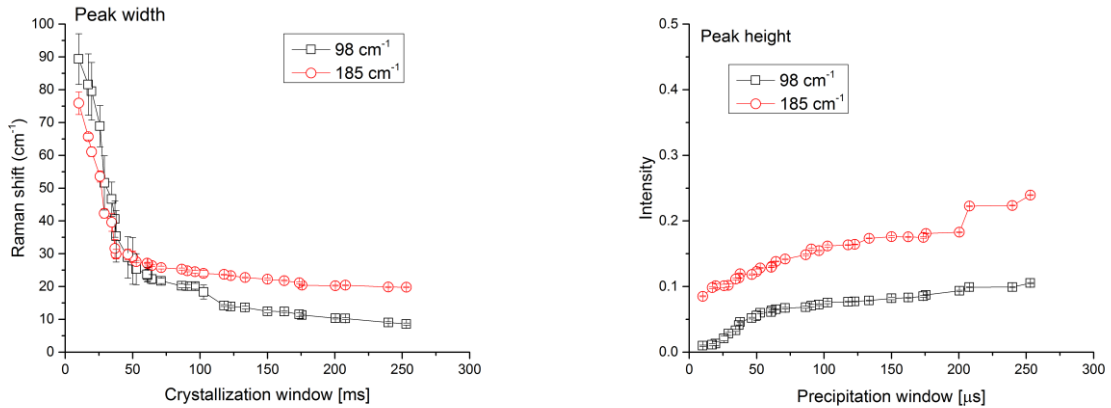
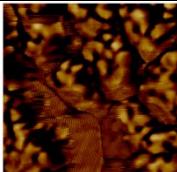
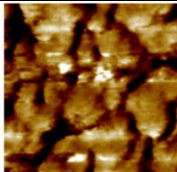
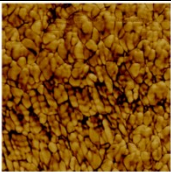
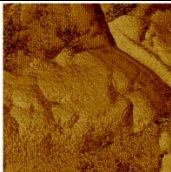
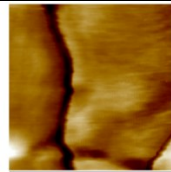
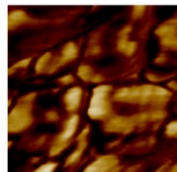
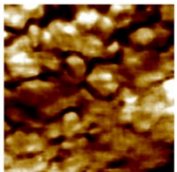
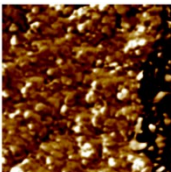
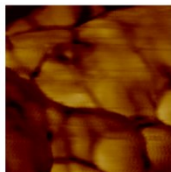
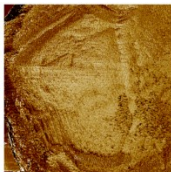
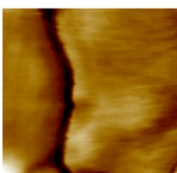
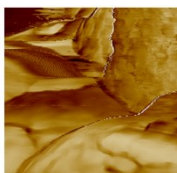
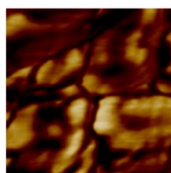
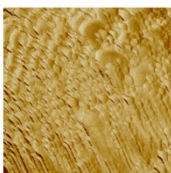

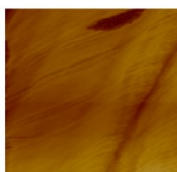

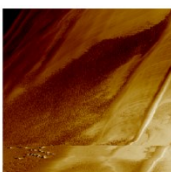
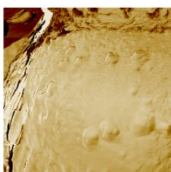
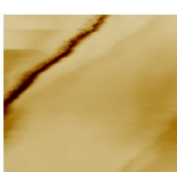
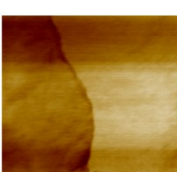



Figure C. 10 Trend of peak width, on the left, and the trend of peak height related to the crystallization window of each case studied.

Appendix D. Analysis of Cohesion Forces between Monodisperse Microparticles with Rough Surfaces

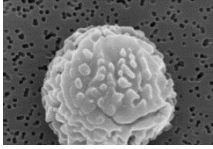
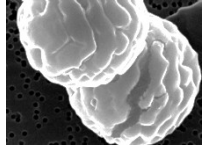
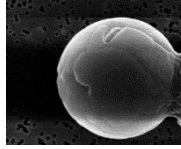
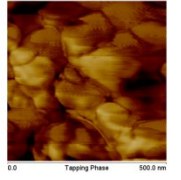
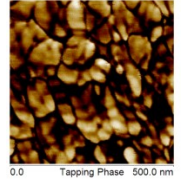
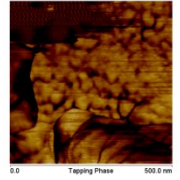
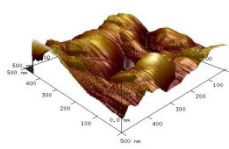
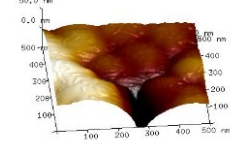
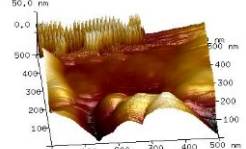
This appendix shows additional material for the results introduced in Chapter 4. In this chapter, AFM is used not only for the calculation of pull off forces. In tapping mode, the AFM is used to analyze the morphology of the microparticles. Different scanning areas are used to evaluate the morphology of the microparticles.

Table D. 1 Examples of the morphology of the microparticles for each case studied. The morphology is shown in a 2D image.

	0.25	0.5	1	5	10
A					
B					
C					
D					
E					

To analyze deeply the trend between precipitation window, Δt_c , and crystal size, three cases with a closer precipitation window are chosen. The images shown in Table D. 2 are related to a scanning area of $0.25 \mu\text{m}^2$.

Table D. 2 SEM and AFM images of three cases studied. These cases are considered because they showed close values of precipitation window.

Δt_c [ms]	2.23	1.64	1.09
Diameter [μm]	4.15 ± 0.15	3.87 ± 0.18	3.51 ± 0.19
SEM			
AFM 2D			
AFM 3D			

From the images shown in Table D. 1, roughness and asperities are obtained for each case. For the value of rms_1 , the following cases are considered: scanning area of 100 for the case A, 25 for the case B, 1 for the case C, 0.25 for the case D and $0.0625 \mu\text{m}^2$ for the case E. The choice of these scanning areas is related to the size of the particles studied; on average the scanning area covers at least half of a microparticle. For the value of rms_2 the following cases are considered: scanning area of 1 for the case A, 0.25 for the case B, 0.0625 for the case C, 0.0625 for the case D and $0.01 \mu\text{m}^2$ for the case E. A smaller scanning area is chosen for the secondary mean squared roughness because smaller peaks can be recorded. One additional scanning area is added for the case E, Table D. 3. With the same scanning areas, asperities and distance between peaks for each case studied

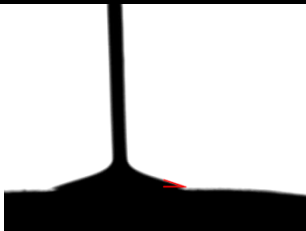
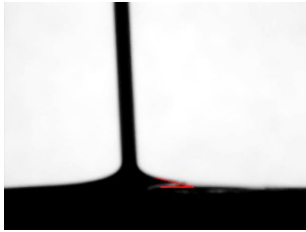
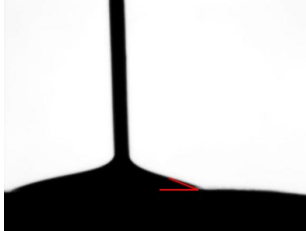
are calculated. The distance between two consecutive peaks (λ) is used for theoretical calculations of pull off forces in Rabinovich and Surface energy Rabinovich models. The asperities are used for theoretical calculations of pull off forces in Rumpf and Modified Rumpf models.

Table D. 3 List of asperities and Lamba values for the cases studied.

Cases	λ_1 [nm]	λ_2 [nm]	Asperities [nm]
A	7275 ± 318	562 ± 33	1079 ± 89
B	4285 ± 662	890 ± 134	1994 ± 392
C	1248 ± 251	1017 ± 119	3248 ± 267
D	936 ± 114	390 ± 29	184 ± 23
E	493 ± 115	297 ± 26	80 ± 5

In the project shown in Chapter 4, most of theoretical models used for the calculation of the cohesion forces between two microparticles require the surface energy of sodium nitrate. The surface energy of sodium nitrate has not been previously shown in the literature. Therefore, it is calculate using the sessile method. Some images of the contact angle between the three liquids used and a smooth surface of sodium nitrate are shown in Table D. 4.

Table D. 4 Images of an example of contact angle between a flat surface of sodium nitrate and a drop of the three solvents used.

Chloroform	
PFOB	
Silicon oil	

Appendix E. Control on the Distribution of Chemical Components in Spray Dried Microparticles

This appendix introduces additional material to the results shown in Chapter 5. In the publication shown in Chapter 5, the project relates to the understanding of which chemical components saturates first on the surface of the final microparticles. Some of the input parameters are not introduced. As a result, few of the important parameters selected for the conditions of the experiments are the following:

- Distance between injection point and collection point = 1 [m];
- Air flow in the flow tube = 2 [L/min];
- Inner diameter of the flow tube = $4 \cdot 10^{-2}$ [m];
- Inner diameter of the piezoceramic dispenser = 30 [μm].

The best explanation for this project is the graphical abstract done for the submitted paper. Figure E. 1 shows the crystallization kinetics effect on the distribution of the chemical components in the final dried microparticles. The component that saturates first on the surface mostly distribute on the surface of the final dried microparticles.

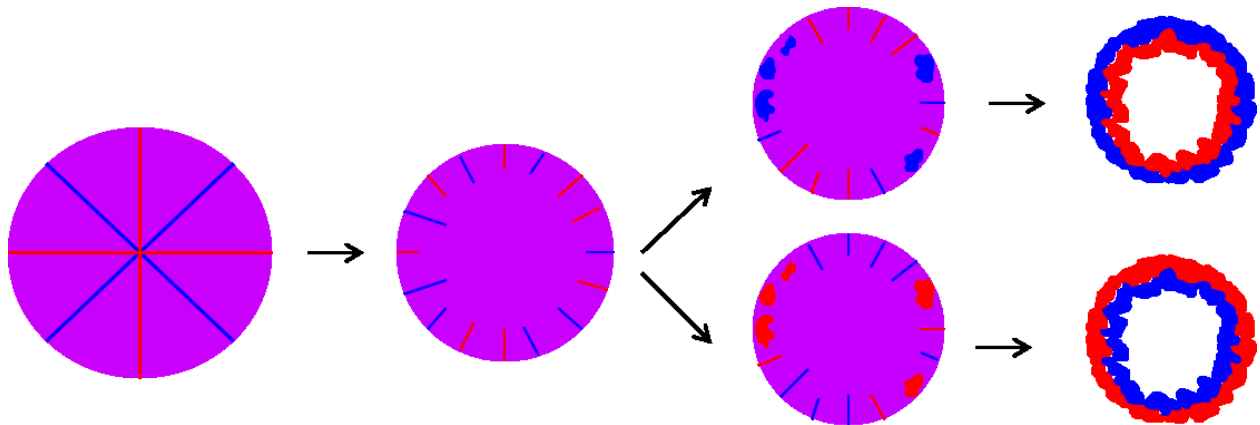
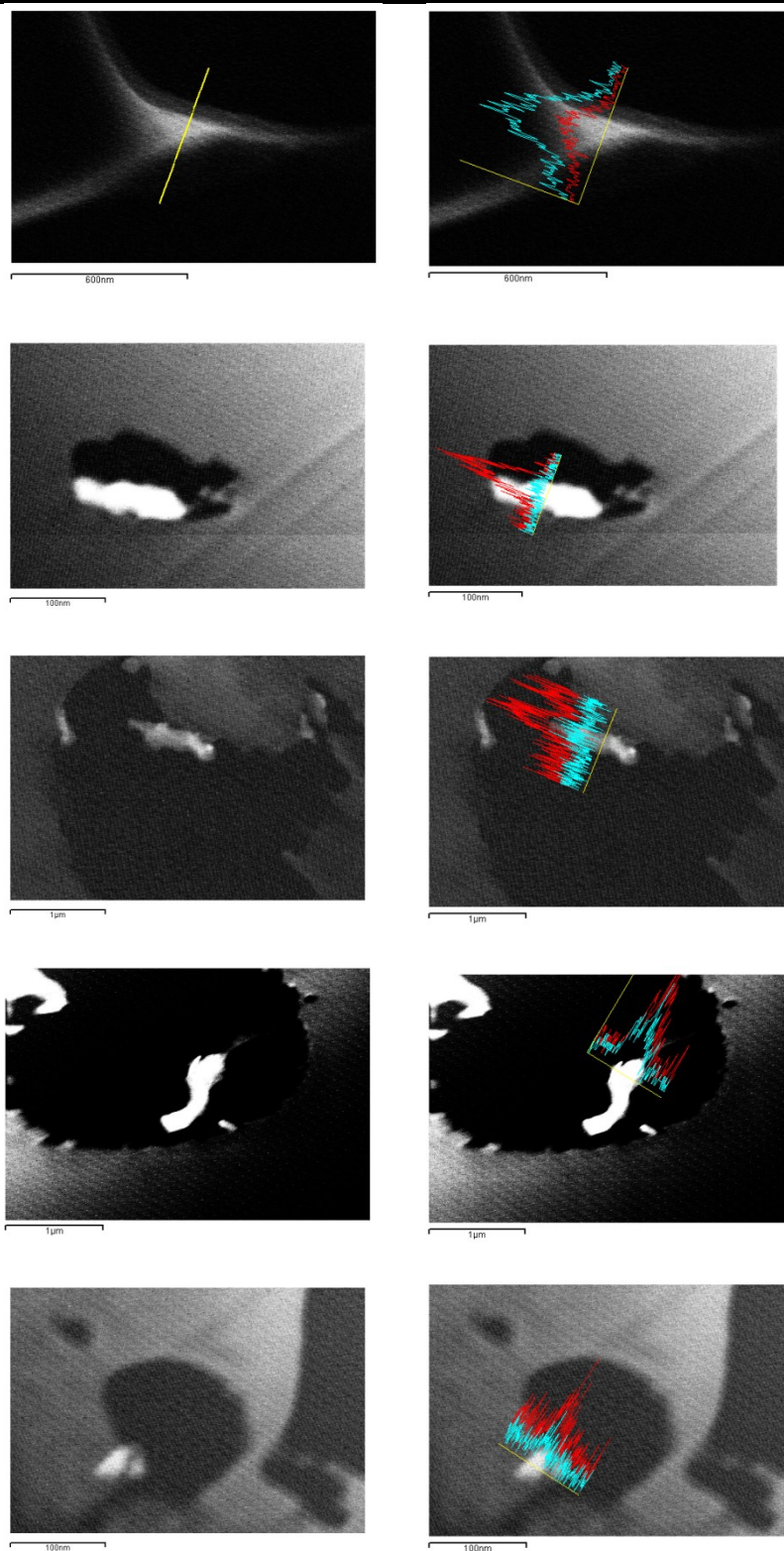


Figure E. 1 Particle formation process of a multicomponent droplet. Crystallization kinetics influences the distribution of the chemical components on the surface and through the shell thickness.

The composition of the chemical components along the shell thickness has been recorded using a S-TEM. In the publication shown in Chapter 5, only two pictures of the sectioned microparticles

are shown. Therefore, Table E. 1 shows some images of sectioned microparticles recorded using a TEM. On the right hand side, the signal of chemical elements of sodium and potassium is shown.

Table E. 1 Examples of images of sectioned microparticles recorded with a TEM.



In the publication shown in Chapter 5, time to reach saturation and time for crystallization are shown. Precipitation and crystallization window can be easily obtained simply subtracting from the time to constant aerodynamic diameter, the time to reach saturation and time for crystallization, Figure E. 2.

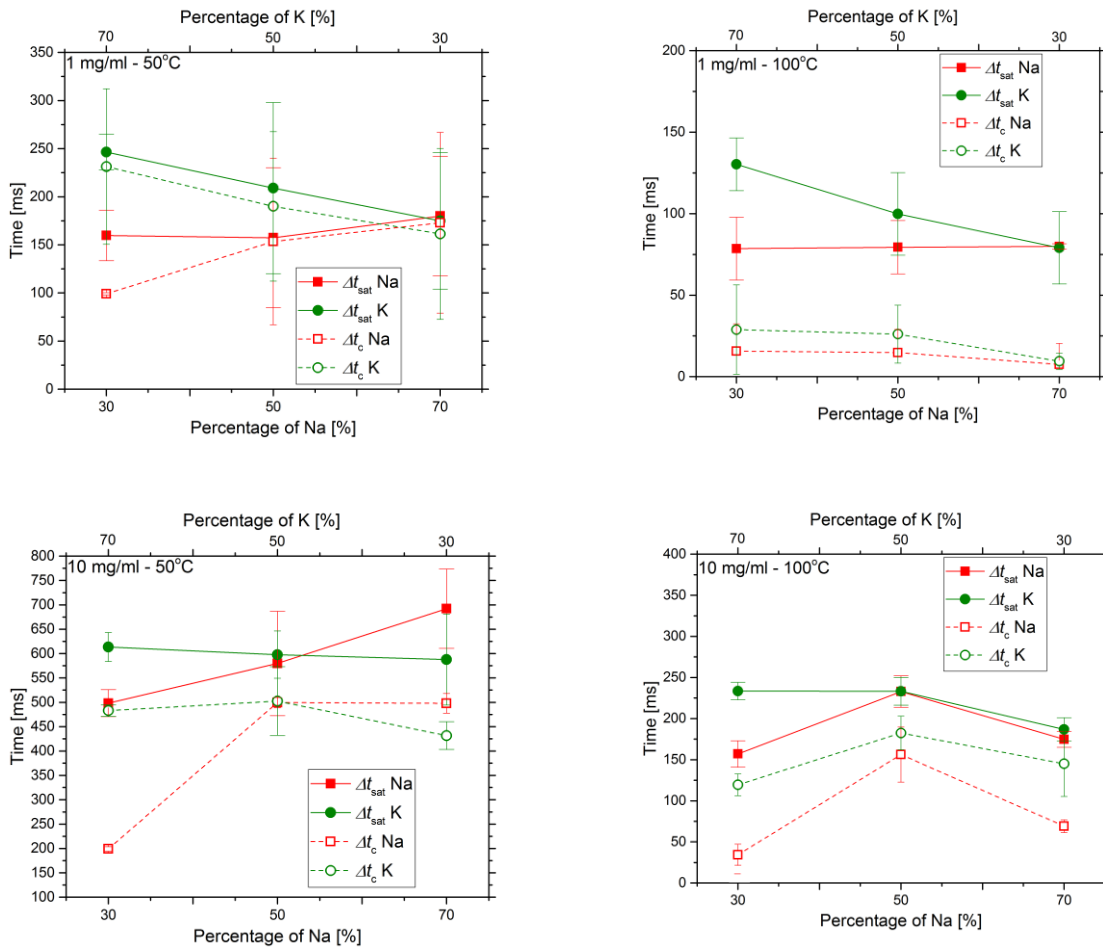


Figure E. 2 Precipitation and crystallization window for all the cases shown in Chapter 5.

Final dried microparticles have been analyzed for different properties. One of them was the solid state. In Chapter 5, only the Raman spectroscopy of two cases was shown: 10 mg/ml at 50°C and 100°C.

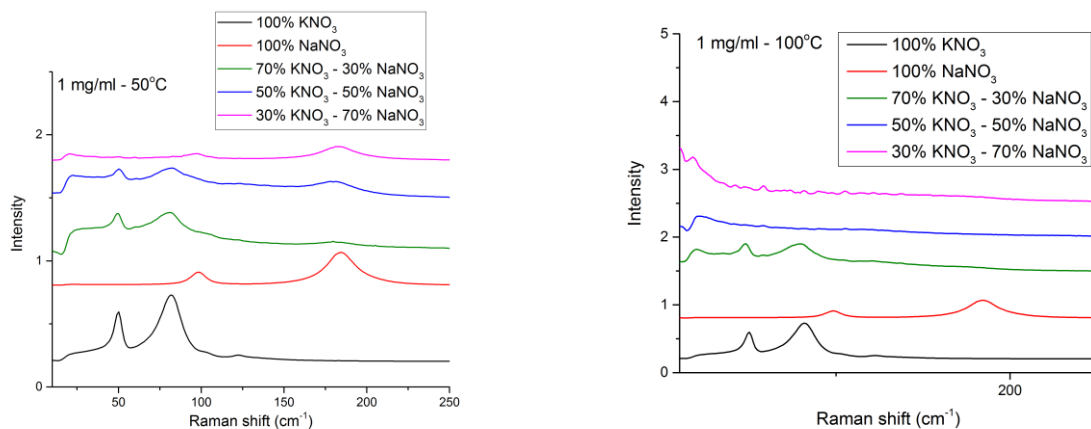


Figure E. 3 Raman spectroscopy of the cases of 1 mg/ml at 50°C and 100°C.

Lastly, the analysis of the distribution of the chemical components in the final dried microparticle was achieved through SEM/EDS, for the distribution on the surface, and S-TEM, for the distribution through the shell thickness of the final dried microparticles. While the images collected using the SEM/EDS are all shown in the publication, the images of S-TEM have been only partially shown. Microparticles have been cut with an ultramicrotome and then analyzed with S-TEM. A line was drawn from the outside to the inside of the shell and, thus, the center of the signal intensity more shifted to the left indicates the component that mostly distributes on the surface.

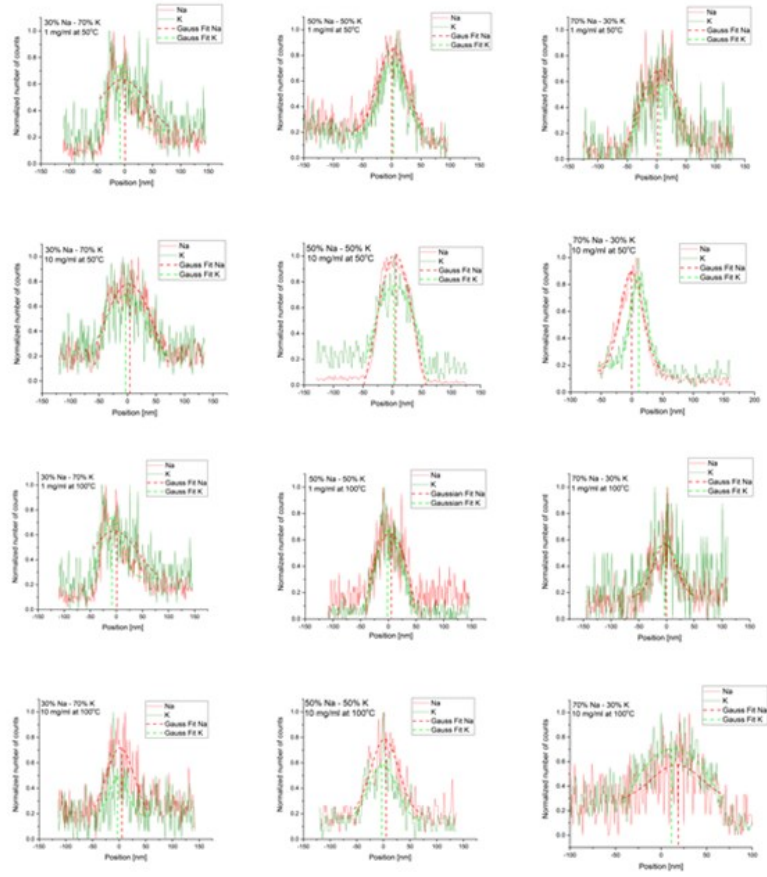


Figure E. 4 S-TEM images of the distribution of the chemical components through the shell thickness of the final dried microparticles.